SAPIENZA
UNIVERSITÀ DI ROMA

Analysis of Actual Multiconductor Transmission Lines: Effects of Non-uniformities and Nonlinearities

Department of Astronautical, Electrical and Energy Engineering.

Ph.D. in Electrical Engineering – Ph.D. Program XXXV

Candidate

Erika Stracqualursi

ID number 1646310

Thesis Advisor

Prof. Salvatore Celozzi

October 2022

Thesis defended on January 17, 2023

Analysis of Actual Multiconductor Transmission Lines: Effects of Non-uniformities and Nonlinearities

Ph.D. Thesis. Sapienza – University of Rome

This thesis has been typeset by LaTeX and the Sapthesis class.

Version: January 17, 2023

Author's email: erika.stracqualursi@uniroma1.it

To my family,
of today and tomorrow

Acknowledgments

My thanks and gratitude go to Professor Salvatore Celozzi for the given opportunity, for supervising and mentoring my work, and to Professor Rodolfo Araneo for supporting my progress. I am dearly grateful for the time and knowledge that they shared with me.

My deepest thanks to Professor Pantelis N. Mikropoulos, and to the team of the High Voltage Laboratory of the Aristotle University of Thessaloniki, Greece, for welcoming me to their laboratory.

Thanks to my family and to everyone who has supported me with unconditional kindness.

Contents

Aim of the work **vii**

1 Multiconductor transmission lines: Time Domain analysis **1**
1.1 From Maxwell's equations to the telegrapher's equations . . . 2
1.1.1 Transient self-impedance . . . 6
1.1.2 Transient ground impedance . . . 7
1.2 Finite-Difference Time-Domain algorithm . . . 9
1.2.1 Lossless MTLs . . . 10
1.2.2 Lossy MTLs . . . 14
1.2.3 Lossy MTLs: implicit scheme . . . 18
1.3 Accuracy, stability and numerical dispersion . . . 22
1.3.1 Accuracy . . . 23
1.3.2 Stability . . . 24
1.3.3 Numerical dispersion . . . 25

2 Distributed and lumped non-uniformities **34**
2.1 Distributed non-uniformities: conductors' catenary . . . 35
2.1.1 Catenary staircase modelling . . . 37
2.1.2 Catenary model and FDTD code . . . 41
2.2 Lumped non-uniformities: periodical grounding, line terminations . . . 43

3 Distributed sources **46**
3.1 The modified telegrapher's equations . . . 47
3.1.1 Electromagnetic field computation . . . 50
3.1.2 Implicit FDTD expressions . . . 53
3.2 Return stroke models . . . 54
3.3 Lightning current waveforms . . . 56
3.3.1 Double-exponential waveform . . . 58
3.3.2 Cigré waveform . . . 59
3.3.3 Andreotti *et al.* waveform . . . 60
3.3.4 Javor *et al.* waveform . . . 61
3.3.5 Heidler *et al.* waveform . . . 61
3.4 Numerical results . . . 63

3.4.1 Electric field computation 63
3.4.2 Induced voltages 65
3.4.3 Catenary effect 68
3.5 Remarks on the adopted approximations 75

4 Distributed nonlinearities 82
4.1 Corona discharge in power lines 82
4.2 Implementation of corona effect for the FDTD scheme 83
4.2.1 Dynamic capacitance approach 84
4.2.2 Voltage-controlled current generator approach 85
4.3 Numerical results 86
4.3.1 Fast-front voltage source 86
4.3.2 Slow-front voltage source 93
4.3.3 Numerical implementation against experimental data . 97
4.4 Soil ionization in extended grounding systems 100

5 Lumped nonlinearities 105
5.1 Line arresters 106
5.1.1 MOVs Circuit model 106
5.1.2 Inclusion of the MOV in the FDTD scheme 107
5.2 Numerical results 112
5.2.1 Parameters setting 112
5.2.2 Results for an MTL equipped with MOVs 113
5.3 Soil ionization: concentrated grounding systems 130
5.3.1 Simulated arrangement 132

6 Frequency and transient response of actual grounding systems 138
6.1 Modelling the soil electrical permittivity and resistivity 140
6.1.1 Longmire and Smith model 141
6.1.2 Messier model 142
6.1.3 Portela model 142
6.2 Frequency response of grounding electrodes and grids 142
6.2.1 Validation 143
6.2.2 Grounding grid 143
6.2.3 Tower grounding systems 150

7 Multiconductor transmission lines: Frequency Domain analysis 166
7.1 Chain matrix analysis of power lines with periodical grounding 167
7.1.1 Computation of fundamental matrices 175
7.2 Numerical results 182
7.2.1 Influence of the line terminations 185
7.2.2 Influence of the grounding impedance modelling 195
7.2.3 Influence of the number of ground wires 198

Conclusions **208**

Appendix A Corona phenomenon **211**
A.1 Corona phenomenology 212
A.2 Corona inception and development 213
A.2.1 Microscopic level 214
A.2.2 Macroscopic level 216
A.2.3 Inception criterion 217
A.3 Corona inception formulas 217
A.4 Models for impulse corona development 221
A.4.1 Physics-based models 221
A.4.2 Empirical models 228
A.4.3 Circuit-based models 231
A.5 Comparison of the models sensitivity to the input parameters 234
A.5.1 Sensitivity curves for physics-based models 236
A.5.2 Sensitivity curves for empirical models 237
A.5.3 Sensitivity curves for circuit-based models 239
A.6 Discussion 240

Appendix B Hybrid method for grounding systems **249**
B.1 Circuit problem 252
B.1.1 Voltages enforcement 254
B.2 Electromagnetic problem 255
B.2.1 Numerical computation of Sommerfeld integrals 257
B.2.2 Spectral domain: TL equivalent problem 259

Appendix C Soil ionization **268**

List of acronyms **272**

Aim of the work

The analysis of transients in electrical networks has been a topic largely investigated in the literature for a long time; however, researchers are still focusing on this topic to progressively improve the available models of devices operating in the electrical system, and to increase the network reliability in case of undesired events (e.g., faults, direct or indirect lightning, etc.) or switching operations.

Adopting a systemic approach, at first different aspects involving transmission line modelling are analysed; the most relevant ones are identified, and chosen as the main focus of the presented research activity. This work aims at analysing transient events occurring along overhead multiconductor transmission lines, evaluating the impact of non-uniformities and nonlinearities, as lightning events, protective devices (surge arresters), and corona effect, on the magnitude of the predicted overvoltages. Although electromagnetic transients programs are available to perform these studies, equivalent circuits and models of electrical devices are frequently embedded and not accessible to the final user. To this aim, an implicit Finite-Difference Time-Domain algorithm with second order accuracy has been implemented in Fortran for the solution of the coupled telegrapher's equations. The main code has been integrated with additional routines, which have been developed to account for the nonlinear behaviour of surge arresters (modelled through lumped equivalent circuits), for the coupling with external electromagnetic fields produced by return stroke currents, and for the corona effect (as a nonlinear distributed physical phenomenon).

Further analysis has been performed in the frequency domain to assess the effect of additional ground wires, installed below the phase conductors, in mitigating the overvoltages across the insulators in lightning studies. In depth considerations are devoted to the validity of the approximation introduced when the tower grounding impedance is modelled by means of a resistive device. Both studies, primarily performed in the frequency domain, are suitable for time domain simulations, when included by means of inverse Fourier transforms and time domain convolutions (as to the transient impedance of grounding systems).

This thesis is organized into distinct chapters, in order to address the research topics and results in a systematic way.

The first chapter is devoted to the introduction of the Crank-Nicolson scheme for the solution of the telegrapher's equations written for the case of lossy multiconductor transmission lines. Each of the next chapters deals with the modeling of specific aspects relevant to the study of transients along transmission lines. The modeling of the conductors' catenary is described in Chapter 2; its effect is considered only in Chapter 3, along with the implementation of the modification of the telegrapher's equations, required to account for the coupling of the line with external electromagnetic fields. The effects of nonlinearities like corona and surge arresters are studied in Chapters 4 and 5, respectively, referring to conducted disturbances, mainly related to direct lightning strokes to the line. Ultimately, a focus on the grounding impendence offered by grounding systems at the towers' footing and the assessment of the contribution of additional ground wires installed above and below the phase conductors are presented in Chapters 6 and 7, through the analysis of results computed primarily by models developed in the frequency domain.

The original contributions in the field of transmission line modelling may be found in the following peer-reviewed works:

Reviewed journals

[J-1] E. Stracqualursi, R. Araneo, G. Lovat, A. Andreotti, P. Burghignoli, J. A. Brandão Faria, and S. Celozzi, "Analysis of metal oxide varistor arresters for protection of multiconductor transmission lines using unconditionally-stable Crank-Nicolson FDTD," *Energies*, vol. 13, no. 8, 2112, Apr. 2020

[J-2] G. Lovat, P. Burghignoli, R. Araneo, E. Stracqualursi, and S. Celozzi, "Analytical evaluation of the low-frequency magnetic shielding of thin planar magnetic and conductive screens," *IEEE Trans. Electromagn. Compat.*, vol. 63, no. 1, pp. 308–312, Feb. 2021

[J-3] E. Stracqualursi, R. Araneo, P. Burghignoli, G. Lovat, and S. Celozzi, "Unconditionally stable implicit schemes for transient analysis of lossy multiconductor lines," *IEEE Trans. Electromagn. Compat.*, vol. 63, no. 2, pp. 640–644, Apr. 2021

[J-4] G. Lovat, P. Burghignoli, R. Araneo, E. Stracqualursi, and S. Celozzi, "Closed-form LF magnetic shielding effectiveness of thin planar screens in coplanar loops configuration," *IEEE Trans. Electromagn. Compat.*, vol. 63, no. 2, pp. 631–635, Apr. 2021

[J-5] E. Stracqualursi, R. Araneo, and S. Celozzi, "The corona phenomenon in overhead lines: Critical overview of most common and reliable available models," *Energies*, vol. 14, no. 20, 6612, Oct. 2021

[J-6] E. Stracqualursi, R. Araneo, J. A. Brandão Faria, and A. Andreotti, "Application of the transfer matrix approach to direct lightning studies of overhead power lines with underbuilt shield wires part I: Theory," *IEEE Trans. Power Del.*, vol. 37, no. 2, pp. 1226–1233, Apr. 2022

[J-7] ——, "Application of the transfer matrix approach to direct lightning studies of overhead power lines with underbuilt shield wires part II: Simulation results," *IEEE Trans. Power Del.*, vol. 37, no. 2, pp. 1234–1241, Apr. 2022

[J-8] E. Stracqualursi, R. Araneo, and A. Andreotti, "The impact of different corona models on FD algorithms for the solution of multiconductor transmission lines equations," *High Voltage*, vol. 6, no. 5, pp. 822–835, Sep. 2021

[J-9] E. Stracqualursi, R. Araneo, J. A. Brandão Faria, and A. Andreotti, "Protection of distribution overhead power lines against direct lightning strokes by means of underbuilt ground wires," *Electric Power Systems Research*, vol. 202, 107571, Jan. 2022

[J-10] E. Stracqualursi, G. Pelliccione, S. Celozzi, and R. Araneo, "Tower models for power systems transients: a review," *Energies*, vol. 15, no. 13, 4893, Jul. 2022

[J-11] A. Andreotti, R. Araneo, J. A. Brandão Faria, J. He, E. Petrache, A. Pierno, and E. Stracqualursi, "On the role of shield wires in mitigating lightning-induced overvoltages in overhead lines-part I: a critical review and a new analysis," *IEEE Trans. Power Del.*, 2022

[J-12] ——, "On the role of shield wires in mitigating lightning-induced overvoltages in overhead lines-part II: Simulation results for practical configurations," *IEEE Trans. Power Del.*, 2022

Conference Proceedings

[C-1] E. Stracqualursi, R. Araneo, P. Burghignoli, S. Celozzi, and G. Lovat, "Offshore wind towers interaction through their grounding systems," in *2018 International Symposium on Electromagnetic Compatibility (EMC EUROPE)*. IEEE, 2018, pp. 908–912

[C-2] E. Stracqualursi, R. Araneo, J. A. Brandão Faria, and A. Andreotti, "Chain matrix analysis of periodically grounded power lines," in *2020 IEEE International Conference on Environment and Electrical Engineering and 2020 IEEE Industrial and Commercial Power Systems Europe (EEEIC/I&CPS Europe)*. IEEE, 2020, pp. 1–5

[C-3] E. Stracqualursi, R. Araneo, G. Lovat, and P. Burghignoli, "FDTD analysis of metal oxide surge arresters for protection of multiconductor transmission lines," in *2020 International Symposium on Electromagnetic Compatibility (EMC EUROPE)*. IEEE, 2020, pp. 1–5

[C-4] E. Stracqualursi and R. Araneo, "Transient impedance of grounding grids with different soil models," in *2021 IEEE International Conference on Environment and Electrical Engineering and 2021 IEEE Industrial and Commercial Power Systems Europe (EEEIC/I&CPS Europe)*. IEEE, 2021, pp. 1–6

[C-5] E. Stracqualursi, R. Araneo, and M. Mitolo, "On the measuring methods of the soil electrical resistivity," in *2021 IEEE International Conference on Environment and Electrical Engineering and 2021 IEEE Industrial and Commercial Power Systems Europe (EEEIC/I&CPS Europe)*. IEEE, 2021, pp. 1–6

[C-6] E. Stracqualursi, R. Araneo, J. A. Brandão Faria, P. Burghignoli, and A. Andreotti, "The Sommerfeld-Goubau theory for the transient response of towers," in *2022 20th International Conference on Harmonics & Quality of Power (ICHQP)*. IEEE, 2022, pp. 1–5

[C-7] E. Stracqualursi, R. Araneo, and A. Andreotti, "Preliminary assessment of protection of distribution lines against direct lightning strokes through multi-chamber arresters and shield wires," in *2022 IEEE International Conference on Environment and Electrical Engineering and 2022 IEEE Industrial and Commercial Power Systems Europe (EEEIC/I&CPS Europe)*. IEEE, 2022, pp. 1–5

[C-8] Z. G. Datsios, E. Stracqualursi, R. Araneo, P. N. Mikropoulos, and T. E. Tsovilis, "Estimation of the minimum backflashover current and backflashover rate of a 150 kV overhead transmission line: Frequency and current-dependent effects of grounding systems," in *2022 IEEE International Conference on Environment and Electrical Engineering and 2022 IEEE Industrial and Commercial Power Systems Europe (EEEIC/I&CPS Europe)*. IEEE, 2022, pp. 1–5

Chapter 1

Multiconductor transmission lines: Time Domain analysis

Notation

- N_{pc} number of power-carrying conductors (or phase conductors);
- N_{sw} number of shield wires;
- $N_{\mathrm{c}} = N_{\mathrm{pc}} + N_{\mathrm{sw}}$ total number of conductors (the ground is not included);
- $\boldsymbol{v}$ vector of node voltages[1], as continuous functions of space and time, of dimension $N_{\mathrm{c}} \times 1$;
- $\boldsymbol{i}$ vector of node currents, as continuous functions of space and time, of dimension $N_{\mathrm{c}} \times 1$;
- $\mathbf{V}$ vector of numerically computed node voltages, as functions of the discretized time and space, of dimension $N_{\mathrm{c}} \times 1$;
- $\mathbf{I}$ vector of numerically computed node currents, as functions of the discretized time and space, of dimension $N_{\mathrm{c}} \times 1$;
- $\mathbf{C}'$ matrix of per unit length capacitances, of dimension $N_{\mathrm{c}} \times N_{\mathrm{c}}$;
- $\mathbf{L}'_{\mathrm{ext}}$ matrix of per unit length external inductances, of dimension $N_{\mathrm{c}} \times N_{\mathrm{c}}$;
- Δx space step;
- Δt time step;
- $[\mathbf{1}]$ identity matrix of order N_{c}.

[1]Voltages are considered with respect to the ground, taken as reference. The ground is equipotential and the voltage drop along its surface is taken into account, as usual, by adding a ground impedance term to the conductors impedances.

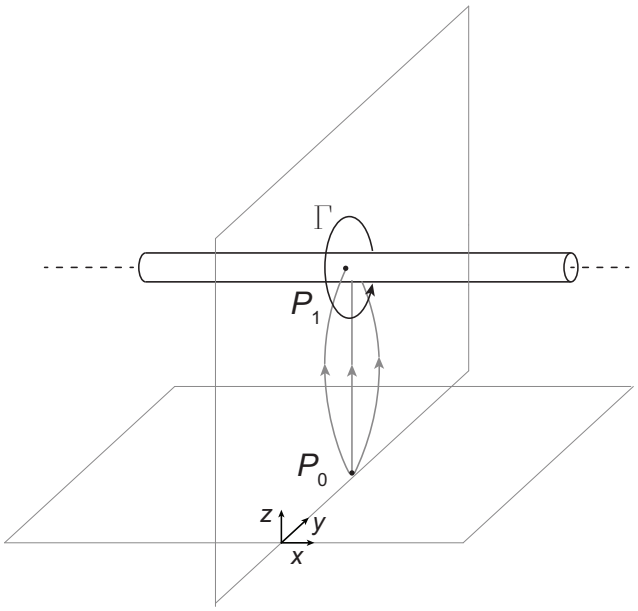

Figure 1.1. Infinite lossless conductor, running parallel to a PEC plane.

1.1 From Maxwell equations to the telegrapher's equations

Propagation along power lines is usually addressed by means of the telegrapher's equations [1]. The simplest case is that of an infinite conductor, at a constant height above a Perfect Electric Conductor (PEC) plane (as in Fig. 1.1); voltages and currents observed at position x along the line may be recovered by solving the following telegrapher's coupled equations in the Time Domain (TD):

$$-\frac{\partial v\left(x,t\right)}{\partial x} = L'_{\text{ext}}\frac{\partial i\left(x,t\right)}{\partial t} \tag{1.1a}$$

$$-\frac{\partial i\left(x,t\right)}{\partial x} = C'\frac{\partial v\left(x,t\right)}{\partial t}\,. \tag{1.1b}$$

Equations (1.1a) and (1.1b) are usually addressed to as the telegrapher's equations for a lossless Transmission Line (TL), where quantities C' and L'_{ext} correspond to the line per unit length (p.u.l.) capacitance and external inductance, respectively. It should be noted that modifications of (1.1), necessary to account for the coupling of the TL conductors with an external electromagnetic field, will be included in Chapter 3.

The main assumption underlying the derivation of the telegrapher's equations is the one allowing a unique definition of the conductor-to-ground voltage (i.e., a definition which is independent of the chosen integration path for the electric field) and of the current flowing along the conductor. The assumption consists in considering, in the case of lossless line over a PEC plane, the Transverse Electromagnetic (TEM) propagation of the electromagnetic field, i.e., the

electric and magnetic field to lay in the plane transverse to the direction of propagation. TEM modes may only be supported by conducting structures consisting of two or more conductors, with the advantage of the absence of cutoff frequencies [2] (unlike Transverse Electric (TE) and Transverse Magnetic (TM) modes, propagating only at frequencies above a specific cutoff frequency).

Equations (1.1) may be recovered by applying the Maxwell's equations and the other fundamental equations of electromagnetism recalled below. Fields, induction terms and current density vectors in the TD (in a medium characterised by electrical resistivity σ, electrical permittivity ϵ, and magnetic permeability μ) are in italic; underlined quantities correspond to vector quantities.

$$\nabla \times \underline{\mathcal{E}}\left(\underline{r}, t\right) = -\underline{\mathcal{J}}_{mi}\left(\underline{r}, t\right) - \frac{\partial \underline{\mathcal{B}}\left(\underline{r}, t\right)}{\partial t} \tag{1.2a}$$

$$\nabla \times \underline{\mathcal{H}}\left(\underline{r}, t\right) = \underline{\mathcal{J}}_{i}\left(\underline{r}, t\right) + \underline{\mathcal{J}}\left(\underline{r}, t\right) + \frac{\partial \underline{\mathcal{D}}\left(\underline{r}, t\right)}{\partial t} \tag{1.2b}$$

$$\nabla \cdot \left(\underline{\mathcal{J}}_{i}\left(\underline{r}, t\right) + \underline{\mathcal{J}}\left(\underline{r}, t\right)\right) = -\frac{\partial \left(\rho\left(\underline{r}, t\right) + \rho_{i}\left(\underline{r}, t\right)\right)}{\partial t} \tag{1.2c}$$

$$\nabla \cdot \underline{\mathcal{J}}_{mi}\left(\underline{r}, t\right) = -\frac{\partial \rho_{mi}\left(\underline{r}, t\right)}{\partial t} \tag{1.2d}$$

$$\underline{\mathcal{D}}\left(\underline{r}, t\right) = \int_{-\infty}^{+\infty} \epsilon\left(t - t'\right) \underline{\mathcal{E}}\left(\underline{r}, t'\right) \mathrm{d}t' \tag{1.2e}$$

$$\underline{\mathcal{B}}\left(\underline{r}, t\right) = \int_{-\infty}^{+\infty} \mu\left(t - t'\right) \underline{\mathcal{H}}\left(\underline{r}, t'\right) \mathrm{d}t' \tag{1.2f}$$

$$\underline{\mathcal{J}}\left(\underline{r}, t\right) = \int_{-\infty}^{+\infty} \sigma\left(t - t'\right) \underline{\mathcal{E}}\left(\underline{r}, t'\right) \mathrm{d}t' \tag{1.2g}$$

In (1.2), $\underline{\mathcal{E}}$ is the electric field, $\underline{\mathcal{D}}$ the electric displacement, $\underline{\mathcal{H}}$ the magnetic field, $\underline{\mathcal{B}}$ the magnetic induction, $\underline{\mathcal{J}}$ the electric current density, and ρ the electric charge density.

Along with Maxwell's equations (i.e., (1.2a) and (1.2b)), equations (1.2c) and (1.2d) express the continuity of electric and magnetic currents, relating these quantities to the electric and magnetic charge densities, respectively. Equations (1.2e), (1.2f), and (1.2g) are the constitutive relations of the medium in which the Electromagnetic (EM) field is to be computed; in order for the latter expressions to hold, the medium has been supposed linear, homogeneous, isotropic, stationary, spatially non-dispersive, but time-dispersive (i.e., the effect may depend on previous values assumed by the corresponding cause, and the parameters are frequency-dependent). In the lossless case, the Right Hand Side (RHS) of (1.2g) is zero, assuming a null value for the electric conductivity of the medium surrounding the conductor.

Considering the configuration in Fig. 1.1, in the absence of electric and magnetic sources of current density (i.e., $\underline{\mathcal{J}}_{i} = 0$ and $\underline{\mathcal{J}}_{mi} = 0$, associated with the impressed electric charge density ρ_i and magnetic charge density ρ_{mi}), and assuming lossless TEM propagation (i.e., the magnetic and electric field

vectors only display their transversal components in the plane yz), equations (1.2a) and (1.2b) may be written introducing the transverse and longitudinal operators ∇_t and ∇_x:

$$(\nabla_t + \nabla_x) \times \underline{\mathcal{E}}_t(\underline{r}, t) = -\frac{\partial \underline{\mathcal{B}}_t(\underline{r}, t)}{\partial t} \tag{1.3a}$$

$$(\nabla_t + \nabla_x) \times \underline{\mathcal{H}}_t(\underline{r}, t) = \frac{\partial \underline{\mathcal{D}}_t(\underline{r}, t)}{\partial t} \tag{1.3b}$$

with

$$\nabla = \hat{x}\frac{\partial}{\partial x} + \left(\hat{y}\frac{\partial}{\partial y} + \hat{z}\frac{\partial}{\partial z}\right) = \nabla_x + \nabla_t\,. \tag{1.4}$$

In (1.3b), the contribution of the displacement currents is only in the transverse plane, since the assumption of isotropic medium forces the electric displacement vector to be parallel to the electric field; the decomposition of expressions (1.3) in their components along the transverse and the longitudinal direction allows to derive the following:

$$\nabla_t \times \underline{\mathcal{E}}_t = 0 \tag{1.5a}$$

$$\nabla_t \times \underline{\mathcal{B}}_t = 0\,, \tag{1.5b}$$

in which the space and time dependence of the fields is omitted for brevity. Equations (1.5) are the same describing conservative fields, i.e., fields with zero circulation. Since the line integral of such fields between two points does not depend on the chosen integration path (which is indeed a feature of static fields), the conductor's voltage and current are uniquely defined:

$$v(x,t) = -\int_{P_0}^{P_1} \underline{\mathcal{E}}_t \cdot \mathrm{d}\underline{l} \tag{1.6a}$$

$$i(x,t) = \oint_{\Gamma} \underline{\mathcal{H}}_t \cdot \mathrm{d}\underline{l}\,, \tag{1.6b}$$

where P_0 is a point at null reference potential, P_1 is a point lying on the conductor's surface, and Γ is a closed path lying on the plane transversal to the direction of propagation (Fig. 1.1).

With reference to the ideal configuration in Fig. 1.2, computing the flux of the electric field curl through the surface S, and the volume integral of the term on the Left Hand Side (LHS) of (1.2c) in the cylindrical volume τ, the telegrapher's equations are recovered [1].

When a more realistic case is to be analyzed, the influence of conductors losses and ground should be accounted. Hence, the resulting longitudinal voltage drops along the conductor and the ground return path should be considered. For instance, the voltage drop along the conductor will be given by:

$$v(x+\Delta x, t) - v(x,t) = -\int_{x}^{x+\Delta x} \mathcal{E}_x(\underline{r}, t)\, dx \tag{1.7}$$

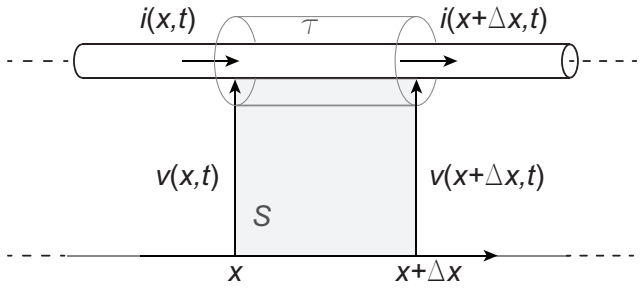

Figure 1.2. Integration domains to derive the telegrapher's equations from Maxwell's equations.

with $\underline{r}$ laying on the conductor surface. Therefore, when lossy ground and conductors are considered, a non-zero component of the longitudinal electric field arises. However, $\mathcal{E}_x$ is assumed not to alter sensibly the distribution of the electromagnetic field in the transverse plane; in other words, the TEM mode is assumed to be predominant compared to other propagating modes associated with the longitudinal component $\mathcal{E}_x$. The relations derived for the case of perfect TEM propagation are considered to hold in the transverse plane, allowing to keep the unique definition for the voltage and the current along the line. This condition is referred to as *quasi-TEM* propagation. Extending the telegrapher's equations associated with the simple case in Fig. 1.2, to the case of a Multiconductor Transmission Line (MTL) with conductors of infinite length, parallel to the ground plane, and including skin-effect and losses both for the conductors and the ground (i.e., assuming quasi-TEM propagation of the electromagnetic field), the following coupled equations hold:

$$-\frac{\partial \boldsymbol{v}(x,t)}{\partial x} = \int_0^t \mathbf{Z}'_\zeta(t-\tau)\frac{\partial \boldsymbol{i}(x,\tau)}{\partial \tau}\mathrm{d}\tau + \mathbf{L}'_{\mathrm{ext}}\frac{\partial \boldsymbol{i}(x,t)}{\partial t} \tag{1.8a}$$

$$-\frac{\partial \boldsymbol{i}(x,t)}{\partial x} = \mathbf{C}'\frac{\partial \boldsymbol{v}(x,t)}{\partial t} + \mathbf{G}'\boldsymbol{v}(x,t) \tag{1.8b}$$

The matrix of conductances $\mathbf{G}'$ accounts for losses in the transversal plane; it is usually neglected in studies of propagation along overhead power lines due to the minor value of the air electrical conductivity ($\sigma < 10^{-9}$ S/m [3]). The simulation of distributed corona discharges along the line may introduce additional modifications to (1.8b), which are analysed in Sec. 4.1 and Appendix A.

It should be noticed that the p.u.l. voltage drops associated with the ground return path and with the conductors finite conductivity are obtained through the following:

$$\mathscr{L}^{-1}\left[\mathbf{Z}'(s)\,\mathbf{i}(s)\right] = \mathscr{L}^{-1}\left[\frac{\mathbf{Z}'(s)}{s}s\mathbf{i}(s)\right] = \int_0^\infty \mathbf{Z}'_\zeta(t-\tau)\frac{\partial \boldsymbol{i}(x,\tau)}{\partial \tau}\mathrm{d}\tau \tag{1.9}$$

with

$$\mathscr{L}^{-1}\left[\frac{\mathbf{Z}'(s)}{s}\right] = \mathbf{Z}'_{\zeta}(t)\ . \tag{1.10}$$

In (1.9) and (1.10), $\mathbf{Z}'(s)$ and $\mathbf{i}$ are the matrix of p.u.l. impedances, and the vector of line currents, respectively (in the Laplace Domain); the operator $\mathscr{L}^{-1}$ denotes the inverse Laplace transform, and s is the variable in the Laplace Domain. All sources are assumed to be null at time instants $t < 0$, and no energy is stored at $t = 0$ in energy storage components (i.e., capacitors and inductors). The transform is written in terms of the current derivative in order to allow the computation of the transient impedance in the TD by means of (1.10).

In the case of an MTL consisting in N_c conductors over a lossy ground (with relative electric permittivity ϵ_{rg}, and finite conductivity σ_g), $\mathbf{Z}'_{\zeta}(t)$ denotes the matrix of p.u.l. transient impedances[2]; through suitable approximations and under specific assumptions (which will be clarified in the following sections) $\mathbf{Z}'_{\zeta}(t)$ accounts in the TD for the frequency-dependent impedance offered by the ground return path and by the conductors. Hence, the elements of $\mathbf{Z}'_{\zeta}(t)$ are defined as

$$z_{\zeta_{ij}}'(t) = \begin{cases} Z_{\zeta_{ij}}'(t) + Z'_{ii}(t)\,, & i = j \\ Z_{\zeta_{ij}}'(t)\,, & i \neq j. \end{cases} \tag{1.11}$$

In (1.11), the terms $Z_{\zeta_{ij}}'$ and Z'_{ii} account for the ground return path impedance and for the internal impedance of the i^{th} conductor, respectively.

The frequency-dependence of these contributions (e.g., frequency dependence of the skin effect for each conductor) results in a TD convolution, namely, the first term on the RHS of (1.8a).

The telegrapher's equations and the validity of the approximation of TEM mode propagation hold up to frequencies such that the geometrical dimensions of the MTL in the transverse plane are electrically short; if the line dimensions are such to allow fields propagation in the transversal plane, equations (1.1a) and (1.1b) would not account for the complete solution for the EM fields, neglecting other coexisting propagating modes, besides the TEM one.

1.1.1 Transient self-impedance

The term $Z'_{ii}(t)$, accounting for the self-impedance of the i^{th} solid cylindrical conductor with radius r_0, is derived by means of the original theory by Schelkunoff on coaxial transmission lines developed in the Frequency Domain (FD) [4], and of Timotin's [5] and Celozzi's [6] approximation for its direct

[2]In the literature, the alternative term *transient resistance* may be used to address the same quantity. Indeed, the term *impedance* rigourously applies to Frequency Domain quantities only; however, some authors still adopt this term in the Time Domain, to recall that it accounts for both the resistive and reactive components of its Frequency Domain counterpart.

application in the TD. In fact, the p.u.l. self-impedance $Z'_{ii}(\omega)$ of a cylindrical conductor (assuming the metallic material to be linear, homogeneous, non-dispersive both in time and in space) is frequency-dependent, due to skin effect developing at increasing frequencies and affecting both the resistive and the inductive components of $Z'_{ii}(\omega)$. A closed formula for the self term $Z'_{ii}(\omega)$ is available in the FD:

$$Z'_{ii}(\omega) = \frac{\eta_{\mathrm{w}}}{2\pi r_0} \frac{I_0(\beta_{\mathrm{w}} r_0)}{I_1(\beta_{\mathrm{w}} r_1)} \tag{1.12}$$

where ω is the angular frequency, $\eta_{\mathrm{w}} = \sqrt{j\omega\mu_{\mathrm{w}}/\sigma_{\mathrm{w}}}$, $\beta_{\mathrm{w}} = \eta_{\mathrm{w}}\sigma_{\mathrm{w}}$; μ_{w} and σ_{w} are the magnetic permeability and electric conductivity of the conductor's material, respectively.

It is a necessary condition (yet, not sufficient) that a function defined in the s domain goes to zero for $s \to \infty$ in order for its inverse Laplace transform to exist [7]. Hence, referring to the approach presented in the previous section, the conductor's impedance is included by computing the transform of the impedance integral with respect to time (i.e., dividing (1.12) by s in the Laplace domain), and *not* the inverse Laplace transform of $Z'_{ii}(\omega)$ itself. Hence, the following [8]:

$$Z'_{ii}(t) = \mathcal{L}^{-1}\left[\frac{Z'_{ii}(s)}{s}\right] = \frac{1}{\pi\sigma_{\mathrm{w}} r_0^2}\left[1 + \sum_{k=1}^{\infty} \exp\left(-x_{k,1}^2 t/\tau_c\right)\right] \tag{1.13}$$

with $\tau_c = \mu_{\mathrm{w}}\sigma_{\mathrm{w}} r_0^2$. In (1.13), $x_{k,1}$ are real quantities, corresponding to the consecutive zeros of the Bessel function of the first kind and order 1. The infinite summation in (1.13) may be truncated after approximately 30 terms when transients in the range of microseconds to milliseconds are to be assessed [6]. Herein, a larger number of terms is considered, including all the consecutive terms which fulfil the condition $\exp\left(-x_{k,1}^2 t/\tau_c\right) > \epsilon_t$, where the tolerance ϵ_t is set to 10^{-12}.

1.1.2 Transient ground impedance

Different approaches have been proposed in the literature to account for the ground return in dealing with power transmission through overhead lines [9]. The well-known theory by Carson [10] is often applied to this aim. In the work by Woodhouse, the assumptions underlying the derivation of Carson's formulas are highlighted and clarified [11]. Indeed, the validity of Carson's theory is limited to low frequency applications, as long as the ground may be approximated as a good conductor, i.e., at frequencies much lower than a critical value given by $f_{\mathrm{cr}} = \frac{\sigma_{\mathrm{g}}}{2\pi\epsilon_{\mathrm{g}}}$ with $\epsilon_{\mathrm{g}} = \epsilon_{r\mathrm{g}}\epsilon_0$. For instance, for common values of the ground conductivity $\sigma_{\mathrm{g}} = 0.01$ S/m and of the relative electric permittivity $\epsilon_{r\mathrm{g}} = 10$, $f \ll f_{\mathrm{cr}} = 17.98$ MHz. When it comes to lightning studies, the frequency spectra covered by first stroke currents are relevant up to hundreds of

kHz; however, subsequent stroke currents may present non-negligible frequency components up to 10 MHz, due to their steeper fronts. The latter cases may require an improved formulation of the transient ground impedance, more accurate at higher frequencies, accounting for the displacement currents in the ground. To this aim, Semlyen's theory may represent a solution [12]. Recalling the useful classification proposed by Semlyen, three working regions in the plane (ρ_{g}, f) with $\rho_{\mathrm{g}} = 1/\sigma_{\mathrm{g}}$, are identified: region A, where the ground may be approximated as a conductor (at frequencies $f \ll f_{\mathrm{cr}}$), and Carson's theory may be adopted; region B, where the ground may be treated as an insulating material (for frequency values above about $2f_{\mathrm{cr}}$); a transition region where both conductive and displacement currents should be taken into consideration.

Therefore, the following expressions in the Laplace domain (or, equivalently, in the FD) for the p.u.l. self $Z'_{\mathrm{g},ii}$ and mutual term $Z'_{\mathrm{g},ij}$ of the matrix of p.u.l. impedances due to the ground return path are adopted for region A

$$Z^{\mathrm{A}\ \prime}_{\mathrm{g},ii}(s) = \frac{s\mu_{\mathrm{g}}}{\pi}\int_0^{\infty} \frac{\exp\left(-2h_i\lambda\right)}{\lambda + \sqrt{s\sigma_{\mathrm{g}}\mu_{\mathrm{g}} + \lambda^2}}\mathrm{d}\lambda \tag{1.14a}$$

$$Z^{\mathrm{A}\ \prime}_{\mathrm{g},ij}(s) = \frac{s\mu_{\mathrm{g}}}{\pi}\int_0^{\infty} \frac{\exp\left(-\left(h_i + h_j\right)\lambda\right)\cos\left(\left|x_i - x_j\right|\lambda\right)}{\lambda + \sqrt{s\sigma_{\mathrm{g}}\mu_{\mathrm{g}} + \lambda^2}}\mathrm{d}\lambda \tag{1.14b}$$

and for region B

$$Z^{\mathrm{B}\ \prime}_{\mathrm{g},ii}(s) = \frac{1}{2\pi h_i}\sqrt{\frac{s\mu_{\mathrm{g}}}{\sigma_{\mathrm{g}} + s\epsilon_{\mathrm{g}}}} \tag{1.15a}$$

$$Z^{\mathrm{B}\ \prime}_{\mathrm{g},ij}(s) = \frac{h_i + h_j}{\pi\left(\left(x_i - x_j\right)^2 + \left(h_i + h_j\right)^2\right)}\sqrt{\frac{s\mu_{\mathrm{g}}}{\sigma_{\mathrm{g}} + s\epsilon_{\mathrm{g}}}} \tag{1.15b}$$

from Carson's theory [10] and Semlyen's theory [12], respectively.

The corresponding TD expressions, given the transform technique displayed in (1.10), valid in region A (for slow transients or late times), and in region B (for fast transients or early times) are here denoted with $Z^{\mathrm{A}\ \prime}_{\zeta,ij}(t)$ and $Z^{\mathrm{B}\ \prime}_{\zeta,ij}(t)$, respectively. Their expressions in the TD are to be found in [13].

For transients covering a large frequency spectrum, the following expression is implemented to deal with the transition region (between regions A and B) [13]:

$$Z'_{\zeta,ij}(t) = \exp\left(-\frac{5t}{\tau_L}\right) Z^{\mathrm{B}\ \prime}_{\zeta,ij}(t) + \left(1 - \exp\left(-\frac{5t}{\tau_L}\right)\right) Z^{\mathrm{A}\ \prime}_{\zeta,ij}(t) \tag{1.16}$$

where $\tau_L = 1/\left(f_L\right)$, and the limiting frequency f_L is given by[3]:

$$f_L = 0.1\min\left(f_{\mathrm{cr}}, \frac{c_0}{2\pi h_{\max}}\right). \tag{1.17}$$

[3] $h_{\max}$ denotes the height of the conductors for self terms, and the average height of the conductors above the ground for mutual terms.

The exponential expression in (1.16) is adopted for $Z'_{\zeta,ij}$ to be suitably computed by the recursive algorithm applied in the developed code for the computation of the voltage drops associated with the conductors internal impedances and ground impedances, which is based on the Prony's algorithm (introduced in the following sections).

1.2 Finite-Difference Time-Domain algorithm

The telegrapher's equations, as derived from Maxwell's equations under the aforementioned assumptions, are to be solved to study propagation of voltage and current waves along power lines, given some boundary conditions at the terminations of the line.

In order to get a numerical solution of the telegrapher's equations, those are first written in terms of a set of finite-difference equations. Herein, the fundamental definitions and notations to deal with Finite-Difference Time-Domain (FDTD) equations are introduced.

Two one-step algorithms (according to the rigorous definition given in Sec. 1.3) will be considered for the solution of (1.1): the explicit algorithm (in Sec. 1.2.1), known as the *Leap-Frog algorithm*, and an implicit algorithm, namely the *Crank-Nicolson algorithm* (in Sec. 1.2.1).

For the sake of clarity, the case of a single conductor parallel to the horizontal ground plane is illustrated first. At the initial stage, the space and time domains for simulations are to be defined, i.e., the total length of the line under study and time frame $t \in [0, T]$ (T being the final time instant). The total length of the line L is divided into N_{sp} subsequent spans.

Solutions of the telegrapher's equations (1.1) are computed numerically discretizing both the space and the time domains into multiple space and time steps, denoted with Δx and Δt, respectively. Under the assumption of TEM propagation along the line, the numerical solution accounts for propagation in the x-direction only, and recurs to statics relations for the electric and magnetic fields in the transverse plane. In particular, voltages are computed at nodes k, with $0 \leq k \leq N_{\Delta x}$; a suitable Δx should be chosen in order to get $L = N_{\Delta x} \cdot \Delta x$, with $N_{\Delta x} \in \mathbb{N}$. Likewise, current nodes are located at $k + 1/2$, with $0 < k < (N_{\Delta x} - 1)$. In Fig. 1.3, the equivalent circuit of two adjacent line cells Δx is depicted, along with the nomenclature adopted for the nodes at which voltages and currents are evaluated.

A remark is needed as to the choice of the discretization steps. Postponing to the devoted Sec. 1.3 the discussion of the requirements to be fulfilled by Δx and Δt to guarantee the stability of the adopted FDTD updating scheme, some considerations are necessary with respect to the transients to be simulated. In fact, the steps Δx and Δt should ensure the proper sampling of the TD waveforms, given the expected frequency content, hence, the steepness of their fronts.

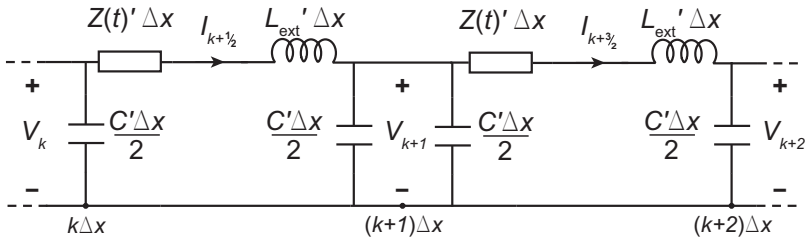

Figure 1.3. Equivalent circuit of adjacent cells, related to the discretization of a generic single-conductor TL.

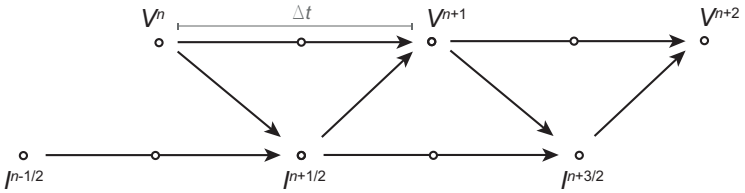

Figure 1.4. Schematic representation of the 1D Leap-Frog updating scheme for voltages and currents.

In the following section, the discretized equations for the explicit and implicit updating schemes are derived, while Sec. 1.2.3 describes the equations adopted as boundary conditions at the line terminations.

1.2.1 Lossless MTLs

This section is devoted to lossless TLs, neglecting losses both in the conductor and in the earth return path. Despite being a theoretical case, not reproducing the real operation conditions of TLs, the study of lossless MTLs still represents a valuable benchmark and an interesting case to be dealt with through FDTD schemes.

Figure 1.3 displays the distributed-parameters equivalent circuit of two adjacent cells of a generic TL (for clarity, the circuit refers to a single-conductor line). The superscript, denoting the time instant at which numerical counterparts of voltages and currents are evaluated, is omitted, since it is characteristic of the applied scheme. As to lossless TLs, $Z'(t) = 0$ (the term $Z'(t)$ includes the internal and ground transient impedances).

Explicit scheme solution

Equations (1.1) have been usually solved through a one-dimensional FDTD method [14]. Applying the Euler method, the following difference equations

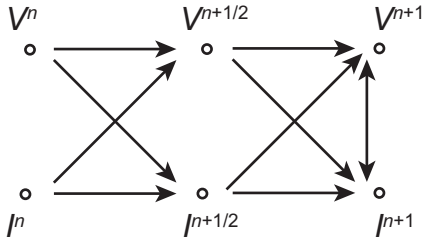

Figure 1.5. Schematic representation of the 1D CN updating scheme for voltages and currents.

are derived for a lossless MTL:

$$-\frac{\mathbf{V}_{k+1}^{n}-\mathbf{V}_{k}^{n}}{\Delta x}=\mathbf{L}'_{\text{ext}}\frac{\mathbf{I}_{k+\frac{1}{2}}^{n+\frac{1}{2}}-\mathbf{I}_{k+\frac{1}{2}}^{n-\frac{1}{2}}}{\Delta t} \tag{1.18a}$$

$$-\frac{\mathbf{I}_{k+\frac{1}{2}}^{n+\frac{1}{2}}-\mathbf{I}_{k-\frac{1}{2}}^{n+\frac{1}{2}}}{\Delta x}=\mathbf{C}'\frac{\mathbf{V}_{k}^{n+1}-\mathbf{V}_{k}^{n}}{\Delta t}\,. \tag{1.18b}$$

To ensure second order accuracy (see Sec. 1.3.1), a time marching Leap-Frog (LF) scheme [15] is used in (1.18); voltages and currents are not collocated in space, being their respective nodes shifted of $\Delta x/2$; likewise, they are not collocated in time, but shifted by $\Delta t/2$. A sketch of the updating algorithm for the unknown variables is depicted in Fig. 1.4. The method allows to directly update voltages and currents vectors from their known values at the previous time step, by rearranging (1.18) suitably

$$\mathbf{I}_{k+\frac{1}{2}}^{n+\frac{1}{2}}=\mathbf{I}_{k+\frac{1}{2}}^{n-\frac{1}{2}}-\left[\frac{\mathbf{L}'_{\text{ext}}}{\Delta t}\right]^{-1}\frac{\mathbf{V}_{k+1}^{n}-\mathbf{V}_{k}^{n}}{\Delta x} \tag{1.19a}$$

$$\mathbf{V}_{k}^{n+1}=\mathbf{V}_{k}^{n}-\left[\frac{\mathbf{C}'}{\Delta t}\right]^{-1}\frac{\mathbf{I}_{k+\frac{1}{2}}^{n+\frac{1}{2}}-\mathbf{I}_{k-\frac{1}{2}}^{n+\frac{1}{2}}}{\Delta x}\,, \tag{1.19b}$$

resulting in a fast updating scheme, and in a trivial translation into numerical code. As a drawback, the choice of the steps Δx and Δt depends on the fulfilment of the Courant–Friedrichs–Lewy (CFL) condition (which will be discussed in Sec. 1.3.2).

Implicit scheme solution

The Crank-Nicolson (CN) scheme is a second order accurate unconditionally stable scheme that allows to study the voltage and current waves propagation along the MTL by splitting each time step Δt into two sub-steps $\Delta t/2$ [16]. The method is also equivalent to the single average Alternating Direction Implicit (ADI) scheme [17]. The space mesh for the evaluation of voltages and currents corresponds to the one adopted by the LF scheme (i.e., nodes of voltages and

currents are separated by half a step $\Delta x/2$), yet they are collocated in time (i.e., both computed at time instants $n\Delta t$), unlike the LF scheme. The first *explicit* sub-step is based on an Euler forward time difference approximation of the derivatives (see Sec. 1.3) computed at time $n\Delta t$:

$$-\frac{\mathbf{V}_{k+1}^{n}-\mathbf{V}_{k}^{n}}{\Delta x}=\mathbf{L}'_{\text{ext}}\frac{\mathbf{I}_{k+\frac{1}{2}}^{n+\frac{1}{2}}-\mathbf{I}_{k+\frac{1}{2}}^{n}}{\Delta t/2} \tag{1.20a}$$

$$-\frac{\mathbf{I}_{k+\frac{1}{2}}^{n}-\mathbf{I}_{k-\frac{1}{2}}^{n}}{\Delta x}=\mathbf{C}'\frac{\mathbf{V}_{k}^{n+\frac{1}{2}}-\mathbf{V}_{k}^{n}}{\Delta t/2}\ . \tag{1.20b}$$

The second *implicit* sub-step is based on a Euler backward time difference approximation of the derivatives computed at time $(n+1)\,\Delta t$

$$-\frac{\mathbf{V}_{k+1}^{n+1}-\mathbf{V}_{k}^{n+1}}{\Delta x}=\mathbf{L}'_{\text{ext}}\frac{\mathbf{I}_{k+\frac{1}{2}}^{n+1}-\mathbf{I}_{k+\frac{1}{2}}^{n+\frac{1}{2}}}{\Delta t/2} \tag{1.21a}$$

$$-\frac{\mathbf{I}_{k+\frac{1}{2}}^{n+1}-\mathbf{I}_{k-\frac{1}{2}}^{n+1}}{\Delta x}=\mathbf{C}'\frac{\mathbf{V}_{k}^{n+1}-\mathbf{V}_{k}^{n+\frac{1}{2}}}{\Delta t/2}\ . \tag{1.21b}$$

Equations (1.21) are implicit since they must be solved in the unknown conductors voltages and currents at time $t=(n+1)\Delta t$, which cannot be directly expressed as functions of voltages and currents at previous time-instants. Manipulation of (1.20) and (1.21) leads to the relations below

$$-\frac{1}{2}\left(\frac{\mathbf{V}_{k+1}^{n+1}-\mathbf{V}_{k}^{n+1}}{\Delta x}+\frac{\mathbf{V}_{k+1}^{n}-\mathbf{V}_{k}^{n}}{\Delta x}\right)=\mathbf{L}'_{\text{ext}}\frac{\mathbf{I}_{k+\frac{1}{2}}^{n+1}-\mathbf{I}_{k+\frac{1}{2}}^{n}}{\Delta t} \tag{1.22a}$$

$$-\frac{1}{2}\left(\frac{\mathbf{I}_{k+\frac{1}{2}}^{n+1}-\mathbf{I}_{k-\frac{1}{2}}^{n+1}}{\Delta x}+\frac{\mathbf{I}_{k+\frac{1}{2}}^{n}-\mathbf{I}_{k-\frac{1}{2}}^{n}}{\Delta x}\right)=\mathbf{C}'\frac{\mathbf{V}_{k}^{n+1}-\mathbf{V}_{k}^{n}}{\Delta t}\ . \tag{1.22b}$$

The last two equations prove that the CN scheme is based on differences centered at time $\left(n+\frac{1}{2}\right)\Delta t$, and on a synchronized average approximation of the space derivative term, for both voltages and currents derivatives. As briefly proved in Sec. 1.3.1, this feature ensures second order accuracy.

The high computational cost to solve the implicit scheme has been always a relevant obstacle to using the CN scheme in practice. One approach consists in deriving the node voltages from (1.22b), substituting the computed expressions into (1.22a) and solving for the unknown currents. Although the number of unknowns would be reduced (namely, from $N_{\text{c}}\cdot(2N_{\Delta x}+1)$ to $N_{\text{c}}\cdot N_{\Delta x}$), the coefficient matrix of the associated solving system of equations would be full, and a subsequent substitution would be needed to recover the voltages from the computed currents. Hence, an alternative solution is proposed [18]. If equations (1.22) are solved alternating a voltage node with a current node in

the column vector of the unknowns, a linear system is obtained, written in the following form:

$$\mathbf{A}\mathbf{X}^{n+1} = \mathbf{B}^{n+1} \tag{1.23}$$

with

$$\mathbf{X}^{n+1} = \begin{bmatrix} \mathbf{V}_0^{n+1} & \mathbf{I}_{\frac{1}{2}}^{n+1} & \mathbf{V}_1^{n+1} & \cdots & \mathbf{V}_{N_{\Delta x}}^{n+1} \end{bmatrix} \tag{1.24a}$$

$$\mathbf{B}^{n+1} = \begin{bmatrix} \mathbf{B}_0^{\mathrm{V}} & \mathbf{B}_{\frac{1}{2}}^{\mathrm{I}} & \mathbf{B}_1^{\mathrm{V}} & \cdots & \mathbf{B}_{N_{\Delta x}}^{\mathrm{V}} \end{bmatrix}. \tag{1.24b}$$

In (1.23), $\mathbf{A}$ is a block tri-diagonal matrix (the size of each block is $N_\mathrm{c} \times N_\mathrm{c}$), with band $2N_\mathrm{c} - 1$:

$$\mathbf{A} = \begin{bmatrix} \mathbf{D}_0^{\mathbf{V}} & [\mathbf{1}] & 0 & 0 & 0 & \cdots & 0 \\ -[\mathbf{1}] & \mathbf{D}_1^{\mathbf{I}} & [\mathbf{1}] & 0 & 0 & \cdots & 0 \\ 0 & -[\mathbf{1}] & \mathbf{D}_1^{\mathbf{V}} & [\mathbf{1}] & 0 & \cdots & 0 \\ \vdots & & & \ddots & & & \vdots \\ 0 & & -[\mathbf{1}] & \mathbf{D}_k^{\mathbf{V}} & [\mathbf{1}] & & 0 \\ \vdots & & & & & \ddots & \vdots \\ 0 & \cdots & 0 & 0 & 0 & -[\mathbf{1}] & \mathbf{D}_{N_{\Delta x}}^{\mathbf{V}} \end{bmatrix} \tag{1.25}$$

with

$$\mathbf{D}_k^{\mathbf{I}} = \frac{2\mathbf{L}'_{\mathrm{ext}}\Delta x}{\Delta t} \tag{1.26a}$$

$$\mathbf{D}_k^{\mathbf{V}} = \left[\frac{2\mathbf{C}'\Delta x}{\Delta t}\right] \tag{1.26b}$$

$$\mathbf{B}_k^{\mathrm{I}} = \frac{2\mathbf{L}'_{\mathrm{ext}}\Delta x}{\Delta t}\mathbf{I}_{k+\frac{1}{2}}^n - \Delta\mathbf{V}_{k,k+1}^n \tag{1.26c}$$

$$\mathbf{B}_k^{\mathrm{V}} = \left[\frac{2\mathbf{C}'\Delta x}{\Delta t}\right]\mathbf{V}_k^n - \Delta\mathbf{I}_{k-\frac{1}{2},k+\frac{1}{2}}^n, \tag{1.26d}$$

where $\Delta\mathbf{V}_{k,k+1}^n = \mathbf{V}_{k+1}^n - \mathbf{V}_k^n$ and $\Delta\mathbf{I}_{k-\frac{1}{2},k+\frac{1}{2}}^n = \mathbf{I}_{k+\frac{1}{2}}^n - \mathbf{I}_{k-\frac{1}{2}}^n$, $k \neq 0, N_{\Delta x}$.

If the p.u.l. parameters of the line are time-independent, the matrix $\mathbf{A}$ in (1.25) is fixed and needs to be computed only once. Moreover, in each matrix-row, two of the three blocks are identity (unitary) matrices $[\mathbf{1}]$ of order N_c. Consequently, the linear system may be efficiently solved storing its matrix of coefficients in band-storage form, reducing memory occupation. The Fortran IMSL routine LSARB, implementing an LU factorization for the solution of systems of linear equations with coefficients matrix in band-storage form, is exploited [19].

1.2.2 Lossy MTLs

Moving to the realistic case of lossy MTLs, the frequency-dependent p.u.l. impedances associated with the conductors and the ground return path (introduced, respectively, in Sec. 1.1.1 and Sec. 1.1.2) are accounted for in the TD telegrapher's equations through the elements of the time-dependent matrix $\mathbf{Z}'_\zeta(t)$.

To reduce the burden of the numerical computation of the integral in (1.8), the Prony method [20] and a recursive algorithm are implemented in the code to approximate the generic term $z'_\zeta(t)$ of $\mathbf{Z}'_\zeta(t)$ defined in (1.11). The aim is to find an approximation of $z'_\zeta(t)$ of the type:

$$z'_\zeta(t) = \sum_{m=1}^{N} A_m \exp(a_m t) \; . \tag{1.27}$$

In (1.27), A_m and a_m, with $m = 1 \dots N$, are unknown constant parameters; a_m should be complex conjugated quantities in pairs, to ensure the element $z'_\zeta(t)$ to be real valued. If the function to be approximated is known at $2N$ – or more – equispaced time instants (e.g., $t_n = n\Delta t$, $t_{n+1} = (n+1)\Delta t$, etc.) the Prony method may be applied to compute the aforementioned $2N$ unknown parameters. An alternative solution, yet with heavier computational burden, would be the solution of a system of nonlinear equations in $2N$ unknowns.

As concerns the transient internal impedances addressed in Sec. 1.1.1, the second term of expression (1.13) is already of the type (1.27), hence, it is suitable for recursive evaluation. However, in order to get satisfactory results, a number of terms larger than that required by Prony's approximation should be included in the series (1.27); this is due to the pattern of zeros of $J_1(\cdot)$ (in particular, to their proximity). Hence, Prony's approximation of the transient self-impedance term enables a simplification in the recursive algorithm and a reduced computational burden.

Prony's method

Prony's method may be briefly summarised in three steps [21–23].

The p.u.l. impedance ${z_\zeta}'_n$, evaluated at time $t = n\Delta t$, is introduced:

$${z_\zeta}'_n = z_\zeta'(n\Delta t) = \sum_{m=1}^{N} A_m \exp(a_m n\Delta t) \; , \tag{1.28}$$

where the subscripts ij, denoting the specific element of the matrix of transient impedances, are omitted to ease the notation. Prony observed that terms of the type (1.28) satisfy the equation:

$${z_\zeta}'_n + \alpha_{N-1}{z_\zeta}'_{n-1} + \alpha_{N-2}{z_\zeta}'_{n-2} + \dots + \alpha_0{z_\zeta}'_{n-N} = 0 \, , \tag{1.29}$$

where α_m (with $m \in \{0, \ldots, N-1\}$) are N unknown constants. Hence, a system of N linear equations may be solved to get the sought α_m:

$$\begin{pmatrix} {z_\zeta}'_{n-1} & {z_\zeta}'_{n-2} & \cdots & {z_\zeta}'_{n-N} \\ {z_\zeta}'_{n} & {z_\zeta}'_{n-1} & \cdots & {z_\zeta}'_{n-N+1} \\ \vdots & & & \vdots \\ {z_\zeta}'_{n+N-2} & {z_\zeta}'_{n+N-3} & \cdots & {z_\zeta}'_{n-1} \end{pmatrix} \begin{pmatrix} \alpha_{N-1} \\ \alpha_{N-2} \\ \vdots \\ \alpha_0 \end{pmatrix} = - \begin{pmatrix} {z_\zeta}'_{n} \\ {z_\zeta}'_{n+1} \\ \vdots \\ {z_\zeta}'_{n+N-1} \end{pmatrix} . \tag{1.30}$$

In fact, the elements of the matrix on the LHS of (1.30) are known, and may be found sampling the known function ${z_\zeta}'(t)$ at time instants $n\Delta t$. With the computed values of α_m, the unknowns a_m may be derived by solving the characteristic polynomial associated with (1.29) in its roots λ_m ($m = 1 \ldots N$) and inverting the expression in (1.31b):

$$\lambda_m^n + \alpha_{N-1}\lambda_m^{n-1} + \alpha_{N-2}\lambda_m^{n-2} + \cdots + \alpha_0 = 0 \tag{1.31a}$$

$$\lambda_m = \exp(a_m \Delta t) \text{ for } m = 1 \ldots N . \tag{1.31b}$$

The interested reader is referred to [24] for the proof of the previous relations. The third step to derive the unknown A_m consists in solving a linear system of the type

$$\begin{pmatrix} 1 & 1 & \cdots & 1 \\ e^{(a_1 \Delta t)} & e^{(a_2 \Delta t)} & \ldots & e^{(a_N \Delta t)} \\ \vdots & & & \vdots \\ e^{(a_1 (N-1) \Delta t)} & e^{(a_2 (N-1) \Delta t)} & \ldots & e^{(a_N (N-1) \Delta t)} \end{pmatrix} \begin{pmatrix} A_1 \\ A_2 \\ \vdots \\ A_N \end{pmatrix} = \begin{pmatrix} {z_\zeta}'_{0} \\ {z_\zeta}'_{1} \\ \vdots \\ {z_\zeta}'_{N-1} \end{pmatrix} . \tag{1.32}$$

Hence, Prony's method allows to approximate a given function of time ${z_\zeta}'(t)$ in the form (1.27), deriving the quantities A_m and a_m through the solution of two linear systems and the computation of the roots of a nonlinear equation of degree N. It is important to notice that the number of poles N to approximate the original function of time is defined by the user, along with the number of considered samples in time. The accuracy of the approximation obtained by means of the Prony's method is affected by both these parameters, along with the selected time range; hence, their choice should be tailored to minimize the absolute or relative error. As an example, Prony's method was implemented to obtain approximations of the elements of the matrix accounting for the impedance offered by the ground return path with reference to the MTL in Fig. 1.6, with electrical and geometrical features in Table 1.1. In Fig. 1.7, the actual impedances, computed according to expressions in Sec. 1.1.2, and their approximation, obtained by means of the Prony's method are displayed; the right axis refers to the absolute error of the adopted approximation. Results

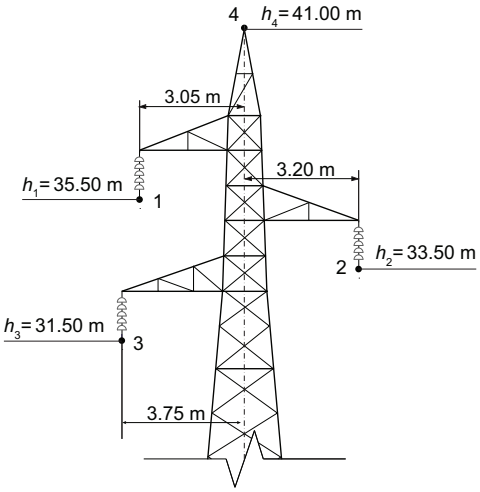

Figure 1.6. Conductors arrangement.

Table 1.1. Parameters used to model the line in Fig. 1.6.

r_{pc}	15.75 mm
r_{sw}	5.75 mm
σ_{w}	27 MS/m
σ_{g}	5 mS/m
ϵ_{g}	$10\epsilon_0$
μ_{g}	μ_0

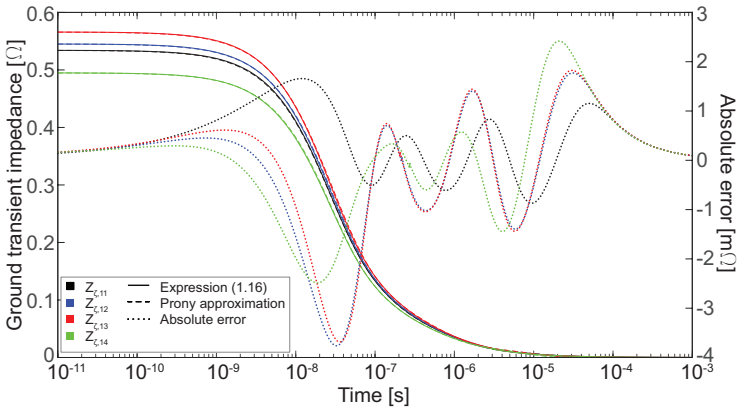

Figure 1.7. P.u.l. transient ground impedances $Z'_{\zeta,ij}(t)$ with $i = 1$ and $j = 1 \ldots 4$, corresponding approximations computed by means of the Prony's method, and absolute error introduced by the adopted approximation, for the MTL in Fig. 1.6.

were derived with a number of poles $N = 6$, in the time interval 10 ps–1 ms, and 20000 equispaced time samples for all the elements of the first row of the matrix of the ground p.u.l. transient impedances (i.e., $Z'_{\zeta_{ij}}(t)$ with $i = 1$, $j = 1 \ldots 4$).

It should be noted that each term of the matrix $\mathbf{Z}'_{\zeta}$ in (1.8) may be better approximated through the suitable choice (which may be also related to the solution of an associated optimization problem) of the number of poles N and sampling points. However, when considering the uncertainty in the knowledge of the actual properties of the soil, and the nonuniformity of its geological structure, the absolute error in Fig. 1.7 is acceptable and reasonable also in the light of a unique choice of N and sampling time instants for the different elements of $\mathbf{Z}'_{\zeta}$, allowing smoother programming solutions and reduced running times.

Time domain recursive evaluation of the integral of transient impedances

The case of a single-conductor TL is considered to illustrate the computation of the integral accounting for transient impedances, overlooking the heavy matrix notation. The line current is $i(x,t)$, and the associated transient p.u.l. impedance is $z_\zeta{}'(t)$. The algorithm derived here in the scalar case may be easily extended to the matrix relation (1.8).

In this section, it will be shown how approximating the term $z_\zeta{}'(t)$ in the form (1.27) allows to compute recursively the generic element of the integral on the RHS side (1.8).

The value of the following integral at position x, and time $t^* = \left(n+\frac{1}{2}\right)\Delta t$, is computed by splitting it in subintervals:

$$\int_0^{t^*} z'_\zeta(t^*-\tau)\frac{\partial i(x,\tau)}{\partial\tau}\mathrm{d}\tau = \int_0^{\left(n-\frac{1}{2}\right)\Delta t} z'_\zeta(t^*-\tau)\frac{\partial i(x,\tau)}{\partial\tau}\mathrm{d}\tau + \\ + \int_{\left(n-\frac{1}{2}\right)\Delta t}^{t^*} z'_\zeta(t^*-\tau)\frac{\partial i(x,\tau)}{\partial\tau}\mathrm{d}\tau = \mathrm{CI}_x^{n-\frac{1}{2}} + \Delta\mathrm{CI}_x^{n+\frac{1}{2}}, \quad (1.33)$$

with

$$\mathrm{CI}_x^{n-\frac{1}{2}} = \int_0^{\left(n-\frac{1}{2}\right)\Delta t} z'_\zeta(t^*-\tau)\frac{\partial i(x,\tau)}{\partial\tau}\mathrm{d}\tau \quad (1.34a)$$

$$\Delta\mathrm{CI}_x^{n+\frac{1}{2}} = \int_{\left(n-\frac{1}{2}\right)\Delta t}^{t^*} z'_\zeta(t^*-\tau)\frac{\partial i(x,\tau)}{\partial\tau}\mathrm{d}\tau\,. \quad (1.34b)$$

Recalling the approximation adopted for $z_\zeta{}'(t)$ in (1.27), the value of the integral computed at the previous time instant $t = \left(n-\frac{1}{2}\right)\Delta t$ is assumed to be known and equal to:

$$\int_0^{\left(n-\frac{1}{2}\right)\Delta t} z'_\zeta\left(\left(n-\frac{1}{2}\right)\Delta t-\tau\right)\frac{\partial i(x,\tau)}{\partial\tau}\mathrm{d}\tau = \\ = \sum_{m=1}^{N}\int_0^{\left(n-\frac{1}{2}\right)\Delta t} A_m e^{\left(a_m\left(\left(n-\frac{1}{2}\right)\Delta t-\tau\right)\right)}\frac{\partial i(x,\tau)}{\partial\tau}\mathrm{d}\tau\,. \quad (1.35)$$

If the term $\mathrm{CI}_x^{n-\frac{1}{2}}$ in (1.34a) is now considered

$$\mathrm{CI}_x^{n-\frac{1}{2}} = \int_0^{\left(n-\frac{1}{2}\right)\Delta t}\sum_{m=1}^{N} A_m e^{\left(a_m\left(\left(n+\frac{1}{2}\right)\Delta t-\tau\right)\right)}\frac{\partial i(x,\tau)}{\partial\tau}\mathrm{d}\tau = \\ = \sum_{m=1}^{N}\int_0^{\left(n-\frac{1}{2}\right)\Delta t} A_m e^{\left(a_m\left(\left(n+\frac{1}{2}\right)\Delta t-\tau\right)\right)}\frac{\partial i(x,\tau)}{\partial\tau}\mathrm{d}\tau = \\ = \sum_{m=1}^{N} e^{(a_m\Delta t)}\int_0^{\left(n-\frac{1}{2}\right)\Delta t} A_m e^{\left(a_m\left(\left(n-\frac{1}{2}\right)\Delta t-\tau\right)\right)}\frac{\partial i(x,\tau)}{\partial\tau}\mathrm{d}\tau\,, \quad (1.36)$$

it is immediate to notice that the terms of the sum in (1.35) and (1.36) differ only by the multiplicatives $e^{(a_m \Delta t)}$, which are constant and depend on the adopted Δt. Hence, the contribution $\mathrm{CI}_x^{n-\frac{1}{2}}$ to the integral (1.33) may be computed at each time step from its previous value with negligible computational burden, i.e., updating each term of the sum by multiplying its value at the previous time step by the corresponding updating factor $e^{(a_m \Delta t)}$.

As to the term $\Delta\mathrm{CI}_x^{n+\frac{1}{2}}$, the trapezoidal rule of integration is applied in the interval $\left[\left(n-\frac{1}{2}\right)\Delta t, \left(n+\frac{1}{2}\right)\Delta t\right]$:

$$\begin{aligned}\Delta\mathrm{CI}_x^{n+\frac{1}{2}} = \frac{1}{2}\left[z_\zeta{}'\left(\left(n+\frac{1}{2}\right)\Delta t - \left(n-\frac{1}{2}\right)\Delta t\right)\frac{\partial i\left(x,\left(n-\frac{1}{2}\right)\Delta t\right)}{\partial t}\right]\Delta t + \\ + \frac{1}{2}\left[z_\zeta{}'\left(\left(n+\frac{1}{2}\right)\Delta t - \left(n+\frac{1}{2}\right)\Delta t\right)\frac{\partial i\left(x,\left(n+\frac{1}{2}\right)\Delta t\right)}{\partial t}\right]\Delta t = \\ z_\zeta{}'\left(\Delta t\right)\frac{i\left(x,n\Delta t\right) - i\left(x,\left(n-1\right)\Delta t\right)}{2} + z_\zeta{}'\left(0\right)\frac{i\left(x,\left(n+1\right)\Delta t\right) - i\left(x,n\Delta t\right)}{2}\,.\end{aligned} \tag{1.37}$$

Therefore, the second contribution to the integral in (1.33) only requires the computation of finite-difference current derivatives and values of $z_\zeta{}'$ at time instants $t = 0$ and $t = \Delta t$. The latter quantities may be computed only once, and used as known constants for subsequent iterations of the FDTD algorithm.

1.2.3 Lossy MTLs: implicit scheme

To add ground losses, it is convenient to insert in (1.22a) the evaluation of losses at time $\left(n+\frac{1}{2}\right)\Delta t$ to maintain a centered synchronized updating equation and second order accuracy. Hence, equation (1.8a), considering each element of the matrix $\mathbf{Z}'_\zeta(t)$ to be approximated by a linear combination of exponential terms through the Prony algorithm in Sec. 1.2.2, may be evaluated by application of the implicit algorithm as:

$$\begin{aligned}-\left(\frac{\mathbf{V}_{k+1}^{n+1} - \mathbf{V}_k^{n+1}}{2\Delta x} + \frac{\mathbf{V}_{k+1}^{n} - \mathbf{V}_k^{n}}{2\Delta x}\right) = \mathbf{L}'_{\mathrm{ext}}\frac{\mathbf{I}_{k+\frac{1}{2}}^{n+1} - \mathbf{I}_{k+\frac{1}{2}}^{n}}{\Delta t} + \\ + \int_0^{\left(n-\frac{1}{2}\right)\Delta t} \boldsymbol{Z}'_\zeta\left(\left(n+\frac{1}{2}\right)\Delta t - \tau\right)\left.\frac{\partial \mathbf{I}}{\partial \tau}\right|_{k+\frac{1}{2}} \mathrm{d}\tau + \\ + \int_{\left(n-\frac{1}{2}\right)\Delta t}^{\left(n+\frac{1}{2}\right)\Delta t} \boldsymbol{Z}'_\zeta\left(\left(n+\frac{1}{2}\right)\Delta t - \tau\right)\left.\frac{\partial \mathbf{I}}{\partial \tau}\right|_{k+\frac{1}{2}} \mathrm{d}\tau\,.\end{aligned} \tag{1.38}$$

Using a trapezoidal rule for the evaluation of the second integral, with centered time differences computation of the currents derivatives, and denoting the first *history* integral as $\mathbf{CI}_{k+\frac{1}{2}}^{n-\frac{1}{2}}$, allows to rewrite (1.38) as (1.39) at a generic node k along the TL.

Generic node - k

$$-\left(\frac{\mathbf{V}_{k+1}^{n+1}-\mathbf{V}_{k}^{n+1}}{2\Delta x}+\frac{\mathbf{V}_{k+1}^{n}-\mathbf{V}_{k}^{n}}{2\Delta x}\right)=\mathbf{L}'_{\text{ext}}\frac{\mathbf{I}_{k+\frac{1}{2}}^{n+1}-\mathbf{I}_{k+\frac{1}{2}}^{n}}{\Delta t}+$$
$$+\mathbf{CI}_{k+\frac{1}{2}}^{n-\frac{1}{2}}+\frac{\boldsymbol{Z}'_{\zeta}(0)}{2}\left(\mathbf{I}_{k+\frac{1}{2}}^{n+1}-\mathbf{I}_{k+\frac{1}{2}}^{n}\right)+\frac{\boldsymbol{Z}'_{\zeta}(\Delta t)}{2}\left(\mathbf{I}_{k+\frac{1}{2}}^{n}-\mathbf{I}_{k+\frac{1}{2}}^{n-1}\right)\,. \quad (1.39)$$

Equation (1.39) is an implicit equation which does not change the block tri-diagonal nature of the scheme. In fact, (1.39) may be rearranged to get the following equation centered on the conductors currents at node $k+\frac{1}{2}$, and interlaced with the conductor-to-ground voltages at nodes k and $k+1$:

Generic node - k

$$-\left[\mathbf{1}\right]\mathbf{V}_{k}^{n+1}+\left\{\Delta x\boldsymbol{Z}'_{\zeta}\left(0\right)+\frac{2\mathbf{L}'_{\text{ext}}\Delta x}{\Delta t}\right\}\mathbf{I}_{k+\frac{1}{2}}^{n+1}+\left[\mathbf{1}\right]\mathbf{V}_{k+1}^{n+1}=$$
$$=\frac{2\mathbf{L}'_{\text{ext}}\Delta x}{\Delta t}\left\{\mathbf{I}_{k+\frac{1}{2}}^{n}-\left[\frac{2\mathbf{L}'_{\text{ext}}}{\Delta t}\right]^{-1}\frac{\Delta\mathbf{V}_{k,k+1}^{n}}{\Delta x}\right\}+$$
$$-2\Delta x\left\{\mathbf{CI}_{k+\frac{1}{2}}^{n-\frac{1}{2}}+\left[-\frac{\boldsymbol{Z}'_{\zeta}\left(0\right)}{2}\mathbf{I}_{k+\frac{1}{2}}^{n}+\frac{\boldsymbol{Z}'_{\zeta}\left(\Delta t\right)}{2}\left(\mathbf{I}_{k+\frac{1}{2}}^{n}-\mathbf{I}_{k+\frac{1}{2}}^{n-1}\right)\right]\right\}\,. \quad (1.40)$$

The second telegrapher's equation (1.22b) may be manipulated to get:

$$-\left[\mathbf{1}\right]\mathbf{I}_{k-\frac{1}{2}}^{n+1}+\left[\frac{2\mathbf{C}'\Delta x}{\Delta t}\right]\mathbf{V}_{k}^{n+1}+\left[\mathbf{1}\right]\mathbf{I}_{k+\frac{1}{2}}^{n+1}=\left[\frac{2\mathbf{C}'\Delta x}{\Delta t}\right]\mathbf{V}_{k}^{n}-\Delta\mathbf{I}_{k-\frac{1}{2},k+\frac{1}{2}}^{n}\,. \quad (1.41)$$

The previous equation is centered on the conductor-to-ground voltages at node k and interlaced with the conductors currents of the adjacent cells, with $k\pm\frac{1}{2}$.

In order to recover the short notation adopted in the matrix expressions (1.23)-(1.25) for the solution of the system, the previous equations (1.40) and (1.41) may be written in the form

$$-\left[\mathbf{1}\right]\mathbf{V}_{k}^{n+1}+\mathbf{D}_{k}^{\mathbf{I}}\mathbf{I}_{k+\frac{1}{2}}^{n+1}+\left[\mathbf{1}\right]\mathbf{V}_{k+1}^{n+1}=\mathbf{B}_{k}^{\mathrm{I}} \quad (1.42a)$$
$$-\left[\mathbf{1}\right]\mathbf{I}_{k-\frac{1}{2}}^{n+1}+\mathbf{D}_{k}^{\mathbf{V}}\mathbf{V}_{k}^{n+1}+\left[\mathbf{1}\right]\mathbf{I}_{k+\frac{1}{2}}^{n+1}=\mathbf{B}_{k}^{\mathrm{V}} \quad (1.42b)$$

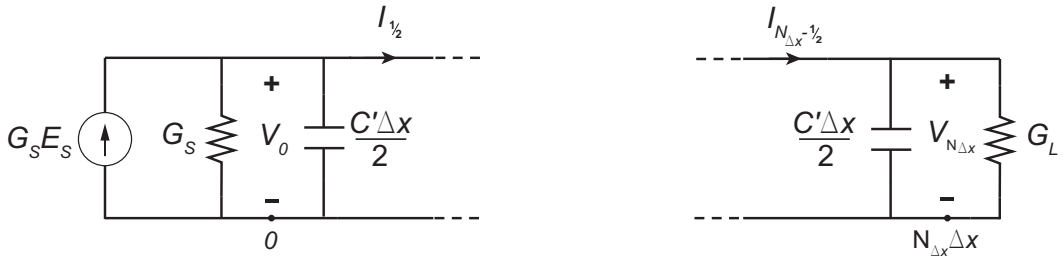

Figure 1.8. Equivalent circuit at the terminations of a single-conductor TL, for $k = 0$ and $k = N_{\Delta x}$.

where the following quantities are defined ($k \neq 0, N_{\Delta x}$):

$$\mathbf{D}_k^{\mathrm{I}} = \left\{ \Delta x \boldsymbol{Z}'_{\zeta}(0) + \frac{2\mathbf{L}'_{\mathrm{ext}}\Delta x}{\Delta t} \right\} \tag{1.43a}$$

$$\mathbf{D}_k^{\mathrm{V}} = \left[\frac{2\mathbf{C}'\Delta x}{\Delta t} \right] \tag{1.43b}$$

$$\begin{aligned} \mathbf{B}_k^{\mathrm{I}} = {} & \frac{2\mathbf{L}'_{\mathrm{ext}}\Delta x}{\Delta t} \left\{ \mathbf{I}_{k+\frac{1}{2}}^{n} - \left[\frac{2\mathbf{L}'_{\mathrm{ext}}}{\Delta t} \right]^{-1} \frac{\Delta \mathbf{V}_{k,k+1}^{n}}{\Delta x} \right\} + \\ & - 2\Delta x \left\{ \mathbf{C}\mathbf{I}_{k+\frac{1}{2}}^{n-\frac{1}{2}} + \left[-\frac{\boldsymbol{Z}'_{\zeta}(0)}{2} \mathbf{I}_{k+\frac{1}{2}}^{n} + \frac{\boldsymbol{Z}'_{\zeta}(\Delta t)}{2} \left(\mathbf{I}_{k+\frac{1}{2}}^{n} - \mathbf{I}_{k+\frac{1}{2}}^{n-1} \right) \right] \right\} \end{aligned} \tag{1.43c}$$

$$\mathbf{B}_k^{\mathrm{V}} = \left[\frac{2\mathbf{C}'\Delta x}{\Delta t} \right] \mathbf{V}_k^{n} - \Delta \mathbf{I}_{k-\frac{1}{2},k+\frac{1}{2}}^{n} \,. \tag{1.43d}$$

Expressions (1.42) and (1.43) represent the generic rows of the solving system of linear equations (1.23) in the unknown line voltages and currents at time instant $t = (n+1)\,\Delta t$.

Equations at the MTL terminations

The very first and last nodes of the MTL, i.e., nodes 0 and $N_{\Delta x}$, deserve to be treated separately, since the line terminations are to be accounted for. The equations to be written at these nodes are voltage centered equations of the same type as (1.41), expressing the Kirchhoff Current Law (KCL). A schematic representation of the line limiting nodes is displayed in Fig. 1.8 (for a single-conductor TL).

First node - $k = 0$

The node 0 is defined as the MTL first node, to be located at the line left termination (see Fig. 1.8), without loss of generality. A voltage source, expressed by the vector $\mathbf{E}_{\mathrm{S}}$ of dimension $N_{\mathrm{c}} \times 1$, is feeding the MTL at node 0. This approach also allows to feed the line with a non-symmetric system of

voltage sources, leaving to the user flexibility to account for different feeding conditions. Denoting with $\mathbf{G}_\mathrm{S}$ the matrix of the series internal conductances (assumed as time-invariant) associated with the voltage source, the following equation may be derived at node 0:

$$\left[\mathbf{G}_\mathrm{S}+\frac{\mathbf{C}'\Delta x}{\Delta t}\right]\mathbf{V}_0^{n+1}+[\mathbf{1}]\,\mathbf{I}_{\frac{1}{2}}^{n+1}=2\mathbf{G}_\mathrm{S}\mathbf{E}_\mathrm{S}^{n+\frac{1}{2}}+\left[\frac{\mathbf{C}'\Delta x}{\Delta t}\right]\mathbf{V}_0^{n}-\left[\mathbf{G}_\mathrm{S}\mathbf{V}_0^{n}+\mathbf{I}_{\frac{1}{2}}^{n}\right]. \tag{1.44}$$

Equation (1.44) may be interpreted as an application of the KCL at node 0, having modelled the voltage source as an equivalent current source with the matrix of its internal conductances to be plugged at the same node, in parallel with half of the total capacitance associated with the line segment Δx. Recalling the notation adopted in (1.23)-(1.25), the previous equation may be synthetically written as

$$\mathbf{D}_0^\mathbf{V}\mathbf{V}_0^{n+1}+[\mathbf{1}]\,\mathbf{I}_{\frac{1}{2}}^{n+1}=\mathbf{B}_0^\mathrm{V}\,, \tag{1.45}$$

with

$$\mathbf{D}_0^\mathbf{V}=\left[\mathbf{G}_\mathrm{S}+\frac{\mathbf{C}'\Delta x}{\Delta t}\right] \tag{1.46a}$$

$$\mathbf{B}_0^\mathrm{V}=2\mathbf{G}_\mathrm{S}\mathbf{E}_\mathrm{S}^{n+\frac{1}{2}}+\left[\frac{\mathbf{C}'\Delta x}{\Delta t}\right]\mathbf{V}_0^{n}-\left[\mathbf{G}_\mathrm{S}\mathbf{V}_0^{n}+\mathbf{I}_{\frac{1}{2}}^{n}\right]. \tag{1.46b}$$

It is straightforward to recognize that (1.45)-(1.46) consist in the first row of the system of linear equations in (1.23).

Last node - $k=N_{\Delta x}$

The node $N_{\Delta x}$ is defined as the MTL last node, to be located at the line right termination (see Fig. 1.8), without loss of generality. If a passive load, modelled by means of its matrix of admittances $\mathbf{G}_\mathrm{L}$ (assumed as time-invariant), is plugged to node $N_{\Delta x}$, the following holds:

$$-[\mathbf{1}]\,\mathbf{I}_{N_{\Delta x}-\frac{1}{2}}^{n+1}+\left[\mathbf{G}_\mathrm{L}+\frac{\mathbf{C}'\Delta x}{\Delta t}\right]\mathbf{V}_{N_{\Delta x}}^{n+1}=\left[\frac{\mathbf{C}'\Delta x}{\Delta t}\right]\mathbf{V}_{N_{\Delta x}}^{n}+\left[\mathbf{I}_{N_{\Delta x}-\frac{1}{2}}^{n}-\mathbf{G}_\mathrm{L}\mathbf{V}_{N_{\Delta x}}^{n}\right]. \tag{1.47}$$

Equation (1.47) may be rearranged to recover the notation of expressions (1.23)-(1.25):

$$-[\mathbf{1}]\,\mathbf{I}_{N_{\Delta x}-\frac{1}{2}}^{n+1}+\mathbf{D}_{N_{\Delta x}}^\mathbf{V}\mathbf{V}_{N_{\Delta x}}^{n+1}=\mathbf{B}_{N_{\Delta x}}^\mathrm{V} \tag{1.48}$$

with

$$\mathbf{D}_{N_{\Delta x}}^\mathbf{V}=\left[\mathbf{G}_\mathrm{L}+\frac{\mathbf{C}'\Delta x}{\Delta t}\right] \tag{1.49a}$$

$$\mathbf{B}_{N_{\Delta x}}^\mathrm{V}=\left[\frac{\mathbf{C}'\Delta x}{\Delta t}\right]\mathbf{V}_{N_{\Delta x}}^{n}+\left[\mathbf{I}_{N_{\Delta x}}^{n}-\mathbf{G}_\mathrm{L}\mathbf{V}_{N_{\Delta x}}^{n}\right]. \tag{1.49b}$$

As with the previous case, equations (1.48) and (1.49) represent the last row of the system in (1.23), written for lossy MTLs. In dealing with arbitrary terminations, the formulation presented in [25] may be followed.

1.3 Accuracy, stability and numerical dispersion

Without loss of generality, a well-behaved time-dependent function $f(t)$ is taken as a reference to be evaluated at time $t = t_0$. The Taylor's expansion of $f(t)$ around t_0 is computed:

$$f(t) = f(t_0) + \left.\frac{\mathrm{d}f(t)}{\mathrm{d}t}\right|_{t_0} (t - t_0) + \left.\frac{\mathrm{d}^2 f(t)}{\mathrm{d}t^2}\right|_{t_0} \frac{(t - t_0)^2}{2!} + \cdots = \\ = f(t_0) + \left.\frac{\mathrm{d}f(t)}{\mathrm{d}t}\right|_{t_0} (t - t_0) + O\left((t - t_0)^2\right) . \quad (1.50)$$

Evaluating $f(t)$ in $t = t_0 + \Delta t$, and considering up to the first term of the Taylor's expansion (1.50), the first derivative of $f(t)$ with respect to time in $t = t_0$ may be approximated by

$$f'(t_0) \simeq \frac{f(t_0 + \Delta t) - f(t_0)}{\Delta t} . \quad (1.51)$$

The time evolution of the continuous function $f(t)$ is here studied in terms of the corresponding TD discretized quantity F^n, where the superscript denotes the time instant at which the function is evaluated, i.e., $t = n\Delta t$.

Likewise, for a generic quantity $g(t, x)$ showing both time and space dependency, the following approximations are adopted:

$$\left.\frac{\partial g(t_0, x_0)}{\partial t}\right|_{\mathrm{fw}} = \frac{G_{k_0}^{n_0+1} - G_{k_0}^{n_0}}{\Delta t} \quad (1.52a)$$

$$\left.\frac{\partial g(t_0, x_0)}{\partial x}\right|_{\mathrm{fw}} = \frac{G_{k_0+1}^{n_0} - G_{k_0}^{n_0}}{\Delta x} , \quad (1.52b)$$

where $t_0 = n_0\Delta t$, and the subscript denotes the position at which the function is evaluated, e.g., $x_0 = k_0\Delta x$. In particular, derivatives in (1.52) are referred to as *forward partial derivatives*. Likewise, recalling the Taylor's expansion of $g(t, x)$ with respect to each of the independent variables, and evaluating the function in $t = t_0 - \Delta t$ and $x = x_0 - \Delta x$, respectively, the *backward partial derivatives* are introduced:

$$\left.\frac{\partial g(t_0, x_0)}{\partial t}\right|_{\mathrm{bw}} = \frac{G_{k_0}^{n_0} - G_{k_0}^{n_0-1}}{\Delta t} \quad (1.53a)$$

$$\left.\frac{\partial g(t_0, x_0)}{\partial x}\right|_{\mathrm{bw}} = \frac{G_{k_0}^{n_0} - G_{k_0-1}^{n_0}}{\Delta x} . \quad (1.53b)$$

These quantities, which have been mentioned for the first time in Sec. 1.2.1, will be further exploited to assess the accuracy of the explicit and implicit numerical methods (in Sec. 1.2.1) which have been implemented to solve the coupled equations (1.8).

A generic numerical method has the aim of reducing differential equations to difference equations allowing to compute the values of the sought function $f(t)$ at time instants t_n (such that $t_{n+1} - t_n = \Delta t$). The computed numerical solution, approximating $f(t_n)$ at $t_n = n\Delta t$, is denoted by F^n. In particular, the sought function is the solution of an Initial Value Problem (IVP) of the form:

$$\begin{cases} \frac{\partial f(t)}{\partial t} = \Phi(t, f(t)) & t > t_0 \\ f(t_0) = f_0 & t = t_0 \,. \end{cases} \tag{1.54}$$

where t_0 is the initial time.

Any numerical method allowing to compute the time evolution of $f(t)$, solution of the IVP in (1.54), may be written in the form:

$$\sum_{j=0}^{k} \alpha_j F^{n+j} = \Delta t \Phi_f \left(F^{n+k}, F^{n+k-1}, \ldots, F^n; \Delta t \right) , \tag{1.55}$$

where quantities α_j are auxiliary coefficients (not to be confused with the ones introduced previously for the Prony method). If the function Φ on the RHS of (1.55) depends on the unknown value F^{n+k} the method is said to be *implicit*; otherwise the method will be *explicit*, since the value of F^{n+k} at the following time step may be retrieved from the already computed values at the previous time steps. Depending on the number k of previous values $F^{n+k-1}, \ldots F^n$ used to compute F^{n+k}, the chosen method will be classified as a k-step numerical method [26].

Finally, it is observed that the LF and CN methods are of the type (1.55), for the solution of the vectorial counterpart of the IVP (1.54).

1.3.1 Accuracy

The order of accuracy p of a numerical method is defined as the largest $p \in \mathbb{N}$ such that for each sufficiently smooth solution of the IVP (1.54), $\kappa > 0$ and Δt_0 exist such that:

$$|T_{n+k}| \leq \kappa \Delta t^p \tag{1.56}$$

for each $\Delta t < \Delta t_0$. T_{n+k} is the local truncation error at time $(n+k)\Delta t$ [26],[27], defined as:

$$T_{n+k} = \sum_{j=0}^{k} \alpha_j f(t_{n+j}) - \Delta t \Phi_f \left(f(t_{n+k}), f(t_{n+k-1}), \ldots, f(t_n); \Delta t \right) . \tag{1.57}$$

Hence, from (1.57), the local truncation error is the difference between the exact and the numerical solution, under the assumption that the numerical

solution is derived from known values of the exact solution at the required previous k time steps (local condition).

The following considerations will be limited to one-step methods (as the LF and CN schemes). If the Taylor's expansion of the sought solution of the IVP is evaluated at time instants $t \pm \Delta t/2$, expressions (1.58) are obtained:

$$f\left(t+\Delta t/2\right) = f\left(t\right) + \frac{\partial f\left(t\right)}{\partial t}\frac{\Delta t}{2} + \frac{1}{2}\frac{\partial^2 f\left(t\right)}{\partial t^2}\left(\frac{\Delta t}{2}\right)^2 + \frac{1}{3!}\frac{\partial^3 f\left(t\right)}{\partial t^3}\left(\frac{\Delta t}{2}\right)^3 + \cdots \tag{1.58a}$$

$$f\left(t-\Delta t/2\right) = f\left(t\right) - \frac{\partial f\left(t\right)}{\partial t}\frac{\Delta t}{2} + \frac{1}{2}\frac{\partial^2 f\left(t\right)}{\partial t^2}\left(\frac{\Delta t}{2}\right)^2 - \frac{1}{3!}\frac{\partial^3 f\left(t\right)}{\partial t^3}\left(\frac{\Delta t}{2}\right)^3 + \cdots . \tag{1.58b}$$

By subtracting (1.58b) from (1.58a), relation (1.59) is retrieved:

$$\frac{f\left(t+\Delta t/2\right) - f\left(t-\Delta t/2\right)}{\Delta t} = \Phi\left(t\right) + \frac{1}{24}\frac{\partial^3 f\left(t\right)}{\partial t^3}\Delta t^2 + \ldots \tag{1.59}$$

where the definition $f'\left(t\right) = \Phi\left(t\right)$ in (1.54) has been used. Comparing (1.59) to the definition of local truncation error in (1.57), and recalling the hypothesis for $f\left(t\right)$ to be sufficiently smooth, κ and Δt_0 can be selected for the truncation error to be of the order $O\left(\Delta t^2\right)$, and for the numerical method to have order of accuracy $p = 2$. This is true as the derivative is computed by means of a centered difference equation, i.e., adopting a symmetrical discretization mesh with respect to the derivative evaluation points.

1.3.2 Stability

As to the explicit LF scheme, the drawback associated with the easy implementation and reduced numerical burden (resulting in a fast updating algorithm) is the imposed limitation on the choice of Δx and Δt. In fact, the choice of the discretization steps depends on the CFL condition, which guarantees the stability of the method.

Stability ensures the solution to be bounded when the initial conditions are subjected to small variations. The CFL condition expresses an upper bound for the choice of the Δt when a Δx is given (the derivation of the upper bound for the 1D updating scheme may be found in [28], and in [29] for the general 3D updating scheme):

$$\frac{\Delta x}{\Delta t} \geq c_0 \,. \tag{1.60}$$

Furthermore, the CFL factor f_c is defined:

$$f_c = \frac{c_0}{\Delta x}\Delta t \,, \tag{1.61}$$

which corresponds to the adopted time step Δt, normalised with respect to its upper bound according to the CFL condition (1.60) (assuming that the space step Δx has been fixed).

An intuitive interpretation of the physical meaning of (1.60) consists in recalling that the discretized equations in Sec. 1.2.1 describe the propagation through subsequent space cells at each time step (e.g., voltage waves propagating from $k\Delta x$ towards $(k+1)\,\Delta x$). The propagation in the explicit scheme is numerically obtained by updating currents and voltages at each node from known currents and voltages at the previous time step, computed at the two adjacent nodes. This is the reason why Δt should be such that, given the maximum admissible wave velocity c_0, the numerically computed solution should be updated at a speed $\Delta x/\Delta t$ higher than c_0 [30], ensuring that in the maximum admissible time step Δt (given by (1.60)) the actual wave has not travelled a distance larger than Δx.

When dealing with problems which need a high resolution in the space discretization and also a large time window for simulation, the fulfilment of the stability bound required by the explicit LF scheme may result in prohibitive simulation times. The 1D implicit algorithm (which, as stated previously, also corresponds to the ADI algorithm) may be adopted. In fact, Zheng, Chen, and Zhang proved the unconditional stability of the ADI algorithm [29] (by means of a transformation in the spectral domain of the updating equations of the implicit scheme in the general 3D case). Therefore, the choice of Δx and Δt for the CN scheme should be only related to considerations on the numerical burden, i.e. running time, on the scheme dispersion error (analysed in the following section), on the geometry of the configuration under study, and on the known or predicted time constants involved in the specific transient study.

1.3.3 Numerical dispersion

Numerical solutions of differential equations to study the propagation of waves in dielectric media in the TD typically suffer from dispersion.

The dispersion phenomenon consists in monochromatic waves displaying a different phase velocity when propagating in the same dielectric medium, depending on their frequency.

In the real case, as to the exact solution of a wave equation, dispersion takes place when the medium is frequency-dispersive (e.g., when the relative electric permittivity $\epsilon_r\,(f)$ is frequency-dependent) or, as a general condition, when the phase velocity of the travelling wave is not constant with frequency. Introducing the propagation constant $k_x = \beta_x - j\alpha_x$ in the FD (which, in the case of the 1D wave equation, corresponds to a scalar complex quantity), the phase velocity of any wave propagating with a given angular frequency ω is defined as $v_p = \omega/\beta_x$. β_x and α_x are known as the phase and the attenuation constants in the x-direction, respectively. It can be deduced that, to get a constant v_p, the phase constant β_x should display a linear dependence on the

angular frequency ω.

When dealing with FDTD methods, the numerical solution typically suffers from dispersion. However, this phenomenon is due to the finite-difference approximation of the derivatives; hence, numerical dispersion may show, depending on the choice of Δx and Δt, even though the exact solution may not suffer from dispersion.

The dispersion relation for the specific numerical algorithm may be derived according to different methods; the method presented in [28] has been adopted. By substitutions and algebraic manipulation of the original updating equations, a relation expressed only as a function of the vectors of discretized voltages (or currents) is obtained; subsequently, it is assumed that the solution in the TD may be expressed as a function of the type:

$$f(x,t) = e^{j(\omega t - k_x x)} \;\rightarrow\; f_k^n = e^{j\left(\omega n \Delta t - \tilde{k}_x k \Delta x\right)}. \tag{1.62}$$

In (1.62), $f(x,t)$ is the exact solution as a continuous function of space and time, and f_k^n is the corresponding numerical solution evaluated at the nodes of the chosen time-space discretization mesh; $\tilde{k}_x = \tilde{\beta}_x - j\tilde{\alpha}_x$ is the numerical counterpart of the propagation constant. From (1.62), it can be observed that the dispersion error cumulates as the wave propagates along the line. In fact, at a given ω, the total phase shift depends linearly on the travelled distance $\tilde{\beta}_x k \Delta x$.

In the simplified case of a single-wire TL with constant (hence, frequency independent) p.u.l. resistance R' and external inductance L', the following dispersion relation is derived when considering the updating equations of the explicit LF scheme:

$$c_0 \frac{\Delta t}{\Delta x} \sin\left(\frac{\tilde{k}_x \Delta x}{2}\right) = \sqrt{1 - \frac{j\Delta t}{2\tau \tan\left(\frac{\omega \Delta t}{2}\right)}}\; \sin\left(\frac{\omega \Delta t}{2}\right) \tag{1.63}$$

where $\tau = L'/R'$. From (1.63), it is clear that the linear dependence of the numerical phase constant $\tilde{\beta}_x$ on ω is not guaranteed; hence, the numerical solution will suffer from a dispersion error.

Taking into consideration the ideal case of a lossless single-conductor TL (i.e., $R' = 0$, $\tilde{k}_x = \tilde{\beta}_x$), equation (1.63) reduces to

$$c_0 \frac{\Delta t}{\Delta x} \sin\left(\frac{\tilde{\beta}_x \Delta x}{2}\right) = \sin\left(\frac{\omega \Delta t}{2}\right). \tag{1.64}$$

Assuming that $\Delta x \to 0$, $\Delta t \to 0$ with the same velocity, i.e., keeping the ratio $\frac{\Delta t}{\Delta x} = \text{const.}$, relation (1.64) reduces to:

$$c_0 \frac{\Delta t}{\Delta x} \tilde{\beta}_x \Delta x \simeq \omega \Delta t \rightarrow \tilde{\beta}_x \simeq \frac{\omega}{c_0}. \tag{1.65}$$

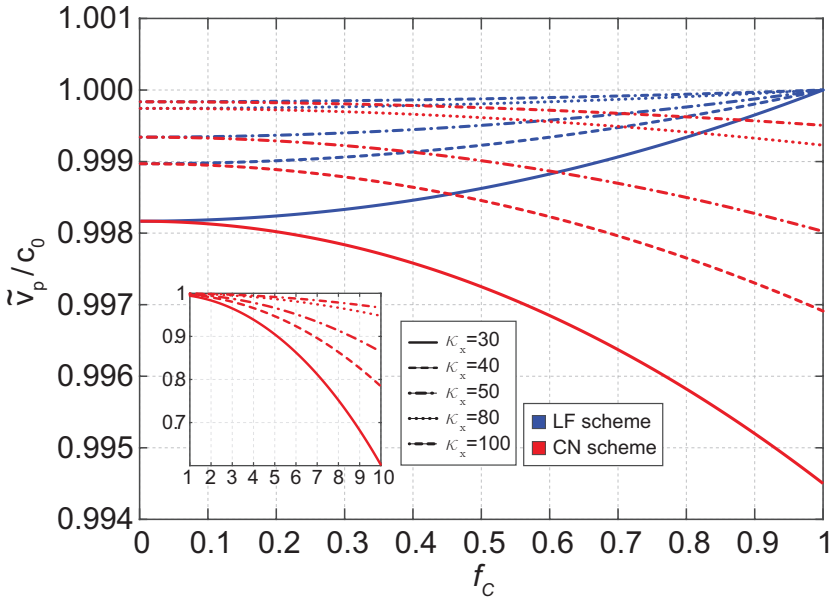

Figure 1.9. Normalized numerical phase velocity $\tilde{v}/c_0$ as a function of f_c with different discretization factors κ_x in the lossless case.

Hence, the numerical phase constant $\tilde{\beta}_x$ converges to the exact β_x when the discretization steps are reduced to zero with the same reduction rate (in other words, reducing the error introduced by the finite-difference approximation). Noticeably, in the lossless single-conductor TL case, the particular choice $\Delta x = c_0 \Delta t$ leads to the same condition (1.65); hence, the limit step (upper bound) for the stability of the explicit LF scheme (Sec. 1.3.2) nullifies the dispersion error in the lossless case, regardless the frequency excited by the source, and the order of magnitude of Δx and Δt.

As to the CN scheme, the following dispersion relation is derived for the lossy case:

$$c_0 \frac{\Delta t}{\Delta x} \sin\left(\frac{\tilde{k}_x \Delta x}{2}\right) = \sqrt{1 - \frac{j\Delta t}{2\tau \tan\left(\frac{\omega \Delta t}{2}\right)}} \tan\left(\frac{\omega \Delta t}{2}\right). \tag{1.66}$$

As to the lossless case, for $\Delta x \to 0$, $\Delta t \to 0$, the same conclusion valid for the LF scheme holds, and the numerical solution computed by the CN scheme converges to the exact solution.

Figure 1.9 displays the normalized numerical phase velocity $\tilde{v}_p/c_0$ in the lossless case according to (1.63) and (1.66), for different CFL factors f_c and different space discretization factors κ_x. The discretization factor is defined as $\kappa_x = \lambda_{\min}/\Delta x$, where $\lambda_{\min}$ is the minimum spectrum wavelength (it has been assumed $\lambda_{\min} = 300$ m, within the range of typical span lengths of Italian high voltage TLs). The inset displays the effect of a CFL factor $f_c > 1$ on the ratio $\tilde{v}_p/c_0$, when implementing the CN scheme. When applying implicit

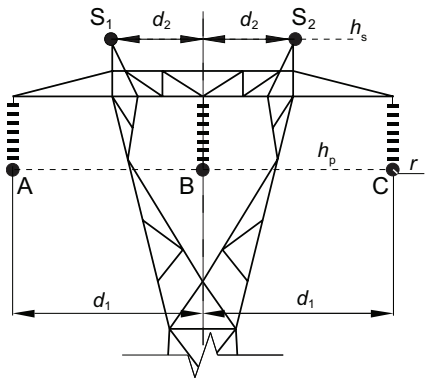

r_p	3.5 cm
r_s	1.0 cm
d_1	7.4 m
d_2	4.715 m
h_p	21 m
h_s	28.4 m

Figure 1.10. Line configuration including $N_\mathrm{pc} = 3$ phase conductors and $N_\mathrm{sw} = 2$ shield wires; geometrical parameters of the configuration are reported in the table on the right.

methods, one has to be careful to find a reasonable tradeoff between accuracy and computational speed.

In order to validate the proposed implicit formulations, the propagation along the High Voltage (HV) overhead power line reported in Fig. 1.10 is simulated. The span length is equal to 300 m and the overall length of the line is assumed to be 7.5 km (i.e., 25 spans). The line is closed at both ends on the diagonal load resistance matrix $R_\mathrm{L} = [475, 475, 475, 490, 490]\ \Omega$ (with $R_\mathrm{L} = G_\mathrm{L}^{-1} = G_\mathrm{S}^{-1}$); the Shield Wires (SWs) are not grounded. The first phase conductor A is excited at the line left termination through a voltage-to-ground generator with instantaneous voltage $v_A(t)$. A power exponential pulse source is considered:

$$v_A(t) = V_0 \left(\frac{t}{T_\mathrm{c}}\right)^{c_\mathrm{n}} e^{-c_\mathrm{n}\left(\frac{t}{T_\mathrm{c}}-1\right)}. \tag{1.67}$$

with $T_\mathrm{c} = 2.5\,\mu$s, $c_\mathrm{n} = 16$ and $V_0 = 1$ kV. The relevant frequency content of the pulse ranges from DC to approximately 1 MHz.

Figures 1.11a and 1.11b show the conductor-to-ground voltages at the middle of the line computed for different values of the CFL factor f_c through the implicit method in the lossless and lossy case, respectively, compared to the results obtained with the LF scheme. Small reflections occurring at $t = 40$ μs are due to the load at the line terminations which is not perfectly matched to the matrix of the line characteristic impedances. The space step was set to $\Delta x = 3$ m, which corresponds to a space sampling resolution $\kappa_x = \lambda_\mathrm{min}/\Delta x = 100$ (assuming $\lambda_\mathrm{min} = 300$ m). In the lossy case, values of the soil electrical conductivity and relative permittivity were set to $\sigma_\mathrm{g} = 5$ mS/m and $\epsilon_{r\mathrm{g}} = 10$, respectively. The CN scheme is accurate up to $f_\mathrm{c} = 5$,

both in the lossless and lossy case. As concerns the accuracy on the peak prediction, the implicit method performance is less satisfactory in the lossy case. In fact, the accuracy of the computation of the recursive convolution for the transient impedances reduces for larger f_c (i.e., for larger time steps Δt, given the space step Δx). However, the accuracy is still reasonable at f_c=5: the error is less than 0.3% in the lossless case, less than 0.5% in the lossy case, and approximately of the same order of magnitude for the voltages of the three phase conductors.

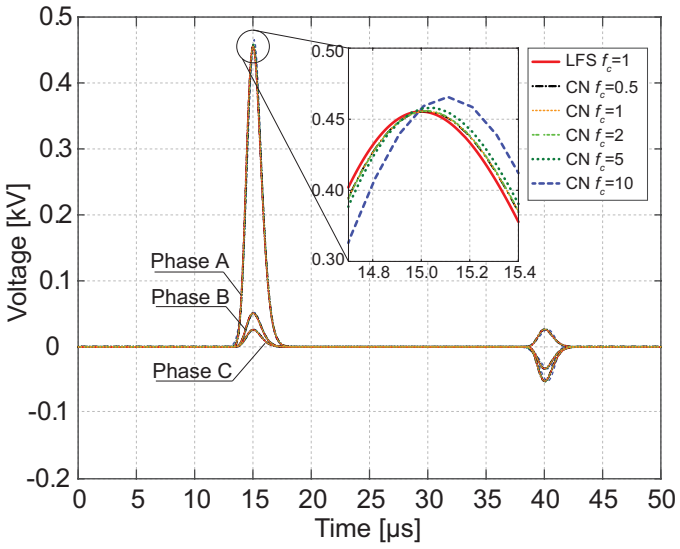

(a)

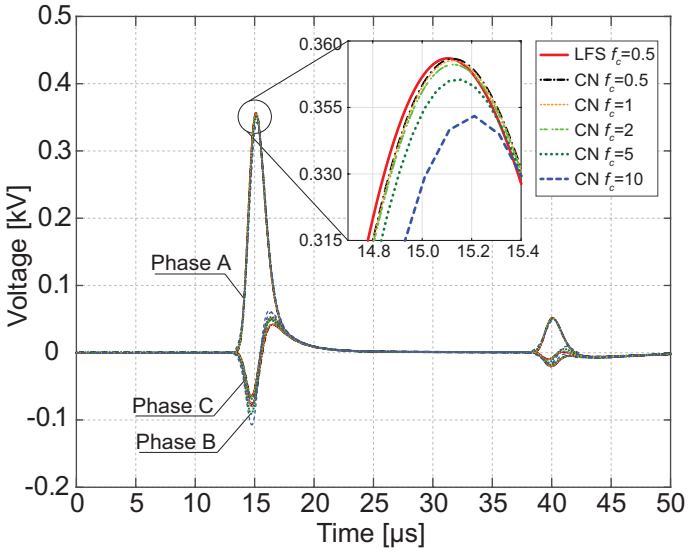

(b)

Figure 1.11. Voltages of the phase conductors for the MTL in Fig. 1.10 computed by the LF and CN schemes. (a) Lossless case. (b) Lossy case.

References

[1] C. R. Paul, *Analysis of Multiconductor Transmission Lines.* John Wiley and Sons, 2008.

[2] E. J. Rothwell and M. J. Cloud, *Electromagnetics.* CRC press, 2018.

[3] E. Seran, M. Godefroy, E. Pili, N. Michielsen, and S. Bondiguel, "What we can learn from measurements of air electric conductivity in ^{222}Rn-rich atmosphere," *Earth and Space Science*, vol. 4, no. 2, pp. 91–106, 2017.

[4] S. A. Schelkunoff, "The electromagnetic theory of coaxial transmission lines and cylindrical shields," *The Bell System Technical Journal*, vol. 13, no. 4, pp. 532–579, 1934.

[5] A. Timotin, "Longitudinal transient parameters of a unifilar line with ground return," *Rev. Roum. Sci. Techn.-Electrotechn. et Energ.*, no. 12, pp. 523–535, 1967.

[6] S. Celozzi, "On the finite element time domain solution of the skin effect equations in multiconductor lines," *IEEE Trans. Magn.*, vol. 30, no. 5, pp. 3180–3183, Sep. 1994.

[7] A. Ghizzetti and A. Ossicini, *Trasformate di Laplace e calcolo simbolico.* Unione tipografico-editrice torinese, 1971.

[8] E. S. M. Mok and G. I. Costache, "Skin-effect considerations on transient response of a transmission line excited by an electromagnetic pulse," *IEEE Trans. Electromagn. Compat.*, vol. 34, no. 3, pp. 320–329, Aug. 1992.

[9] F. Rachidi and S. Tkachenko, *Electromagnetic Field Interaction with Transmission Lines: From Classical Theory to HF Radiation Effects (Advances in Electrical Engineering and Electromagnetics)*, W. Press, Ed., 2008.

[10] J. R. Carson, "Wave propagation in overhead lines with ground return," *Bell Sys. Tech. J.*, no. 5, pp. 539–554., 1926.

[11] D. Woodhouse, "On the theoretical basis of Carson's equations," in *2012 IEEE International Conference on Power System Technology (POWERCON)*. IEEE, 2012, pp. 1–6.

[12] A. Semlyen, "Ground return parameters of transmission lines an asymptotic analysis for very high frequencies," *IEEE Trans. Power App. Syst.*, no. 3, pp. 1031–1038, 1981.

[13] R. Araneo and S. Celozzi, "Direct time-domain analysis of transmission lines above a lossy ground," *IEE Proceedings - Science, Measurement and Technology*, vol. 148, no. 2, pp. 73–79, Mar. 2001.

[14] J. A. Roden, C. R. Paul, W. T. Smith, and S. D. Gedney, "Finite-Difference Time-Domain analysis of lossy transmission lines," *IEEE Trans. Electromagn. Compat.*, vol. 38, no. 1, pp. 15–24, Feb 1996.

[15] K. Yee, "Numerical solution of initial boundary value problems involving Maxwell's equations in isotropic media," *IEEE Trans. Antennas Propag.*, vol. 14, no. 3, pp. 302–307, May 1966.

[16] S. Kim, E. F. Kuester, C. L. Holloway, A. D. Scher, and J. Baker-Jervis, "Boundary effects on the determination of metamaterial parameters from normal incidence reflection and transmission measurements," *IEEE Trans. Antennas Propag.*, vol. 59, no. 6, pp. 2226–2240, Jun. 2011.

[17] J. A. Pereda, A. Grande, O. Gonzalez, and N. Vegas, "The 1D ADI-FDTD method in lossy media," *IEEE Antennas Wireless Propag. Lett.*, vol. 7, pp. 477–480, 2008.

[18] E. Stracqualursi, R. Araneo, P. Burghignoli, G. Lovat, and S. Celozzi, "Unconditionally stable implicit schemes for transient analysis of lossy multiconductor lines," *IEEE Trans. Electromagn. Compat.*, vol. 63, no. 2, pp. 640–644, Apr. 2021.

[19] Visual Numerics, "IMSL Fortran numerical library user's guide, version 7.0," 2010.

[20] R. Prony, "Essai experimental et analitique," *J. de l'Ecole Polytechnique*, vol. 2, 1795.

[21] L. G. Kelly, *Handbook of numerical methods and applications*. Addison-Wesley, 1967.

[22] M. Van Blaricum and R. Mittra, "A technique for extracting the poles and residues of a system directly from its transient response," vol. 23, no. 6, pp. 777–781, 1975.

[23] M. A. Schamberger, S. Kosanovich, and R. Mittra, "Parameter extraction and correction for transmission lines and discontinuities using the finite-difference time-domain method," *IEEE Trans. Microw. Theory Tech.*, vol. 44, no. 6, pp. 919–925, 1996.

[24] J. R. Tomlison, "Functional techniques for data analysis," Ph.D. dissertation, Texas Tech University, 1997.

[25] A. Orlandi and C. R. Paul, "FDTDc analysis of lossy, multiconductor transmission lines terminated in arbitrary loads," *IEEE Trans. Electromagn. Compat.*, vol. 38, no. 3, pp. 388–399, Aug. 1996.

[26] J. D. Lambert, *Numerical methods for ordinary differential systems: the initial value problem*. John Wiley & Sons, Inc., 1991.

[27] D. F. Griffiths and D. J. Higham, *Numerical methods for ordinary differential equations: initial value problems*. Springer, 2010, vol. 5.

[28] S. D. Gedney, "Introduction to the Finite-Difference Time-Domain (FDTD) method for electromagnetics," *Synthesis Lectures on Computational Electromagnetics*, vol. 6, no. 1, pp. 1–250, 2011.

[29] A. Taflove, *Computational Electrodynamics: The Finite-Difference Time-Domain Method*. Norwood, MA: Artech House, 1995.

[30] K. S. Kunz and R. J. Luebbers, *The finite difference time domain method for electromagnetics*. CRC press, 1993.

Chapter 2

Distributed and lumped non-uniformities

Different aspects should be considered when assessing the charge distribution along an actual overhead line:

- the conductor is not parallel to the ground: its height is not constant in the x-direction;
- the total length of the conductor, commonly assumed equal to the distance between consecutive towers, should account for the actual conductor's sag and stranding angle;
- the presence of the line towers, and other devices (arcing horns, terminations, etc.) affects the charge distribution along the conductors;
- the soil is characterised by a finite value of relative electric permittivity ϵ_{rg}, which introduces an error in the computation of the matrices of p.u.l. capacitances.

With regard to the last point, matrices of p.u.l. capacitances are derived under the hypothesis $\epsilon_{rg} \gg 1$. However, when the common value $\epsilon_{rg} = 20$ is assumed and perfect images of the conductors are considered in the place of the actual ones, 10% error is introduced in the values of the conductors' image charges approximately. On the other side, ϵ_{rg} strongly depends on the local characteristics of the soil and on meteorological conditions. The approximation $\epsilon_{rg} \gg 1$ is acceptable, given the possible range of variation of ϵ_{rg} and the uncertainty on its actual value.

The definition of the p.u.l. parameters for MTL modelling is based on two main hypotheses: the line has infinite length and the conductors keep a constant height above the horizontal reference plane. Indeed, the error introduced by making the former assumption holds minor impact when the line under analysis is long enough to assume that the influence of the field distribution at its terminations turns negligible at a suitable distance (the

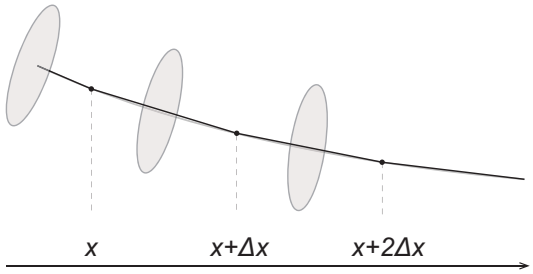

Figure 2.1. Planes orthogonal to the direction of propagation of travelling waves at different points x along the span.

approximation being unsatisfactory in any case in the proximity of the line endpoints). As to the latter assumption, the actual variability of the line conductors' height above the ground is limited when the wires are subjected to large mechanical tension, and also depends on the designed span length and regularity of the ground plane [1].

Under these simplifying assumptions, quasi-TEM propagation may be considered (or TEM propagation if the lossless line case is to be assessed). Hence, the magnetic and electric field along the TL are derived from the local value of current and p.u.l. charge by means of electro- and magneto-statics relations, since the predominant components of the fields lay in the transverse plane with respect to the direction of propagation.

This is not the case if the hypothesis of constant height of the conductor above the ground is removed, and the effect of the sag is considered as a distributed non-uniformity of the line [2]. Focusing on the charge distribution and observing the line section sketched in Fig. 2.1, it is clear that the field components at x are no longer independent on the field produced by the neighbouring line sections, which display a tangent vector with different incline and variable position above the ground.

2.1 Distributed non-uniformities: conductors' catenary

The typical conductor's profile, known as *catenary* and depending on structural and mechanical characteristics of the conductors, is described by the following expression [3]:

$$h\left(x'\right) = h_{\min} + 2\alpha\left[\sinh\left(\frac{x'}{2\alpha}\right)\right]^2, \tag{2.1}$$

where $h_{\min}$ is the height of the lowest point of the catenary, x' is to be considered as in Fig. 2.2a, and α, depending on the conductor mechanical tension and

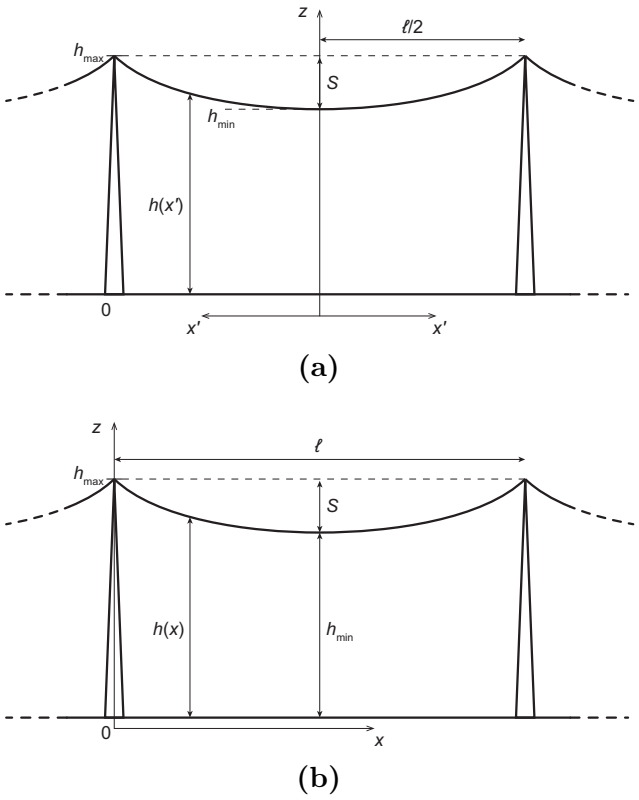

Figure 2.2. Representation of the actual variation of the conductor's height above a reference plane in the case of symmetric span (i.e., same towers and conductor tension at the span terminations). (a) Origin of the coordinate system at midspan; (b) origin of the coordinate system at the span left termination.

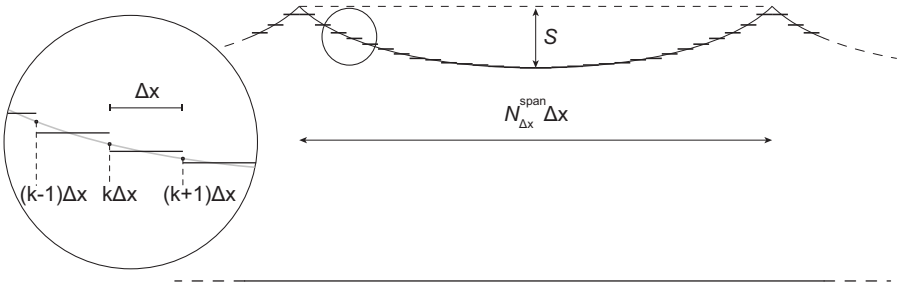

Figure 2.3. Sketch of the 2D staircase approximation of the line catenary.

p.u.l. weight, is found as the solution of the equation

$$h_{\max} = h_{\min} + 2\alpha \left[\sinh\left(\frac{\ell}{4\alpha}\right)\right]^2 . \tag{2.2}$$

With reference to Fig. 2.2, assuming stationary conditions and equipotentiality to be reached by all the sections of the span, a nonuniform charge distribution will be found along the conductor; the electric field at x is to be computed as the integral superposition of the vectorial electric fields produced by the p.u.l. charges, non uniformly distributed along the line.

The most accurate approach would be the one of performing a 3D simulation of the whole line, accounting for the mutual effect between charges distributed along consecutive spans. In the literature, simplifying approaches, introducing a constant charge density along the conductors ([4], [5]), were proposed to account for the effect of the sag on the electric field distribution, and were compared to 2D approaches with conductors at constant height. Later, the charge simulation method (retrieving the charge distribution by imposing known values of potential at chosen boundary points on the conductor's surface) was implemented in conjunction with the image method in [3], in order to account also for the influence of the towers on the charge distribution along the spans, and for phase bundles.

2.1.1 Catenary staircase modelling

In the present section, a simplified method will be adopted to assess the charge distribution along the line, considering the variable height $h(x)$ of the conductors above the ground. The span is discretized into sections with length Δx, as for the implementation of the FDTD algorithms.

According to the common practice, the catenary profile of a single conductor, suspended by means of the insulator strings between two towers, may be also approximated by a second order polynomial (i.e., a parabola) [6]:

$$h(x) = h_{\max} - \frac{4S}{\ell}x + \frac{4S}{\ell^2}x^2 \tag{2.3}$$

where ℓ denotes the length of the span, S is the average sag (which depends on the conductor p.u.l. weight, installation configuration, external temperature, environmental conditions), and $h_{\max}$ is the maximum height of the conductor along the span, i.e., in correspondence of a tower. x, which in the remainder of the text denotes the line direction, only here is to be intended in the range $0 \leq x \leq \ell$ ($x = 0$ and $x = \ell$ correspond to the left and right points of suspension of the conductor, respectively). The quantity $h(x)$ denotes the height of the conductor above the ground as a function of x. The relevant geometrical quantities are displayed in Fig. 2.2b. Herein, an horizontal ground plane and equal heights of the conductors at the towers have been assumed; hence, due to the symmetry of the catenary, the maximum deviation between the highest and the lowest point of the conductor (namely, the conductor's sag S) is found at the middle of the span.

Each segment of the line is approximated by a horizontal conductor, parallel to the ground, with length Δx. As a result, the contribution of the projection of the line segment in the vertical direction, in terms of increased length of the span (hence, of travelling time), and on the total electric and magnetic field, is neglected. The degree of accuracy of the approximation is more satisfactory for the segments close to midspan, being approximately horizontal.

In order to realize the line staircase model, the height of the conductor is first computed at the nodes $k\Delta x$ with $0 \leq k \leq N_{\Delta x}^{\text{span}}$ according to expression (2.3) ($N_{\Delta x}^{\text{span}}$ denotes the number of discretized segments in a span). Successively, the height $h_{k,k+1}$ of the horizontal segment delimited by the nodes of the span located at $x = k\Delta x$ and $x = (k+1)\Delta x$ is computed as:

$$h_{k,k+1} = \frac{h(k\Delta x) + h((k+1)\Delta x)}{2}. \tag{2.4}$$

The quantity $h_{k,k+1}$ is used to derive the conductor p.u.l. self-capacitance $C'_{k,k+1}$, accounting for the corresponding image conductor with radius r_0, located at depth $-h_{k,k+1}$ below the soil-air interface (assuming $\epsilon_g \gg \epsilon_0$)

$$C'_{k,k+1} = \frac{2\pi\epsilon_0}{\ln\left(\frac{2h_{k,k+1}}{r}\right)}. \tag{2.5}$$

Expression 2.5 neglects any proximity effect which actually exists between the catenary segments. Rigourously, if the incline of the segment was taken into account, the electric field would not be confined in the zy plane (in the case of lossless line), but would show a non-zero component in the x-direction (Fig. 2.1), affecting the charge density distribution along the whole line.

Nevertheless, a similar simplified approach was also adopted in [7] for the computation of the magnetic field accounting for the conductor's sag, resulting in satisfactory approximation when compared to the exact solution. In [8], the *modified 2D method* was compared with a 3D solution (obtained by means of a custom-made code) in terms of the maximum electric field along the line;

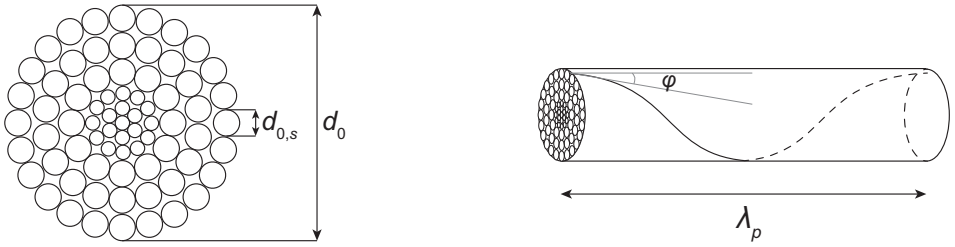

(a) (b)

Figure 2.4. Section of the reference aluminum conductor steel-reinforced (a) and helicoidal arrangement of the conductor strands (b).

electric fields computed by the *modified 2D method* at midspan showed a more satisfactory agreement than that achieved by fields computed close to the span terminations, taking the 3D solution as a reference.

Herein, charge distributions along a single conductor, accounting for its catenary arrangement above a horizontal ground, or considering an equivalent constant height will be compared. The geometrical average height, commonly adopted in propagation studies along MTLs, and implemented in EMTPs [9], is given by [6]:

$$h_{\text{ave}} = h_{\max} - \frac{2}{3} S \,. \tag{2.6}$$

A simple configuration of a single conductor over a horizontal PEC plane will be considered. The span is assumed symmetrical as in Fig. 2.2b; the height of the conductor (with diameter $d_0 = 2r_0 = 31.5$ mm) at the poles is equal to $h_{\max} = 27$ m, with $S = 10$ m and $\ell = 400$ m (e.g., the phase conductor of a typical Italian subtransmission line)[1]. The equivalent height, as by expression (2.6), is $h_{\text{ave}} \simeq 20.3$ m. The error due to approximating the actual conductors' length within the span (i.e., the computed length 400.7 m of the parabola segment between the poles) with the distance ℓ between consecutive towers is negligible, being less than 0.2%.

As to the influence of the helicoidal disposition of the conductors' strands on the lay length, an average stranding angle of $\varphi = 14°$ with respect to the conductor's axis is commonly adopted in the design of conductors for TL applications. As a simple reference, a typical aluminum conductor steel-reinforced for HV applications is considered with external diameter $d_0 = 31.5$ mm; it displays 24 strands with diameter $d_{0,s} = 3.50$ mm on its most external layer [11]. The conductor section and stranding angle are depicted (not in scale) in Fig. 2.4. Quantities λ_p and λ_h denote the helix pitch length and the actual length of each external strand between two consecutive helix

[1]The approximate value of the conductor's sag $S = 10$ m was chosen considering the conductor (ACSR – aluminum: 54×3.50 mm – steel: 19×2.10 mm) p.u.l. weight 1.953 kg/m and horizontal component of tension in the range 20-25% of the rated tensile strength 168.52 kN in normal conditions [10].

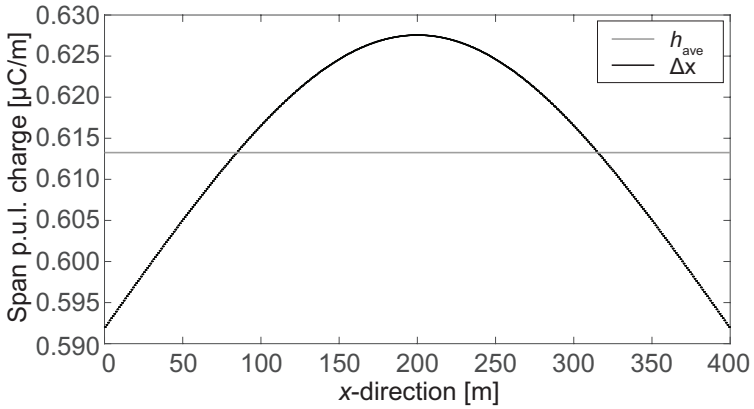

Figure 2.5. Charge distribution computed considering $h(x) = h_{\text{ave}}$, and by means of the proposed 2D method, with $\Delta x = 1$ m, and time-invariant line potential equal to $150/\sqrt{3}$ kV.

turns, respectively; by using the following expression

$$\Delta\lambda_{\%} = \frac{\lambda_h - \lambda_p}{\lambda_h} = [1 - \cos(\varphi)] \cdot 100\,, \tag{2.7}$$

the computed deviation $\Delta\lambda_{\%}$ of the pitch length with respect to the strand actual length is found to be less than the 3% (strands belonging to the inner layers of the section will display smaller φ, hence, a different deviation (2.7)).

The charge distribution computed by means of the proposed method, subdividing the line into segments $\Delta x = 1$ m, and assuming a known value of (time-invariant) line potential equal to $150/\sqrt{3}$ kV is displayed in Fig. 2.5. The total charge along a single span, computed by modelling the conductor with a constant height h_{ave}, is approximately 0.2% lower than the value associated with the 2D discretization approach (taken as a reference).

The finest line discretization is considered to be the one with $\Delta x = 1$ m, with total charge $Q(1\,\text{m})$ along the span. The percentage deviation $\Delta\epsilon_{\%}$ of the computed total charge $Q(\Delta x)$ along the span with respect to $Q(1\,\text{m})$ is derived as in (2.8), and displayed in Fig. 2.6 as a function of Δx for coarser discretizations. In Fig. 2.6, the values chosen for Δx are dotted, while the solid black line was obtained by fitting the results by means of a third order polynomial. It can be observed that the choice $\Delta x > 73$ m would introduce a wider error (approximately equal to the 0.16%) than the one expected considering the constant height h_{ave}.

$$\Delta\epsilon_{\%} = \frac{Q(1\,\text{m}) - Q(\Delta x)}{Q(1\,\text{m})} \cdot 100 \tag{2.8}$$

This simple approach locally adopts equations which are rigourously valid for an infinite line at constant height above the ground plane, and does not rely on the integral summation of effects due to the actual conductors profile along the

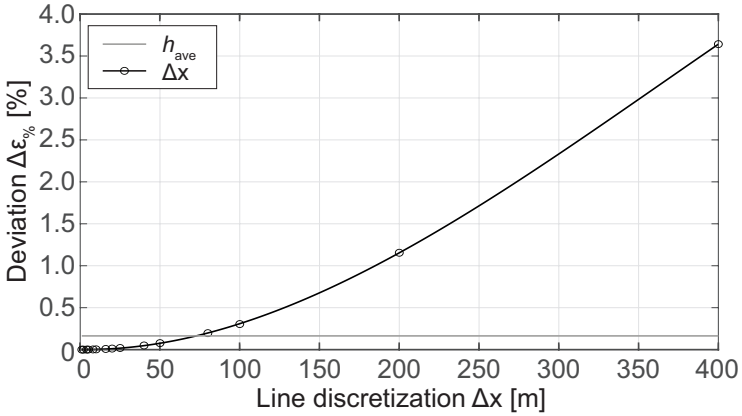

Figure 2.6. Percentage deviation $\Delta\epsilon_{\%}$ of the total charge along the span $Q(\Delta x)$ as a function of the line discretization Δx with $h(x)$ (black line), and for $h(x) = h_{\text{ave}}$ (grey line) with respect to $Q(1\,\text{m})$.

whole line; nevertheless, it is suitable to be implemented into FDTD algorithms, introducing x-dependent matrices of p.u.l. capacitances and inductances.

Furthermore, the adoption of a customized expression of the type (2.4) allows to account for different characteristics of the line when detailed information on its geometry is available: spans with different lengths and sags (due to environmental and/or safety restrictions, as from the local regulatory framework); non-symmetrical configuration of the conductors within the span (e.g., when the points of suspension at the span terminations present different heights); different sags, typically associated with the different p.u.l. weights and tensions of the SWs and phase conductors (in this case, the mutual distance between the conductors, variable along the span, represents an additional distributed non-uniformity).

2.1.2 Catenary model and FDTD code

When solving the telegrapher's equations (1.1) through an FDTD method, it should be clarified that the reference circuit of the line derives from modelling each line segment through an equivalent Pi-circuit; the effect of the total capacitance associated with the line section of length Δx is considered as concentrated at the segment terminations (Fig. 1.3). Hence, equations of the type (1.18a) are modified to account for the conductor's catenary, holding the following (written for the explicit FDTD method, in the simple case of a lossless single-conductor line):

$$-\frac{I_{k+\frac{1}{2}}^{n+\frac{1}{2}} - I_{k-\frac{1}{2}}^{n+\frac{1}{2}}}{\Delta x} = \left(\frac{C'_{k-1,k} + C'_{k,k+1}}{2}\right) \frac{V_k^{n+1} - V_k^n}{\Delta t}\,. \tag{2.9}$$

In the following example, the lossless single-conductor TL described in the previous section, with $\ell = 400$ m and total length equal to 2 km, was taken as

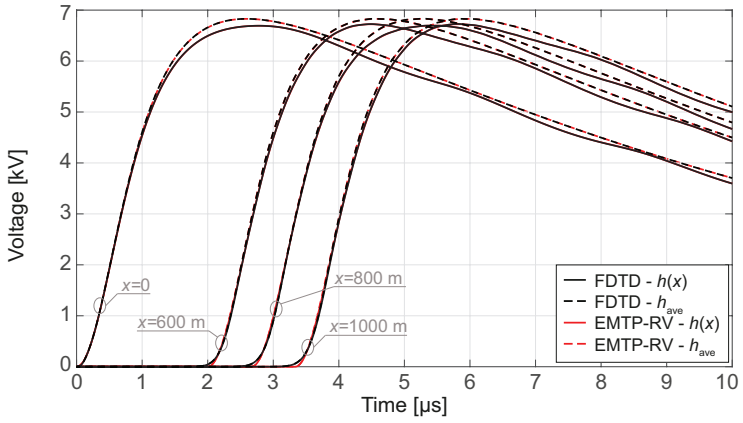

Figure 2.7. Voltages along the lossless single-conductor TL with catenary profile $h(x)$ described in 2.1.1, and total length 2 km. Results account for the variable $h(x)$ or for the constant h_{ave}.

a reference to simulate the effect of the catenary profile on the propagation of a simple voltage wave. The conductor's sag is expected to affect also voltages induced by external EM fields [12]; however, this topic is not referred here and will be dealt with in Chapter 3.

The line was fed at the left termination ($x = 0$) by means of a surge voltage generator with a series internal resistance $R_{\text{S}} = G_{\text{S}}^{-1} = 488\ \Omega$ (i.e., the value of the resistive characteristic impedance of the lossless line at $x = 0$, where $h(0) = 27$ m). The line is closed at the right termination on the resistive load $R_{\text{L}} = R_{\text{S}}$. The space discretization $\Delta x = 25$ m was chosen to ease the realization of the same configuration in EMTP-RV, modelling each span as the cascade of 16 CP-line devices ($N_{\Delta x}^{\text{span}} = 16$). Each CP-line device includes the length of the line section (25 m), null p.u.l. resistance, propagation speed equal to c_0, and characteristic impedance corresponding to $\sqrt{L'_{\text{ext}}(x)/C'(x)}$. The adopted values of $L'_{\text{ext}}(x)$ and $C'(x)$ were computed as from the staircase model implemented in the FDTD code (as a function of x). For the sake of simplicity, the surge voltage generator $v(t)$ is modelled by means of a single Heidler function of the type:

$$v(t) = \frac{V_0}{\eta} \frac{\left(\frac{t}{\tau_1}\right)^n}{1 + \left(\frac{t}{\tau_1}\right)^n} \exp\left(-\frac{t}{\tau_2}\right) \tag{2.10}$$

where, $V_0 = 13$ kV, $n = 2$, $\eta = 0.639$, $\tau_1 = 1\ \mu$s, $\tau_2 = 10\ \mu$s.

In Fig. 2.7, results from the implicit FDTD code and those computed by means of EMTP-RV are practically superimposed. In the simple simulated configuration and for the chosen voltage source, it can be observed that the predicted voltages peak values (at the displayed observation points along the line) accounting for the influence of the variable height of the conductor and those computed for the corresponding uniform TL at h_{ave} differ approximately

by 2%[2]. The effect of the variable height is evident also in the low-frequency oscillatory behaviour superimposed to the main voltage waveform, which is to be observed more easily at the tail. Indeed, its period $\simeq 2.67$ μs is related to $2\ell/c_0$.

Although being an approximated approach, the 2D method investigated here may represent an acceptable compromise between the exact solution and the constant height approach; in fact, it is characterised by an easy implementation and avoids the computational burden of 3D approaches, which, despite being more accurate, would also require detailed modelling (i.e., knowledge) of the line configuration, towers and other devices affecting the charge distribution along the spans. Furthermore, when implementing the staircase model in any FDTD code, the user is allowed to easily change the level of detail with which the catenary profile is reproduced.

2.2 Lumped non-uniformities: periodical grounding, line terminations

Lumped non-uniformities may be represented by the grounding of the SWs at the towers and by the line terminations.

Common technical practice involves the periodical connection of the SWs to the grounding systems buried at the base of the towers. In Chapter 7, the effects of this practice are assessed, including different values of the grounding resistance associated with the towers grounding systems; the analysis is carried out in the FD through the development of a suitable method based on the chain matrix analysis.

As to the line terminations, different technical solutions are possible, depending on the line location, and on the specific role of the line at a system/network level (e.g., high voltage TLs connected to bus-bars in electrical substations, transition of an overhead TL to a buried cable solution, etc.). Sections at the endpoints of the line typically experience harsher variations of incline and height above the ground; these lumped non-uniformities deserve dedicated modelling, depending on the specific configuration under analysis, since they locally affect the computation of matrices of p.u.l. capacitances ad inductances of the line.

[2]Simulations for the line at constant height are performed analogously, considering $R_L = R_S = 460$ Ω, corresponding to the value of the characteristic impedance of the conductor at h_{ave}.

References

[1] H. Sendaula, R. Johnson, D. Hilson, and R. Meyer, "Electric fields induced by EHV transmission over irregular terrain," *IEEE Trans. Power App. Syst.*, no. 5, pp. 1452–1458, 1983.

[2] C. Baum, J. Nitsch, and R. Sturm, "Analytical solution for uniform and nonuniform multiconductor transmission lines with sources," *Review of Radio Science*, vol. 1996, pp. 433–464, 1993.

[3] A. Z. El Dein, "Parameters affecting the charge distribution along overhead transmission lines' conductors and their resulting electric field," *Electric power systems research*, vol. 108, pp. 198–210, 2014.

[4] A. Z. El Dein, M. A. Wahab, M. M. Hamada, and T. H. Emmary, "The effects of the span configurations and conductor sag on the electric-field distribution under overhead transmission lines," *IEEE Trans. Power Del.*, vol. 25, no. 4, pp. 2891–2902, 2010.

[5] R. Amiri, H. Hadi, and M. Marich, "The influence of sag in the electric field calculation around high voltage overhead transmission lines," in *2006 IEEE Conference on Electrical Insulation and Dielectric Phenomena*. IEEE, 2006, pp. 206–209.

[6] N. Tleis, *Power systems modelling and fault analysis: theory and practice*. Elsevier, 2007.

[7] A. Mamishev, R. Nevels, and B. Russell, "Effects of conductor sag on spatial distribution of power line magnetic field," *IEEE Trans. Power Del.*, vol. 11, no. 3, pp. 1571–1576, 1996.

[8] J. C. Salari, A. Mpalantinos, and J. I. Silva, "Comparative analysis of 2-and 3-D methods for computing electric and magnetic fields generated by overhead transmission lines," *IEEE Trans. Power Del.*, vol. 24, no. 1, pp. 338–344, 2008.

[9] EMTP, "Line constants," https://www.emtp.com/documents/EMTP%20Documentation/doc/line_const/line_constants_EMTP_V3.pdf, (accessed Oct. 2022).

[10] *CIGRE Technical Brochure 324: Sag-Tension calculation methods for overhead lines*, CIGRE Std., 2016.

[11] "Caratteristiche generali delle linee elettriche aeree facenti parte della RTN," https://www.terna.it/DesktopModules/AdactoBackend/API/directdownload/get?file=0000/0113/81.pdf&popUp=true, (accessed Oct. 2022).

[12] D. Li, C. Wang, and X. Liu, "Investigation of lightning-induced overvoltages affected by the sag of the overhead transmission line," in *2011 IEEE Power Engineering and Automation Conference*, vol. 1. IEEE, 2011, pp. 335–338.

Chapter 3

Distributed sources

External fields, propagating through the media surrounding MTLs, may induce voltages and currents travelling along their conductors. Such external fields may be due to:

- natural phenomena like lightning strikes, geomagnetic storms, solar storms;
- man-made sources installed for other purposes (e.g., TLC antennas);
- man-made sources designed for intentional interferences.

Depending on the distance of the source, its polarity, and the amplitude of the produced fields, induced disturbances may provoke Electromagnetic Interference (EMI) in the victim (the observed line); its correct operation may be compromised and its performances impaired [1]. Due to the portability and reduced dimensions that sources may display, growing attention has been devoted in the last decades to Intentional Electromagnetic Interference (IEMI), defined as *intentional malicious generation of electromagnetic energy introducing noise or signals into electric and electronic systems, thus disrupting, confusing or damaging these systems for terrorist or criminal purposes* [1].

Along with the primary role of TLs conductors, consisting in carrying energy at long distances at power frequency (50 Hz or 60 Hz) or through High Voltage Direct Current (HVDC) systems, they may be employed (as an additional function) for power line communication, consisting in bidirectional exchange of data and information among smart devices, carrying signals with frequency in the order of magnitude of hundreds of kilohertz (broadband or narrowband). Indeed, these devices, installed more and more pervasively especially throughout distribution networks [2], are used for the purpose of monitoring the lines' status and for network protection, to support emergency operations and changes in the network configuration [3]. Hence, external electromagnetic fields may represent a cause of EMI or IEMI as to the correct operation of transmission and distribution lines.

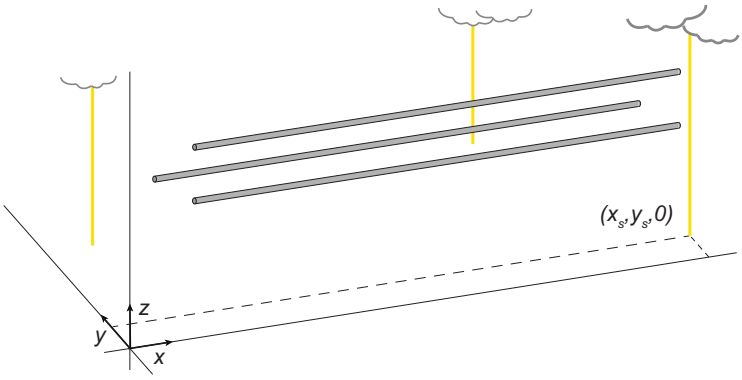

Figure 3.1. Sketch of indirect lightning events. The base of the lightning channel is located at $(x_s, y_s, 0)$.

As regards lightning events, whenever the connecting upward leader has not incepted from a TL's conductor, yet by an object/building in its proximity or by the ground, the electromagnetic field produced by the return stroke current, flowing through the lightning channel, induces overvoltages on the line's conductors. Therefore, indirect lightning may be classified as a source of EMI for operating MTLs.

Indirect lightning events represent a threat mainly for distributions lines [4], [5]. The proportionality between direct and indirect strikes to distribution lines is affected by several parameters, such as altitude of the site, height of the line conductors and poles, and configuration of the surrounding landscape (e.g., presence of taller structures, mountains, buildings, transmission lines, or trees, partially shielding the line from direct strikes). Indeed, HV TLs present larger insulating distances; for this reason, their lightning performance is determined predominantly by direct lightning strikes (hitting the towers top or the SWs, due to their height). Renovated attention is being dedicated to the lightning performance of distribution lines due to the more strict requirements for the quality of power supplied to the users.

In this chapter, the telegrapher's equations will be modified to account for the coupling of incident transient electromagnetic fields with MTLs. Specific attention will be devoted to lightning intercepted by the ground at a distance from the observed MTL, computing overvoltages induced by electromagnetic fields produced by return stroke currents. The use of distributed sources will be limited to this chapter, the remainder of the thesis being devoted to the effects of direct lightning strikes.

3.1 The modified telegrapher's equations

Three main formulations have been proposed in the literature to study the interaction between indirect lightning and power lines, namely those by Taylor

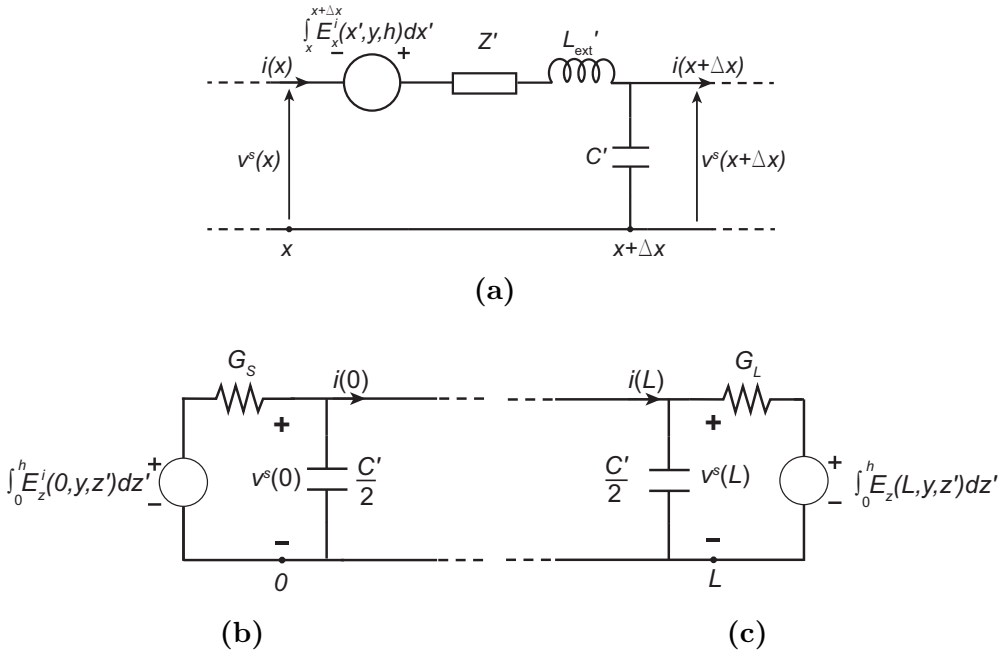

Figure 3.2. Circuit model, related to the modified telegrapher's equations for a single-conductor TL with height h, according to the Agrawal *et al.* coupling model [7] – the time dependence of the displayed quantities is omitted to ease the notation. (a) Generic section of the discretized line; (b) line left termination; (c) line right termination.

et al. [6], Agrawal *et al.* [7], and Rachidi [8], who has also proved the equivalence of the aforementioned approaches [9]. The reader interested in a comprehensive dissertation on the assumptions and derivation of the different field-to-line coupling models is referred to [10–12], authored by Nucci, Rachidi, Rubinstein, Cooray, and Piantini who devoted in depth research activity to this topic.

Other models (e.g., Rusck model and Chowduri model [13],[14]) were introduced. Nevertheless, revisions by Cooray [15] and Nucci *et al.* [16] revealed that some terms and field contributions were missing in these original formulations. In particular, as to Rusck coupling model, it did not account for the contribution of the vertical component of the magnetic vector potential in the computation of the forcing terms; on the other hand, the contribution of the magnetic induction was neglected by Chowduri's approach.

Without loss of generality, due to the equivalence of the models, the Agrawal *et al.* model will be briefly reviewed and implemented in the FDTD code.

The configuration under analysis is depicted in Fig. 3.1. The electric field and magnetic induction generated by a lightning current striking the ground at point $(x_s, y_s, 0)$ are denoted as $\overrightarrow{E}^i$ and $\overrightarrow{B}^i$, respectively. $\overrightarrow{E}^i$ and $\overrightarrow{B}^i$ are the incident fields, which would be produced in the absence of the MTL, and include the effect of the field scattered by the ground half-space (whether

modelled as a PEC plane or accounting for its finite conductivity σ_{g}).

$$\overrightarrow{E}(x,y,z,t) = \overrightarrow{E}^{i}(x,y,z,t) + \overrightarrow{E}^{s}(x,y,z,t) \tag{3.1a}$$

$$\overrightarrow{B}(x,y,z,t) = \overrightarrow{B}^{i}(x,y,z,t) + \overrightarrow{B}^{s}(x,y,z,t)\ . \tag{3.1b}$$

In (3.1), $\overrightarrow{E}$ and $\overrightarrow{B}$ are the total electric field and magnetic induction, expressed as the sum of incident and scattered quantities (denoted by superscript i and s, respectively). The latter quantities only account for the fields due to currents actually flowing along the MTL. The total fields may be also expressed in terms of their vector components in the directions $\hat{x}$, $\hat{y}$, $\hat{z}$:

$$\overrightarrow{E}(x,y,z,t) = E_x(x,y,z,t)\,\hat{x} + E_y(x,y,z,t)\,\hat{y} + E_z(x,y,z,t)\,\hat{z} \tag{3.2a}$$

$$\overrightarrow{B}(x,y,z,t) = B_x(x,y,z,t)\,\hat{x} + B_y(x,y,z,t)\,\hat{y} + B_z(x,y,z,t)\,\hat{z}\,. \tag{3.2b}$$

Recalling the fields decomposition into incident and scattered fields in (3.1), and assuming the response of the line to the external excitation field to be quasi-TEM, the scattered voltage v^s may be expressed as follows

$$v^s(x,t) = v(x,t) + \int_0^h E_z^i(x,y,z,t)\,dz\,, \tag{3.3}$$

leading to the modified telegrapher's equations (field-to-line coupling equations) in the scattered voltages as proposed by Agrawal *et al.* [7], accounting for the lossy ground[1]:

$$-\frac{\partial v^s(x,t)}{\partial x} = \int_0^t Z'_\zeta(t-\tau)\,\frac{\partial i(x,\tau)}{\partial \tau}\mathrm{d}\tau + L'_{\mathrm{ext}}\frac{\partial i(x,t)}{\partial t} - E_x^i(x,y,h,t) \tag{3.4a}$$

$$-\frac{\partial i(x,t)}{\partial x} = C'\frac{\partial v^s(x,t)}{\partial t} \tag{3.4b}$$

with relations (3.5) to be considered at the line terminations

$$v^s(0,t) = -G_S^{-1} i(0,t) + \int_0^h E_z^i(0,y,z',t)\,dz' \tag{3.5a}$$

$$v^s(L,t) = G_L^{-1} i(L,t) + \int_0^h E_z^i(L,y,z',t)\,dz'\,. \tag{3.5b}$$

The corresponding circuit model representing the modified telegrapher's equations is depicted in Fig. 3.2.

New approaches to accelerate the computation of the electromagnetic fields produced by an external lightning stroke have been recently proposed [18–20];

[1]The step-by-step derivation may be found in the paper by Cooray, Rachidi, and Rubinstein [17].

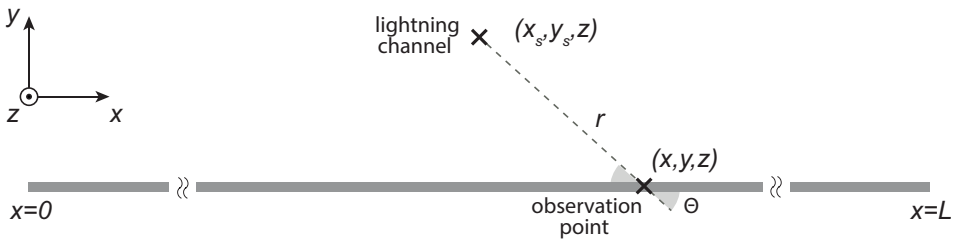

Figure 3.3. Observation point located at (x, y, h) along a reference single-conductor TL extending from $x = 0$ to $x = L$ (top view). The line is illuminated by the electromagnetic field produced by the return stroke current with channel base at $(x_s, y_s, 0)$.

herein, the classical approach is adopted: the electric and magnetic fields are computed by means of the integral summation of the fields produced by vertical dipoles laying along the direction of the lightning channel (in Sec. 3.1.1). Electromagnetic fields, produced by a vertical current on a PEC plane, are computed according to [21], [22]; the effect of lossy ground is accounted by the correction term introduced by Cooray and Rubinstein [23], [24], in its TD implementation by Andreotti *et al.* [25].

In terms of computational efficiency, the Agrawal *et al.* model only requires to evaluate the radial component of the incident electric field and two integral contributions of the vertical component of the incident electric field at the line terminations. Instead, the distributed voltage and current sources required by the Taylor *et al.* model are linked to the computation of the magnetic and electric fields at each discretized section of the line. However, while the latter approach describes the propagation of the total voltage (including incident and scattered voltages), the Agrawal *et al.* model accounts for the scattered voltage waves only; hence, additional integrations must be performed in order to get the total voltage at the chosen observation points. The total voltage $v\,(x,t)$ at point x and time t may be restored by applying (3.3):

$$v\,(x,t) = v^s\,(x,t) - \int_0^h E_z^i\,(x,y,z',t)\,dz'\,. \tag{3.6}$$

3.1.1 Electromagnetic field computation

In order to implement the field-to-line coupling model by Agrawal *et al.*, expressions of the electric field are to be computed in the $\hat{z}$ direction and in the $\hat{x}$ direction (i.e., in the direction of propagation of voltage and current traveling waves, displayed in Fig. 3.3).

Considering the lightning channel to be vertical with respect to the ground plane[2], $\overrightarrow{E}^i$ and $\overrightarrow{B}^i$ are more conveniently expressed by their components with respect to a cylindrical coordinate system, due to the axial symmetry of the configuration:

$$\overrightarrow{E}^i(x,y,z) = E_r^i(x-x_s, y-y_s, z-z_s)\,\hat{r} + E_z^i(x-x_s, y-y_s, z-z_s)\,\hat{z} \tag{3.7a}$$

$$\overrightarrow{B}^i(x,y,z) = B_\phi^i(x-x_s, y-y_s, z-z_s)\,\hat{\varphi} \tag{3.7b}$$

with

$$\overrightarrow{r} = (x-x_s)\,\hat{x} + (y-y_s)\,\hat{y} \tag{3.8a}$$

$$\hat{r} = \frac{\overrightarrow{r}}{|\overrightarrow{r}|}\,. \tag{3.8b}$$

The horizontal electric field $E_r^i\hat{r}$ (laying on the xy plane) may be computed in closed form for a lightning striking a PEC plane at $(x_s, y_s, 0)$. However, in practical applications, the ground displays a finite conductivity σ_g. Different approximate approaches were proposed to account for the finite conductivity of the soil in the computation of E_r^i [28]; these approaches have been revised and their accuracy assessed in the work by Cooray [28]. In particular, the surface impedance approach, as derived by Cooray [23] and Rubinstein [24], is the most frequently applied approach, giving E_r^i as the sum of two contributions

$$E_r^i(z,r,t) = \Delta E_r^i(z,r,t) + E_{r_0}^i(z,r,t)\,. \tag{3.9}$$

The term $E_{r_0}^i$ on the RHS of (3.9) is the electric field at (z,r) above a PEC plane, while ΔE_r^i is the correction term accounting for the lossy ground. The importance of the correction term grows at increasing distances from the lightning channel, since the term $E_{r_0}^i$ tends to vanish, and the electric field tends to coincide with the correction term itself ΔE_r^i [24]. Electric fields $E_{z_0}^i$ and $E_{r_0}^i$ in the presence of a PEC half-space are computed through the following expressions:

$$\begin{aligned} E_{z_0}^i(z,r,t) = \frac{1}{4\pi\epsilon_0}\Bigg[&\int_{-H}^{H}\frac{2(z-z')^2 - r^2}{R^5}\int_0^t i(z',\tau - R/c_0)\,d\tau dz' + \\ &+\int_{-H}^{H}\frac{2(z-z')^2 - r^2}{c_0 R^4} i(z',t-R/c_0)\,dz' + \\ &-\int_{-H}^{H}\frac{r^2}{c_0^2 R^3}\frac{\partial i(z',t-R/c_0)}{\partial t}dz'\Bigg] \end{aligned} \tag{3.10}$$

[2]It should be noted that this is a relevant approximation, which neglects the actual tortuosity of the lightning channel in the computation of the electric and magnetic fields produced by the return stroke current [26], [27].

$$E^i_{r_0}(z,r,t) = \frac{1}{4\pi\epsilon_0}\left[\int_{-H}^{H}\frac{3r\,(z-z')}{R^5}\int_0^t i\,(z',\tau-R/c_0)\,d\tau dz' + \right.$$
$$+\int_{-H}^{H}\frac{3r\,(z-z')}{c_0R^4}i\,(z',t-R/c_0)\,dz' +$$
$$\left.+\int_{-H}^{H}\frac{r\,(z-z')}{c_0^2R^3}\frac{\partial i\,(z',t-R/c_0)}{\partial t}dz'\right] \quad (3.11)$$

with

$$R = \sqrt{r^2+(z-z')^2}\,. \quad (3.12)$$

The Cooray-Rubinstein term for the correction of the horizontal (or radial) component of the electric field produced by the return stroke current was originally derived in the FD [24]. Denoting with E^i_r, E^i_{r0} the horizontal electric field in the presence of a lossy and lossless ground plane, respectively, and with $\mathrm{H}^i_{\phi 0}$ the magnetic field above a PEC plane, the following relation holds for these quantities in the FD:

$$\mathrm{E}^i_r(h,r,\omega) = -\mathrm{H}^i_{\phi 0}(0,r,\omega)\frac{\sqrt{\mu_0}}{\sqrt{\epsilon_\mathrm{g}+\sigma_\mathrm{g}/j\omega}} + \mathrm{E}^i_{r0}(h,r,\omega)\,, \quad (3.13)$$

where, the first term on the RHS represents the Fourier transform of the correction term denoted by ΔE^i_r in (3.9). The corresponding TD expression proposed by Andreotti *et al.* was implemented (for $t>0$) in the FDTD code:

$$\Delta E^i_r(z,r,t) = -\eta_g\int_0^t \underbrace{\exp\left(-\alpha\,(t-\tau)\right)I_0\left[\alpha\,(t-\tau)\right]}_{f_\alpha(t-\tau)}\cdot\frac{\partial H^i_{\phi 0}(0,r,\tau)}{\partial\tau}d\tau\,. \quad (3.14)$$

In (3.14), $\eta_g = \sqrt{\mu_0/\epsilon_\mathrm{g}}$ is the ground characteristic impedance, I_0 is the modified Bessel function of first type and order 0, and $H^i_{\phi_0}$ is given by:

$$H^i_{\phi_0}(z,r,t) = \frac{1}{4\pi}\left[\int_{-H}^{H}\frac{r}{R^3}i\,(z',t-R/c_0)\,dz' + \right.$$
$$\left.+\int_{-H}^{H}\frac{r}{c_0R^2}\frac{\partial i\,(z',t-R/c_0)}{\partial t}dz'\right]\,. \quad (3.15)$$

It should be noted that the implementation of (3.4a) requires the computation of the electric field component E^i_x in the x direction; taking the configuration in Fig. 3.3 as a reference, E^i_x may be obtained easily:

$$E^i_x(z,r,t) = E^i_r(z,r,t)\cos(\Theta) = E^i_r(z,r,t)\,\frac{x-x_s}{r}\,. \quad (3.16)$$

3.1.2 Implicit FDTD expressions

When expressions of the type (1.40) are to be modified to account for field-to-line coupling, the following may be derived[3]:

$$
\begin{aligned}
-[\mathbf{1}]\,\mathbf{V}^{n+1}_{\mathbf{s}_k} + \left\{\Delta x \boldsymbol{Z}'_\zeta(0) + \frac{2\mathbf{L}'_{\text{ext}}\Delta x}{\Delta t}\right\}\mathbf{I}^{n+1}_{k+\frac{1}{2}} + [\mathbf{1}]\,\mathbf{V}^{n+1}_{\mathbf{s}_{k+1}} = \\
= \frac{2\mathbf{L}'_{\text{ext}}\Delta x}{\Delta t}\left\{\mathbf{I}^{n}_{k+\frac{1}{2}} - \left[\frac{2\mathbf{L}'_{\text{ext}}}{\Delta t}\right]^{-1}\frac{\Delta \mathbf{V}^{n}_{\mathbf{s}_{k,k+1}}}{\Delta x}\right\} + \\
-2\Delta x\left\{\mathbf{CI}^{n-\frac{1}{2}}_{k+\frac{1}{2}} + \left[-\frac{\boldsymbol{Z}'_\zeta(0)}{2}\mathbf{I}^{n}_{k+\frac{1}{2}} + \frac{\boldsymbol{Z}'_\zeta(\Delta t)}{2}\left(\mathbf{I}^{n}_{k+\frac{1}{2}} - \mathbf{I}^{n-1}_{k+\frac{1}{2}}\right)\right]\right\} + \\
+\left(\mathbf{E}^{n}_{\mathbf{x}_{k+\frac{1}{2}}} + \mathbf{E}^{n+1}_{\mathbf{x}_{k+\frac{1}{2}}}\right)\Delta x \qquad (3.17)
\end{aligned}
$$

with

$$
\mathbf{E}^{n}_{\mathbf{x}_{k+\frac{1}{2}}} = \boldsymbol{\Delta}\mathbf{E}_{\mathbf{x}}{}^{n}_{k+\frac{1}{2}} + \mathbf{E}^{n}_{\mathbf{x0}_{k+\frac{1}{2}}}\,. \qquad (3.18)
$$

In (3.17) and (3.18), $\mathbf{V}^{n}_{s_k}$ is the vector of dimension $N_\text{c}\times 1$ of scattered voltages at node $k\Delta x$ and time $n\Delta t$; $\mathbf{E}^{n}_{\mathbf{x}_{k+\frac{1}{2}}}$ is the vector of p.u.l. voltage sources of dimension $N_\text{c}\times 1$, accounting for the contribution of the horizontal component of the incident electric field in the x direction[4]. In (3.18), the latter vector is given by the sum of $\mathbf{E}^{n}_{\mathbf{x0}_{k+\frac{1}{2}}}$ (i.e., the corresponding term computed with a PEC plane) and $\boldsymbol{\Delta}\mathbf{E}^{n}_{\mathbf{x}_{k+\frac{1}{2}}}$, of dimension $N_\text{c}\times 1$, corresponding to the finite-difference counterpart of (3.14):

$$
\boldsymbol{\Delta}\mathbf{E}_{\mathbf{x}}{}^{n}_{k+\frac{1}{2}} = -\eta_g\sum_{m=1}^{n} f_\alpha\left[(n-m)\,\Delta t + \frac{\Delta t}{2}\right]\cdot\left[\mathbf{H}^{m}_{\mathbf{\Phi 0}_{k+\frac{1}{2}}} - \mathbf{H}^{m-1}_{\mathbf{\Phi 0}_{k+\frac{1}{2}}}\right]. \qquad (3.19)
$$

Function f_α in (3.19) is defined in (3.14); the elements of the $N_\text{c}\times 1$ vector $\mathbf{H}_{\mathbf{\Phi 0}_{k+\frac{1}{2}}}$ correspond to the magnetic field computed in the lossless case at height $z=0$, $x=\left(k+\frac{1}{2}\right)\Delta x$, and y equal to the average value of the y coordinates of the conductors of the TL under study. The summation (3.19) is to be performed at every time step; however, suitable storage of previously calculated terms allows to evaluate efficiently (3.19), by only computing two additional quantities at the next time step n: the value of the magnetic field $\mathbf{H}^{n}_{\mathbf{\Phi 0}_{k+\frac{1}{2}}}$ and the kernel function $f_\alpha\left[(n-1)\,\Delta t + \Delta t/2\right]$.

Equations (1.44) and (1.47), relative to node $k=0$ and $k=N_{\Delta x}$, are

[3]Henceforth, the superscript i, used to denote incident fields, will be omitted in FDTD expressions, for the sake of clarity of the notation.

[4]It is recalled that $[\mathbf{1}]$ denotes the identity matrix of order N_c.

modified into (3.20) and (3.21), respectively:

$$\left\{\mathbf{G}_{\mathrm{S}}+\frac{\mathbf{C}'\Delta x}{\Delta t}\right\}\mathbf{V}_{\mathbf{s}_0}^{n+1}+[\mathbf{1}]\,\mathbf{I}_{\frac{1}{2}}^{n+1}=2\mathbf{G}_{\mathrm{S}}\mathbf{E}_{\mathrm{S}}^{n+\frac{1}{2}}+\frac{\mathbf{C}'\Delta x}{\Delta t}\mathbf{V}_{\mathbf{s}_0}^{n}+ \\ -\left[\mathbf{G}_{\mathrm{S}}\mathbf{V}_{\mathbf{s}_0}^{n}+\mathbf{I}_{\frac{1}{2}}^{n}\right]+\mathbf{G}_{\mathrm{S}}\left[\left(E_{z_0}^{n}+E_{z_0}^{n+1}\right)\mathbf{h_c}\right] \quad (3.20)$$

$$-[\mathbf{1}]\,\mathbf{I}_{N_{\Delta x}-\frac{1}{2}}^{n+1}+\left\{\mathbf{G}_{\mathrm{L}}+\frac{\mathbf{C}'\Delta x}{\Delta t}\right\}\mathbf{V}_{\mathbf{s}_{N_{\Delta x}}}^{n+1}=\left[\frac{\mathbf{C}'\Delta x}{\Delta t}\right]\mathbf{V}_{\mathbf{s}_{N_{\Delta x}}}^{n}+ \\ +\left[\mathbf{I}_{N_{\Delta x}-\frac{1}{2}}^{n}-\mathbf{G}_{\mathrm{L}}\mathbf{V}_{\mathbf{s}_{N_{\Delta x}}}^{n}\right]+\mathbf{G}_{\mathrm{S}}\left[\left(E_{z_{N_{\Delta x}}}^{n}+E_{z_{N_{\Delta x}}}^{n+1}\right)\mathbf{h_c}\right], \quad (3.21)$$

where E_{z_0} ($E_{z_{N_{\Delta x}}}$) is the vertical component of the incident electric field computed at $z=0$, $x=0$ ($x=N_{\Delta x}\Delta x$), y (as from the definition above). $\mathbf{h_c}$ is the $N_{\mathrm{c}}\times 1$ vector of the conductors heights above ground.

3.2 Return stroke models

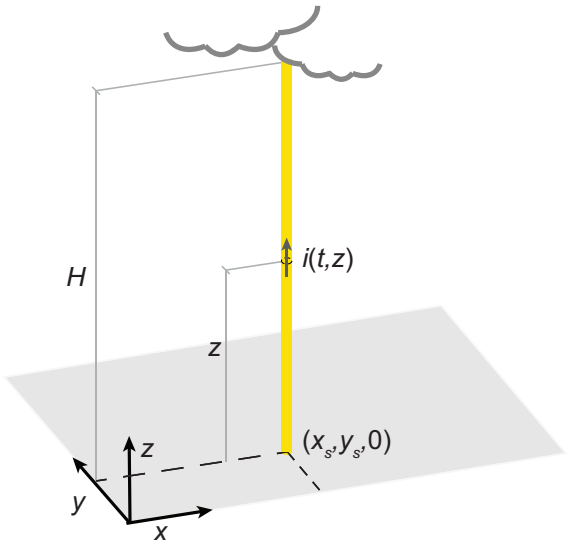

Figure 3.4. Representation of the lightning channel and return stroke current $i\,(t,z)$ in the adopted system of coordinate axes.

Computation of the fields produced by a return stroke current, which is needed to derive the p.u.l. sources to assess induced effects on neighbouring TLs, relies on the analytical expression of the return stroke current, as a function of time t and distance z from the ground plane.

Rakov and Uman [29], Cooray [30], and Gomes and Cooray [31] authored comprehensive reviews of the return stroke models available in the literature, including gas electro-thermodynamic models, electromagnetic models,

distributed-circuit models, and engineering models. While the first three approaches attempt to incorporate aspects of the physics of the lightning phenomenon at different levels, the simplicity of engineering approaches (reflected by the reduced number of required parameters) partially overshadows the physics implicated in lightning modelling.

In [30], engineering models from the literature are classified into three categories: current propagation models, current generation models, and current dissipation models. Transmission Line model [32], Dennis and Pierce model [33], Modified Transmission Line model with Linear attenuation (MTLL) (Rakov *et al.* [34]), Modified Transmission Line model with Exponential attenuation (MTLE) (Nucci *et al.* as from [29]), often adopted in field-to-line coupling studies, may be ascribed to the first category. Here, modified transmission line models are chosen for implementation. Indeed, MTLL is judged satisfactory in terms of results and implementation simplicity [29].

Transmission Line and Modified Transmission Line models including Linear and Exponential attenuation in the z direction will be briefly reviewed.

With reference to Fig. 3.4, the general expression for the return stroke current $i\,(t, z)$ at time t and height z above the ground according to Modified Transmission Line models is given by:

$$i\,(t, z) = u\,(t - z/\nu_f)\,P\,(z)\,i\,(t - z/\nu_0, 0) \tag{3.22}$$

where $u\,(t)$ is the Heaviside function, and

$$P\,(z) = \begin{cases} 1 - \frac{z}{H} & \text{for MTLL} \\ \exp\,(-z/\lambda_d) & \text{for MTLE} \\ 1 & \text{for TL model.} \end{cases} \tag{3.23}$$

In (3.23), the most frequently adopted current peak attenuation functions $P\,(z)$ are included[5]; H is the assumed height of the lightning channel (which is expected to be within some kilometers, depending on the geographical location of the lightning event), and λ_d is the current decay constant; the value of ν_0 is taken as the velocity of the charge moving upwards through the lightning channel. The quantity ν_f is used to denote the speed of propagation of the return stroke front, assumed constant or variable with the height above the ground. However, the hypothesis $\nu_f = \nu_0$ is commonly adopted for simulations.

It should be noted that engineering models approximate the lightning channel to a perfectly vertical cylinder, extending from $z = 0$ to $z = H$, not accounting for its branches and actual tortuous path. Furthermore, since these models do not account for reflections at the upper termination of the lightning channel [35], any evaluation of (3.22) at time $t > H/\nu_0$ may lead to unreliable results.

[5]Polynomial expressions, rational and exponential functions for $P\,(z)$ are also proposed by Rakov and Dulzon in [34].

Recently, a Modified Transmission Line model with Derived attenuation function (MTLD) was proposed by Cooray, Rubinstein, and Rachidi [36]; the model is consistent with the aforementioned MTLL and MTLE for suitable values of the parameters required by the corresponding attenuation functions. Starting from the measured electric field in the z direction at very large distances from the lightning channel (in order to ensure that E_z^i may be satisfactorily approximated just by the radiation contribution), the authors derive the attenuation function from the known propagation speed ν_0 and current waveform at the channel base (which are to be measured for the same lightning event). The introduction of current dispersion in the MTLD allows to reproduce the second peak (referred to as *subsidiary peak*) experimentally observed in the produced electric field, which other Modified Transmission Line models are not able to simulate considering reasonable attenuation functions, propagation speed, and single-peaked return stroke currents.

3.3 Lightning current waveforms

In the present section, the most common analytical expressions used in the literature to describe waveforms $i(t) = i(t, 0)$ of return stroke currents as functions of time t, are briefly reviewed. Expressions included in this section may be exploited to address studies involving indirect and direct lightning to MV and HV lines.

As to the features which are desirable for the channel base current waveform $i(t)$, these may be synthesised by the following:

- to be a continuous function of time;
- to approximate available measured waveforms of the channel base return stroke current;
- to be differentiable and integrable.

The last condition turns out particularly useful when it comes to indirect lightning studies, i.e., when the lightning current derivative and integral are required to compute the produced electromagnetic field through analytical formulas (e.g., in Sec. 3.1.1).

An additional favourable feature would be for the waveform to depend on parameters which affect independently some physical quantities of interest, as rise-time, time to half-value, steepness, etc.

An indicative comparison between the five lightning current expressions, briefly reviewed in the following sections, is proposed in Fig. 3.5a. The parameters required by each approach[6] (in Table 3.1) were set to obtain

[6]Herein, some symbols may be adopted to denote different quantities; hence, the validity of the adopted notation is limited to the paragraph in which each waveform is introduced.

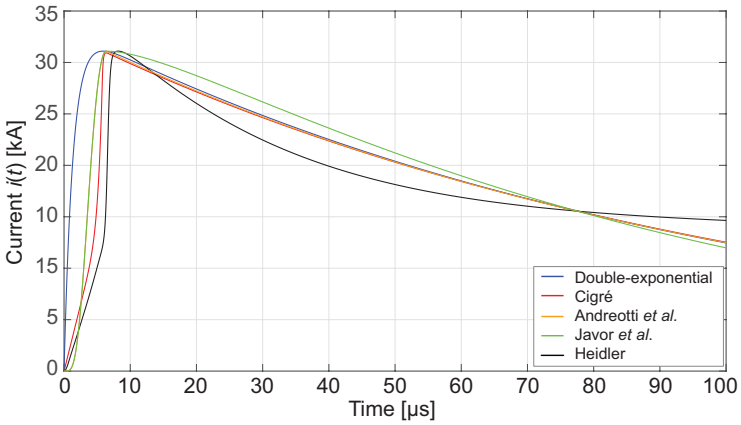

(a)

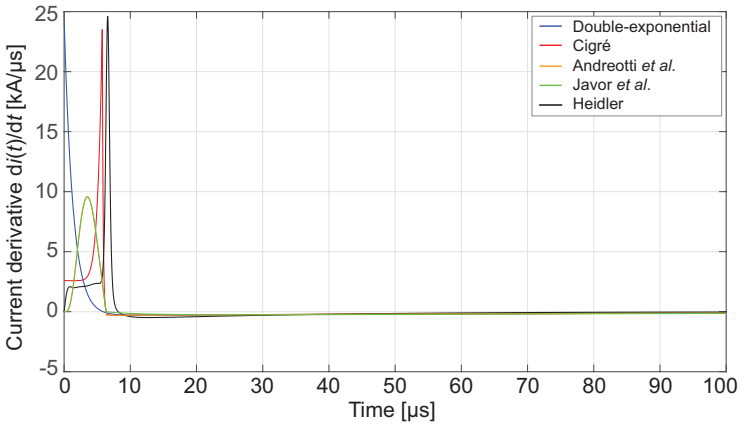

(b)

Figure 3.5. (a) Current waveform $i\,(t)$ as a function of time. (b) Current first order derivative $\mathrm{d}i\,(t)\,/\mathrm{d}t$ as a function of time.

Table 3.1. Parameters used to reproduce lightning currents in Fig. 3.5.

Double-exponential waveform	Cigré waveform	Andreotti *et al.* waveform	Javor *et al.* waveform
$\alpha = 7.43 \cdot 10^5$ s^{-1}	$t_f = 3.63$ μs	$\tau_1 = 6.35$ μs	$t_m = 6.35$ μs
$\beta = 9.86 \cdot 10^3$ s^{-1}	$t_h = 77.5$ μs	$\tau_2 = 101.3$ μs	$a=5$, $n=1$
$I_0 = 33.4$ kA	$I_{peak} = 31.1$ kA	$n = 5$	$b = 0.0796$
		$I_0 = 31.1$ kA	$I_0 = 31.1$ kA

Heidler waveform				
k	$I_{peak,k}$ [kA]	τ_{1k} [μs]	τ_{2k} [μs]	n_k
1	2.8	1.18	101.2	2
2	4.8	3.14	101	3
3	2.9	4.79	27	5
4	4.1	6	60	7
5	16.7	6.6	44	36
6	11	100	600	2

currents with peak and time to half-value approximately equal to 31.1 kA and 77.5 μs, respectively, and time $t_{d30} = T_{30}/0.6 \simeq 3.72$ μs[7] (median values for negative first stroke currents as from [37]).

3.3.1 Double-exponential waveform

The double-exponential waveform was first proposed by Bewley [38]:

$$i\,(t) = I_0 \left[\exp\left(-\alpha t\right) - \exp\left(-\beta t\right)\right] . \tag{3.24}$$

Expression (3.24) depends on the three parameters I_0, α, and β, allowing to affect three of the waveform characteristics, namely, *crest, wave length, and front* [38]. The three terms refer to the peak value I_{peak}, decay time t_2 (or time at which the current value is reduced to a fraction p of its peak value I_{peak}) and front time t_1 (to be here intended as time to peak). Although each parameter affects a specific characteristic of the final waveform predominantly, their effects are not completely independent. In fact, the following system of equations should be solved in the unknowns I_0, α, β, given t_1, t_2, I_{peak}:

$$\begin{cases} -\alpha \exp\left(-\alpha t_1\right) + \beta \exp\left(-\beta t_1\right) = 0 \\ I_0 \left[\exp\left(-\alpha t_1\right) - \exp\left(-\beta t_1\right)\right] = I_{peak} \\ \left[\exp\left(-\alpha t_2\right) - \exp\left(-\beta t_2\right)\right] = p\,, \end{cases} \tag{3.25}$$

[7] T_{30} is time elapsed between instants at which the current reaches the 30% and 90% of its peak value.

where the first equation forces the current derivative to be null at time t_1 (requiring a stationary point at t_1). A frequently adopted alternative expression for (3.24) is:

$$i(t) = \frac{I_{peak}}{\eta} \left[\exp(-\alpha t) - \exp(-\beta t)\right] \tag{3.26}$$

with

$$\eta = \exp(-\alpha t_1) - \exp(-\beta t_1) \tag{3.27a}$$

$$t_1 = \frac{1}{\beta - \alpha} \ln\left(\frac{\beta}{\alpha}\right) . \tag{3.27b}$$

In (3.26) and (3.27), η is a peak correction factor.

The main numerical downside of expression (3.24) is to be found in the discontinuity of the first derivative at $t = 0$ (in Fig. 3.5b), while the predicted convex front (in Fig. 3.5a) is not in agreement with measured waveforms of actual lightning currents; the resulting curve is not suitable to reproduce waveforms with different shapes [39].

To solve the issue of the discontinuity of the first derivative at time $t = 0$, an alternative expression was introduced in the field of electromagnetic pulse analysis [40], yet not commonly used by the research community on lightning:

$$i(t) = I_{peak} \frac{\delta \exp(\alpha t)}{1 + \exp(\beta (t - t_p))} \tag{3.28}$$

where $\delta = \beta (\beta - \alpha)^{(\alpha/\beta - 1)} \alpha^{-\alpha/\beta} \exp(-\alpha t_p)$; parameters and α, β, t_p should be adjusted to meet the requirements relative to front and decay time.

3.3.2 Cigré waveform

The lightning current is described by two functions of time [37]. The point of connection between the two functions is at time $t = t_n$, i.e., when the maximum steepness of the waveform is predicted:

$$i(t) = \begin{cases} At + Bt^n & t \le t_n \\ I_1 \exp\left(-\frac{t - t_n}{t_1}\right) - I_2 \exp\left(-\frac{t - t_n}{t_2}\right) & t > t_n \end{cases} \tag{3.29}$$

with

$$A = \frac{1}{n-1}\left[0.9n\frac{I_{peak}}{t_n} - S_m\right] \tag{3.30a}$$

$$B = \frac{1}{t_n^n\,(n-1)}\left[S_m t_n - 0.9I_{peak}\right] \tag{3.30b}$$

$$t_1 = (t_h - t_n)\,/\ln(2) \tag{3.30c}$$

$$t_2 = 0.1I_{peak}/S_m \tag{3.30d}$$

$$I_1 = \frac{t_1 t_2}{t_1 - t_2}\left[S_m + 0.9\frac{I_{peak}}{t_2}\right] \tag{3.30e}$$

$$I_2 = \frac{t_1 t_2}{t_1 - t_2}\left[S_m + 0.9\frac{I_{peak}}{t_1}\right]. \tag{3.30f}$$

The quantities S_m and t_h denote the maximum rate or rise (occurring at $t = t_n$, with $i(t_n) = 0.9I_{peak}$) and the time to half-value, respectively.
Approximated expressions are given in [37] for quantities t_n and n (which should be rigourously found by the iterative solution of a nonlinear equation):

$$n = 1 + 2\,(S_N - 1)\left(2 + \frac{1}{S_N}\right) \tag{3.31a}$$

$$t_n = 0.6t_f\left[3\frac{S_N^2}{1 + S_N^2}\right] \tag{3.31b}$$

where $S_N = S_m t_f / I_{peak}$, and t_f is the front time (in [37], it is recommended to refer to t_{d30} as the front time).

In Fig. 3.5a, the characteristic concave-to-convex front may be observed; the inflection point is to be found in correspondence with the time of occurrence of the maximum of the first current derivative (computed numerically, Fig. 3.5b). The first order time derivative of expression (3.29) shows a discontinuity at time $t = 0$, which, generally, is not as harsh as the one presented by the double-exponential waveform in Sec. 3.3.1; indeed, the value of the parameter A determines the discontinuity of the current first derivative at time $t = 0$, being $di(0)/dt = A$ for $n > 1$.

3.3.3 Andreotti *et al.* waveform

Andreotti *et al.* proposed an expression for the lightning current waveform allowing to change independently front time, front steepness, peak value and time to half-value [41]:

$$i(t) = I_0 \begin{cases} \left(\frac{t}{\tau_1}\right)^n e^{n\left(1-\frac{t}{\tau_1}\right)}, & 0 \le \frac{t}{\tau_1} \le 1 + \frac{a}{n} \\ \left(\frac{n+a}{n}\right)^n e^{-\frac{an}{n+a}\frac{t}{\tau_1}}, & \frac{t}{\tau_1} > 1 + \frac{a}{n}. \end{cases} \tag{3.32}$$

In (3.32), $a = \tau_1/\tau_2$, I_0 is the current peak value, τ_1 is the time to peak, τ_2 affects the decaying time, and $n \in \mathbb{N}$ affects the front steepness ($n \ge 2$ should be chosen to get a null first order derivative of $i(t)$ at time $t = 0$).

Similarly to the waveform proposed by Cigré 3.3.2, the current waveform in (3.32) is described by two functions of time; nevertheless, the break point is to be found after the time of occurrence of the current peak. In [41], the closed-form expression of the time integral and Fourier transform of (3.32), useful to FD studies, are given.

In Fig. 3.5 the current waveform and its derivative, with parameters in Table 3.1, are displayed. The chosen front time and steepness factor n result in lower values of the first derivative compared to those related to the other waveforms in Fig. 3.5. Furthermore, the second order time derivative of the decaying portion is positive-valued, regardless of the chosen $\tau_1, \tau_2 > 0$; hence, the current tail displays a characteristic convex shape.

3.3.4 Javor *et al.* waveform

A class of functions was introduced by Javor *et al.* to model the lightning channel base current [42]:

$$i\left(t\right) = I_0 \begin{cases} \left(\frac{t}{t_m}\right)^a e^{a\left(1-\frac{t}{t_m}\right)}, & 0 \leq t \leq t_m \\ \sum_{k=1}^{n} c_k \left(\frac{t}{t_m}\right)^{b_k} e^{b_k\left(1-\frac{t}{t_m}\right)}, & t_m \leq t \leq \infty. \end{cases} \tag{3.33}$$

In (3.33), I_0 is the current peak value, and t_m denotes the time to peak. It should be noted that the same expression is adopted by Javor *et al.* and Andreotti *et al.* as to the current raising portion, although with a different break point. The parameter a (analogously to n in Sec. 3.3.3) is to be chosen to set the front steepness.
The decaying part is obtained by superimposing the weighted contributions of n decaying exponential functions with weights c_k (such that $\sum_{k=1}^{n} c_k = 1$).

Expressions for the time derivative and integral of (3.33) may be found in [39].

As expected, the current waveform and its first order time derivative (with parameters in Table 3.1) are superimposed to the ones from Andreotti *et al.* at time $0 \leq t \leq t_m$ (Fig. 3.5a). Nevertheless, differences are observed for $t > t_m$.

3.3.5 Heidler *et al.* waveform

The main advantage of the expression proposed by Heidler *et al.* ([43], [44]) is the removal of the first derivative discontinuity at time $t = 0$, which is a downside of the double-exponential formulation (Sec. 3.3.1). Furthermore, the proposed waveform is able to reproduce the observed concave front, characteristic of measured currents.

$$i\left(t\right) = \frac{I_{peak}}{\eta} \frac{\left(\frac{t}{\tau_1}\right)^n}{1+\left(\frac{t}{\tau_1}\right)^n} \exp\left(-\frac{t}{\tau_2}\right) \tag{3.34}$$

with

$$\eta = \exp\left[-\frac{\tau_1}{\tau_2}\left(\frac{n\tau_2}{\tau_1}\right)^{\frac{1}{n}}\right] . \tag{3.35}$$

Expression (3.34), suggested by IEC 61312-1 as the analytical expression to describe lightning strokes [45], is the product of three functions: the first one (constant) accounting for the waveform peak value through I_{peak} and a peak correction factor η; the second one affects the front of the waveform, and depends on the time constant τ_1 and the parameter n; the third one, depending on the time constant τ_2, determines the decaying portion of the waveform. Indeed (3.34) may be written also in the form

$$i\,(t) = i_0 x\,(t)\, y\,(t) \tag{3.36}$$

with

$$i_0 = \frac{I_{peak}}{\eta} \tag{3.37a}$$

$$x\,(t) = \frac{\left(\frac{t}{\tau_1}\right)^n}{1+\left(\frac{t}{\tau_1}\right)^n} \tag{3.37b}$$

$$y\,(t) = \exp\left(-\frac{t}{\tau_2}\right) . \tag{3.37c}$$

The main idea is for the function $x\,(t)$ $(y\,(t))$ to tend to unity for $t \to \infty$ $(t \to 0)$, i.e., to mainly affect the waveform rising portion (waveform tail). However, these functions do not affect the current features independently. Hence, τ_1, τ_2 and n should be suitably selected to obtain the desired front-time and decay-time.

The superposition of an arbitrary number N_H of functions of the type (3.34) (with suitable parameters) has been used in [46] to describe the median first stroke and subsequent stroke currents, with positive and negative polarity, and in [47] to reproduce measured current waveforms. Additionally, the superposition of multiple Heidler's functions may allow to represent different lightning current shapes, e.g., double-peaked first strokes. The resulting waveform may be expressed by

$$i\,(t) = \sum_{k=1}^{N_H} \frac{I_{peak,k}}{\eta_k} \frac{\left(\frac{t}{\tau_{1k}}\right)^{n_k}}{1+\left(\frac{t}{\tau_{1k}}\right)^{n_k}} \exp\left(-\frac{t}{\tau_{2k}}\right) \tag{3.38}$$

with

$$\eta_k = \exp\left[-\frac{\tau_{1k}}{\tau_{2k}}\left(\frac{n\tau_{2k}}{\tau_{1k}}\right)^{\frac{1}{n_k}}\right] . \tag{3.39}$$

Figure 3.5a displays a current of the type (3.38), with $N_H = 6$ and parameters in Table 3.1. Similarly to the current computed by the Cigré approach with

Table 3.2. Values adopted for return stroke current parameters, as from the Modified Transmission Line model with Exponential attenuation function in Sec. 3.2.

Caligaris *et al.* [50]	$\nu_0 = 1.5 \cdot 10^8$ m/s	$\lambda_d = 2.0$ km
Nucci *et al.* [51]	$\nu_0 = 1.3 \cdot 10^8$ m/s	$\lambda_d = 1.7$ km

paramenters in Table 3.1, the current waveform shows a very sharp increase of the first order derivative in proximity of the inflection point. At time $t = 0$, the first derivative is null (Fig. 3.5b).

In the present work, Heidler's functions were mainly adopted to account for lightning currents in direct and indirect lightning studies, being widely used by the scientific community, and suggested by relevant standards and guidelines [48]. Furthermore, with reference to Sec. 3.1.1, the electric and magnetic fields generated by return stroke currents, which are needed for the computation of the p.u.l. distributed sources for the implementation of field-to-line coupling models, are functions of the lightning current time integral and first order derivative. The analytical, closed-form expressions of the derivative and integral of (3.38) may be found in [46] and [49], respectively.

3.4 Numerical results

3.4.1 Electric field computation

In this section, results computed by means of the developed routines for the FDTD algorithm (with $\Delta t = 66.7$ ns) will be compared with components of the electric field in the vertical and horizontal directions from the literature. These routines are responsible for the computation of the distributed sources along the TL, accounting for the effects of indirect lightning.

Figures 3.6a and 3.6b display the computed E_z^i and E_x^i in the ideal case (return stroke current above a PEC plane), against fields from [51] and [50], respectively. The MTLE was adopted; the relevant parameters used for the implementation of the MTLE are included in Table 3.2. The return stroke current at the channel base is modelled as the sum of two Heidler's functions with parameters in Table 3.3.

Figure 3.7 displays the computed vertical component of the incident electric field E_z^i, including the effect of a lossy ground with $\sigma_g = 0.01$ S/m and $\epsilon_{rg} = 10$, against results in [50]. Results obtained by means of the developed routines agree more than satisfactorily with fields from the literature.

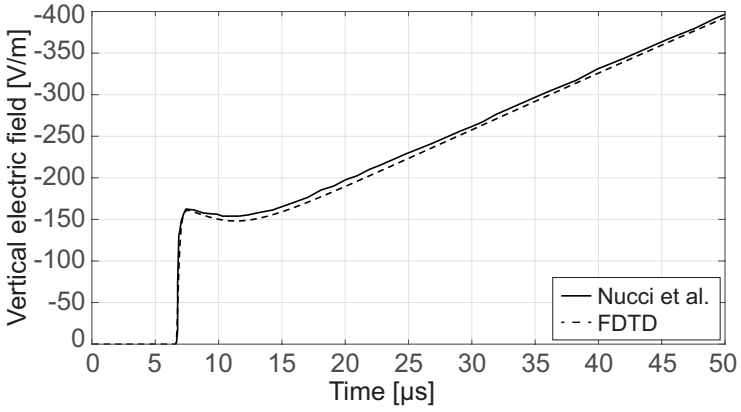

(a)

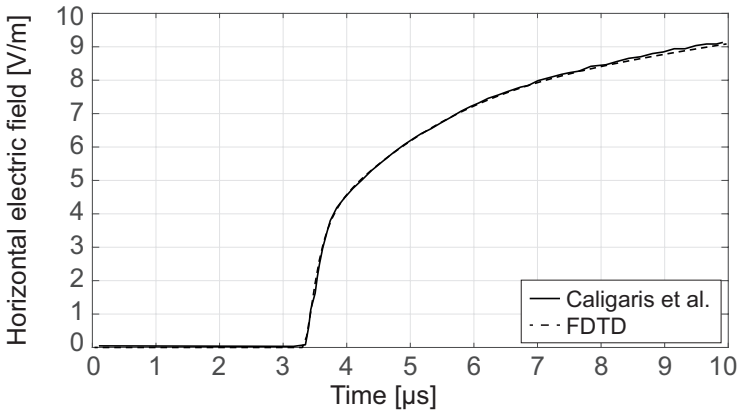

(b)

Figure 3.6. Electric field at (r_o, z_o) above a PEC plane computed by means of the routine developed for the FDTD code against fields from the literature. (a) Vertical electric field E_z^i for $z_o = 0$ and $r_o = 2$ km [51]; (b) horizontal electric field E_r^i for $z_o = 10$ m and $r_o = 1$ km [50].

Table 3.3. Return stroke current parameters [52].

	$I_{peak,k}$ [kA]	τ_{1k} [μs]	τ_{2k} [μs]	n_k
k=1	10.7	0.25	2.5	2
k=2	6.5	2.1	230	2

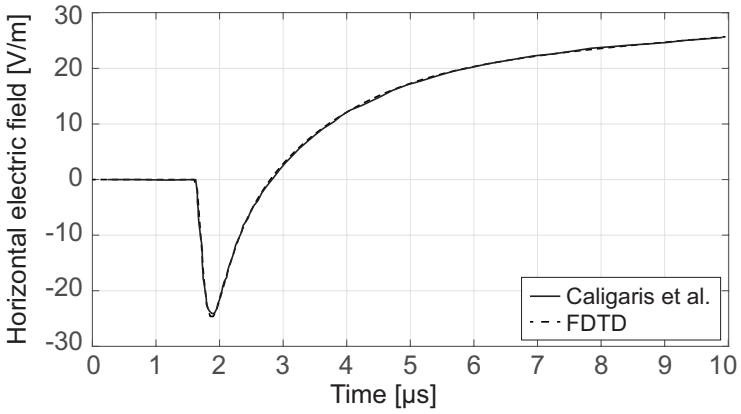

Figure 3.7. Horizontal electric field at (r_o, z_o) computed by means of the routine developed for the FDTD code against field from [50] for $z_o = 6$ m, $r_o = 500$ m, and soil with $\epsilon_{rg} = 10$ and $\sigma_g = 0.01$ S/m.

3.4.2 Induced voltages

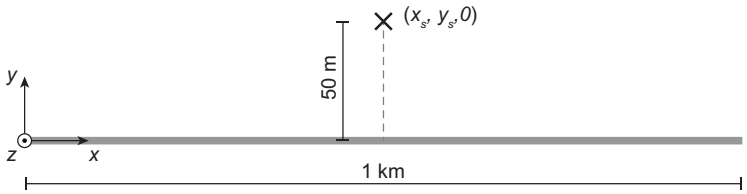

Figure 3.8. Reference single-conductor lossless TL used for simulations, and relative position of the lightning channel base at $(x_s, y_s, 0)$.

Results computed by means of the developed code have been validated by comparison with results obtained in EMTP-RV by means of the LIOV code [53] for a reference case, illustrated below.

The simulated configuration consists in a single-conductor lossless TL located at height $h = 10.2$ m above a PEC plane. The line is 1 km long and closed at both terminations on its resistive characteristic impedance $Z_c = 498.8\ \Omega$.

The adopted return stroke current is expressed by the sum of two Heidler's functions (in Sec. 3.3.5) with parameters in Table 3.3. The TL model in Sec. 3.2 was adopted, with $\nu_0 = 1.5 \cdot 10^8$ m/s and $P(z) = 1$.

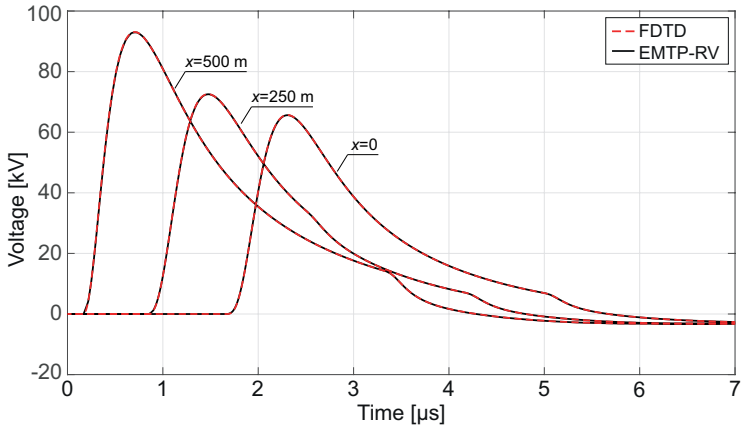

Figure 3.9. Conductor-to-ground voltages computed by means of the implicit FDTD code and by the LIOV code for the configuration in Fig. 3.8 (line over a PEC plane).

The configuration under analysis, and the adopted coordinate system are depicted in Fig. 3.8, with the lightning current striking the PEC plane at $x_s = 500$ m and $y_s = 50$ m; voltages are displayed in Fig. 3.9 for three observation points located at $x = 0$, $x = 250$ m, and $x = 500$ m. The chosen discretization steps are $\Delta x = 1$ m and $\Delta t = 3.3$ ns, resulting in $f_c = 1$. Voltages computed by means of the implicit FDTD code and the LIOV code are practically superimposed.

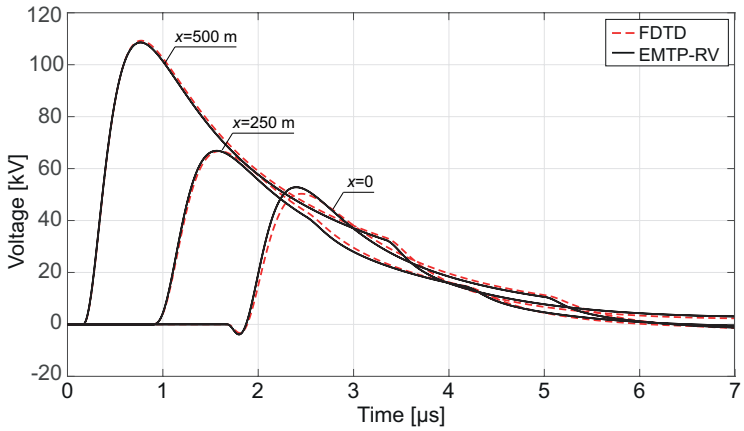

Figure 3.10. Conductor-to-ground voltages computed by means of the implicit FDTD code and by the LIOV code for the configuration in Fig. 3.8 with $\epsilon_{rg} = 10$, $\sigma_g = 0.01$ S/m. Propagation along the line does not account for the internal and ground transient impedances.

The LIOV module, here used to assess the reliability of the developed code, allows to account for the influence of the electrical properties of the soil on the propagation of the incident field. However, it neglects p.u.l. transient impedances along the MTL (i.e., it does not account for the internal and

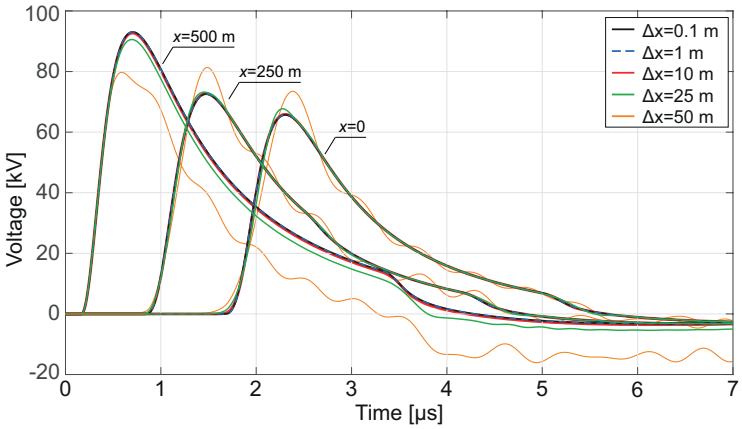

Figure 3.11. Voltages computed for the lossless TL in Fig. 3.8, with $\Delta t = 3.33$ ns and different values of the discretization step $0.1\,\text{m} \leq \Delta x \leq 50\,\text{m}$.

ground transient impedances in Sec. 1.2.2) [54]. Excluding the contributions of these impedances in the implicit FDTD code, results computed for the configuration in Fig. 3.8, accounting for $\sigma_g = 0.01$ S/m and $\epsilon_{rg} = 10$ in the computation of the correction term for the horizontal electric field, are compared to conductor-to-ground voltages by the LIOV code in Fig. 3.10. Good agreement is obtained; any difference observable at points located farther from the lightning channel or at the voltage tails should be probably ascribed to the different implementation of the Cooray-Rubinstein formula in the TD and/or to numerical dispersion.

Remarks

The risers terms at the line terminations and the contributions of the incident voltage at the observation points, involving the line integral of E_z^i in the z direction, have been approximated by the following expression (according to [51]):

$$\int_0^h E_z^i\,(x,y,z',t)\,dz' \simeq E_z^i\,(x,y,0,t)\,h \simeq E_{z_0}^i\,(x,y,0,t)\,h\,. \tag{3.40}$$

The first approximation in (3.40), adopted also in the LIOV code [53], is justified by the limited variability of the vertical component of the incident electric field with the height [51]; the second approximation is due to the minor impact of the ground finite conductivity on the constructive superposition of the fields produced by the lightning current and its image [24].

As to the contribution of the horizontal component of the incident electric field E_x^i in the direction of the line under study, the corresponding voltage source has been computed by evaluating $E_x^i\,(\hat{x},0,h)$, with $\hat{x} = (k+1/2)\,\Delta x$, i.e., at the midpoint of each discretization segment. However, such an assumption is equivalent to neglecting any variation of the electric field in $k\Delta x < x <$

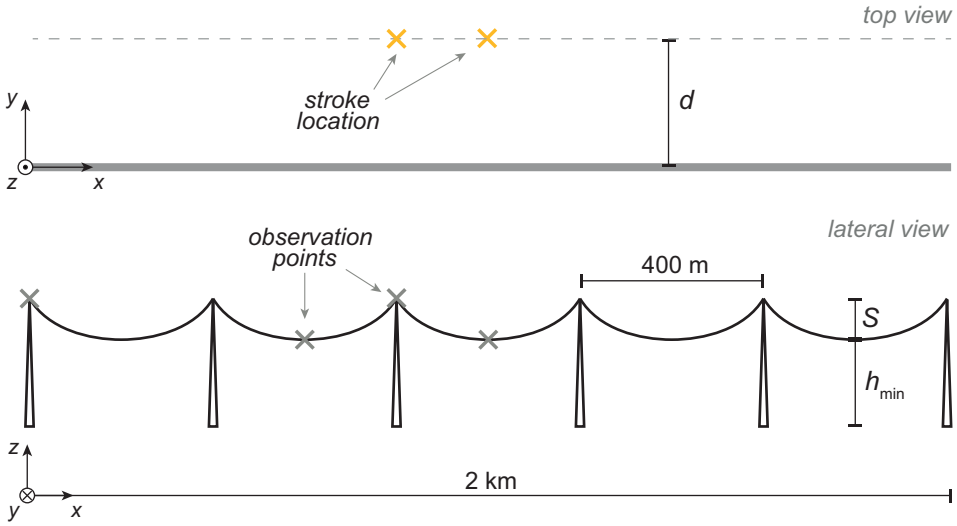

Figure 3.12. Sketch of the single-conductor TL under study. Yellow crosses represent the assumed positions of the lightning channel base; grey crosses represent the observation points along the line.

$(k+1)\,\Delta x$; this may result in an inaccurate approximation of the value of the series voltage sources for large Δx. To address this point, additional simulations have been performed for the same (lossless) configuration and return stroke current, with $\Delta x = 0.1$ m, $\Delta x = 1$ m, $\Delta x = 10$ m, $\Delta x = 25$ m, and $\Delta x = 50$ m, corresponding to $f_c = 10$, $f_c = 1$, $f_c = 0.1$, $f_c = 0.04$, and $f_c = 0.02$, respectively. The former case allows to investigate on the possible effect due to a finer discretization of the line, while keeping the same Δt; the remaining simulations with $\Delta x > 1$ m investigate on the influence of a coarser space mesh, while keeping the same time step $\Delta t = 3.3$ ns. Results, displayed in Fig. 3.11, show that a discretization up to $\Delta x = 10$ m still provides satisfactory results; if a deviation below the 4% is accepted in the peak value of the computed induced overvoltages, the coarser discretization $\Delta x = 25$ m may be adopted as well. On the contrary, choosing $\Delta x = 50$ m not only results in minor accuracy of the predicted peak values, but also in the unreliability of the obtained voltage waveform.

3.4.3 Catenary effect

The current given by the superposition of the two Heidler's functions with parameters in Table 3.3 has been employed to study the propagation of induced overvoltages on a 2 km lossless TL[8]. Simulation results refer to a single conductor with diameter $d_0 = 2r_0 = 31.5$ mm, maximum height at the poles $h_{\max} = 27$ m, and sag $S = 10$ m. The configuration is depicted in Fig. 3.12.

[8]The assumption of non-branched vertical lightning channel, as from the MTLL, is expected to be more suitable to represent subsequent stroke currents [29].

The staircase approximation of the conductor height above the ground, introduced in Chapter 2, has been adopted. The line is divided into 5 spans, each of length equal to $\ell = 400$ m. The catenary profile of the conductor within a span is symmetric with respect to its midpoint.

Observation points are at the line left termination, and at $x = 600$ m, $x = 800$ m and $x = 1000$ m. Two different positions are considered for the channel base location: $x_s = 800$ m–$y_s = 50$ m (opposite to one of the points of maximum height of the conductor), and $x_s = 1000$ m–$y_s = 50$ m (opposite to one of the points where the conductor displays the minimum height $h_{\min} = h_{\max} - S = 17$ m). The line is closed at both terminations on its resistive characteristic impedance computed for the corresponding lossless case. In particular, the value $Z_C = 488\ \Omega$ is adopted for simulations accounting for the effect of the sag[9], while the value $Z_C = 471\ \Omega$ is adopted for simulations in which the line is modelled with a constant height $h_{\text{ave}} = 20.3$ m, computed according to (2.6).

The MTLL with $H = 7.5$ km and $\nu_0 = 1.5 \cdot 10^8$ m/s is used to model the propagation of the subsequent stroke current along the lightning channel.

Following the considerations made in the previous section about Fig. 3.11, the space discretization $\Delta x = 10$ m was adopted for the simulations. Furthermore, in order to focus on the influence of the catenary, results will be presented for a single-conductor, in the case of lossless line and propagation of the electromagnetic field produced by the lightning current over a PEC plane.

Starting from the first location of the channel base at $x_s = 800$ m–$y_s = 50$ m, overvoltages at the observation points are displayed in Fig. 3.13. The different curves refer to simulations accounting for the sag, for a constant height $h = h_{\text{ave}}$ or for $h_{\max} = 27$ m (i.e., overestimating the conductor height for the whole TL length). Since observation points at $x = 600$ m and $x = 1000$ m are located symmetrically with respect to the lightning channel, the corresponding voltages are superimposed until the wave reflected by the left termination first shows at $x = 600$ m, at $\simeq 4.7\ \mu$s. The time of arrival of the reflected wave is computed as the sum of the time necessary for the electromagnetic field produced by the lightning current to propagate up to $x = 0$–$y = 0$, and the time required for the reflected wave to travel a distance of 600 m.

It can be observed that at the point opposite to the lightning channel, the computed overvoltage not only exceeds by the $\simeq 47\%$ the peak value of the voltage computed accounting for h_{ave}, but also the one computed with $h_{\max}$ by the $\simeq 5\%$[10]. In Fig. 3.13, a low frequency oscillation may be noted in the voltage tail obtained with $h = h(x)$ at $x = 800$ m; its period, approximately

[9]The value of Z_C is computed recalling that $h = h_{\max}$ at the line terminations in the proposed configuration. Hence, a slight mismatch exists between the computed Z_C and the characteristic impedance of the very first and last line sections, which depends on the average height of the conductor within the discretization cell Δx, as from the staircase model.

[10]Percentages are computed with respect to the peak values obtained by the corresponding simulations with constant height above the ground.

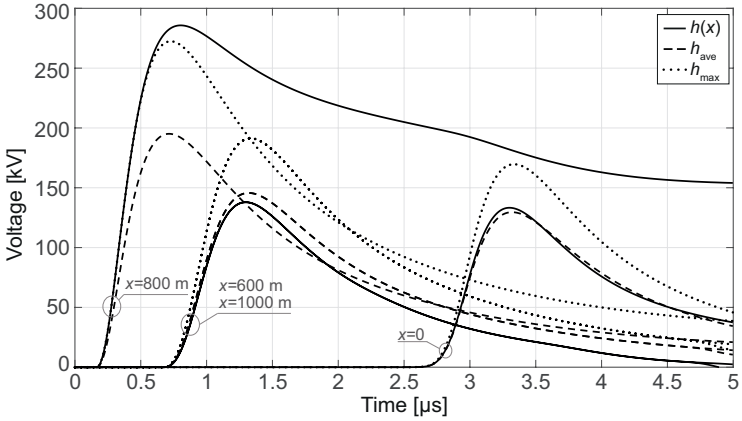

(a)

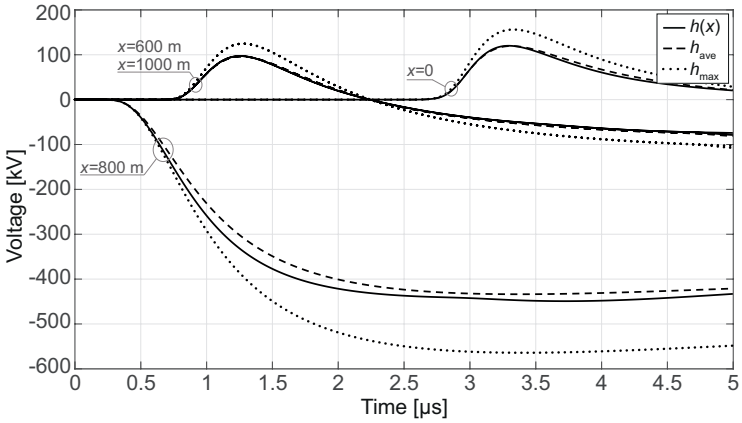

(b)

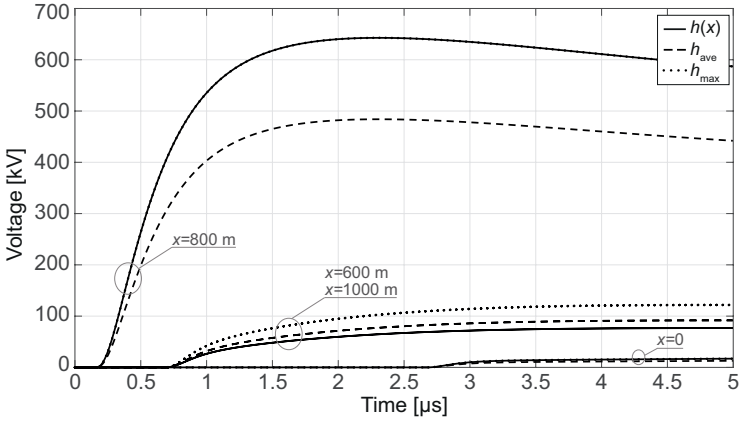

(c)

Figure 3.13. Results computed for the first lightning location at $x_s = 800$ m–$y_s = 50$ m accounting for the catenary profile, or for a constant height of the lossless TL above the PEC plane. (a) Induced voltages; (b) scattered voltages; (c) incident voltages.

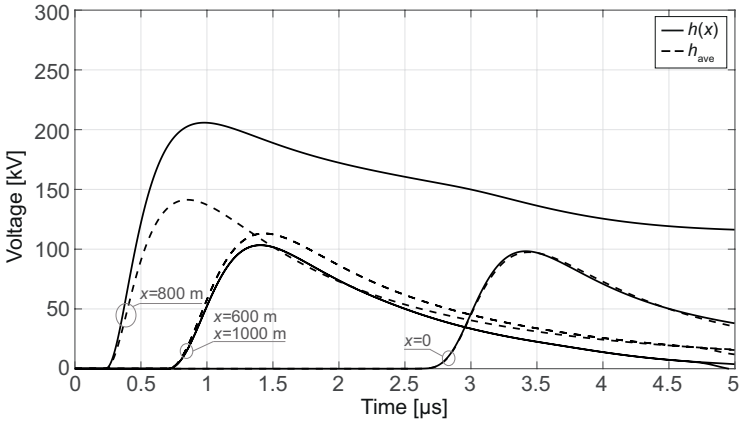

Figure 3.14. Induced voltages computed for the first lightning location at $x_s = 800$ m–$y_s = 70$ m, accounting for the catenary profile, or for a constant height of the lossless TL above the PEC plane.

equal to 2.7 μs, reveals that this is an effect related to the periodicity of the catenary profile, i.e., to the time employed by travelling waves to travel back and forth the distance of a span.

An interesting characteristic is the lower time constant governing the decay of the overvoltage, compared to the one associated with simulations with $h_{\max}$; since at $x = 800$ m the vertical component of the incident electric field contributes equally to the total voltages in the two cases (the corresponding curves are superimposed in Fig. 3.13c, being $h\,(800\,\mathrm{m}) = h_{\max}$), the discrepancy at the tail rises because of the different contribution of the scattered voltages (related to the distributed voltage generators and to the risers at the line terminations). In fact, the absolute value of the scattered voltage computed with $h_{\max}$ at $x = 800$ m presents a higher rate of increase compared to the one with $h\,(x)$, determining the faster decay of the voltage tail. The polarity of the scattered voltages in Fig. 3.13b is coherent with the ones found in the literature for similar configurations [51]. Analogous observations may be made as to results in Fig. 3.14, for the lightning channel base at $y_s = 70$ m; evidently, the amplitude of the induced overvoltages is sensibly reduced.

The amplitude of the induced overvoltages in Fig. 3.15 associated with the second lightning location, i.e., $x_s = 1000$ m–$y_s = 50$ m, is reduced compared to the previous case. In this configuration, the lightning channel is opposite to line midpoint, which also displays the minimum height $h_{\min}$ above the PEC plane. Voltages computed with a constant height $h = h_{\min}$ are presented for reference too. Modelling the conductor as an equivalent uniform TL with $h = h_{\mathrm{ave}}$ leads to an overestimation of the overvoltage at the point of the TL closest to the lightning channel (approximately equal to the 24% of the actual peak voltage computed with $h\,(x)$). When the line is modelled as a uniform TL at $h_{\min}$, the peak value of the induced voltages at $x = 1000$ m is close to the one computed accounting for $h\,(x)$; nevertheless, as expected, this assumption leads to an

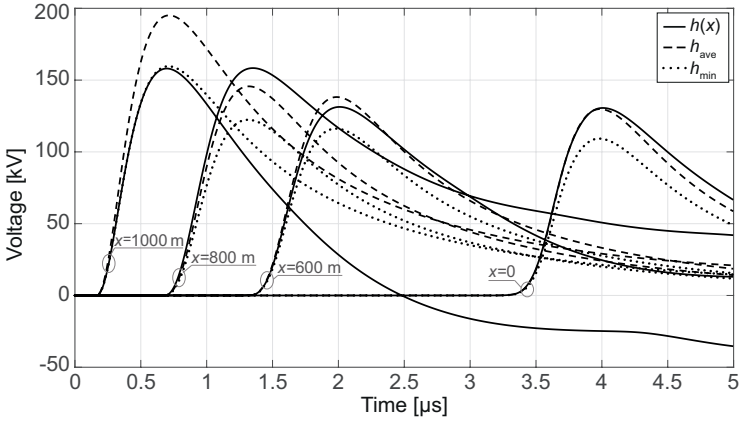

(a)

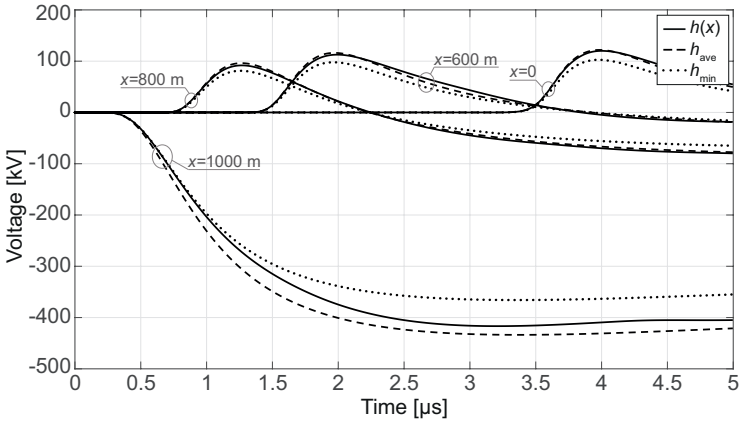

(b)

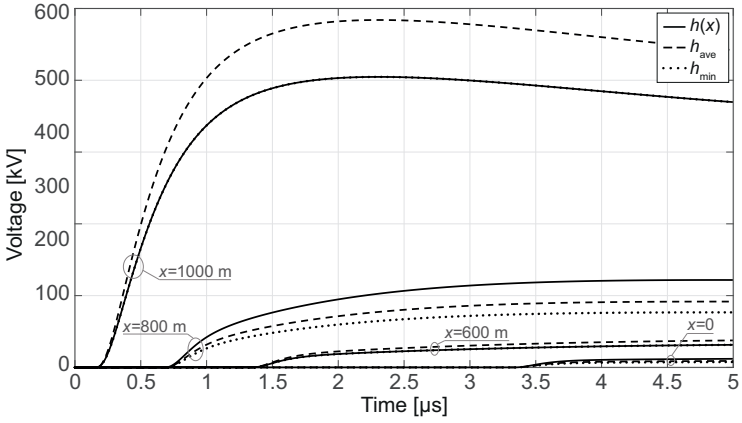

(c)

Figure 3.15. Results computed for the second lightning location at $x_s = 1000$ m–$y_s = 50$ m, accounting for the catenary profile, or for a constant height of the lossless TL above the PEC plane. (a) Induced voltages; (b) scattered voltages; (c) incident voltages.

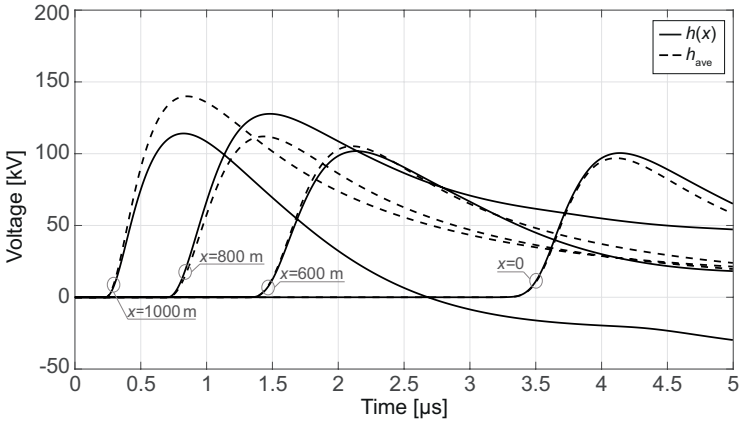

Figure 3.16. Induced voltages computed for the second lightning location at $x_s = 1000$ m–$y_s = 70$ m, accounting for the catenary profile, or for a constant height of the lossless TL above the PEC plane.

unsatisfactory assessment of the voltages at larger distances, sensibly underestimating their amplitude.

At $x = 1000$ m, the different behaviour found at the tail of the induced voltage when the catenary profile is simulated, along with the polarity reversal in Fig. 3.15a are to be mainly attributed the contribution of E_z^i in Fig. 3.15c. In fact, while the scattered voltage in Fig. 3.15b is of the same order of magnitude as the one for $h = h_{\text{ave}}$, the incident voltage at $h\,(1000\,\text{m}) = h_{\min}$ is much lower than the corresponding one at the average height $h_{\text{ave}} = 20.33$ m, the reduction factor being related to the ratio $h_{\min}/h_{\text{ave}}$.

Analogously to the previous configuration, a low frequency oscillation is superimposed to the main waveform, due to the periodicity of the catenary profile; the period is to be established with more difficulty, being the observation point located at midspan.

In Fig. 3.15a it can be observed that voltages induced at $x = 1000$ m and $x = 800$ m are of the same order of magnitude for simulations including the effect of $h\,(x)$. This is partially justified by the larger conductor height at 800 m, which results in an enhanced contribution of the incident voltage (in Fig. 3.15c); in fact, it is evident that the cumulative effect of the distributed voltage generators and of the risers leads to similar scattered voltages for the cases $h = h\,(x)$ and $h = h_{\text{ave}}$ (in Fig. 3.15b). As the lightning channel location is moved farther to $y_s = 70$ m (Fig. 3.16), this aspect is more evident. In fact, the scattered voltages tend to converge for the two cases, while E_z^i is less sensitive to the different distances of the lightning channel from observation points at $x = 800$ m and $x = 1000$ m; hence, when computing the locally incident voltage as the product $E_z^i\,(x, 0, 0, t)\,h\,(x)$, the value of $h\,(x)$ may contribute significantly to differentiating the final voltages at the two observation points.

A common feature of the overvoltages consists in the more pronounced difference in the results to be at the observation points closer to the stroke

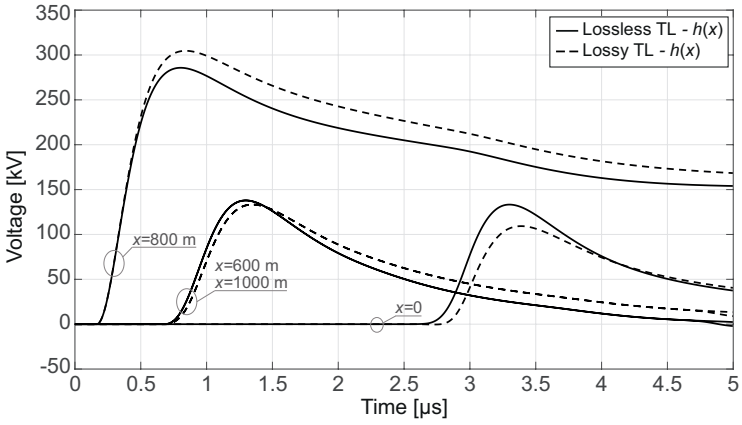

Figure 3.17. Induced voltages computed for the first lightning location at $x_s = 800$ m–$y_s = 50$ m, accounting for the catenary profile. Results for the case of lossless and lossy TL are compared.

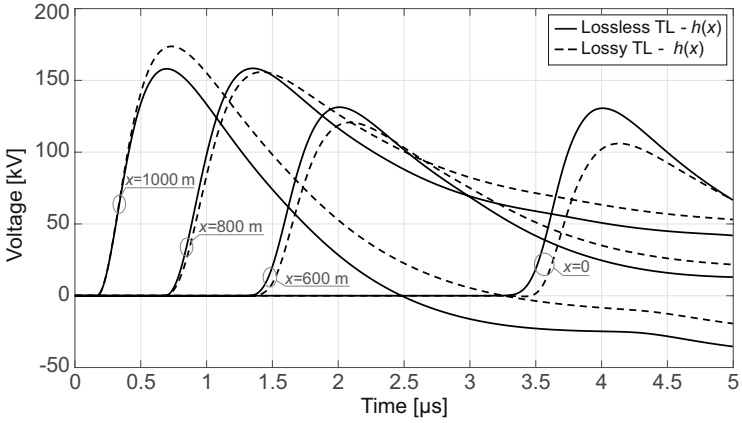

Figure 3.18. Induced voltages computed for the second lightning location at $x_s = 1000$ m–$y_s = 50$ m, accounting for the catenary profile. Results for the case of lossless and lossy TL are compared.

location, whether accounting for the variable height $h(x)$ or not. Indeed, the discrepancy decreases at observation points located at larger distance from the lightning channel. This is reasonably due to the fact that, at larger distances the contribution of the scattered field is predominant with respect to the one of the incident field (as it can be deduced by comparing Fig. 3.13b with Fig. 3.13c, and Fig. 3.15b with Fig. 3.15c); reaching the farthest observation points, the scattered voltage accounts for the average effect of the propagation along successive spans.

As to the discussed configuration, the influence of the incident voltage can be observed at larger distances in the fact that at positions along the line where $h(x) > h_{\text{ave}}$ ($h(x) < h_{\text{ave}}$) the voltage peak obtained when accounting for the sag effect is slightly larger (smaller) than that relative to simulations

with h_{ave} (Figs. 3.13a–3.15a).

For the sake of completeness, Figs. 3.17 and 3.18 display induced overvoltages for the two lightning locations $x_s = 800$ m–$y_s = 50$ m and $x_s = 1000$ m–$y_s = 50$ m, respectively, when the propagation of the lightning current electromagnetic field over a lossy soil ($\epsilon_{rg} = 10$ and $\sigma_{\text{g}} = 0.01$ S/m), the transient impedance of the ground, and the conductor transient internal impedance are included in simulations. The resulting voltages show larger amplitudes at observation points closer to the lightning channel (as in [55]), being attenuated as the voltage waves propagate along the TL, due to the contributions of the transient impedances offered by the conductor and by the ground return path.

The influence of the sag in the determination of the lightning induced overvoltages seems worthy of further investigation, since modelling the TL by means of an average constant height above the ground does not always guarantee precautionary results, depending on the relative position of the lightning channel with respect to the line conductors, the current characteristics, the adopted return stroke model, etc.

3.5 Remarks on the adopted approximations

The following hypothesis and observations should be recalled when implementing equations (3.20) and (3.21) in the implicit FDTD code to assess MTLs coupling with incident transient electromagnetic fields produced by an external source:

Lightning modelling

- The return stroke lightning current is supposed to flow along a vertical channel above the ground plane, neglecting the effects related to the actual channel tortuosity.
- A simplified engineering model (Modified Transmission Line model) is adopted to describe the return stroke current propagation along the lightning channel, with a constant velocity $\nu_f = \nu_0$, neglecting possible localised inception of corona discharges along the channel [30].

Field computation

- The electromagnetic fields produced by the return stroke current are derived by the application of the theory of perfect images, hence, considering a PEC half-plane.
- The effect of the propagation above a soil with finite conductivity is neglected in the computation of the magnetic field used in the horizontal electric field correction term (3.13), according to Cooray-Rubinstein formula.

- The incident electric field above the lossy soil in the z direction E_z^i is approximated with the vertical electric field E_{z0}^i above a PEC plane (i.e., $E_z \simeq E_{z0}$).
- The soil is a good conductor ($\sigma_g > 1$ mS/m in [24]).
- The variation of the incident electric field in the vertical direction E_z^i is assumed to be negligible in the range $0 < z < h$. Hence, the integral terms in (3.5), expressing the risers contributions to the propagation of the scattered voltage waves, are approximated by the product of E_z^i at ground level and h, i.e., the conductor's height above ground.
- The contribution of the horizontal electric field in the x direction in (3.4a), is approximated by the product $E_x^i \cdot \Delta x$ (E_x^i being computed at the cells' midpoint and at $z = h$).

FDTD implementation

- The line is assumed to be electrically short in the transversal plane, i.e., the conductors' radii and heights are assumed to be much shorter than the minimum wavelength associated with the highest frequency excited by the studied phenomenon.
- The line supports TEM or quasi-TEM propagation, with the electric and magnetic fields confined in the plane orthogonal to the direction of propagation.
- Only the TL mode is considered to propagate along the line, the ground half-plane representing the return path for the currents flowing along the conductors in the x direction.
- The computation of the field-to-line coupling sources is accelerated by computing fields at the average conductors position $y = (y_1 + \ldots + y_{N_c})/N_c$ (allowing to compute a single integral for the Cooray-Rubinstein correction term, and one for the contribution of E_z^i at each observation point).

Some of the aforementioned assumptions impair the accuracy of the Cooray-Rubinstein correction term at short distances from the lightning channel (e.g., for $r < 50$ m with $\sigma_g = 0.01$ S/m). Nevertheless, the error introduced in the computation of the total horizontal electric field is partially compensated, since the term E_{r_0} is predominant in (3.9) when r is small [28]. For large r (depending on the considered value of σ_g), satisfactory accuracy might be obtained if propagation effects are accounted for in the computation of the azimuthal magnetic induction.

The observations above are of primary importance to frame the limits of validity of the computed results, as well as to devise further developments and improvements to achieve better accuracy.

References

[1] *CIGRE Technical Brochure 600: Protection of High Voltage Power Network Control Electronics Against Intentional Electromagnetic Interference (IEMI)*, CIGRE Std., 2014.

[2] A. Borghetti and C. A. Nucci, "Integration of distributed energy resources in distribution power systems," in *Integration of Distributed Energy Resources in Power Systems*. Elsevier, 2016, pp. 15–50.

[3] T. A. Papadopoulos, C. G. Kaloudas, A. I. Chrysochos, and G. K. Papagiannis, "Application of narrowband power-line communication in medium-voltage smart distribution grids," *IEEE Trans. Power Del.*, vol. 28, no. 2, pp. 981–988, 2013.

[4] M. Paolone, F. Rachidi-Haeri, and C. A. Nucci, "IEEE guide for improving the lightning performance of electric power overhead distribution lines," IEEE, Tech. Rep., 2010.

[5] C. A. Nucci and F. Rachidi, "Interaction of electromagnetic fields generated by lightning with overhead electrical networks," in *The lightning flash*, V. Cooray, Ed. IET, 2003, ch. 12.

[6] C. D. Taylor, R. Satterwhite, and C. W. Harrison, "The response of a terminated two-wire transmission line excited by a nonuniform electromagnetic field," vol. AP-12, pp. 987–989, 1965.

[7] A. K. Agrawal, H. J. Price, and S. H. Gurbaxani, "Transient response of multiconductor transmission lines excited by a nonuniform electromagnetic field," *IEEE Trans. Electromagn. Compat.*, no. 2, pp. 119–129, 1980.

[8] F. Rachidi, "Formulation of the field-to-transmission line coupling equations in terms of magnetic excitation field," *IEEE Trans. Electromagn. Compat.*, vol. 35, no. 3, pp. 404–407, 1993.

[9] ——, "A review of field-to-transmission line coupling models with special emphasis to lightning-induced voltages on overhead lines," *IEEE Trans. Electromagn. Compat.*, vol. 54, no. 4, pp. 898–911, 2012.

[10] C. A. Nucci, F. Rachidi, and M. Rubinstein, "Derivation of telegrapher's equations and field-to-transmission line interaction," *Electromagnetic Field Interaction with Transmission Lines: From Classical Theory to HF Radiation Effects*, vol. 5, p. 3, 2008.

[11] V. Cooray, M. Rubinstein, and F. Rachidi, "Field-to-transmission line coupling models with special attention to the Cooray–Rubinstein approximation," *IEEE Trans. Electromagn. Compat.*, vol. 63, no. 2, pp. 484–493, 2020.

[12] V. Cooray, C. A. Nucci, A. Piantini, F. Rachidi, and M. Rubinstein, "Field-to-transmission line coupling models," in *Lightning Interaction with Power Systems – Volume 1: Fundamentals and modelling*, A. Piantini, Ed. IET, 2020, ch. 6.

[13] P. Chowdhuri and E. T. Gross, "Voltage surges induced on overhead lines by lightning strokes," in *Proceedings of the Institution of Electrical Engineers*, vol. 114, no. 12. IET, 1967, pp. 1899–1907.

[14] P. Chowdhuri, "Analysis of lightning-induced voltages on overhead lines," *IEEE Trans. Power Del.*, vol. 4, no. 1, pp. 479–492, 1989.

[15] V. Cooray, "Calculating lightning-induced overvoltages in power lines. A comparison of two coupling models," *IEEE Trans. Electromagn. Compat.*, vol. 36, no. 3, pp. 179–182, 1994.

[16] C. Nucci, F. Rachidi, M. Ianoz, and C. Mazzetti, "Comparison of two coupling models for lightning-induced overvoltage calculations," *IEEE Trans. Power Del.*, vol. 10, no. 1, pp. 330–339, 1995.

[17] V. Cooray, F. Rachidi, and M. Rubinstein, "Formulation of the field-to-transmission line coupling equations in terms of scalar and vector potentials," *IEEE Trans. Electromagn. Compat.*, vol. 59, no. 5, pp. 1586–1591, 2017.

[18] M. Brignone, R. Procopio, D. Mestriner, M. Rossi, F. Delfino, F. Rachidi, and M. Rubinstein, "Analytical expressions for lightning electromagnetic fields with arbitrary channel-base current — Part I: Theory," *IEEE Trans. Electromagn. Compat.*, vol. 63, no. 2, pp. 525–533, 2020.

[19] D. Mestriner, M. Brignone, R. Procopio, M. Rossi, F. Delfino, F. Rachidi, and M. Rubinstein, "Analytical expressions for lightning electromagnetic fields with arbitrary channel-base current. part II: Validation and computational performance," *IEEE Trans. Electromagn. Compat.*, vol. 63, no. 2, pp. 534–541, 2020.

[20] M. Brignone, R. Procopio, M. Nicora, D. Mestriner, F. Rachidi, and M. Rubinstein, "A Prony-based approach for accelerating the lightning electromagnetic fields computation above a perfectly conducting ground," *Electric Power Systems Research*, vol. 210, p. 108125, 2022.

[21] F. Rachidi, C. A. Nucci, M. Ianoz, and C. Mazzetti, "Influence of a lossy ground on lightning-induced voltages on overhead lines," *IEEE Trans. Electromagn. Compat.*, vol. 38, no. 3, pp. 250–264, Aug. 1996.

[22] ——, "Corrections to "Influence of a lossy ground on lightning-induced voltages on overhead lines"," *IEEE Trans. Electromagn. Compat.*, vol. 39, no. 2, pp. 187–187, 1997.

[23] V. Cooray, "Horizontal fields generated by return strokes," *Radio science*, vol. 27, no. 04, pp. 529–537, 1992.

[24] M. Rubinstein, "An approximate formula for the calculation of the horizontal electric field from lightning at close, intermediate, and long range," *IEEE Trans. Electromagn. Compat.*, vol. 38, no. 3, pp. 531–535, 1996.

[25] A. Andreotti, F. Rachidi, and L. Verolino, "A new formulation of the Cooray–Rubinstein expression in time domain," *IEEE Trans. Electromagn. Compat.*, vol. 57, no. 3, pp. 391–396, 2015.

[26] R. Hill, "Analysis of irregular paths of lightning channels," *Journal of Geophysical Research*, vol. 73, no. 6, pp. 1897–1906, 1968.

[27] ——, "Tortuosity of lightning," *Atmospheric research*, vol. 22, no. 3, pp. 217–233, 1988.

[28] V. Cooray, "Horizontal electric field above-and underground produced by lightning flashes," *IEEE Trans. Electromagn. Compat.*, vol. 52, no. 4, pp. 936–943, 2010.

[29] V. A. Rakov and M. A. Uman, "Review and evaluation of lightning return stroke models including some aspects of their application," *IEEE Trans. Electromagn. Compat.*, vol. 40, no. 4, pp. 403–426, 1998.

[30] V. Cooray, *The lightning flash*. IET, 2003.

[31] C. Gomes and V. Cooray, "Concepts of lightning return stroke models," *IEEE Trans. Electromagn. Compat.*, vol. 42, no. 1, pp. 82–96, 2000.

[32] M. A. Uman and D. K. McLain, "Magnetic field of lightning return stroke," *Journal of Geophysical Research*, vol. 74, no. 28, pp. 6899–6910, 1969.

[33] A. Dennis and E. Pierce, "The return stroke of the lightning flash to earth as a source of VLF atmospherics," *Radio Sci. D*, vol. 68, pp. 777–794, 1964.

[34] V. Rakov and A. Dulzon, "A modified transmission line model for lightning return stroke field calculations," in *Proc. 9th Int. Symp. Electromagn. Compat*, 1991, pp. 229–235.

[35] C. A. Nucci, G. Diendorfer, M. A. Uman, F. Rachidi, M. Ianoz, and C. Mazzetti, "Lightning return stroke current models with specified channel-base current: A review and comparison," *Journal of Geophysical Research: Atmospheres*, vol. 95, no. D12, pp. 20 395–20 408, 1990.

[36] V. Cooray, M. Rubinstein, and F. Rachidi, "Modified transmission line model with a current attenuation function derived from the lightning radiation field—-MTLD model," *Atmosphere*, vol. 12, no. 2, p. 249, 2021.

[37] *CIGRE Technical Brochure 63: Guide to procedures for estimating the lightning performance of trasmission lines*, CIGRE Std., 1991.

[38] L. Bewley, "Traveling waves due to lightning," *Transactions of the American Institute of Electrical Engineers*, vol. 48, no. 3, pp. 1050–1064, 1929.

[39] V. Javor, "New functions for representing IEC 62305 standard and other typical lightning stroke currents," *Journal of lightning research*, vol. 4, no. 1, 2012.

[40] S. Campione and L. K. Warne, "Double exponential approximation and inverse double exponential fit for Bell Labs and International-Military Standard EMP waveforms." Sandia National Lab.(SNL-NM), Albuquerque, NM (United States), Tech. Rep., 2020.

[41] A. Andreotti and L. Verolino, "A new channel-base current function for lightning studies," *IEEE Trans. Electromagn. Compat.*, vol. 57, no. 6, pp. 1539–1546, 2015.

[42] V. Javor and P. D. Rancic, "A channel-base current function for lightning return-stroke modeling," *IEEE Trans. Electromagn. Compat.*, vol. 53, no. 1, pp. 245–249, 2010.

[43] F. Heidler and J. Cvetić, "A class of analytical functions to study the lightning effects associated with the current front," *European Transactions on Electrical Power*, vol. 12, no. 2, pp. 141–150, 2007.

[44] F. Heidler, J. M. Cvetic, and B. V. Stanic, "Calculation of lightning current parameters," *IEEE Trans. Power Del.*, vol. 14, no. 3, pp. 399–404, Apr. 1999.

[45] "IEC 62305-1: Protection against lightning, Part 1: General principles," 2010.

[46] W. R. Gamerota, J. O. Elismé, M. A. Uman, and V. A. Rakov, "Current waveforms for lightning simulation," *IEEE Trans. Electromagn. Compat.*, vol. 54, no. 4, pp. 880–888, Aug. 2012.

[47] A. D. Conti and S. Visacro, "Analytical representation of single- and double-peaked lightning current waveforms," *IEEE Trans. Electromagn. Compat.*, vol. 49, no. 2, pp. 448–451, 2007.

[48] Working Group C4.407 (Rakov, V. A. and Borghetti, A. and Bouqeugneau, C. and Chisholm, W. A. and Cummins, K. and Diendorfer, G. and Heidler, F. and Hussein, A. M. and Ishii, M. and Nucci, C. A. and Piantini, A. and Pinto, O. and Qie, X. and Rachidi, F. and Saba, M. and Shindo, T. and Schulz, W. and Thottappillil, R. and Visacro, S. and Zischank, W), "Lightning parameters for engineering applications," *Brochure*, vol. 549, 2013.

[49] A. Andreotti, S. Falco, and L. Verolino, "Some integrals involving Heidler's lightning return stroke current expression," *Electrical Engineering*, vol. 87, no. 3, pp. 121–128, Apr. 2005.

[50] C. Caligaris, F. Delfino, and R. Procopio, "Cooray–Rubinstein formula for the evaluation of lightning radial electric fields: Derivation and implementation in the time domain," *IEEE Trans. Electromagn. Compat.*, vol. 50, no. 1, pp. 194–197, 2008.

[51] C. A. Nucci, F. Rachidi, M. V. Ianoz, and C. Mazzetti, "Lightning-induced voltages on overhead lines," *IEEE Trans. Electromagn. Compat.*, vol. 35, no. 1, pp. 75–85, Feb. 1993.

[52] F. H. Silveira, A. De Conti, and S. Visacro, "Lightning overvoltage due to first strokes considering a realistic current representation," *IEEE Trans. Electromagn. Compat.*, vol. 52, no. 4, pp. 929–935, Nov. 2010.

[53] EMTP, "LIOV toolbox," https://www.emtp.com/products/liov-toolbox, (accessed Oct. 2022).

[54] F. Napolitano, A. Borghetti, C. Nucci, M. Paolone, F. Rachidi, and J. Mahseredjian, "An advanced interface between the LIOV code and the EMTP-RV," in *Proc. 29th Int. Conf. Lightning Protection*, no. 6b-6, 2008.

[55] H. K. Hoidalen, "Analytical formulation of lightning-induced voltages on multiconductor overhead lines above lossy ground," *IEEE Trans. Electromagn. Compat.*, vol. 45, no. 1, pp. 92–100, 2003.

Chapter 4

Distributed nonlinearities

Studies in the FD on the propagation of voltage and current waves along overhead MTLs may be carried out rigorously as long as the involved phenomena are of the linear type. When nonlinearities are to be accounted for, propagation studies in the TD are adequate for the purpose.

This chapter is focused on the implementation and the analysis of the corona phenomenon, as a distributed nonlinearity occurring along overhead transmission lines whenever the electric field in the proximity of the conductors overcomes locally the insulation strength of the surrounding insulating medium (air). Indeed, overvoltages with sufficiently large amplitude, travelling with a propagation velocity within the order of magnitude of the speed of light, may cause the inception of discharges along wide sections of the line; the time development of these discharge processes, primarily depending on the local instantaneous value of the voltage, requires time domain analysis and a distributed parameters approach for accurate modelling.

Similarly, circuits with distributed parameters are referred briefly in section 4.4 to model extended grounding systems, installed in low-conductivities soils for the grounding of HV transmission line towers; studies in the TD are employed to assess the impact of soil ionization on current dispersion, and on the grounding impedance offered by extended grounding systems. Further reference to soil ionization is made in Chapter 5. Indeed, soil ionization occurring in the proximity of buried electrodes may be simulated as a lumped nonlinearity too, depending on the leading dimension of the grounding system under analysis.

4.1 Corona discharge in power lines

Assessment of overvoltages in HV overhead power lines is essential for both sizing of components and insulation coordination [1]. Corona effect is a physical phenomenon consisting in a nonlinear discharge mechanism, which occurs when the electric field intensity reaches a critical inception value.

Since the early works by Peek [2] and the experimental investigations by Wagner [3], HV engineering is still focusing on the contribution of corona discharge to propagation, and on its implementation for TD simulation of power lines. Indeed, corona discharge is responsible for additional attenuation and distortion of traveling surges and for power losses.

Since the phenomenon is nonlinear and characterized by a hysteretic q-v loop, a dynamic, nonlinear and time-varying capacitance is generally introduced to replace the standard geometric capacitance associated with the TL under study. However, the implementation of a routine for the inclusion of the corona phenomenon in any commercial or customized tool relies on the choice of the particular model used to reproduce the complexity of the phenomenon.

This section also questions the general applicability of the traditional dynamic capacitance approach (considering both theoretical and numerical aspects), proposing a stable solution, yet numerically friendly, for the inclusion of this strongly nonlinear phenomenon in FDTD codes. Hence, distributed voltage-controlled current generators are proposed to account for corona, and are implemented in the implicit CN time-stepping scheme. This scheme may ease several sources of numerical instabilities characterizing the explicit schemes, especially when dealing with nonlinear phenomena.

Appendix A is devoted to inception, development and secondary effects (luminosity, noise, interference) associated with corona discharge along TLs [4]; furthermore, the most relevant models proposed in the literature for corona simulation (at macroscopic level) are reviewed.

4.2 Implementation of corona effect for the FDTD scheme

Approaches found in the literature to account for the corona effect often involve the definition of a time-dependent p.u.l. capacitance of the cylindrical conductor; it is derived by means of a time-dependent equivalent radius of the conductor, delimiting a highly conductive area associated with the radial development of corona charges (e.g., A.4.1).

Herein, a method to integrate corona discharge models into the implicit CN updating scheme for MTLs is proposed. Voltage-controlled current sources are connected to the line nodes, simulating the current associated with the corona discharge, flowing in the transversal direction towards the ground.

Due to its unconditional stability, the implicit scheme is particularly suitable for the study of waves propagating along power lines in the presence of corona; when dealing with propagation, corona may be identified as a nonlinearity of the system, and also as an additional non-uniformity, since it may develop at different sections of the line, depending on the instantaneous value of the electric field in the proximity of the conductors surface.

The critical aspects of numerical implementation involve the initial stage of corona inception and development: indeed, the abrupt change in the capacitive behaviour of the line causes the abrupt (and local) change of the wave propagation velocity, along with transients displaying oscillatory values of the time derivatives of the conductor-to-ground voltages.

4.2.1 Dynamic capacitance approach

Different definitions of capacitance were discussed by Pearson in [5]. The time derivative of the p.u.l. charge associated with a conductor j above the ground plane, with p.u.l. capacitance $C'_j(t)$, may be expressed as follows:

$$\frac{\mathrm{d}q'_j(v(t))}{\mathrm{d}t} = C'_j(t)\frac{\mathrm{d}v(t)}{\mathrm{d}t} + \frac{\mathrm{d}C'_j(t)}{\mathrm{d}t}v(t) \ . \tag{4.1}$$

In (4.1), the p.u.l. capacitive current in the plane transversal to the direction of propagation is expressed as the sum of a static contribution (including also the effect of the configuration geometry), and a contribution accounting for the possible dynamic characteristic of the conductor capacitance with time.

In these regards, the additional damping of traveling voltage waves, along with the reduction of propagation velocity associated with corona discharge, may be taken into account through the dynamic capacitances matrix $\mathbf{C}'_{\mathrm{dyn}}$ in place of $\mathbf{C}'$. Conductors-to-ground voltages at time $(n+1)\Delta t$, computed through the solution of the linear system (1.38), are employed to assess any inception or further development of corona for each conductor of the MTL.

After the selection of a model suitable for the simulation of corona, the p.u.l. dynamic capacitance C'_{dyn_j} of conductor j at time t may be evaluated as a function of the corresponding voltage v at the specific observation point along the line; starting from the time derivative of the p.u.l. charge q'_j, expression (4.1) is alternatively written as follows:

$$\frac{\mathrm{d}q'_j(v(t))}{\mathrm{d}t} = \frac{\mathrm{d}q'_j(v)}{\mathrm{d}v}\frac{\mathrm{d}v(t)}{\mathrm{d}t} = C'_{\mathrm{dyn}_j}\frac{\mathrm{d}v(t)}{\mathrm{d}t} \ , \tag{4.2}$$

with $C'_{\mathrm{dyn}_j} = \mathrm{d}q'_j(v)/\mathrm{d}v$.

At each $k\Delta x$ and time $(n+1)\Delta t$, the matrix of p.u.l. dynamic capacitances[1] $\mathbf{C}^{n+1,k}_{\mathrm{dyn}}$ may be computed by inversion of the matrix of potential coefficients $\mathbf{P}^{n+1,k}$, whose elements are modified according to the degree of development of corona discharge for each conductor (when its voltage overcomes the corresponding value for corona inception).

In the case of a single-conductor TL, the updated $\mathbf{C}^{n+1,k}_{\mathrm{dyn}}$ may be plugged into equations (1.20), and (1.21) in the place of the geometrical capacitance

[1]The superscript identifying the capacitance as a p.u.l. quantity will be omitted to ease the notation of FDTD expressions.

for the solution of the subsequent time step, i.e., to evaluate unknown voltages and currents at time $(n+2)\,\Delta t$ starting from known values at time $(n+1)\,\Delta t$.

However, the computation of the matrix of dynamic capacitances introduces an additional computational cost due to the inversion of the modified matrix of potential coefficients, when at least one of the conductors is showing corona. Although the implementation of $\mathbf{C}_{\mathrm{dyn}}$ represents a frequently adopted approach in the literature [6] (also in indirect lightning studies [7]), it lacks generality; indeed, the capacitance, as a circuital element, should account for the instantaneous (i.e., local in time) relationship between voltage and charge, while some corona models (e.g., [8], [9]) assume the p.u.l. charge to depend not only on the instantaneous conductor-to-ground voltage, but also on the voltage past values, which influence the charge formation after a time delay τ.

Furthermore, evaluation of the charge derivative in equation (4.2) through its corresponding finite-difference form, whether it is computed by a two-points or a multiple points differentiation formula, is a difficult task to be performed with accuracy: from a practical point of view, intervals with weakly ringing, slowly varying, or constant voltage may lead to an undeterminate numerical form of the ratio $\mathrm{d}q/\mathrm{d}v$, which is not easy to treat numerically with sufficient accuracy, also due to numerical noise.

4.2.2 Voltage-controlled current generator approach

For the reasons mentioned above, an alternative and general approach has been chosen, simulating corona through a voltage-controlled current generator connected in parallel with the p.u.l. geometric capacitance of the conductors. Therefore, equations of the type (1.22b) would turn into the following:

$$-\frac{1}{2}\left(\frac{\mathbf{I}^{n+1}_{k+\frac{1}{2}}-\mathbf{I}^{n+1}_{k-\frac{1}{2}}}{\Delta x}+\frac{\mathbf{I}^{n}_{k+\frac{1}{2}}-\mathbf{I}^{n}_{k-\frac{1}{2}}}{\Delta x}\right)=\mathbf{C}'\frac{\mathbf{V}^{n+1}_{k}-\mathbf{V}^{n}_{k}}{\Delta t}+\mathbf{I}^{n,k}_{\mathrm{co}}\,, \tag{4.3}$$

where $\mathbf{I}^{n,k}_{\mathrm{co}}$ represents the vector of (p.u.l.) transversal currents drained from each conductor at node k, due to corona discharge at time $n\Delta t$, employed for the computation of the unknowns at time $(n+1)\,\Delta t$.

Limitations

Similarly to the method adopted for simulations involving MOVs in Chapter 5, a time shift exists between the time $t = n\Delta t$ at which the voltage-controlled current sources are evaluated, and the time $t = (n+1/2)\,\Delta t$ at which equation 4.3 is centered. The inaccuracy due to the resulting time shift, equal to half a time step $\Delta t/2$, holds minor impact if small time steps are adopted. This is the case for corona simulations, which require small time steps to reproduce the complex dynamic of the nonlinear phenomenon.

The present approach does not account for variations of the capacitive coupling among conductors of an MTL due to corona, which should be examined in future work; the computed capacitive coupling depends only on the geometrical arrangement of the line's conductors, which is accounted by the standard matrix of p.u.l. geometric capacitances.

4.3 Numerical results

Results are presented with reference to a 15 km long MTL. The conductors arrangement at the towers is depicted in Fig. 4.1. The phase conductors, denoted with P1, P2 and P3, terminated at the line endpoints on their characteristic impedances (computed for the corresponding lossless line), are located at heights $h_{\mathrm{P1}} = 28$ m, $h_{\mathrm{P2}} = 26$ m, and $h_{\mathrm{P3}} = 24$ m above a lossy ground with conductivity $\sigma_{\mathrm{g}} = 0.01$ S/m and electric permittivity $\epsilon_{\mathrm{g}} = 10\epsilon_0$. The SW is at height $h_{\mathrm{SW}} = 33.5$ m and is grounded at both line terminations. The radii of the aluminum phase conductors and SW are, respectively, 1.58 cm and 0.58 cm. The corona development models proposed by Malik (physics-based model), Gary, and Suliciu *et al.* (empirical models) are implemented; it is shown that different corona models may predict overvoltages with huge discrepancies, depending on the transient waveform and on the propagation distance, despite the similarity of the q-v hysteresis curves computed by the same models. Details on the implementation of these models may be found in Appendix A.

The following expression is adopted for the voltage source feeding the phase conductor P1 at the line left termination:

$$v\left(t\right) = \frac{V_0}{\eta} \frac{\left(\frac{t}{\tau_1}\right)^n}{1 + \left(\frac{t}{\tau_1}\right)^n} \exp^{-\frac{t}{\tau_2}}, \tag{4.4}$$

with

$$\eta = e^{-\frac{\tau_1}{\tau_2}\left[n\left(\frac{\tau_2}{\tau_1}\right)\right]^{\frac{1}{n}}} \tag{4.5}$$

where n is a constant, τ_1 and τ_2 are time constants affecting the rise time and the time to half-value. The cases of a fast-front and a slow-front voltage source are assessed; hence, the values of τ_1 and τ_2 are chosen according to the definition of rise time and time to half-value in [10] for lightning impulse and switching impulse voltage applications, respectively. In (4.5), η is the amplitude correction factor.

4.3.1 Fast-front voltage source

Parameters in Table 4.1, required to implement the reviewed models in Appendix A, have been chosen in order to get q-v curves with similar shape when

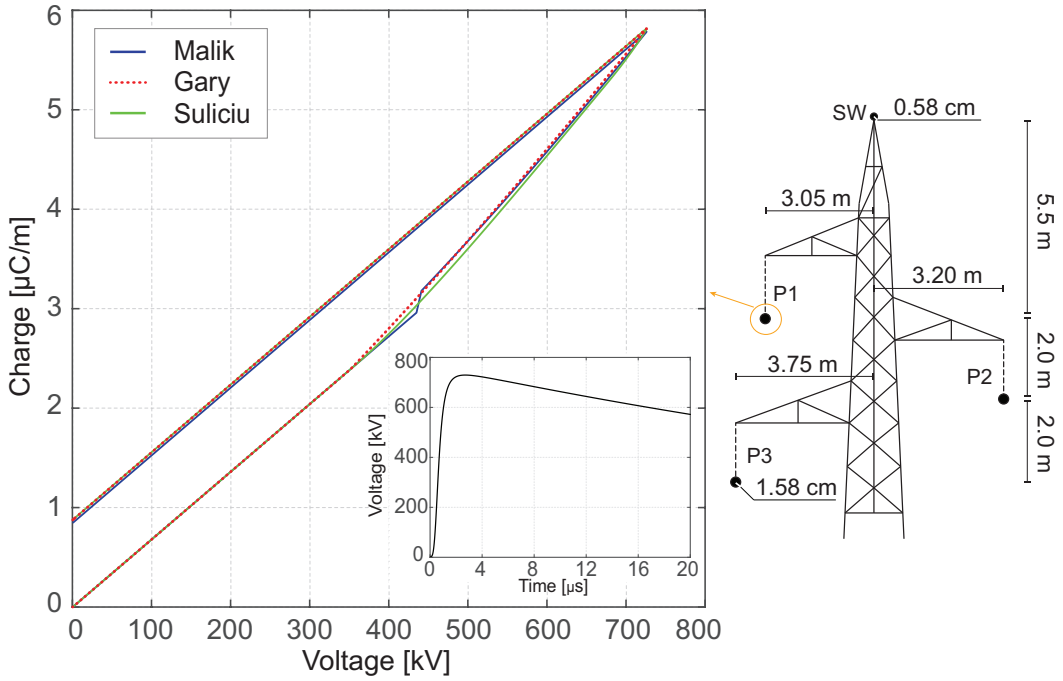

(a) (b)

Figure 4.1. (a) Charge-voltage curves computed by the implemented models with parameters in Table 4.1. (b) Arrangement and relevant geometric parameters of the conductors for the chosen MTL.

a single conductor is fed by an ideal voltage source (Fig. 4.1a), given by the expression (4.4), with $n = 3$, and $\tau_1 = 0.63$ μs, and $\tau_2 = 67.3$ μs, corresponding to front time 1.2 μs, and time to half-value 50 μs; V_0 has been set to twice the inception voltage of a conductor of radius 1.58 cm, computed as in equation (A.1) (inception voltage according to Peek's formula), i.e., $V_{\text{inc}} = 358.9$ kV with $m = 0.75$, $\delta = 1$, $f_{\text{p}} = 1$. The parameters were selected for a conductor with height $h = 28$ m and radius $r_0 = 1.58$ cm, since the following results will deal with conductor P1 in Fig. 4.1 being fed at the TL left termination. The internal impedance of the voltage source is matched to the (lossless) line characteristic impedance; hence, the peak value of the feeding voltage is doubled in order to approximately account for the voltage divider represented by the matched internal impedance of the source and the matrix of characteristic impedances of the line.

In order to assess the validity of the code developed in the TD, Fig. 4.2 displays results for the MTL (in Fig. 4.1) at 0 km, and 1 km from the line left termination, in the absence of corona, computed with the implicit FDTD scheme and in the frequency domain (followed by an inverse Fourier transform), by means of the code introduced in Chapter 7. Phase P1 is fed through a matching impedance by the aforementioned voltage source. Negligible differences (mainly in late time voltages of the non-fed conductors) may be noticed, probably due

Table 4.1. Parameters required for the implementation of the corona models proposed by Suliciu *et al.*, Malik, and Gary (Appendix A).

Suliciu	$C_1 = 8.9$ pF/m	$C_2 = 9.2$ pF/m
	$K_1 = 8$ MHz	$K_2 = 4$ MHz
	$V_1 = V_{\text{inc}}$	$V_2 = V_{\text{inc}}$
Malik	$\tau = 0.1$ µs	$\alpha = 0.3$
Gary	$B = 1.121 + 6.8 r_0$	

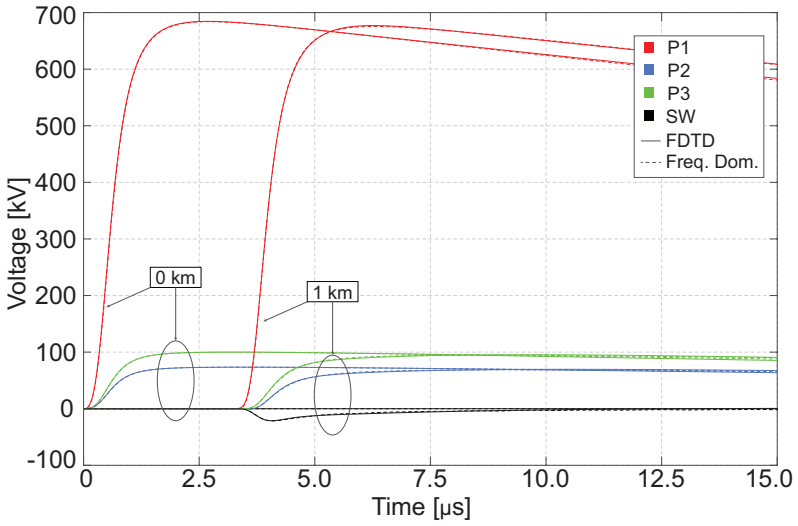

Figure 4.2. Comparison of results computed by the implicit FDTD scheme ($\Delta x = 4$ m, $\Delta t \approx 12$ ns) and by inverse Fourier Transform of frequency domain results for the TL in Fig. 4.1. P1 is fed by a 1.2/50 µs voltage source; simulations do not include the corona effect.

to the implementation of Prony method for the evaluation of losses in the time domain (referred to in Chapter 1), and to the influence of numerical dispersion at larger travelling distances.

Figures 4.3 show voltages-to-ground of the fed phase, i.e., conductor P1, at 0 km, 1 km, and 7 km from the line left termination, evaluated with the three corona models. The solid grey line displays the voltage in the absence of corona; along with attenuation, a relevant reduction in the propagation velocity may be observed at larger distances from the fed termination.

Results from Suliciu's and Gary's models are in satisfactory agreement; differences with respect to Malik's model, which are negligible at 0 km, are progressively enhanced at 1 km (Fig. 4.3b) and 7 km (Fig. 4.3c).

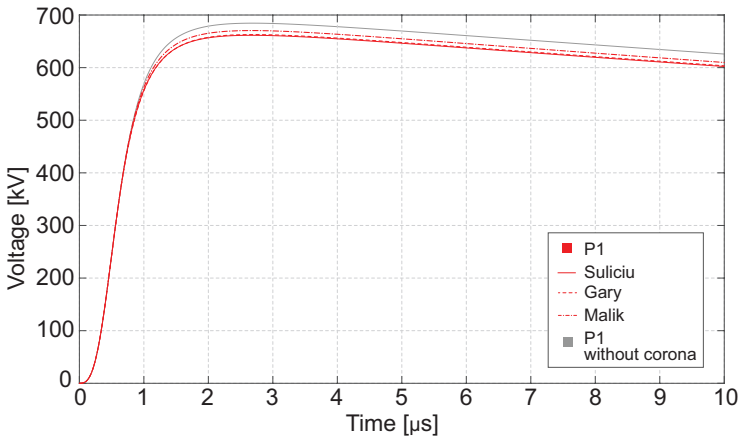

(a)

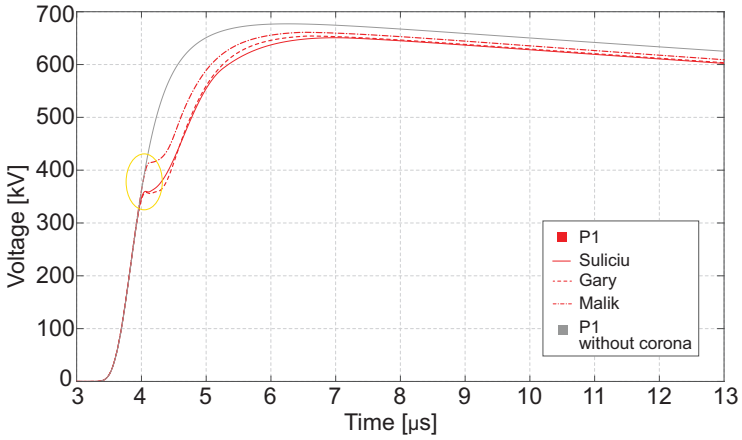

(b)

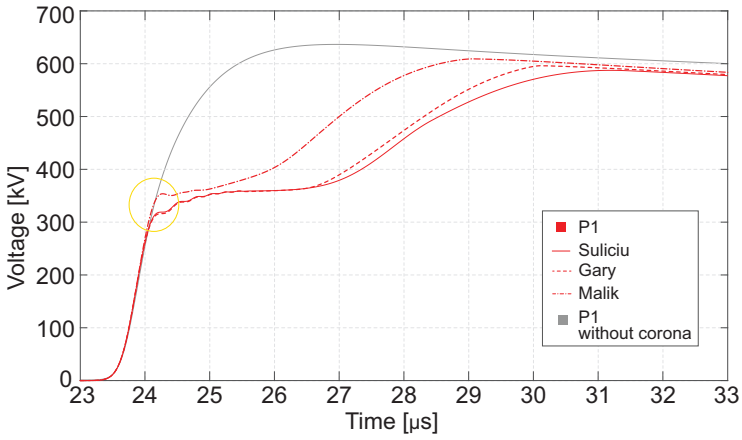

(c)

Figure 4.3. Conductor P1 voltage-to-ground computed with the corona models by Suliciu *et al.*, Malik, and Gary (Appendix A), and 1.2/50 μs voltage source; (a) voltages at the line left termination; (b) voltages at 1 km from the left termination; (c) voltages at 7 km from the left termination.

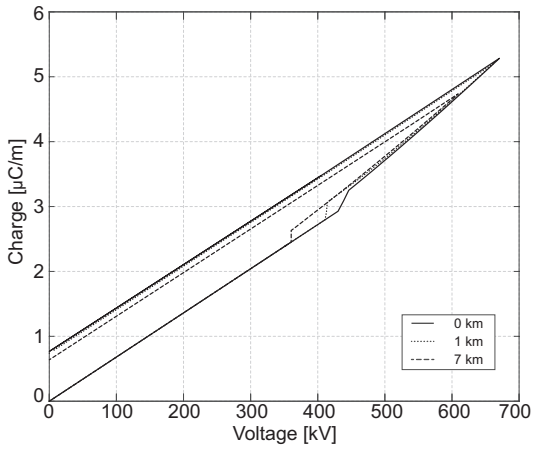

(a)

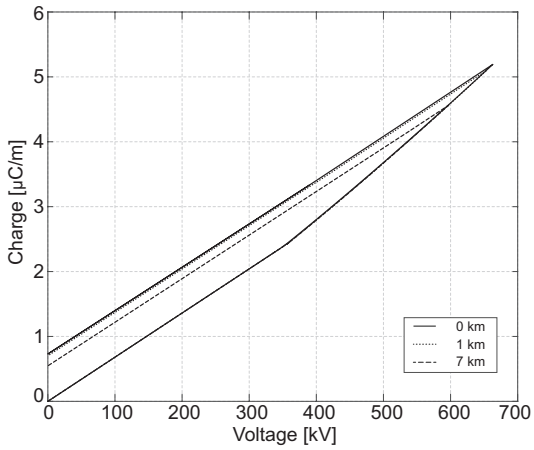

(b)

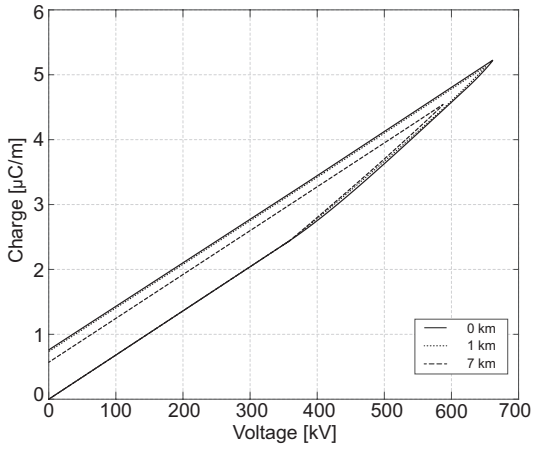

(c)

Figure 4.4. Hysteretic q-v loops linked to voltages-to-ground of conductor P1 in Figs. 4.3, with 1.2/50 μs voltage source; (a) Malik's model; (b) Gary's model; (c) Suliciu's model.

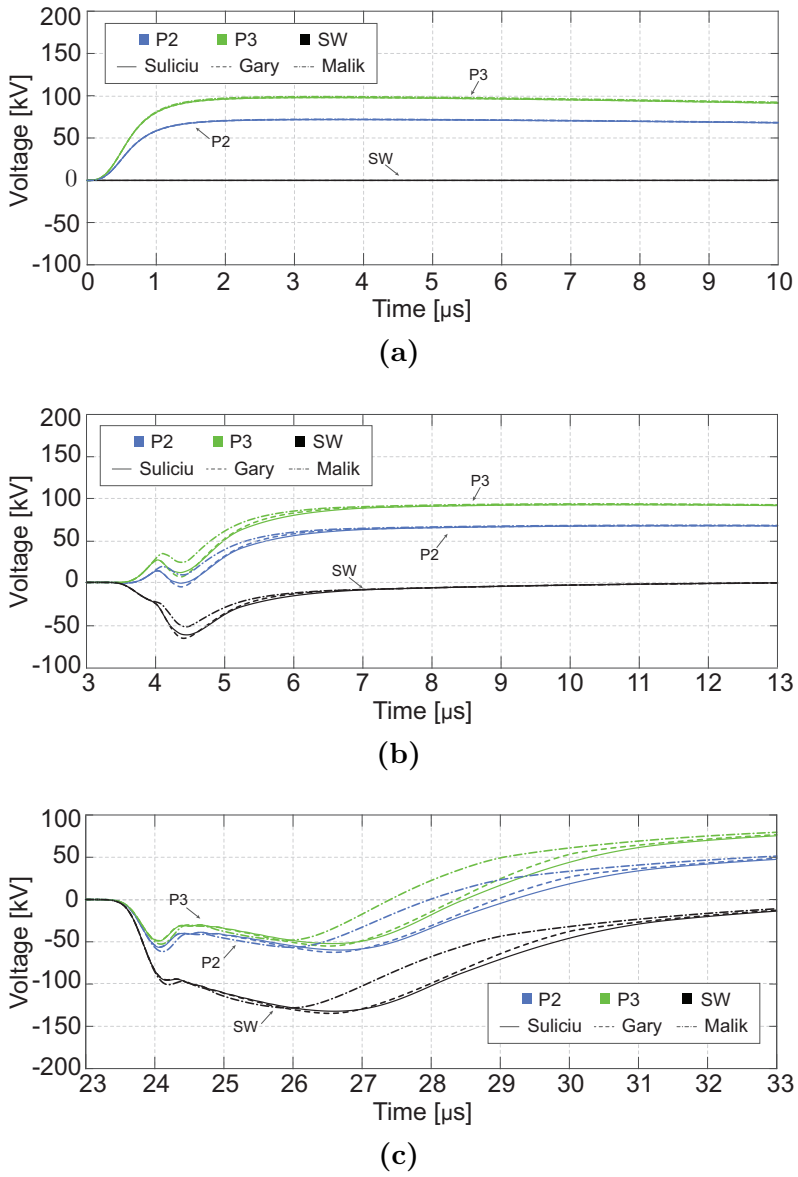

Figure 4.5. Voltages-to-ground of conductors P2, P3, and of the SW induced by conductor P1 (fed by a 1.2/50 μs voltage source, and accounting for corona); (a) voltages at the line left termination; (b) voltages at 1 km from the left termination; (c) voltages at 7 km from the left termination.

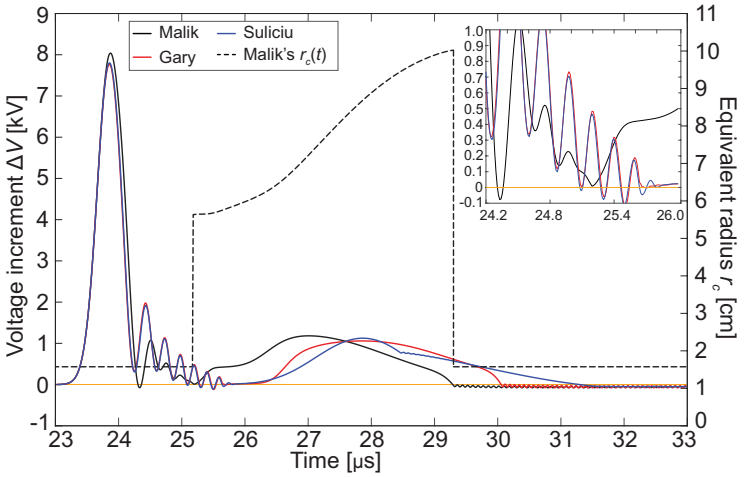

Figure 4.6. Increment $\Delta V\,(t)$ of voltage of conductor P1 (difference between the value of voltage computed at $(n+1)\,\Delta t$ and that at $n\Delta t$, as a function of time) at 7 km from the fed termination for the three models, and $r_{\mathrm{c}}\,(t)$ by Malik's approach, in the same conditions of Fig. 4.3c.

Explanation may be found from the analysis of Fig. 4.4, in which q-v curves evaluated for conductor P1 at 0, 1, and 7 km are depicted. While loops obtained from Suliciu's and Gary's models are comparable at the observed points along the line, the discontinuity in Malik's curves, due to the abrupt change of the corona equivalent radius, deserves some remarks.

The reduced area of the charge-voltage loop at 7 km in Fig. 4.4a, compared to the corresponding area at 7 km in Figs. 4.4b and 4.4c, is consistent with the less pronounced voltage attenuation given by Malik's model.

The reduction of the q-v loop area is mainly due to the different voltage at which the charge discontinuity occurs, approximately at 440 kV and 360 kV at 0 km and 7 km, respectively.

Indeed, due to the delay τ (introduced by Malik's model) in the formation of the corona charge with respect to the inception time, the first formation of corona over-charge occurs in correspondence with larger voltage values at points closer to the voltage source; conversely, milder rates of voltage raise at larger distances, due to distributed losses along the line, keep the discontinuity at lower voltage values, further reducing the q-v loop area. The effect of τ on surge propagation is marked in orange in Figs. 4.3b, 4.3c.

Figure 4.5 shows voltages induced on the other conductors of the MTL; results given by the implemented corona models differ more consistently at 7 km from the voltage source, as expected from the discrepancies observed for the voltage of the fed conductor at the same distance (Fig. 4.3).

Figure 4.6 has been included in order to support observations in Sec. 4.2.1 on the accuracy and difficult numerical implementation of the dynamic capacitance approach. The voltage-to-ground increment ΔV (difference between the value

of voltage computed at $(n+1)\,\Delta t$ and that at $n\Delta t$, as a function of time) of conductor P1 at 7 km from the fed termination for the three implemented models, and the equivalent radius given by Malik's approach are displayed with different scale. The approach presented in Sec. 4.2.1 is based on the numerical computation of C_{dyn} as the ratio $\Delta q/\Delta V$. From Fig. 4.6, it can be observed that after the inception of corona, due to the abrupt increase of the p.u.l. line capacitance, the line voltage $v\,(t)$ is oscillating and the ΔV crosses the 0 V axis. Hence, the computation of the aforementioned ratio may result in numerical problems and/or poor accuracy. The voltage-controlled current generator approach overcomes this problem, by direct evaluation of the corona current.

4.3.2 Slow-front voltage source

Results for a typical slow-front voltage source have been included for comparison of corona effects on propagation with respect to previously discussed results for a fast-front surge. Parameters of the voltage source, feeding conductor P1 through a matched impedance, are: $\tau_1 = 75.5$ µs, $\tau_2 = 3124.0$ µs, $n = 3$, and $V_0 = 2V_{\mathrm{inc}}$. The applied source amplitude is doubled to account for the voltage divider at the line left termination. Voltages-to-ground of the fed conductor P1 at 0, 1, and 7 km from the line left termination are depicted in Fig. 4.7, while voltages of conductors P2, P3, and of the SW are depicted, at the same observation points along the line, in Fig. 4.8. For the same V_0, in this case corona holds minor impact on propagation, due to the reduced front steepness of the voltage wave, i.e., to smaller contributions by the transversal corona currents (which depend on $\mathrm{d}v/\mathrm{d}t$).

Furthermore, it may be observed that discrepancies in the shape of the traveling surge obtained by different corona models reduce at growing distances from the fed termination; in fact, the deviation in their peak value with respect to the case in which corona is not included in the simulations is less then 1% at 7 km from the line left termination. This point might be addressed through inspection of q-v curves relative to the fed conductor, computed through the implemented corona models, and included as insets of Fig. 4.7. The value of the voltage at which the charge discontinuity occurs in the q-v loops from Malik's model, (which was previously indicated as the main cause for increasing differences with other models at larger distances from the feeding point) is not sensibly affected by the position of the observation point along the line, contrary to results in Fig. 4.4; in fact, with the switching impulse, the impact of the time delay τ on the loop shape is strongly limited, due to the milder front of the surge, leading to results comparable with other models.

In Figs. 4.8, the voltages of the other conductors are displayed in a different scale, and are compared to voltages induced in the absence of corona (light grey solid line).

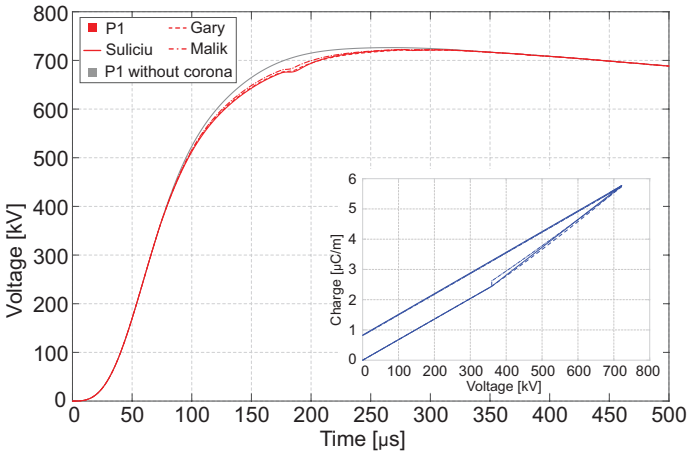

(a)

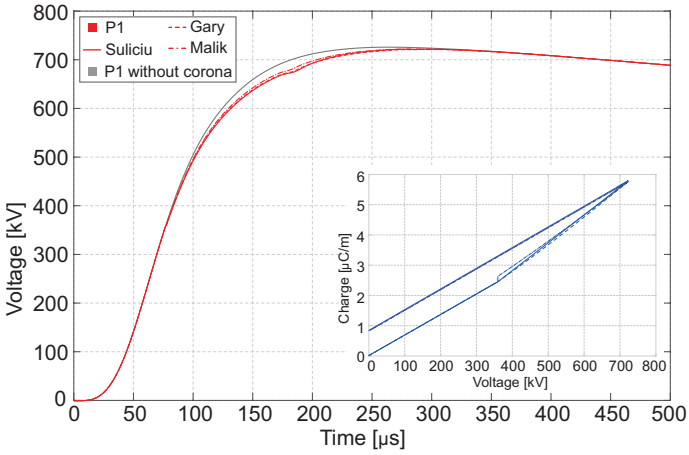

(b)

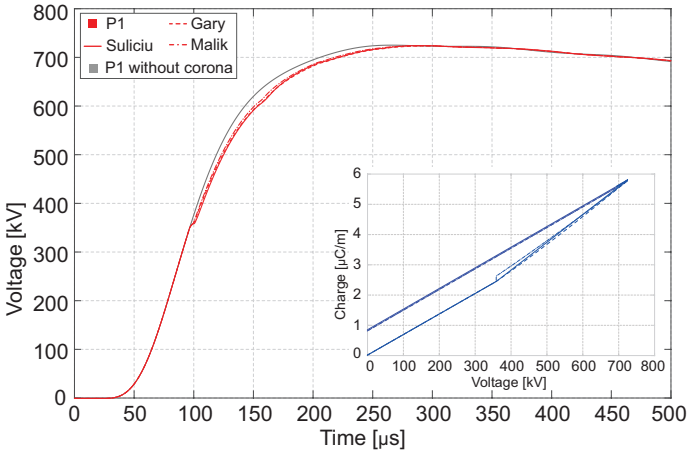

(c)

Figure 4.7. Conductor P1 voltage-to-ground computed with the corona models by Suliciu *et al.*, Malik, and Gary (Appendix A), and slow-front voltage source; (a) voltages at the line left termination; (b) voltages at 1 km from the left termination; (c) voltages at 7 km from the left termination.

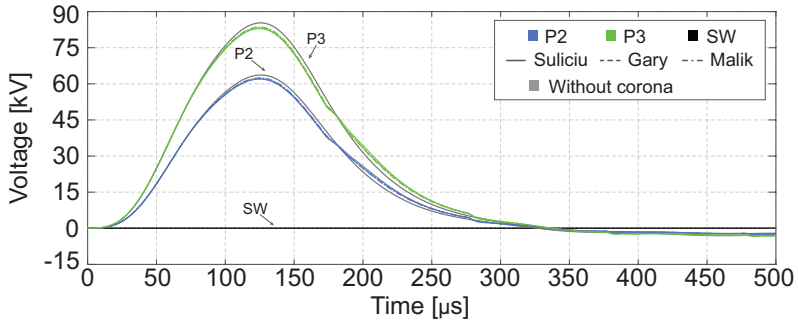

(a)

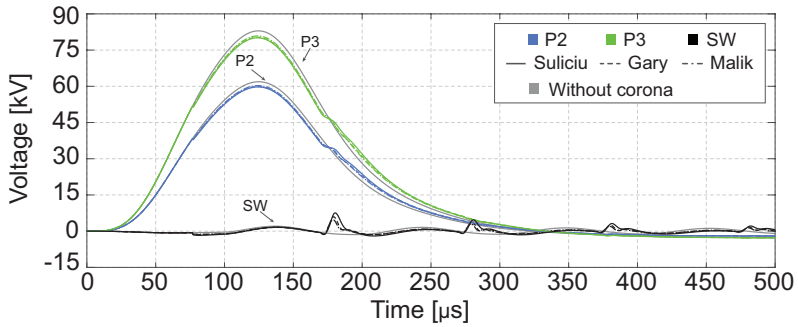

(b)

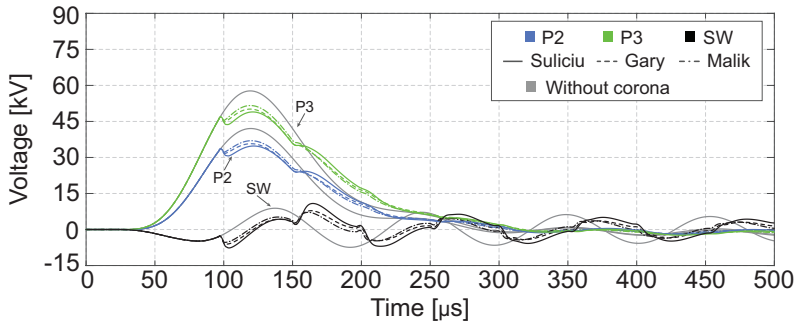

(c)

Figure 4.8. Voltages-to-ground of conductors P2, P3, and of the SW induced by conductor P1 (fed by a slow-front voltage source, and accounting for corona); (a) voltages at the line left termination; (b) voltages at 1 km from the left termination; (c) voltages at 7 km from the left termination.

Reflections at the line terminations are more evident when corona discharge is simulated. This phenomenon is linked to the enhancement in the already existing mismatch between the line adopted terminations (i.e., constant resistive loads), and the characteristic impedance of the lossy line; indeed, the simulation of corona discharge causes a further deviation of the line capacitive behaviour from its linear one, associated only with the conductors arrangement and geometry. In particular, with reference to Fig. 4.8a, no deviation from the reference voltages in the absence of corona can be observed, until corona inception for conductor P1 occurs at around 73 μs; at later times, enhanced reflections are visible at intervals of about 100 μs, corresponding to the time necessary for the traveling wave to go back to the feeding point, after reflection at the right termination. Analogous observations can be made for outputs in Figs. 4.8b, 4.8c, considering suitable time intervals for the expected reflections from the line endpoints.

As to the computational burden of the algorithm, the total running time to get results associated with the 15 km line discussed here ($\Delta t \approx 12$ ns, $\Delta x = 4$ m), in the case of fast-front voltage source, was approximately 3 minutes on a desktop computer (AMD Ryzen 7 1800X, 64 GB RAM).

Remarks

q-v models in the literature, from which suitable expressions for the corona current were derived, are frequently tailored on experimental data referring to configurations which are different from the common ones involving TLs, and do not consider the stochastic nature of the corona phenomenon [11]. In fact, they often refer to short cylindrical conductors fed by known voltage sources, the charge being considered as the output of a system with a given input voltage.

Instead, in propagation studies, corona over-charge, developed in response to a voltage excitation, has an influence on the voltage waveform itself, due to the reduced propagation velocity and additional losses introduced by the hysteretic capacitive behaviour of the conductor under corona. These aspects are not predictable *a priori*, and are to be considered when trying to include corona in FDTD schemes through the dynamic capacitances approach; while models are based on conductors fed by voltage sources which are strictly monotonically increasing until their peak value, this might not be the case in applications involving propagation: delays associated with corona discharge may result in intervals with very slow, or no variation in conductor-to-ground voltages at large distances from the source (e.g., results from Suliciu's model in Fig. 4.3c, at about 26 μs), leading to a numerically unfriendly, undeterminate form of the ratio $\mathrm{d}q/\mathrm{d}v$.

Furthermore, charge given by models relying on a q-v time dispersive relation are expected to depend on the voltage derivative, i.e., to present different hysteretic loops for different excitation voltages [12]. This further justifies the agreement between Gary's and Suliciu's approaches, which model

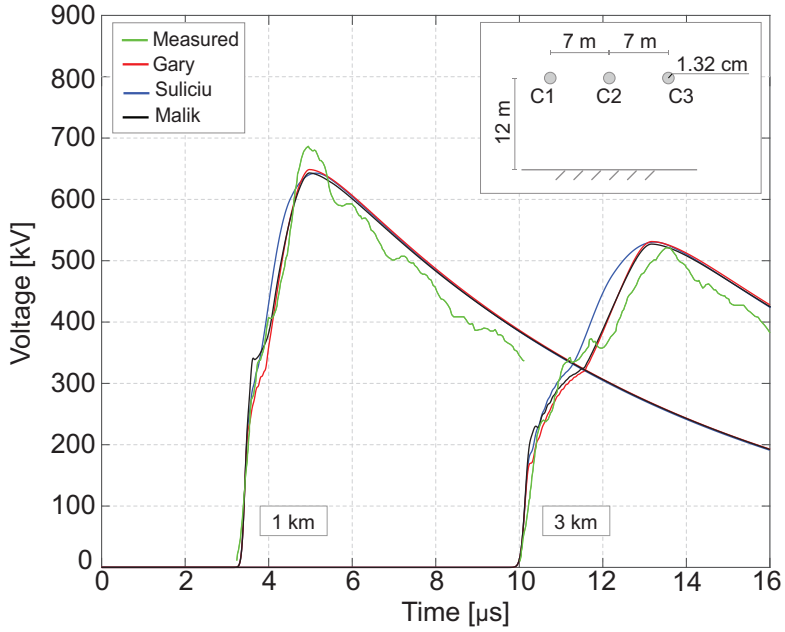

Figure 4.9. Comparison of results with corona models by Suliciu *et al.*, Malik, and Gary (Appendix A) and measured voltages for the fed conductor C1 of the test line in the inset [13].

charge as an instantaneous nonlinear response of the system to a voltage input, and, on the other hand, the discrepancy with Malik's model, which relies on the sum of an instantaneous linear response (i.e., $C'_{\text{geo}} v\,(t+\tau)$ in equation (A.18)) and a nonlinear delayed one (depending on $r_c\,(t)$ in (A.18)).

4.3.3 Numerical implementation against experimental data

Corona models by Suliciu *et al.*, Malik, and Gary (Appendix A), with parameters in Table 4.1 and $\Delta t \approx 2.7$ ns, have been additionally tested with a different waveform, and adopted to reproduce experimental data.

The first set of data is found in the literature from Gary [13]; voltages-to-ground are measured for a three conductors test line, with horizontal configuration, arranged as depicted in the inset of Fig. 4.9. The line is 65 km long, short circuited at the right termination; at the left termination, the external conductor C1 is fed by a voltage source by means of an unmatched impedance, resulting, at the sending end, in the following waveform (expressed in kV, with time in μs, and including a typographic correction) [13]:

$$v\,(t) = 850\left[0.988\,\mathrm{e}^{-0.123t} - 1.051\,\mathrm{e}^{-4.1t}\sin\left(12.3t + 70^{\circ}\right)\right]. \tag{4.6}$$

Results computed by means of the implicit FDTD scheme are compared to the measured voltage of the fed conductor C1, at 1 km and 3 km from

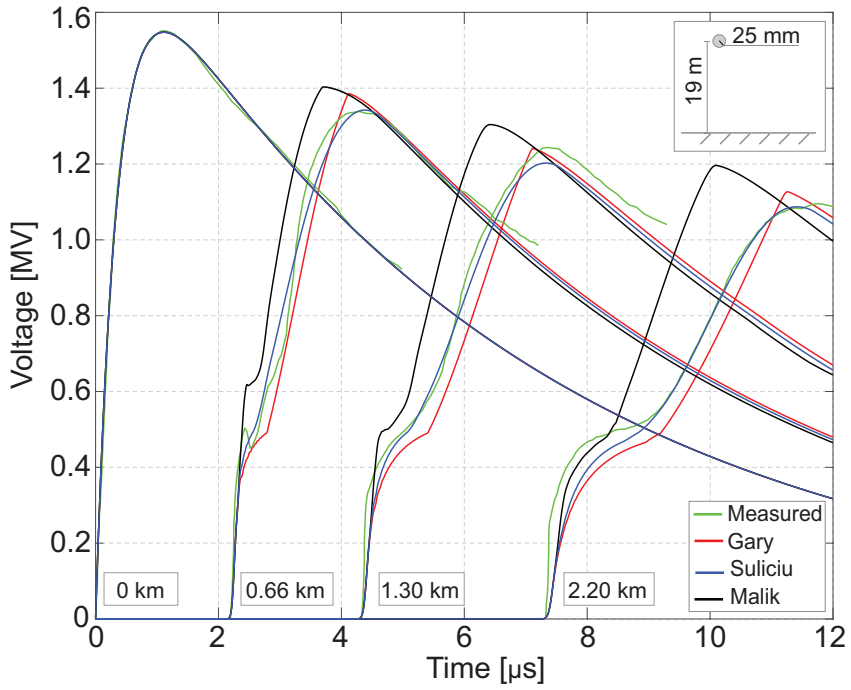

Figure 4.10. Comparison of results computed with corona models by Suliciu *et al.*, Malik, and Gary (Appendix A) and measured voltages for the fed conductor displayed in the inset, at different distances from the fed termination [3].

the left termination. Uncertainties related to the soil electrical properties ($\sigma_g = 250$ S/m, and $\epsilon_g = 10\epsilon_0$ are assumed), and to the impedance of the feeding source, produce a difference of about 6% and 2% of the peak values computed by the FDTD algorithm with respect to the corresponding peak values measured at 1 km and 3 km. The same parameters in Table 4.1 have been employed for the implementation of the models, still resulting in good agreement of the numerical results with experimental data involving this first configuration.

The models have been additionally exploited to reproduce measurements of voltage surges by Wagner, Gross and Lloyd along a test line located in Ohio [3]. Data chosen here for comparison refer to an ACSR (aluminium-conductor steel-reinforced) single conductor with radius $r_0 = 25$ mm and about 2,2 km long, fed by a surge generator; at the other termination, the line is closed on a resistor with resistance approximately equal to the line characteristic impedance (about 439 Ω). Starting from the description of the original test site, the geometrical configuration under analysis is displayed in the inset of Fig. 4.10. As to the properties of the soil, the relative electrical permittivity is set to 10, while 500 Ωm is the chosen value for the soil resistivity, considering the average values given by the World Atlas of Ground Conductivities [14] in the test site area. Since the analytical expression of the applied voltage source is not provided, a double exponential function is found in order to fit the given

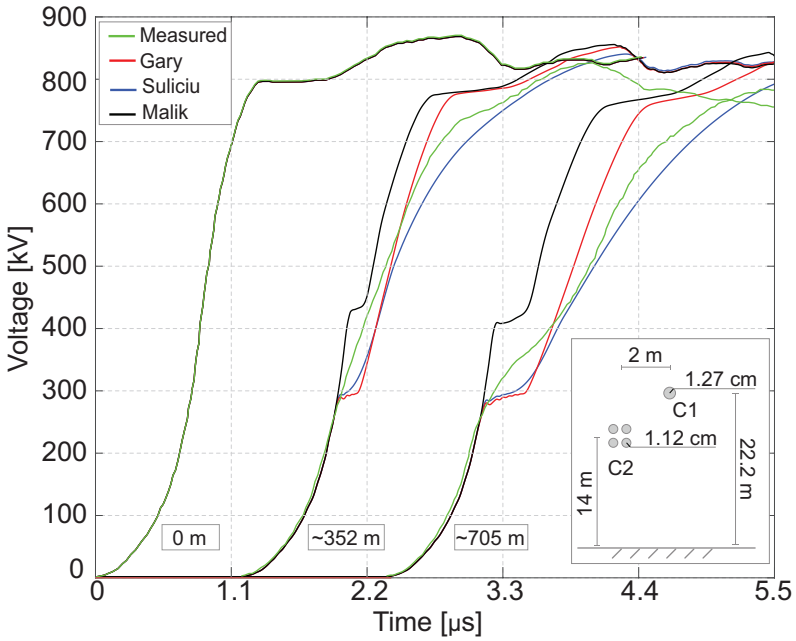

Figure 4.11. Comparison of results with corona models by Suliciu *et al.*, Malik, and Gary (Appendix A) and measured voltages for the fed conductor C1 in the inset at different distances from the fed termination [15].

voltage curve measured at the fed termination (expressed in kV):

$$v\left(t\right) = 1551.5 f_p \left(\mathrm{e}^{-\frac{t}{\tau_1}} - \mathrm{e}^{-\frac{t}{\tau_2}}\right) , \tag{4.7}$$

with

$$f_p = \left[\exp\left(-t_m/\tau_1\right) - \exp\left(-t_m/\tau_2\right)\right]^{-1} \tag{4.8a}$$

$$t_m = \frac{\tau_1 \tau_2}{\tau_1 - \tau_2} \ln\left(\tau_1/\tau_2\right) , \tag{4.8b}$$

and $\tau_1 = 6.64$ μs, $\tau_2 = 3.61$ μs. The parameters required by the different models have been chosen in order to better match experimental data measured at 660 m, 1300 m from the fed termination, and at the line endpoint. The values adopted are: $\tau = 0.1$ μs, and $\alpha = 0.3$ for Malik's model; $B = 1.212 + 6.8 r_0$ for Gary's model; $C_1 = 10$ pF/m, $C_2 = 13$ pF/m, $K_1 = 9$ MHz, $K_2 = 4$ MHz, and $V_1 = V_2 = V_{\mathrm{inc}} \approx 489.9$ kV for Suliciu's model. Comparing the curves in Fig. 4.10, the effect of Malik's delay time τ, already underlined in Sec. 4.3.1, contributes to differentiating Malik's results from those computed with the other models. Instead, with Gary's and Suliciu's approaches, more accurate results in terms of voltage derivative at the front and peak value of the surge along the line may be obtained; the results confirm the versatility of Suliciu's model, due to the available number of degrees of freedom, i.e., the larger number of parameters which can be adjusted and set to match measured data.

Figure 4.11 shows the voltages computed for conductor C1 belonging to the line displayed in the inset (with total length equal to 1410 m), compared to experimental data from [15] (in Japanese). Conductor C1 is closed at the end termination on a resistive impedance of 490 Ω, while conductor C2 is open at both terminations. The soil electrical relative permittivity and resistivity are set to 10 and 100 Ωm, respectively [16]. The applied voltage corresponds to the waveform displayed for 0 km. Since the analytical expression of the applied voltage at 0 km is not provided, this one was obtained from interpolation of results available in [15] and [16], and imposed at the fed termination of C1. Parameters adopted for the implementation of the models are left unchanged from the previous configuration, updating the inception voltage of conductor C1 to the value $V_{\text{inc}} \approx 294.2$ kV. Fig. 4.11 endorses the versatility of Suliciu's model which presents again the best agreement with measured voltages; yet, the overall results prove that the simulation of corona phenomena requires an accurate setting of the fundamental parameters of the model.

4.4 Soil ionization in extended grounding systems

Electrical discharges occurring in the vicinity of grounding electrodes, briefly described in Appendix C on soil ionization, are to be classified as nonlinear phenomena.

Extended grounding systems, with leading dimension larger than 30 m, are commonly adopted along HV TLs to connect the installed SWs to ground, lowering the low frequency value of the grounding resistance in the unfavourable condition of large values of local electrical resistivity of the soil.

As to the literature regarding extended grounding systems, closed-form formulas are not available allowing to account in a general way for soil ionization in the proximity of the grounding device, as the current propagating along the electrodes is progressively dispersed into the soil. Indeed, the response of the grounding system is influenced by its dimensions and design.

An approximated approach is suggested in [17], consisting in dividing the extended grounding system into sections with a maximum length of 30 m; each section should be treated as a concentrated grounding system (to be modelled as described in Sec. 5.3), considering a constant average velocity, approximately equal to $c_0/2$, to assess current propagation along consecutive sections.

Numerical approaches have been proposed in the literature based on TL-type approximations of the grounding system. For instance, Gazzana *et al.* [18], [19] include a shunt, time-varying p.u.l. conductance in parallel to the

p.u.l. capacitance in the TL equivalent circuit:

$$G'(t, x_k) = G'_0 \sqrt{1 + \frac{\Delta I(t, x_k)}{I_g}} \,. \tag{4.9}$$

In (4.9), G'_0 corresponds to the p.u.l. conductance (to be multiplied by the k^{th} segment length l_k) associated with each conductor with radius a_k (buried vertically or horizontally) in the absence of soil ionization; the second term is in the form of the one suggested by Cigré [17] for concentrated grounding systems, in which $\Delta I(t, x_k)$ is the current leaked by the specific segment to the soil. The current-dependence of the longitudinal conductance $G(t)$ is taken into account, and its value updated, as the electric field on the electrodes surface $E(t, J)$ reaches the critical value E_g, with

$$E(t, x_k) = \rho_0 J(t, x_k) = \rho_0 \frac{\Delta I(t, x_k)}{2\pi a l_k} \,, \tag{4.10}$$

adopting the approximation of a uniform current dispersion through the external surface of the electrode segment. In (4.10), the quantity ρ_0 denotes the soil electrical resistivity in the absence of ionization (Appendix C). The other relevant parameters of the TL equivalent circuit of the grounding system (namely, values of p.u.l. shunt capacitances, and longitudinal inductances and resistances) are considered constant, computed according to the device geometry, magnetic and electrical properties of the soil in the absence of ionization.

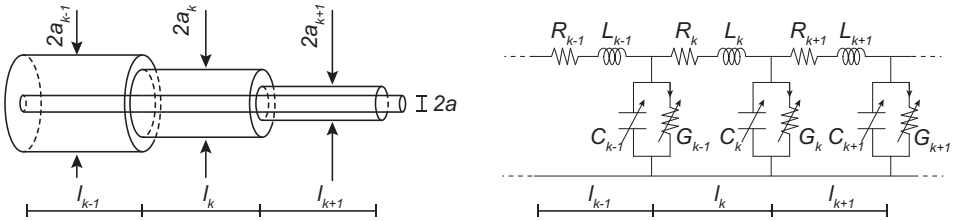

Figure 4.12. (a) Discretization of the grounding conductors into segments with length l_k and equivalent radius a_k; (b) TL equivalent circuit including current-dependent capacitances and conductances to ground (adapted from [20]).

In these regards, Zeng *et al.* [20] adopted a time-varying p.u.l. capacitance for their TL equivalent circuit, considering a time-varying equivalent radius a_k for each discretized segment k. The radius a_k, accounting for the soil ionization, corresponds to the radial distance from the electrode axis where the computed electric field is equal (or lower) to E_g[2]:

$$a_k(t) = \frac{\rho_0}{E_g} \frac{\Delta I(t, x_k)}{2\pi l_k} \tag{4.11}$$

[2] E_g is the critical electric field causing the start of soil ionization.

where $\Delta I\,(t, x_k)$ is the current leaked by the k^{th} segment, l_k and a_k are to be intended as the length and the variable radius of the k^{th} segment, as from Fig. 4.12. Instead, the values of longitudinal inductances and resistances are considered not to be affected by soil ionization, assuming that a decoupling exists between the currents flowing longitudinally along the conductors and those ones being injected radially into the soil; the former currents are confined into the actual metallic structure, and do not flow across the additional cross-section due to the apparent increment of the conductor radius. Mutual inductive coupling between the electrodes segments is taken into account (not represented in Fig. 4.12).

Eventually, in [21], soil ionization is included to study the TD response of grounding systems to injected impulse currents. A code, based on the discretization of the grounding system into branches connected by nodes, allows to compute (under simplifying assumptions) the response of the device under study. Ionization is included by means of lumped circuits, consisting of dedicated constant admittances to ground and time-varying ideal current generators (accounting for the actual development of the ionization phenomenon), connected to the nodes of the discretized structure.

References

[1] A. R. Hileman, *Insulation Coordination for Power Systems*, C. Press, Ed., 1999.

[2] F. W. Peek, *Dielectric phenomena in high voltage engineering.* McGraw-Hill Book Company, Incorporated, 1920.

[3] C. F. Wagner, I. W. Gross, and B. L. Lloyd, "High-voltage impulse tests on transmission lines," *Transactions of the American Institute of Electrical Engineers. Part III: Power Apparatus and Systems*, vol. 73, no. 2, pp. 196–210, Apr. 1954.

[4] E. Stracqualursi, R. Araneo, and A. Andreotti, "The impact of different corona models on FD algorithms for the solution of multiconductor transmission lines equations," *High Voltage*, vol. 6, no. 5, pp. 822–835, Sep. 2021.

[5] J. D. Pearson and D. H. Trevena, "Definition of capacitance," *Journal of Electronics and Control*, vol. 6, no. 1, pp. 74–74, 1959.

[6] G. Florea, G. Dragan, I. Rodean, L. Lipan, E. Mateescu, and M. Oltean, "Considerations on the line capacitance under surge corona discharge," in *International Symposium on Electromagnetic Compatibility-EMC EUROPE.* IEEE, 2012, pp. 1–6.

[7] X. Liu, J. Yang, G. Liang, and L. Wang, "Modified field-to-line coupling model for simulating the corona effect on the lightning induced voltages of multi-conductor transmission lines over a lossy ground," *IET Generation, Transmission & Distribution*, vol. 11, no. 7, pp. 1865–1876, 2017.

[8] X.-R. Li, O. P. Malik, and Z.-D. Zhao, "A practical mathematical model of corona for calculation of transients on transmission lines," *IEEE Power Eng. Rev.*, vol. 9, no. 4, pp. 75–75, Apr. 1989.

[9] C. De Jesus and M. T. Correia De Barros, "Modelling of corona dynamics for surge propagation studies," *IEEE Trans. Power Del.*, vol. 9, no. 3, pp. 1564–1569, 1994.

[10] IEEE Std 4-2013, *IEEE Standard for High-Voltage Testing Techniques*. IEEE, 2013.

[11] E. Bousiou, P. Mikropoulos, and V. Zagkanas, "Application of the critical volume theory to estimating impulse corona characteristics in the coaxial cylindrical electrode arrangement," in *2017 52nd International Universities Power Engineering Conference (UPEC)*. IEEE, 2017, pp. 1–5.

[12] E. Bousiou and P. Mikropoulos, "Experimental investigation on corona charge-voltage characteristics in the coaxial configuration under lightning impulse voltages," in *2018 IEEE International Conference on High Voltage Engineering and Application (ICHVE)*. IEEE, 2018, pp. 1–4.

[13] C. Gary, *Attenuation of travelling waves caused by corona. CIGRE Report 22-13*, 1978.

[14] O. ITU-R, "World atlas of ground conductivities," 1999.

[15] A. Inoue, "Study on propagation characteristics of high-voltage traveling waves with corona discharge," *CRIEPI Report*, vol. 114, 1983.

[16] T. H. Thang, Y. Baba, N. Nagaoka, A. Ametani, J. Takami, S. Okabe, and V. A. Rakov, "FDTD simulation of lightning surges on overhead wires in the presence of corona discharge," *IEEE Trans. Electromagn. Compat.*, vol. 54, no. 6, pp. 1234–1243, 2012.

[17] *CIGRE Technical Brochure 63: Guide to procedures for estimating the lightning performance of trasmission lines*, CIGRE Std., 1991.

[18] D. S. Gazzana, A. S. Bretas, G. A. Dias, M. Telló, D. W. Thomas, and C. Christopoulos, "The transmission line modeling method to represent the soil ionization phenomenon in grounding systems," *IEEE Trans. Magn.*, vol. 50, no. 2, pp. 505–508, 2014.

[19] D. S. Gazzana, A. B. Tronchoni, R. C. Leborgne, A. S. Bretas, D. W. Thomas, and C. Christopoulos, "An improved soil ionization representation to numerical simulation of impulsive grounding systems," *IEEE Trans. Magn.*, vol. 54, no. 3, pp. 1–4, 2017.

[20] R. Zeng, X. Gong, J. He, B. Zhang, and Y. Gao, "Lightning impulse performances of grounding grids for substations considering soil ionization," *IEEE Trans. Power Del.*, vol. 23, no. 2, pp. 667–675, 2008.

[21] A. Geri, "Behaviour of grounding systems excited by high impulse currents: the model and its validation," *IEEE Trans. Power Del.*, vol. 14, no. 3, pp. 1008–1017, Jul. 1999.

Chapter 5

Lumped nonlinearities

In consideration of the long distances covered by MTLs and their large power transmission capacity, insulation coordination measures need to include protection for fast and slow-front transient overvoltages caused by lightning strokes or switching operations since they may represent a threat for connected equipment [1]. Protection practice usually relies on the use of overhead SWs which are grounded at the towers. However, the grounding resistance should be kept as low as possible because the discharge of lightning currents through the grounding system may result in a Ground Potential Rise (GPR)[1], causing the voltage across the insulator strings to overcome their Basic Insulation Level (BIL).

A first phenomenon which may be treated as a lumped nonlinearity occurring at the towers is soil ionization (previously introduced in Chapter 4), consisting in localized discharges extending in the soil area surrounding the grounding system. Soil ionization may be studied by means of a fictitious, current-dependent increase of the grounding electrode's dimensions [3], or considering an equivalent average decrease of the electric resistivity of the soil layers close to the grounding electrodes [4]. As a consequence, when a threshold value of electric field is reached on the electrode surface, associated with a critical current density being dispersed into the ground, the grounding resistance value displays a nonlinearly decreasing trend for increasing dispersed currents, favourably limiting the GPR.

A second aspect deserving attention regards the installation of nonlinear devices for overvoltages limitation, consisting in arcing horns, surge arresters or Metal Oxide Varistor (MOV) [5] which may be effectively located along power lines. Optimized surge arrester allocation strategies, through the application of the genetic algorithm or of other techniques, have been proposed (e.g., [6]). In particular, MOVs may represent an efficient choice for limiting lightning and line-switching surges, significantly reducing the outage rate of the line.

[1]According to safety standards [2], the GPR is defined as the product of the grounding resistance and the peak value of the ground fault current; however, in the present chapter it refers to the actual voltage at the ground node in the TD.

It is documented [7] that the use of MOVs may offer additional advantages, reducing the need for complex solutions to limit switching overvoltages, e.g., controlled closing of circuit breakers equipped with preinsertion resistors.

Gapless light-weight metal oxide-type line surge arresters represent a very promising solution; indeed, they can improve the protection level, offering special features inherent in the gapless structure, e.g., quick response to surges, high energy dissipation capability, and minor influence of pollution on the intervention characteristic, that may introduce spurious resistive components [8].

5.1 Line arresters

The metal-oxide granular structure and chemical properties confer to MOVs their nonlinear V-I characteristic [9]. The nonlinear behaviour allows the device to limit the voltage drop at its terminations, and to dissipate part of the energy associated with the travelling surge by draining current. However, energy absorbtion capabilities of the installed devices should not be neglected in order to avoid unsolicited damages. For this reason, in [10] it is concluded that a correct coordination among MOVs withstand capability, number of SWs, and grounding resistance at the towers is necessary to limit permanent damage to surge arresters and obtain an effective lightning protection.

Several models have been proposed to describe the MOV behaviour [11], the most popular being: IEEE model recommended by Working Group (WG) 3.4.11 [12], Pinceti *et al.* model [13], Valsalal *et al.* model [14], and Fernandez *et al.* model [15]. Different characteristics are associated with different construction features, the choice of which is linked to the required performance. Appropriate modelling of MOV dynamic characteristics is of primary importance for insulation coordination and arrester location studies [6].

In this chapter, a novel numerical methodology is described to study the dynamic behaviour of MOVs in power lines [16]. The analysis is carried out by including the behaviour of the device in the implicit Crank-Nicolson FDTD updating scheme. Starting from the circuit model recommended by IEEE [12], a set of nonlinear equations is implemented which ensures robustness and second-order accuracy, representing a convenient strategy to include the MOV model inside the overall implicit scheme.

5.1.1 MOVs Circuit model

The nonlinear circuit model of surge arresters presented by WG 3.4.11 [12] is depicted in Fig. 5.1. It consists of two R-L filters and two nonlinear resistors (denoted by A_0 and A_1), one of which is connected in parallel with the capacitor C.

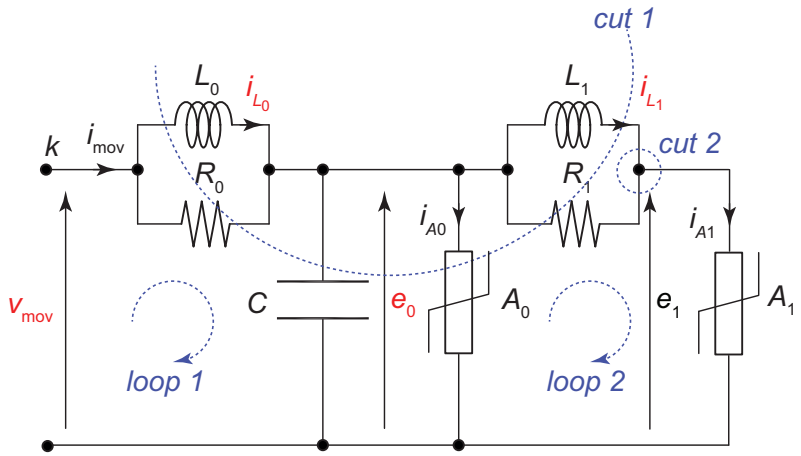

Figure 5.1. Surge arrester circuit model proposed by IEEE [12].

Under slow transients, the effect of the two R-L filters is negligible with respect to the resistance offered by the nonlinear branches; hence, A_0 and A_1 are essentially connected in parallel under the port voltage v_{mov}. Under fast transients, the filters impedances cannot be neglected due to the wider range of frequencies excited, resulting in a significant voltage drop between the two nonlinear branches. The high-frequency current is forced by the R_1-L_1 filter to flow more in A_0 than in A_1.

The requirement that the nonlinear resistor A_0 has higher voltage than A_1 at a given current, as in Fig. 5.2 and in [12], leads to the arrester model producing higher residual voltages at higher frequencies.

Several other models have been proposed in the literature [17]. The model shown in Figure 5.3a was proposed by Pinceti *et al.* [13], who developed a procedure for the parameters calculation. In [15], Fernandez *et al.* suggested the model in Fig. 5.3b which is also based on the IEEE model, proposing an iterative trial and error procedure to optimize the selection of the parameters. In [14], Valsalal *et al.* developed an arrester model for very fast transients (in Fig. 5.3c) derived from a simplified IEEE model with the inclusion of the arrester block capacitance C_{bp} and stray capacitance C_{g}.

5.1.2 Inclusion of the MOV in the FDTD scheme

Since the circuit has two nonlinear resistors, A_0 presenting higher voltage values than A_1 for a given current, as shown in Fig. 5.2, the set of variables and equations describing the electrical behaviour of the MOV should be properly chosen to ensure stability and robustness of the final FDTD scheme. The behaviour of the circuit is captured by a set of equations that are formulated by combining the constitutive equations of the circuit elements and Kirchhoff's Current and Voltage Laws (KCL and KVL, respectively).

Three quantities, which are associated with energy storing components of

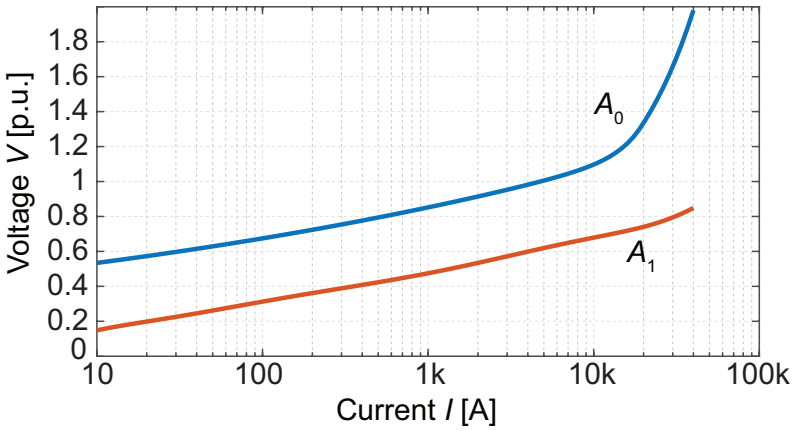

Figure 5.2. Voltage–current characteristics used to model the nonlinear resistors A_0 and A_1 for the selected MOV.

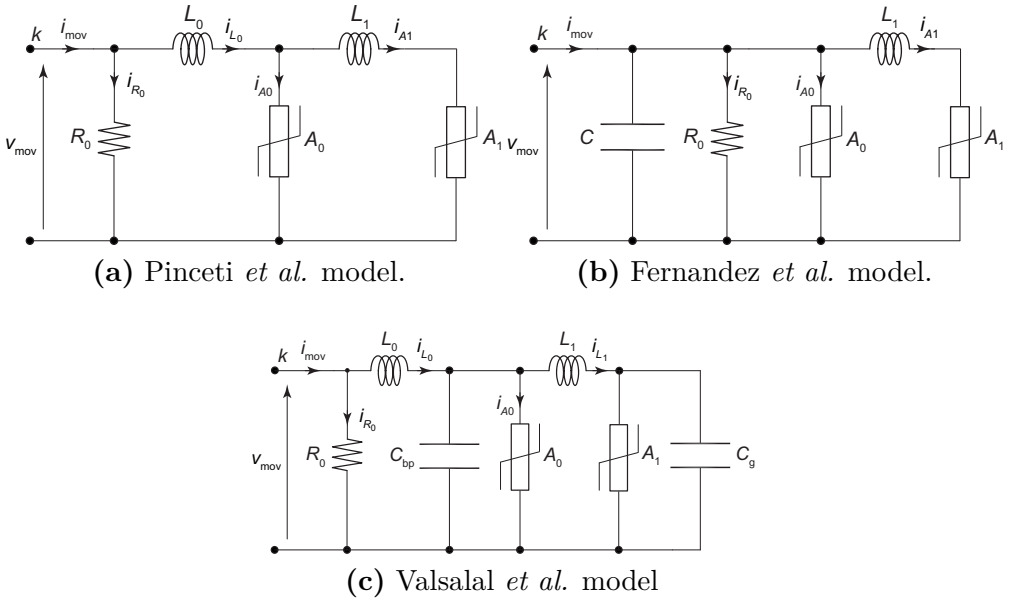

(a) Pinceti *et al.* model.

(b) Fernandez *et al.* model.

(c) Valsalal *et al.* model

Figure 5.3. Most used circuit models of surge arrester.

the equivalent circuit in Fig. 5.1, are chosen as state variables: currents i_{L_0} and i_{L_1} flowing through the inductors L_0 and L_1, respectively, and the voltage e_0 across the parallel C-A_0 (in the IEEE model). The voltage e_0 is used to control the nonlinear resistor A_0, which is modelled as a voltage-controlled current source; the current i_{A0} is found through the corresponding nonlinear constitutive relation. Likewise, the nonlinear resistor A_1 is modelled as another voltage-controlled current source: the voltage e_1 is derived applying the KVL, and the current i_{A1} is computed through its nonlinear constitutive relation.

With reference to the loops and the cut sets displayed in Fig. 5.1, the following expressions may be written:

$$L_0 \frac{\mathrm{d}i_{L_0}}{\mathrm{d}t} + e_0 - v_{\mathrm{mov}} = 0 \tag{5.1a}$$

$$i_{L_0} + \frac{v_{\mathrm{mov}} - e_0}{R_0} - C\frac{\mathrm{d}e_0}{\mathrm{d}t} - i_{A0}\left(v_{A0}\right) - i_{L_1} - \frac{L_1}{R_1}\frac{\mathrm{d}i_{L_1}}{\mathrm{d}t} = 0 \tag{5.1b}$$

$$i_{L_1} + \frac{L_1}{R_1}\frac{\mathrm{d}i_{L_1}}{\mathrm{d}t} - i_{A1}\left(v_{A1}\right) = 0 \tag{5.1c}$$

with

$$v_{A0} = e_0 \tag{5.2a}$$

$$v_{A1} = e_0 - L_1\frac{\mathrm{d}i_{L_1}}{\mathrm{d}t}\,. \tag{5.2b}$$

Equation (5.1a) corresponds to the KVL written for loop 1 in Fig. 5.1; application of the KCL for currents included into cut set 1 in Fig. 5.1 leads to (5.1b); the combination of equations deriving from the application of KVL and KCL to loop 2 and cut set 2, respectively, gives (5.1c).

Using a central difference combined with an average in time (as discussed in Chapter 1) leads to the discrete version of (5.1):

$$L_0\frac{\mathrm{i}_{L_0}^{n+1} - \mathrm{i}_{L_0}^{n}}{\Delta t} + \hat{\mathrm{e}}_0 - \hat{\mathrm{v}}_{\mathrm{mov}} = 0 \tag{5.3a}$$

$$\hat{\mathrm{i}}_{L_0} + \frac{\hat{\mathrm{v}}_{\mathrm{mov}} - \hat{\mathrm{e}}_0}{R_0} - C\frac{\mathrm{e}_0^{n+1} - \mathrm{e}_0^{n}}{\Delta t} - \hat{\mathrm{i}}_{A0}\left(\hat{\mathrm{e}}_0\right) - \hat{\mathrm{i}}_{L_1} - \frac{L_1}{R_1}\frac{\mathrm{i}_{L_1}^{n+1} - \mathrm{i}_{L_1}^{n}}{\Delta t} = 0 \tag{5.3b}$$

$$\hat{\mathrm{i}}_{L_1} + \frac{L_1}{R_1}\frac{\mathrm{i}_{L_1}^{n+1} - \mathrm{i}_{L_1}^{n}}{\Delta t} - \hat{\mathrm{i}}_{A1}\left(\hat{\mathrm{e}}_0 - L_1\frac{\mathrm{i}_{L_1}^{n+1} - \mathrm{i}_{L_1}^{n}}{\Delta t}\right) = 0\,, \tag{5.3c}$$

where the shorthand notation $\hat{\mathrm{v}} = \left(\mathrm{v}^{n+1} + \mathrm{v}^{n}\right)/2$ is used to denote averaged quantities in time. The set of equations (5.3) holds for a single MOV installed across the insulator of the corresponding phase conductor; in case of multiple MOVs, each device requires a single set of equations of the type (5.3). In (5.3), $\mathrm{v}_{\mathrm{mov}}$ is the voltage at the input terminals of the MOV; the current $\mathrm{i}_{\mathrm{mov}}$ at time $t = (n + 1/2)\,\Delta t$ entering into the MOV can be computed as the sum of the resistive and inductive currents flowing through R_0 and L_0:

$$\mathrm{i}_{\mathrm{mov}} = \hat{\mathrm{i}}_{L_0} + \frac{L_0}{R_0}\frac{\mathrm{i}_{L_0}^{n+1} - \mathrm{i}_{L_0}^{n}}{\Delta t}\,. \tag{5.4}$$

By application of the substitution theorem, the MOVs models are included into the main FDTD scheme for the MTL by means of ideal current sources $\boldsymbol{j}$ connected to the nodes $x = x_k$ where these devices are installed (in correspondence of the line towers). The set of equations (5.3) must be solved in conjunction with the MTL voltage equations at the k^{th} node where the arresters are installed; hence, (1.8b) in Chapter 1 is modified to include the vector of the MOVs current sources $\boldsymbol{j}$ (assuming $\mathbf{G}' = 0$):

$$\frac{\partial \boldsymbol{i}\,(x,t)}{\partial x} + \mathbf{C}'\frac{\partial \boldsymbol{v}\,(x,t)}{\partial t} + \delta\,(x - x_k)\,\boldsymbol{j} = 0 \tag{5.5}$$

where $\delta\,(x)$ is the Dirac delta function.

As illustrated in Fig. 5.4, displaying the case of an MTL with three phase conductors and two SWs, the vector of the current sources $\mathbf{j}_k$ (discretized in space and time) at the k^{th} node can be expressed as

$$\mathbf{j}_k = \begin{bmatrix} \mathrm{j}_{k,1} \\ \mathrm{j}_{k,2} \\ \mathrm{j}_{k,3} \\ \mathrm{j}_{k,4} \\ \mathrm{j}_{k,5} \end{bmatrix} = \begin{bmatrix} \mathrm{i}_{k,\mathrm{mov_A}} \\ \mathrm{i}_{k,\mathrm{mov_B}} \\ \mathrm{i}_{k,\mathrm{mov_C}} \\ G_{\mathrm{s1}}\,(\mathrm{v}_{k,4} - \mathrm{v}_{k,0}) \\ G_{\mathrm{s2}}\,(\mathrm{v}_{k,5} - \mathrm{v}_{k,0}) \end{bmatrix} = \begin{bmatrix} \mathbf{i}_{k,\mathrm{mov}} \\ G_{\mathrm{s1}}\,(\mathrm{v}_{k,4} - \mathrm{v}_{k,0}) \\ G_{\mathrm{s2}}\,(\mathrm{v}_{k,5} - \mathrm{v}_{k,0}) \end{bmatrix}, \tag{5.6}$$

where

$$\mathrm{v}_{k,0} = R_{\mathrm{g}} \sum_{m=1}^{5} \mathrm{j}_{k,m} \tag{5.7}$$

and $R_{\mathrm{g}} = G_{\mathrm{g}}^{-1}$ is the grounding resistance at the base of the tower. G_{s1} and G_{s2} are introduced to account for the conductances of the electrical connection of the SWs to the tower grounding system. Using a central difference combined with an average in time, the time-discrete equation (5.5) is written as in (5.8):

$$\left(\frac{\mathbf{I}_{k+\frac{1}{2}}^{n+1} - \mathbf{I}_{k-\frac{1}{2}}^{n+1}}{2} + \frac{\mathbf{I}_{k+\frac{1}{2}}^{n} - \mathbf{I}_{k-\frac{1}{2}}^{n}}{2}\right) + \mathbf{C}'\Delta x\left(\frac{\mathbf{V}_k^{n+1} - \mathbf{V}_k^{n}}{\Delta t}\right) + \hat{\mathbf{j}}_k = 0\,. \tag{5.8}$$

The nonlinear system must be solved in three unknowns for each MOV (namely, i_{L_0}, i_{L_1}, and e_0). In (5.8), the subscript k is added to $\hat{\mathbf{j}}$ in order to denote the specific vector of currents at the k^{th} node.

The nonlinear system in (5.3) is solved through the NEQNF IMSL subroutine [18], which uses a modified Powell hybrid algorithm and a finite-difference approximation to the Jacobian. A fourth-order extrapolation method is used to obtain an initial guess of the unknown variables at each time iteration. This resulted crucial to favour the convergence of the solver.

The exact procedure would require the solution of a matrix system of $N_{\mathrm{c}} \times (2N_{\Delta x} + 1)$ linear equations along with $3 \times N_{\mathrm{pc}} \times (N_{\mathrm{span}} + 1)$ nonlinear

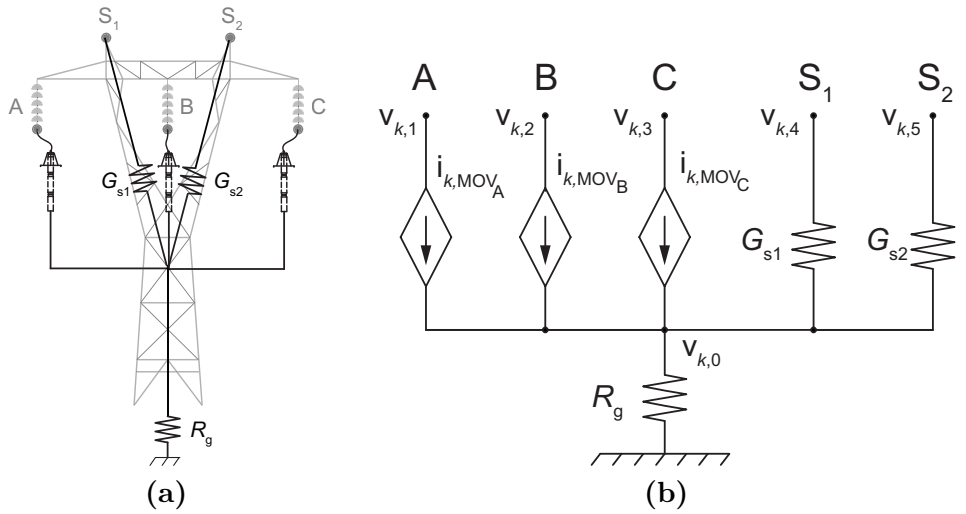

Figure 5.4. (a) Sketch of the line equipped with surge arresters. (b) Equivalent circuit adopted for the implementation in the FDTD code.

equations (which is the largest dimension allowed for the system, associated with configurations with three surge arresters installed at each tower)[2]. However, not every tower is expected to be equipped with surge arresters.

The inclusion of nonlinear elements reduces the problem to a system of nonlinear equations. Solving such systems is not trivial and, in fact, is much harder than solving systems of linear equations. In addition, the block tri-diagonal nature of the $\mathbf{A}$ matrix would be lost, along with the key advantages related to its storage and to the system solution.

A multiple step strategy is implemented to simplify the scheme and thereby reduce its computational cost. It consists of two steps. First, the original system of linear equations is solved in the unknowns $\mathbf{V}^{n+1}$ and $\mathbf{I}^{n+1}$ through the linear block tri-diagonal system of the type (1.23). The matrix $\mathbf{A}$ is left unchanged regardless the possible presence of surge arresters; this is done by introducing an approximation: the effect of the grounded SWs and MOVs currents is accounted through the vector $\mathbf{j}_k^n$ computed at the previous time step $t = n\Delta t$. The updated vectors of currents at $t = (n+1)\,\Delta t$ are used to solve the nonlinear equations (5.3) and (5.6), compute the MOVs variables, update vectors $\mathbf{V}_k^{n+1}$ at the specific voltage nodes identifying nodes at the towers, and derive the current generators $\mathbf{j}_k^{n+1}$ to be used at the successive time step. The implemented solving procedure proved to be stable, as shown in the next section.

[2]The quantity N_{span} denotes the number of spans of the line under study.

5.2 Numerical results

In the following, details will be given on the solution chosen as a protective measure for the studied TL; results computed by numerical simulations will be discussed.

5.2.1 Parameters setting

The chosen protective measure consists in line surge arresters, i.e., in polymer-housed surge devices to be installed in parallel to the protected insulators as a compact solution to limit overvoltages.

The studied line has a rated voltage equal to U_s =132 kV. The selection procedure proposed in [19] was followed to guide the selection of the ZnO surge arrester model PEXLIM P with U_r =120 kV [20]. In particular the arrester minimum rated voltge U_r was computed as $0.74 \cdot U_s$. If the value 650 kV is considered as the insulator withstand voltage (in a conservative approach), the average protection margin associated with the surge arrester intervention under lightning currents with a peak value of 10 kA would be approximately equal to the 138% of the arrester lightning impulse protection level ($\simeq 2.27 \cdot U_r$).

In Table 5.1 the main characteristics of the arrester are displayed, namely, its rated voltage U_r and maximum values of residual voltages $U_{r,max}$ at its terminations when 8/20 μs impulse current with peak value I_{peak} is injected.

Table 5.1. Characteristics of the PEXLIM P surge arrester as from the data sheet [20].

I_{peak} [kA]	$U_{r,max}$ [kV_{peak}]	$\hat{U}_{r,max}$ [kV_{peak}]	ΔU [%]
5	260	250.0	3.8
10	273	273.8	0.3
20	299	297.1	0.6
40	328	329.4	0.4
U_s	[kV]	132	
U_r	[kV]	120	

A first approximation of the values to be given to the resistive, inductive, and capacitive parameters is derived from known values of the MOV height h_{mov} [m] and number n of parallel columns [12]: $L_0 = 0.2\,h_{\text{mov}}/n$ [µH], $R_0 = 100\,h_{\text{mov}}/n$ [Ω], $L_1 = 15\,h_{\text{mov}}/n$ [µH], $R_1 = 65\,h_{\text{mov}}/n$ [Ω], $C = 100\,n/h_{\text{mov}}$ [pF].

The voltage–current characteristics of the two nonlinear varistors A_0 and A_1 have been represented by several analytical formulas or numerical models [12] determined from results of experimental investigations on arresters. These

characteristics show a typical power-law trend, the voltage being expressed in per unit of the MOV maximum residual voltage when draining a 10 kA, 8/20 μs impulse current.

As from the IEEE guidelines [12], values of the parameters must be optimized to reproduce the voltage–current characteristic of the MOV under analysis [21]. The Matlab optimization toolbox was used to obtain the best model parameters for the chosen MOV, i.e., the parameters which minimize the error between the maximum transient voltage obtained by feeding the circuit with 8/20 μs impulse currents with peak value equal to 5 kA, 10 kA, 20 kA, 40 kA, and the corresponding voltage values as from the data sheet (in Table 5.1). The objective function to be minimized was defined as the following root mean square deviation:

$$y = \sqrt{\sum_{k=1}^{4} \left(\hat{U}_{r,max_k} - U_{r,max_k} \right)^2} \tag{5.9}$$

where $k = 1 \dots 4$, U_{r,max_k} are the maximum residual voltages in Table 5.1, and $\hat{U}_{r,max_k}$ are the corresponding quantities estimated by means of the MOV circuit model with the set parameters. In Table 5.1, values $\hat{U}_{r,max_k}$ obtained as output of the calibrated circuit model, and the percentage variation with respect to the corresponding value U_{r,max_k} from the data sheet of the device are displayed. It is important to underline that different MOV parameters may be needed to adequately represent the response of the device with different current excitation (namely, presenting sensibly different time to peak and time to-half value).

The characteristics of the varistors A_0 and A_1 in Fig. 5.2 (in which the voltage values are normalised with respect to 273 kV, i.e., $U_{r,max}$ for 10 kA peak injected current), successively multiplied by factors $\kappa_0 = 1.1$ and $\kappa_1 = 1.5$, respectively, were adjusted through the Matlab optimization toolbox too. The values found for the electrical quantities required by the equivalent circuit are: $R_0 = 49.52\ \Omega$, $R_1 = 518.15\ \Omega$, $L_0 = 42.32$ pH, $L_1 = 47.55$ pH, $C = 9.96$ pF.

5.2.2 Results for an MTL equipped with MOVs

The direct lightning of the SW of the MTL in Fig. 5.5 (with rated voltage U_{r} =132 kV) will be simulated. Relevant geometrical features of the line and the conductors arrangement at the towers are displayed in Fig. 5.6: the line is composed of four conductors, three phase conductors and one SW. The phase conductors and SW radii are equal to 15.75 mm and 5.75 mm, respectively. The span length ℓ is equal to 300 m (within the typical range of span lengths adopted in Italy for high voltage TLs) and the overall length L of the line is assumed to be 9.3 km (namely, 31 spans). The line is closed at both terminations on the dense matrix of its resistive characteristic impedances (computed for the lossless case) [22]. The insulator gap length is $L_{ins} = 1.35$ m.

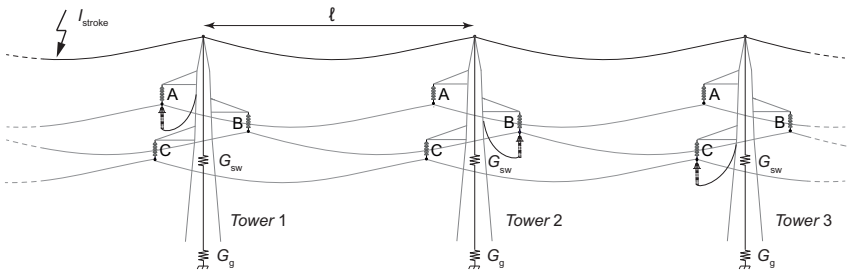

Figure 5.5. Configuration under study; one surge arrester is installed across the insulators of alternating phases at three consecutive towers.

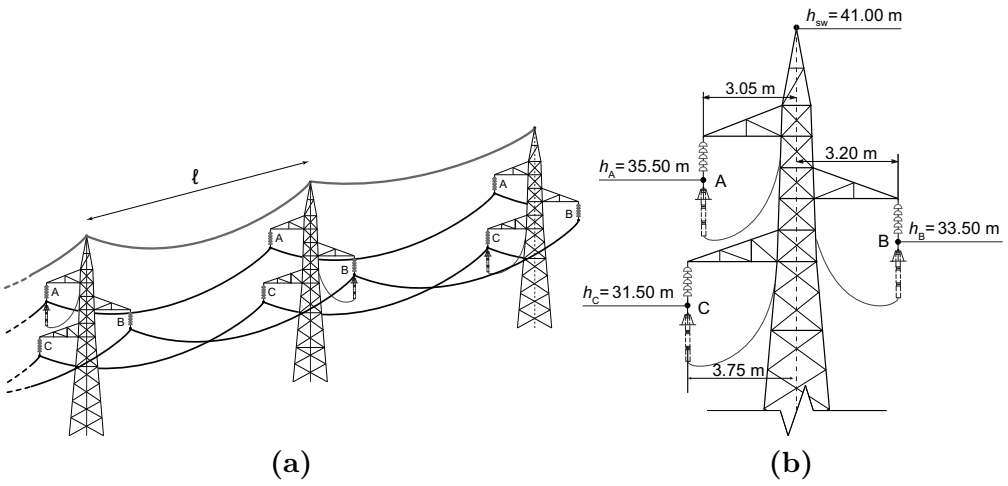

Figure 5.6. Typical Italian subtransmission line (rated voltage 132 kV). (a) Sketch (not according to scale) of the MTL, with one MOV installed across the insulators of alternating phases at three consecutive towers. (b) Conductors arrangement at the tower with three MOVs and main geometrical features.

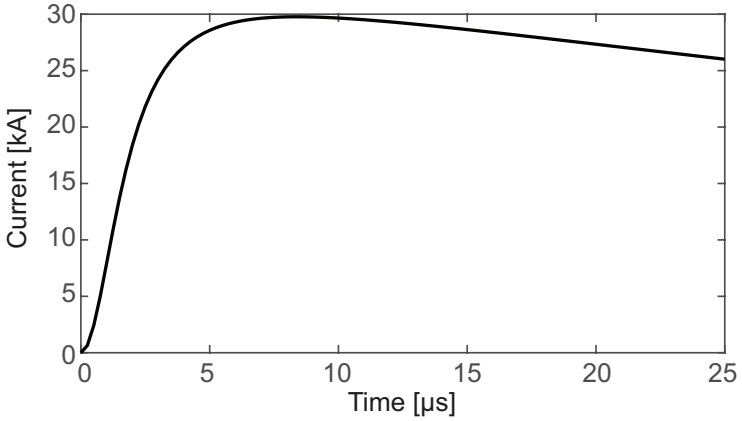

Figure 5.7. Waveform of the injected lightning current [24].

The SW can be grounded at poles as depicted in Fig. 5.5. In the real practice, efforts are made to keep the tower grounding resistance below 20 Ω; herein, the values $R_{\mathrm{g}} = 1/G_{\mathrm{g}} = 5\ \Omega$ or $10\ \Omega$ are used. The MOVs installed along the line are ABB PEXLIM P 120 kV. The tower (which may be modeled through several distributed parameters equivalent circuits [23]) and the surge arrester connections (which may be modeled through lumped equivalent resistive-inductive impedances) are not included in the simulations, as to draw attention solely on the contribution of the arresters.

The lightning stroke is assumed to hit the SW at distance $d = 4.650$ km from the MTL endpoints, in the middle of the central span. The lightning current is modelled as a single Heidler impulse (as in Sec. 3.3.5) with parameters $\tau_1 = 1.8\ \mu$s, $\tau_2 = 95\ \mu$s, $n = 2$, $I_{peak} = 28$ kA [24]. The waveform of the lightning current is shown in Fig. 5.7. Normal operation AC voltages are not taken into account.

Several different scenarios will be investigated:

Scenario *A*: Shield wire grounded only at tower 1; no MOVs installed along the line;

Scenario *B*: Shield wire grounded only at tower 1, where a single MOV is installed across the insulator of conductor A;

Scenario *C*: Shield wire grounded only at tower 1, where two MOVs are installed across the insulators of conductors A and B;

Scenario *D*: Shield wire grounded only at tower 1, where three MOVs are installed across the insulators of conductors A, B and C.

Scenario *E*: Shield wire grounded only at tower 1, 2, and 3; no MOVs are installed along the line;

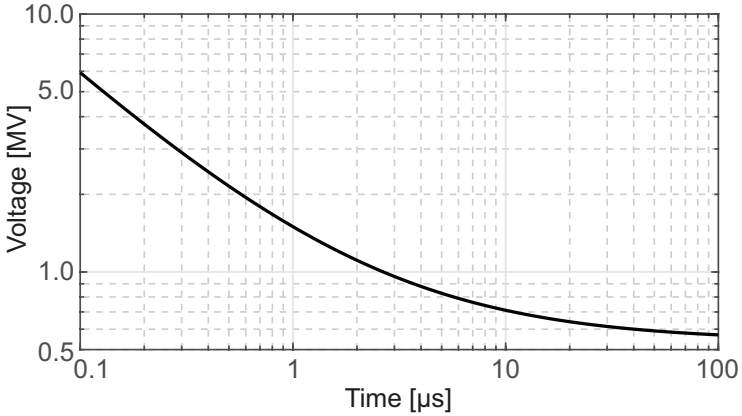

Figure 5.8. Volt-time characteristic of the insulators as in (5.10).

Scenario *F*: Shield wire grounded at towers 1, 2 and 3; MOVs are installed across the insulators of alternating phases of consecutive spans.

This simplified assumption, i.e., the single-point grounding of the SW, avoids multiple reflections among towers due to the periodic grounding and allows to better focus on the role played by the combination of protection practices, i.e., grounding of SW and MOVs.

Backflashover occurs when the voltage across the insulator string – i.e., the difference between the voltage of the tower, assumed equal to that of the SW (v_4), and the voltage of the phase conductor v_i with $i = 1, 2, 3$ – displays amplitude and time duration which are able to provoke a discharge along the insulator surface, hence, to cause an insulation failure. Indeed, the withstand voltage capability of insulator strings is higher under surge voltages and pulses of short duration, while it reduces for transient with longer duration. Without recurring to probabilistic approaches and statistical procedures, simulation results will be discussed in terms of the simplified expression of the volt-time characteristic for flashover modelling across insulators, as proposed in [25]:

$$V_{\mathrm{F}} = \left(400 + \frac{710}{t_{\mu\mathrm{s}}^{0.75}}\right) L_{ins}\,, \tag{5.10}$$

where V_{F} is the withstanding voltage expressed in kilovolt, L_{ins} is the length of the insulator string and $t_{\mu\mathrm{s}}$ is the time to flashover expressed in microseconds. The volt-time curve for the insulator of the considered 132 kV rated-voltage line is reported in Fig. 5.8.

As to the actual implementation, the line is discretized into segments with length $\Delta x = 3$ m, resulting into $N_{\Delta x} + 1$ voltage nodes (with $N_{\Delta x} = 3100$). The voltage centered equation at node $k = 1550$ of the line was modified to account for the injection of the lightning current, in the form of an ideal current generator; the voltage equation at nodes $k = 1600$, $k = 1700$, $k = 1800$ was modified according to (5.8) to account for the installed protective devices in the

aforementioned scenarios. The implementation rationale may be summarised as follows:

1. At time $t = 0$, the variables of the system are initialized (their value is set to zero).

2. The system (1.23) is solved accounting for the known excitation source and for the modification in (5.8), to get voltages and currents at time $t = \Delta t$.

3. If N_{MOV} denotes the number of protective devices installed at the k^{th} node of interest (with $0 \leq N_{\mathrm{MOV}} \leq 3$), a system of dimension $N_{\mathrm{c}} + 3N_{\mathrm{MOV}} + 1$ is solved at this node.
   The system includes $3N_{\mathrm{MOV}}$ equations for the installed MOVs (5.3), and N_{c} voltage centered equations in the matrix form (5.8); however, since the former equations are written in the unknown voltages at the MOVs' input terminals, an additional equation is written in the unknown ground potential $\mathrm{v}_{k,0}$:
   $$\mathrm{v}_{k,0} = R_{\mathrm{g}} \sum_{m=1}^{N_{\mathrm{c}}} \mathrm{j}_{k,m} \,. \tag{5.11}$$
   This additional equation accounts for the currents flowing to ground due to the intervention of the surge arresters and the grounding of the SWs at the corresponding towers. Consequently, the line voltages at node k, required by equations (5.8), are obtained as the series of two unknown voltage drops:
   $$\mathrm{v}_{k,m} = \begin{cases} \mathrm{v}_{k,0} + \mathrm{v}_{k,\mathrm{mov}_m} & \text{for } m = 1, \ldots, N_{\mathrm{pc}} \\ \mathrm{v}_{k,0} + G_{\mathrm{sw}}^{-1} \mathrm{j}_{k,m} & \text{for } m = N_{\mathrm{pc}} + 1, \ldots, N_{\mathrm{c}}. \end{cases} \tag{5.12}$$
   where $\mathrm{v}_{k,0}$, defined in (5.11), is the unknown voltage drop across the grounding resistance $R_{\mathrm{g}} = G_{\mathrm{g}}^{-1}$; the second term on the RHS of (5.12) for $m = N_{\mathrm{pc}} + 1, \ldots, N_{\mathrm{c}}$ is the voltage drop across the conductance representing the connection of the SWs to the grounding system; as to equations with $m = 1, \ldots, N_{\mathrm{pc}}$, if the insulator of phase m is not protected by a surge arrester, the unknown quantity $\mathrm{v}_{k,\mathrm{mov}_m}$ simply denotes an auxiliary variable, i.e., the difference between the phase conductor voltage and the ground potential at node k, and not the voltage drop across the terminals of an MOV. Analogously, the entries of the vector $\mathbf{j}_k$ are set to null value at nodes k within the spans, or when considering nodes coinciding with towers neither equipped with MOVs nor with grounded wires.
   The line currents are considered known, computed at the previous step. From the solution of these systems of equations, the elements of $\mathbf{j}_k$ and the line voltages at the corresponding nodes are updated, due to the possible intervention of the surge arresters.

4. The time step is updated and system (1.23) is solved accounting for the known excitation at the current time step, while the elements of the vector $\mathbf{j}_k$ are the ones found in step 3.

5. Step 3 and 4 are iterated for consecutive time steps to update the sought voltages and currents.

It should be noted that, at each time step $(n+1)\,\Delta t$, expression (5.8) is exploited twice. Indeed, it is first used as an equation of the block tri-diagonal solving system, assuming for the elements of vector $\hat{\mathbf{j}}_k$ to be known quantities (actually approximated to $\mathbf{j}_k^n$); the same equations are then solved again along with the MOVs' equations, considering the elements of $\hat{\mathbf{j}}$ as unknowns. The first step allows to estimate the line voltages and currents, while the second step allows to update the voltages at the nodes k where MOVs are installed, and the entries of $\mathbf{j}_k^{n+1}$ to be used as known quantities for the first stage of the following time step. The general working principle of the proposed algorithm is shown in Fig. 5.9.

The adopted approach, allowing to preserve the block tri-diagonal structure of the solving system (hence, its efficient solution), introduces a compromise: as to the implicit CN scheme, $\hat{\mathbf{j}}$ in (5.8) is computed at time $t = n\Delta t$ and not properly centered at time $t = (n + 1/2)\,\Delta t$, allowing an error of $\Delta t/2$.

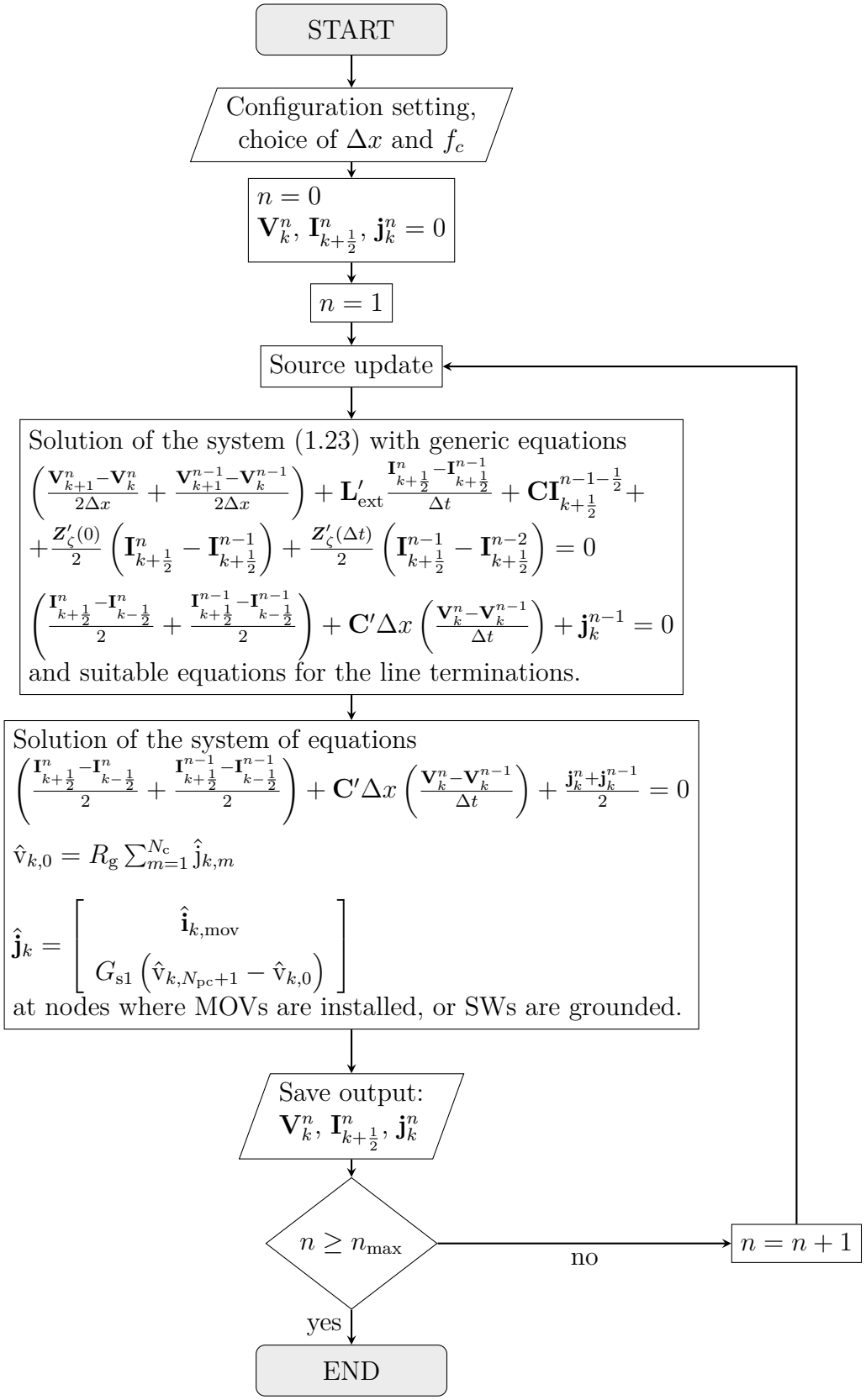

Figure 5.9. Working principle of the proposed advancing scheme, including the simulation of MOVs, and a single SW (simulation stop time: $t = n_{\max}\Delta t$).

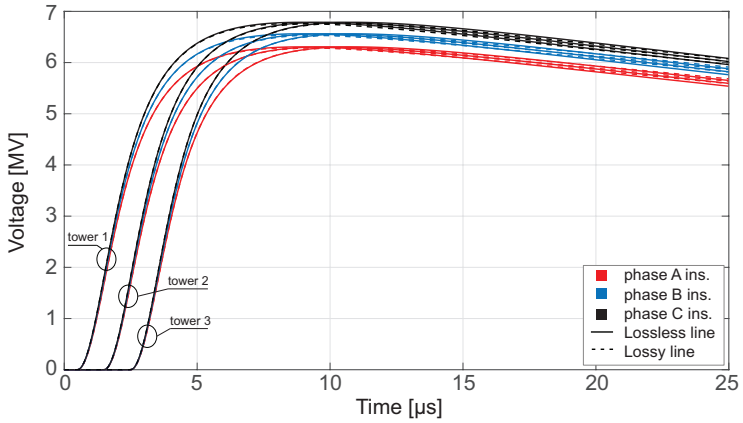

Figure 5.10. Voltage drop across the insulators at towers 1, 2, 3. The SW is not grounded and no MOVs are installed.

However, this approximation is accepted here, since, when dealing with nonlinear devices, small time steps are usually adopted, reducing the error deriving from the approximation.

Figure 5.10 shows the voltage drop across the insulators at towers 1, 2, 3 when the line is protected only by the SW, which, not being grounded, holds mainly its shielding purpose, without the advantages deriving from the grounding practice. Results are displayed for the lossless line, or considering the conductors and the ground transient impedances (with $\rho_g = 200$ Ωm, $\epsilon_{rg} = 10$), with a Courant factor $f_c = 1$, and space discretization step $\Delta x = 3$ m. In this case, which holds little practical interest, a direct stroke on the SW would cause an insulation failure.

The following results, including the connection of the SW to the tower grounding system ($G_{s1} = 50$ S), will take into account the two different constant values of the grounding resistance $R_g = 5$ Ω and $R_g = 10$ Ω. These values are coherent with the ones found for specific grounding system designs for subtransmission lines in Chapter 6, and ground resistivity lower than 200 Ωm. Suitable grounding systems, with different structures from the ones in Fig. 6.9, may be installed to easily get such values of R_g with the considered soil properties.

Scenario *A*

The SW is grounded only at tower 1, and no MOVs are installed along the line. The single point grounding of the SW allows to reduce the transient overvoltages across the insulators considerably (in Fig. 5.11); doubling the grounding resistance results in approximately doubling the peak value of the computed overvoltages (in Fig. 5.12).

Although the insulator overvoltages in the simulated case (i.e., with the chosen lightning current and values of R_g) are not high enough to cause

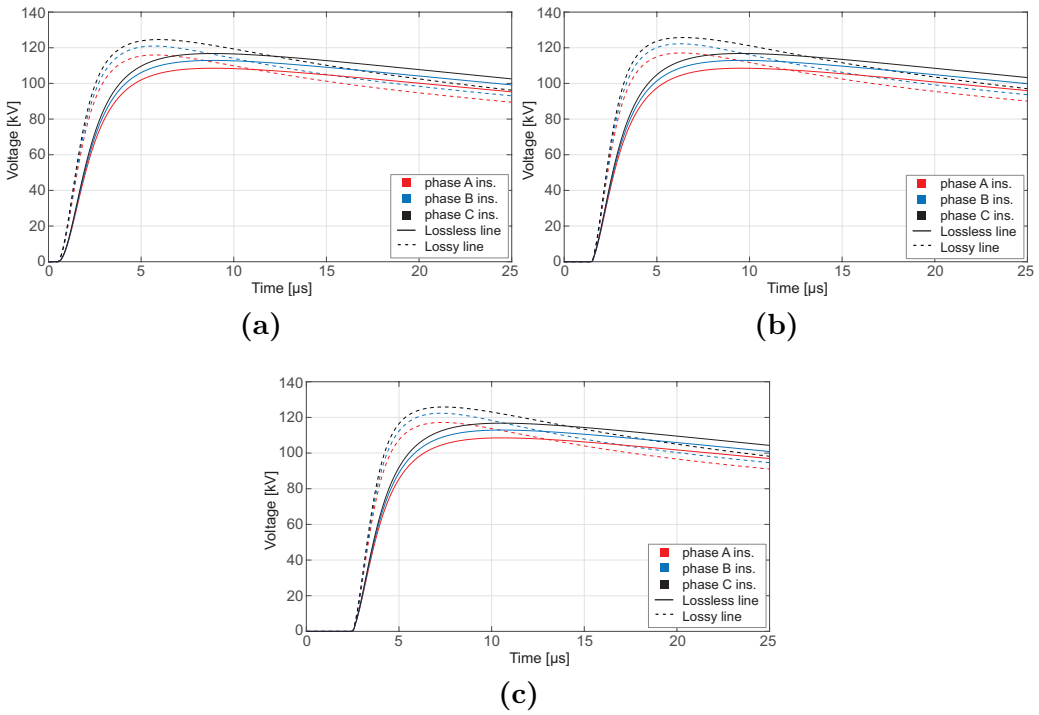

Figure 5.11. Voltage drop across the insulators in scenario *A*. The SW is grounded at tower 1 and $R_g = 5\ \Omega$. Voltages at tower 1 (a), tower 2 (b) and tower 3 (c).

insulation failures according to the proposed approach (with reference to Fig. 5.8), they are high enough for the MOVs to drain current, especially for the case $R_g = 10\ \Omega$.

Scenario *B*

The SW is grounded only at tower 1, where a single MOV is installed across the insulator of phase A. In Fig. 5.13, only the voltages computed at tower 1 and 3 are displayed for the readability of the figure.

When $R_g = 5\ \Omega$, the surge arrester's contribution is limited because of the effective mitigation effect of the SW grounding on the insulator voltages. The overvoltages are further limited below 100 kV by the conduction of the MOV installed across the insulator of phase A (Fig. 5.13a). In less favourable grounding conditions, with $R_g = 10\ \Omega$, the intervention of the MOV is clearly visible in Fig. 5.13b.

With reference to the overvoltages computed at the tower closest to the striking point (tower 1), the overvoltages across the insulators of phases B and C (with lossless line) are reduced only by the 2-3% with respect to results in Fig. 5.11, due to the limited contribution offered by the MOV with $R_g = 5\ \Omega$.

In Fig. 5.13b, with $R_g = 10\ \Omega$, a reduction in the range 7-8% is observed as to the voltages across the same insulators (phases B and C) with respect

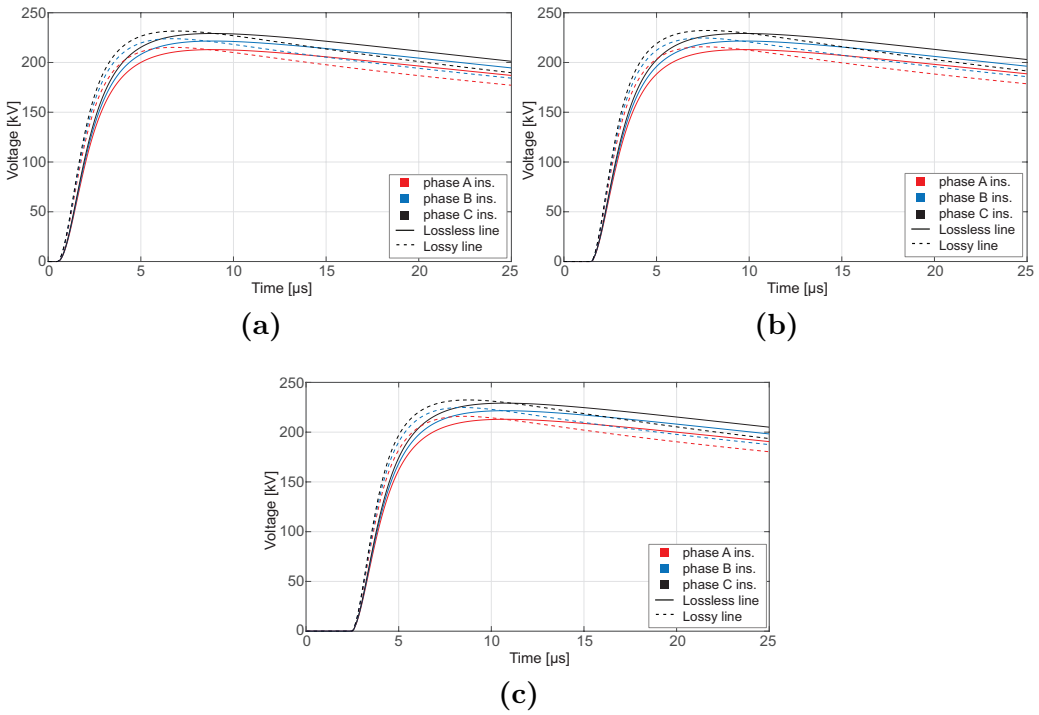

Figure 5.12. Voltage drop across the insulators in scenario *A*. The SW is grounded at tower 1 and $R_g = 10\ \Omega$. Voltages at tower 1 (a), tower 2 (b) and tower 3 (c).

to those computed in the lossless case in Fig. 5.12. Indeed, with an increased value of the grounding resistance, larger currents are drained by the installed MOV, increasing the voltage of phase A; the mutual coupling between the phases determines higher induced voltages on phases B and C, hence, reduced overvoltages across the corresponding insulators.

When the internal and the ground transient impedances terms are included in the simulation, voltages across the insulators reach higher peak values with increased steepness of the rising front, displaying an inductive behaviour contributed by these impedances.

Scenario *C*

The SW is grounded only at tower 1, where two MOVs are installed across the insulators of phases A and B. In Fig. 5.14, only the voltages computed at tower 1 and 3 are displayed for the readability of the figure.

As previously discussed in Sec. 5.2.2, the contribution due to the currents drained by the MOVs, in terms of induced voltages on phase C with an unprotected insulator, is limited for the case $R_g = 5\ \Omega$. In fact, with reference to the tower closest to the striking point (tower 1), the overvoltage across the insulators of phase C is reduced only by 5% with respect to results in Fig. 5.11, for the simulated cases of lossless and lossy line.

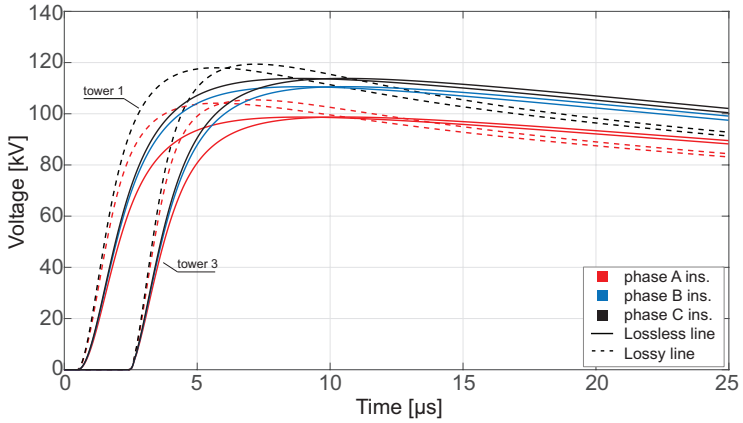

(a)

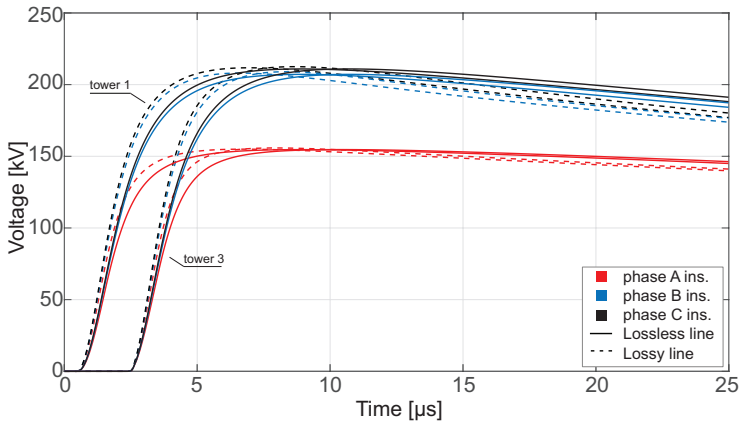

(b)

Figure 5.13. Voltage drop across the insulators at tower 1 and 3 in scenario *B*. The SW is grounded at tower 1 and a single MOV is installed across the insulator of phase A. (a) $R_g = 5\ \Omega$; (b) $R_g = 10\ \Omega$.

With $R_g = 10\ \Omega$, the mutual coupling of the SW, phases A and B (which are subjected to higher voltages due to the larger currents conducted by the MOVs) with phase C, determines the insulator voltage of the unprotected insulator to be reduced of 13% and 14% in the lossless and lossy case, respectively.

Peak voltages $V^{\mathrm{p}}_{\mathrm{ins},k}$ across the insulators of phase k (with k =A, B, C) for the lossless and lossy line cases are gathered in Table 5.2; values $\Delta V^{\mathrm{p}}_{\mathrm{ins},k}$, denoting the reduction of the peak voltages across the unprotected insulators in p.u. of the corresponding peak values obtained when no MOVs are installed, are also displayed in Table 5.2.

Scenario *D*

The SW is grounded only at tower 1, where three MOVs are installed across the insulators of phases A, B and C. In Fig. 5.15 only the voltages computed

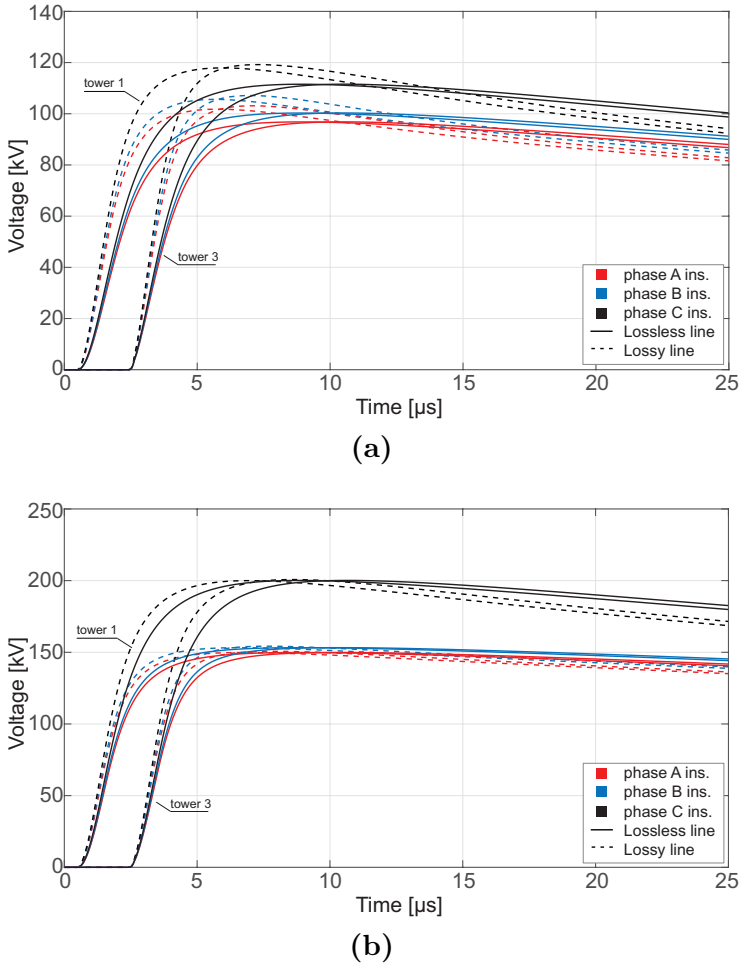

Figure 5.14. Voltage drop across the insulators at tower 1 and 3 in scenario *C*. The SW is grounded at tower 1, two MOVs are installed across the insulators of phase A and B. (a) $R_g = 5\ \Omega$; (b) $R_g = 10\ \Omega$.

at tower 1 and 3 are displayed for the readability of the figure.

Although all the insulators experience a noticeable reduction of the voltage across their terminals due to the conduction of the MOVs, the same pattern of the voltages is maintained: insulator A displays the lowest voltage, while the insulator corresponding to the phase farthest from the SW (i.e., phase C) is subjected to the highest electrical stress.

Scenario *E*

The SW is grounded at tower 1, 2, and 3 and no MOVs are installed along the line. Results of the overvoltages computed across the insulators at the different towers (for the cases of lossless and lossy line) are displayed in Fig. 5.16a and 5.16b, when the adopted grounding resistance value R_g is equal to 5 Ω and 10 Ω, respectively.

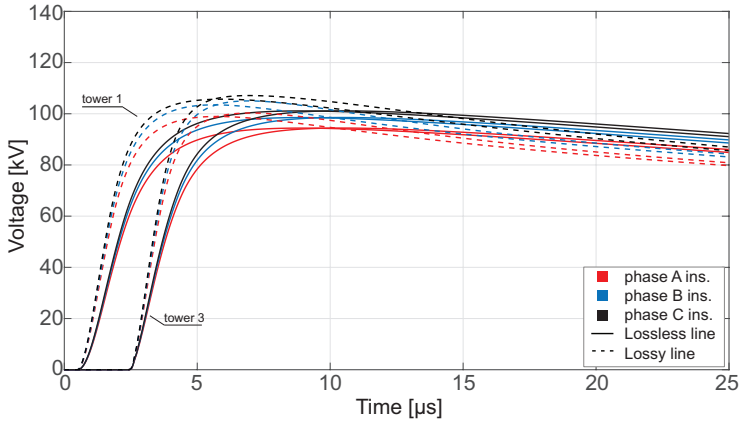

(a)

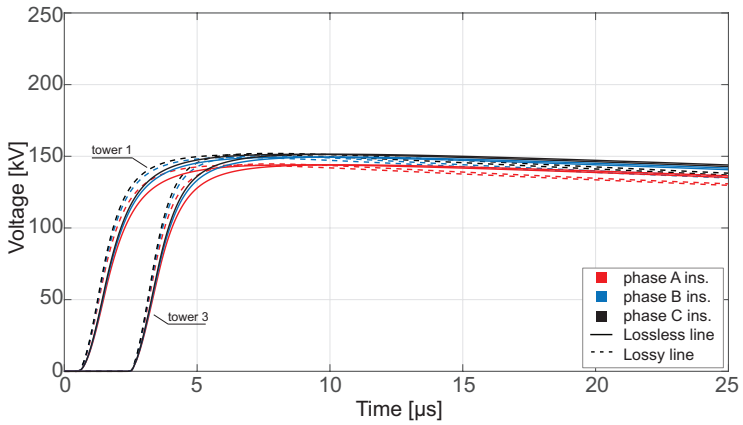

(b)

Figure 5.15. Voltage drop across the insulators at tower 1 and 3 in scenario D. The SW is grounded at tower 1, where all the insulators are equipped with an MOV. (a) $R_g = 5\ \Omega$; (b) $R_g = 10\ \Omega$.

The steepest rising fronts of the voltage are observed when losses are included; this is mainly due to the contribution of the impedance associated with the ground return path. However, the computed waveforms tails converge at late time, i.e., when the influence of the reactive component of the internal and ground transient impedances is reduced. Reflections from the line terminations are observed after approximately 28.5 μs at tower 3, and successively at tower 2 and 1, only in the lossy case, due to the mismatch between the frequency-dependent matrix of characteristic impedances of the lossy line, and the constant-valued matrix of resistive characteristic impedances, computed for the lossless line, adopted to model the line terminations.

With $R_g = 10\ \Omega$, focusing on tower 2, it can be noticed that the insulator overvoltages present an increasing trend before the first reflections from the line terminations reach the observed node of the line. This may be related to the reduced currents dispersed to ground, the consequent higher amplitude of

Table 5.2. Voltage reduction across the terminals of the insulators at tower 1 due to the intervention of MOVs in different scenarios.

		Lossless line				Lossy line			
Scen.		*A*	*B*	*C*	*D*	*A*	*B*	*C*	*D*
	k	$V^{\mathrm{p}}_{\mathrm{ins},k}$	$\Delta V^{\mathrm{p}}_{\mathrm{ins},k}$	$\Delta V^{\mathrm{p}}_{\mathrm{ins},k}$	$\Delta V^{\mathrm{p}}_{\mathrm{ins},k}$	$V^{\mathrm{p}}_{\mathrm{ins},k}$	$\Delta V^{\mathrm{p}}_{\mathrm{ins},k}$	$\Delta V^{\mathrm{p}}_{\mathrm{ins},k}$	$\Delta V^{\mathrm{p}}_{\mathrm{ins},k}$
	-	[kV]	[p.u.]	[p.u.]	[p.u.]	[kV]	[p.u.]	[p.u.]	[p.u.]
$R_{\mathrm{g}}=5\ \Omega$	A	108.5	0.09	0.11	0.13	115.9	0.10	0.12	0.15
	B	112.9	0.02	0.11	0.13	121.0	0.02	0.13	0.14
	C	116.8	0.03	0.05	0.13	124.6	0.03	0.05	0.15
$R_{\mathrm{g}}=10\ \Omega$	A	212.9	0.27	0.30	0.32	215.2	0.28	0.30	0.33
	B	221.5	0.07	0.31	0.33	223.9	0.07	0.32	0.33
	C	229.1	0.08	0.13	0.34	231.6	0.09	0.14	0.35

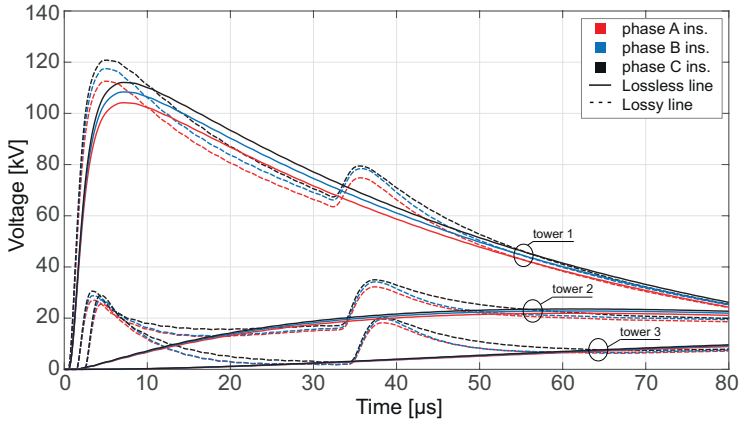

(a)

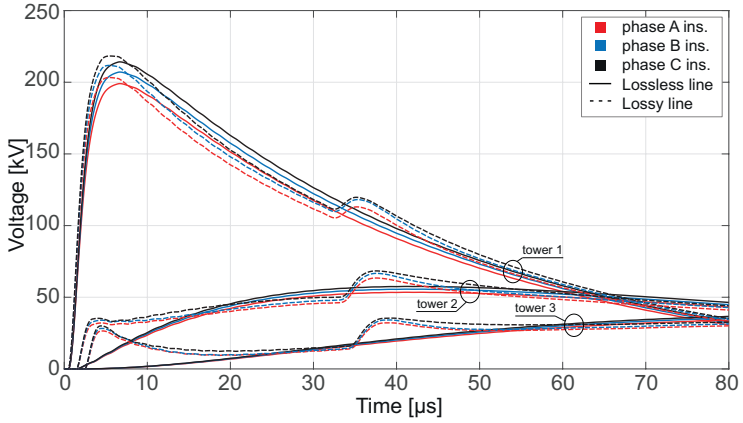

(b)

Figure 5.16. Voltage drop across the insulators in scenario *E*. The SW is grounded at tower 1, 2, and 3, where no MOVs are installed. (a) $R_{\mathrm{g}} = 5\ \Omega$; (b) $R_{\mathrm{g}} = 10\ \Omega$.

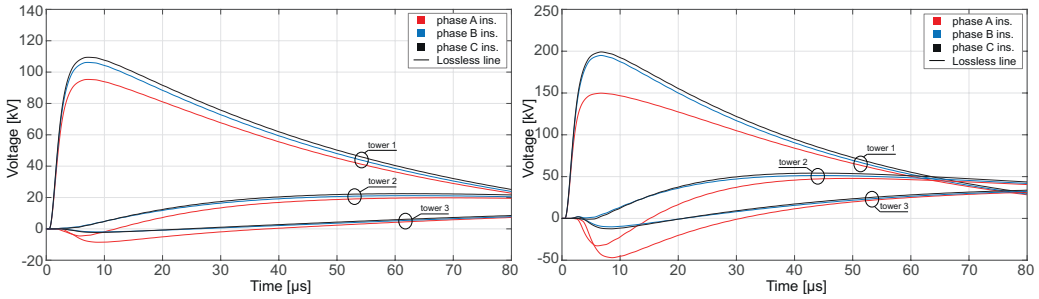

(a) (b)

Figure 5.17. Voltage drop across the insulators for scenario *F* (lossless line). The SW is grounded at tower 1, 2, and 3, where a single MOV is installed across the insulator of alternating phases of consecutive spans. (a) $R_g = 5\ \Omega$; (b) $R_g = 10\ \Omega$.

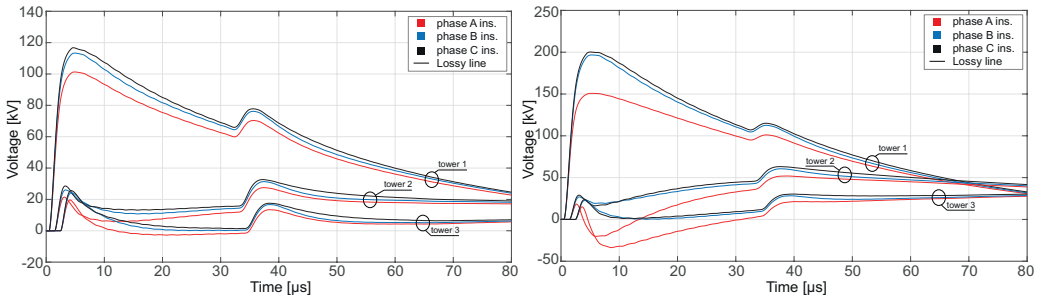

(a) (b)

Figure 5.18. Voltage drop across the insulators for scenario *F* (lossy line). The SW is grounded at tower 1, 2, and 3,where a single MOV is installed across the insulator of alternating phases of consecutive spans. (a) $R_g = 5\ \Omega$; (b) $R_g = 10\ \Omega$.

the voltage wave travelling along the SW, and its higher steepness with respect to the case with $R_g = 5\ \Omega$.

Scenario *F*

The SW is grounded at towers 1, 2 and 3; MOVs are installed across the insulators of alternating phases of consecutive spans (i.e., a single MOV across the insulator of phase A at tower 1, one MOV across the insulator of phase B at tower 2, and one MOV across the insulator of phase C at tower 3).

At tower 1, the closest to the struck point, the computed waveforms in Figs. 5.17 and 5.18 are comparable to results in Figs. 5.13, obtained in scenario *B*. Differences in the peak values of the overvoltages are due to reflections from subsequent grounded towers, which are located close enough to tower

1 to display reflected waves already after few microseconds (i.e., before the insulator voltages at tower 1 reach their peak value).

Nevertheless, voltages at towers 2 and 3 display a different waveshape. In order to address the physical reason underlying this voltage pattern, the lossless case with $R_g = 10\ \Omega$ will be analysed as a reference. At tower 1, a current is injected through the MOV from the SW to conductor A, increasing its voltage and allowing to reduce the stress across the corresponding insulator. However, due to the additional grounding points, the magnitude and steepness of the SW voltage observed at tower 2 and 3 present smaller magnitude and lower steepness with respect to the travelling voltage wave on the phases: hence, the reversed polarity of the insulator voltages observed in Fig. 5.17b. It should be noted that the installed MOVs at towers 2 and 3 hold minor influence due to the lower peak values reached by the corresponding overvoltages at the insulators of phases B and C[3].

To clarify this point, Fig. 5.19 displays the voltages of the four line conductors when the SW is grounded at towers 1, 2 and 3 and MOVs are in place (scenario *F*, lossless case, $R_g = 10\ \Omega$). The observed increase in the amplitude of the voltage wave travelling along phase A (due to the current discharged through the MOV at tower 1) and the reduced SW voltage at towers 2 and 3 determine the polarity reversal of voltages across the insulator at early times.

The latter example is employed to further illustrate two aspects: the increased voltages computed on the unprotected phases at tower 1 when the MOVs are in place (this phenomenon has been already discussed with reference to scenario *B*); the weak oscillations in the inset of Fig. 5.19a, which displays a portion of the SW voltage at tower 1. These oscillations are due to reflected waves propagating backwards from the adjacent grounding points at towers 2 and 3 (as confirmed by the period of occurrence, approximately equal to 2 μs).

[3]No reversal in the overvoltages polarity was observed in scenario *B* due to the absence of multiple grounding points at the towers, hence, of any further reduction of the SW voltage at towers 2 and 3.

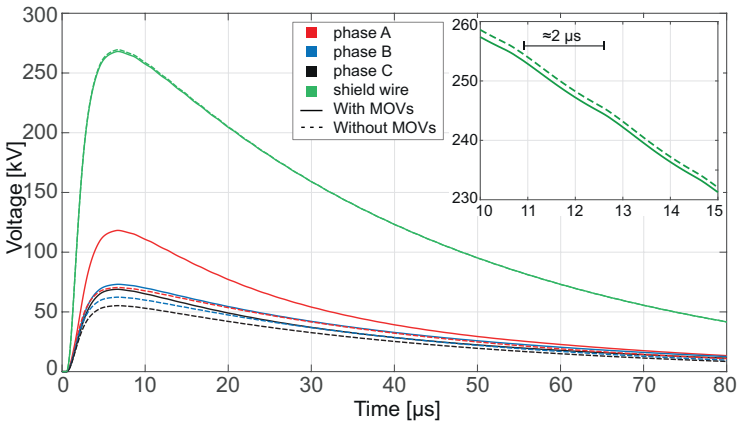

(a) Voltages - Tower 1

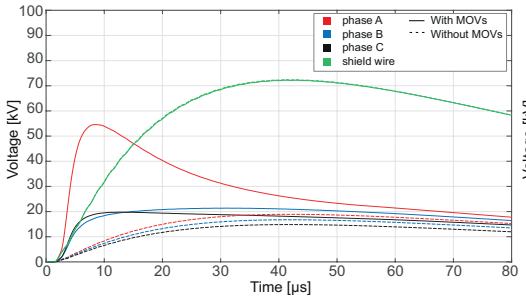

(b) Voltages - Tower 2

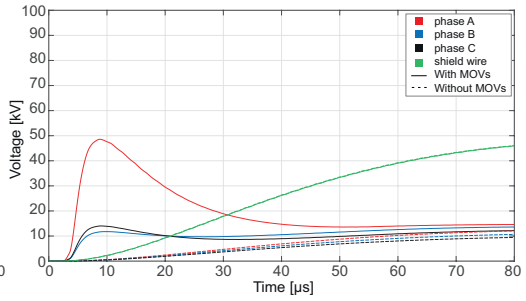

(c) Voltages - Tower 3

Figure 5.19. Voltages-to-ground of the line conductors in scenario F, in the lossless line case with $R_g = 10\ \Omega$. The SW is grounded at tower 1, 2, and 3, where the insulators of phases A, B and C, respectively, are equipped with an MOV.

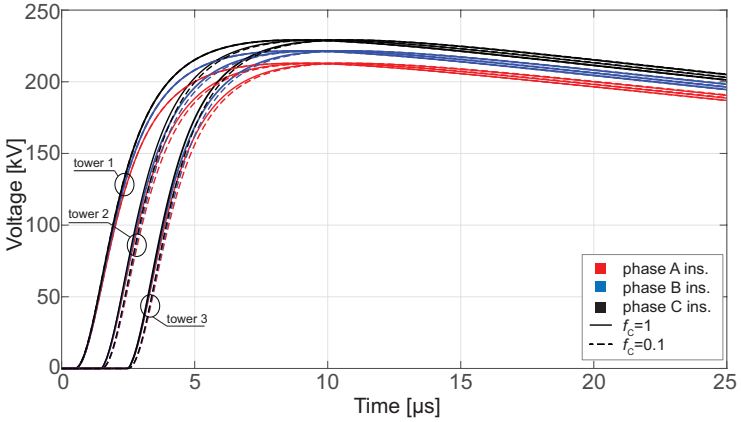

Figure 5.20. Comparison of insulator voltages (scenario A, $R_g = 10\ \Omega$, lossless line) computed with $f_c = 1$ and $f_c = 0.1$.

Remarks

In the previous sections, the value $f_c = 1$ was adopted as a compromise between accuracy and running time of the implicit algorithm. Figure 5.20 displays a comparison between results presented in 5.2.2 (scenario A, $R_g = 10\ \Omega$, lossless line) and those derived with $f_c = 0.1$.

Slightly different results are obtained as to the rising portion of the overvoltages, when the smallest Courant factor is selected (the running time being increased by 10 times as a drawback); this is due to numerical dispersion, and to the half a time step delay introduced by the adopted approach between the perturbation (here, the SW grounding) and the solution of the standard equations of the updating scheme. However, the deviation in the predicted peak voltages is negligible. Once a suitable time step has been selected, the scheme lends itself to solving a large number of simulations (e.g., when performing worst case analyses, insulation coordination studies, etc.), and to easily changing the simulation parameters in the same simulation environment through simple input text files.

As a final remark, it should be noted that the lossless case is not cautionary. In fact, losses are responsible for increasing the amplitude of the insulator voltages at the pole closest to the lightning striking point, whether or not the insulator strings are protected by a line surge arrester.

Future studies should account for the energy capability of the installed arresters and for the statistical distribution of the peak value and front time of the lightning current waveform.

5.3 Soil ionization: concentrated grounding systems

As to the simulation of concentrated grounding systems, an empirical approach was made available by Cigré [26] to model soil ionization as a lumped nonlinearity, which may occur when intense current densities injected into the ground cause an enhancement of the local electric field (Appendix C). The model proposed by the Cigré Working Group is based on experimental data by Berger, further interpreted by Wreck and Oettlé. An expression is given for the current-dependent grounding resistance of a hemispherical electrode, as ionization occurs [1]:

$$R(I) = R_0\sqrt{\frac{I_g}{I}}\,. \tag{5.13}$$

In (5.13), I is the current injected into the hemispherical electrode of radius r_0; R_0 is the grounding resistance in the absence of soil ionization; I_g is the critical current injected into the electrode, producing an electric field on the electrode surface equal to the ionization gradient E_g. Indeed, for configurations with

hemispherical electrodes, the critical current I_g may be computed as:

$$I_g = \frac{2\pi r_0^2 E_g}{\rho_0} = \frac{E_g \rho_0}{2\pi R_0^2}\,, \tag{5.14}$$

where ρ_0 is the soil electrical resistivity in the absence of ionization (Appendix C).

A modification of (5.13) is proposed for short rods, with leading dimension smaller than approximately 30 m, with length ℓ and radius a:

$$R\,(I) = \frac{R_0}{\sqrt{1 + (I/I_g)}} \tag{5.15}$$

This modification allows to account for the initial decrease of the grounding resistance due to the soil ionization in the proximity of the rod, and subsequent approximation of the ionized area to an hemisphere (in fact, expression (5.15) converges to the one for hemispherical electrode (5.13) when $I \gg I_g$). The second expression given on the RHS of (5.14) is used to estimate the value of the critical current I_g for rod electrodes as well.

An alternative approach was proposed by Liew *et al.* [4] consisting in evaluating the impulse resistance of the grounding system as the series of resistances offered by soil layers with thickness dr, i.e., as an integral summation of the type[4]:

$$R\,(t, I) = \int_a^\infty \frac{\rho_g\,(t, J\,(t, r))}{2\pi r} \frac{1}{\ell + r} \mathrm{d}r\,. \tag{5.16}$$

The time- and current-dependent resistivity $\rho_g\,(t, J\,(t, r))$ is computed according to the expressions in (C.1), evaluating the current density at radial distance r from the rod axis as

$$J\,(t, r) = \frac{I\,(t)}{2\pi r\,(\ell + r)}\,. \tag{5.17}$$

Depending on the computed current density, each soil layer displays a different value of resistivity, contributing to the value of the total impulse grounding resistance. Closed form expressions to compute the current density in the vicinity of two, three, and four rods grounding configurations are given in the Appendix of [4].

[4]The quantity r is to be intended as from Fig. 5.21.

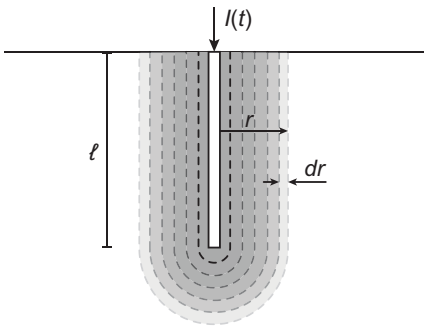

Figure 5.21. Reference configuration for the application of the method of circular potentials by Liew *et al.*

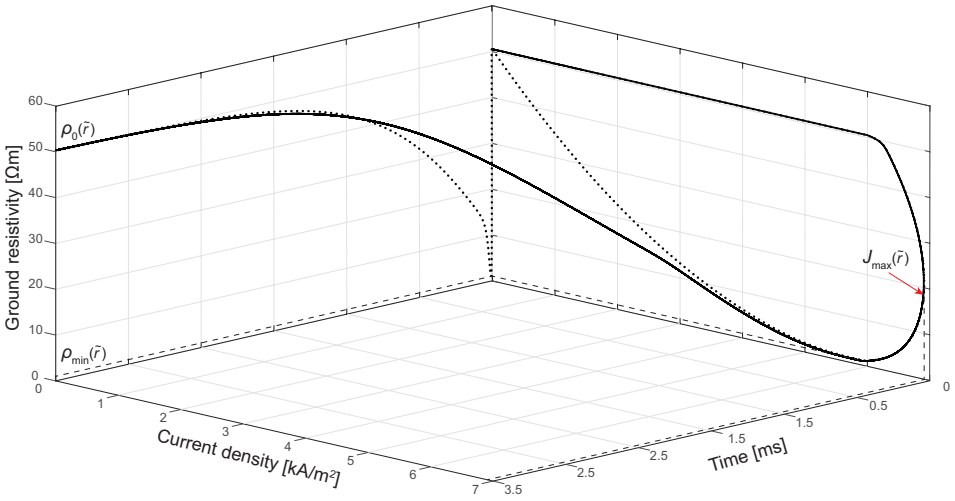

Figure 5.22. Ground resistivity associated with an elementary soil layer at radial distance $\tilde{r} = 13.2$ cm from the axis of the rod in Fig. 5.21 as a function of time and current density.

5.3.1 Simulated arrangement

In order to clarify the impact of soil ionization on the computed value of grounding resistance associated with a grounding system, a simple configuration will be considered.

The impulse grounding resistance offered by a concentrated grounding system, i.e., the single rod in Fig. 5.21 with length $\ell = 1.83$ m and radius $a = 12.7$ mm, is computed by the Cigré formula (5.15) and by implementing the circular equipotentials method by Liew *et al.*

As to the latter method, the soil surrounding the rod has been discretized into layers (Fig. 5.21) with thickness $\mathrm{d}r = 1$ mm from the rod external surface up to a radial distance $r_{\max} = 50 \cdot a$ (large enough not to expect ionization to occur at $r_{\max}$). The thickness $\mathrm{d}r$ of the discretization layers was chosen to keep the relative error of the computed grounding resistance below the 1% of the resistance R_0, derived by the closed expression (5.18) in the absence of

Table 5.3. Lightning current parameters [27].

k	$I_{peak,k}$ [kA]	n_k	τ_{1k} [μs]	τ_{2k} [μs]
1	7.5	55	1.1	15
2	5.0	2	1.2	500

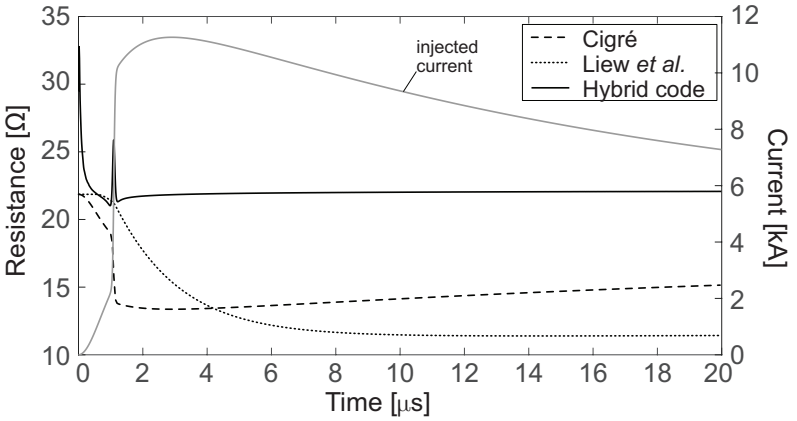

Figure 5.23. Injected current waveform, and transient resistances computed accounting for the frequency-dependent response of the rod in Fig. 5.21, and for the soil ionization models by Cigré and Liew *et al.*

ionization [4]:

$$R_0 = \frac{\rho_0}{2\pi\ell} \ln\left(\frac{a+\ell}{a}\right) . \tag{5.18}$$

The contribution of the soil extending from $r_{\max}$ to infinity was accounted by means of (5.18), replacing a with $r_{\max}$.

The soil electrical resistivity and relative permittivity in the absence of ionization are set as $\rho_0 = 50.5$ Ωm, and $\epsilon_r = 10$. The current injected into the rod is given by the superposition of two Heidler's functions (as from Sec. 3.3.5), with parameters in Table 5.3 [27], and peak value equal to 11.3 kA.

For illustration purposes, the trend of the ground resistivity associated with an elementary soil layer at radial distance $\tilde{r} = 13.2$ cm from the rod axis is shown in Fig. 5.22 as a function of time and current density. The projection of the tridimensional curve on the ρ_g–J plane recalls the sketch in Fig. C.1 of Appendix C. The minimum soil resistivity $\rho_{\min}(\tilde{r})$ and maximum current density $J_{\max}(\tilde{r})$ are indicated too.

Figure 5.23 displays, along with the injected current $I(t)$, the time-dependent resistance accounting for the frequency-dependent response of the rod[5] (computing $R(t)$ as the ratio of the IFT of the GPR –originally derived in the FD–

[5]The response of the rod in the FD is derived by the application of the hybrid method in Appendix B.

over the injected current in the TD[6]), implementing the Cigré soil ionization model, and Liew *et al.* soil ionization model, respectively. It should be noted that the GPR associated with this time-dependent resistance is not rigourously defined; indeed, it is associated with the simple product between the injected current and $R(t)$ (strictly related to the waveform of the injected current), and not to their convolution in the TD.

The low frequency grounding resistance R_0^{HC} computed at 100 Hz by means of the hybrid code in Appendix B (the rod being discretized into branches with length 2.5 cm) is equal to 22.1 Ω. The same quantity, derived by using expression (5.18) $R_0 = 21.9$ Ω, was adopted to implement the Cigré model, along with a critical electric field $E_g = 400$ kV/m as suggested by the Cigré Guidelines. As to the Liew *et al.* model, the following values of the characteristic time constants and critical electric field were adopted [4]: $t_1 = 2$ μs, $t_2 = 4.5$ μs, $E_g = 300$ kV/m.

Comparison of the time-dependent grounding resistances obtained by modelling the grounding system by means of its frequency-dependent response, or by including the effect of soil ionization (as from the Cigré model, or by implementing Liew *et al.* approach) clarifies that the soil ionization deserves further investigation, being its influence non-negligible. Indeed, when soil ionization is simulated, the value of the time-dependent resistance drops, reaching minimum values in a range between the 50% and the 60% of $R_0 \simeq 22$ Ω; hence, reduced GPRs are expected with respect to the ones computed accounting only for the rod frequency response.

[6]The adopted definition of grounding impedance is introduced in Chapter 6, with reference to expression (6.2). It should be noticed that the value of resistance is not well-defined at $t = 0$; hence, the corresponding indeterminate value is excluded from the corresponding curve displayed in Fig. 5.23.

References

[1] A. R. Hileman, *Insulation Coordination for Power Systems*, C. Press, Ed., 1999.

[2] "IEEE guide for safety in AC substation grounding," *IEEE Std 80-2013 (Revision of IEEE Std 80-2000/ Incorporates IEEE Std 80-2013/Cor 1-2015)*, pp. 1–226, 2015.

[3] Z. G. Datsios, P. N. Mikropoulos, E. T. Staikos, T. E. Tsovilis, D. Vlachopoulos, and S. Ganatsios, "Laboratory measurement of the impulse characteristics of wet sand," in *2020 IEEE International Conference on Environment and Electrical Engineering and 2020 IEEE Industrial and Commercial Power Systems Europe (EEEIC/I&CPS Europe)*. IEEE, 2020, pp. 1–6.

[4] A. Liew and M. Darveniza, "Dynamic model of impulse characteristics of concentrated earths," in *Proceedings of the Institution of electrical Engineers*, vol. 121, no. 2. IET, 1974, pp. 123–135.

[5] P. Meng, C. Yuan, H. Xu, S. Wan, Q. Xie, J. He, H. Zhao, J. Hu, and J. He, "Improving the protective effect of surge arresters by optimizing the electrical property of ZnO varistors," *Electr. Power Syst. Res.*, vol. 178, p. 106041, 2020.

[6] G. V. S. Rocha, R. P. d. S. Barradas, J. R. S. Muniz, U. H. Bezerra, I. M. d. Araújo, D. d. S. A. d. Costa, A. C. d. Silva, M. V. A. Nunes, and J. S. e. Silva, "Optimized surge arrester allocation based on genetic algorithm and atp simulation in electric distribution systems," *Energies*, vol. 12, no. 21, 4110, 2019.

[7] P. Mestas and M. C. Tavares, "Comparative analysis of techniques for control of switching overvoltages during transmission lines energization," *Electric Power Systems Research*, vol. 80, no. 1, pp. 115 – 120, 2010.

[8] N. A. Latiff, H. A. Illias, A. H. Bakar, and S. Z. Dabbak, "Measurement and modelling of leakage current behaviour in ZnO surge arresters under various applied voltage amplitudes and pollution conditions," *Energies*, vol. 11, no. 4, 875, 2018.

[9] J. He, *Metal oxide varistors*. Wiley-VCH Verlag GmbH & Co. KGaA, 2019.

[10] S. Yokoyama and A. Asakawa, "Experimental study of response of power distribution lines to direct lightning hits," *IEEE Trans. Power Del.*, vol. 4, no. 4, pp. 2242–2248, Oct. 1989.

[11] V. S. Brito, G. R. S. Lira, E. G. Costa, and M. J. A. Maia, "A wide-range model for metal-oxide surge arrester," *IEEE Trans. Power Del.*, vol. 33, no. 1, pp. 102–109, Feb. 2018.

[12] IEEE Working Group 3.4.11, "Modeling of metal oxide surge arresters," *IEEE Trans. Power Del.*, vol. 7, no. 1, pp. 302–309, Jan. 1992.

[13] P. Pinceti and M. Giannettoni, "A simplified model for zinc oxide surge arresters," *IEEE Trans. Power Del.*, vol. 14, no. 2, pp. 393–398, Apr. 1999.

[14] P. Valsalal, K. Udayakumar *et al.*, "Modelling of metal oxide arrester for very fast transients," *IET science, measurement & technology*, vol. 5, no. 4, pp. 140–146, 2011.

[15] F. Fernandez and R. Diaz, "Metal oxide surge arrester model for fast transient simulations," in *Proc. of the International Conference on Power System Transients*, vol. 1. Citeseer, 2001, pp. 144–149.

[16] E. Stracqualursi, R. Araneo, G. Lovat, A. Andreotti, P. Burghignoli, J. A. Brandão Faria, and S. Celozzi, "Analysis of metal oxide varistor arresters for protection of multiconductor transmission lines using unconditionally-stable Crank-Nicolson FDTD," *Energies*, vol. 13, no. 8, 2112, Apr. 2020.

[17] K. Raju and V. Prasad, "Modelling and validation of metal oxide surge arrester for very fast transients," *High Voltage*, vol. 3, pp. 147–153, 2018.

[18] Visual Numerics, "IMSL Fortran numerical library user's guide, version 7.0," 2010.

[19] ABB Buyer's Guide, "High voltage surge arresters," *Edition*, vol. 5, pp. 1–132, 2019.

[20] "High-Voltage surge arresters - Buyer's guide," https://library.e.abb.com/public/98c0666e9d3aa82ac1257b130057b790/Surge%20Arrester%20Buyers%20Guide%20Ed51%20-%20Section%20PEXLIM%20P.pdf, (accessed Oct. 2022).

[21] C. A. Christodoulou, V. Vita, G. Perantzakis, L. Ekonomou, and G. Milushev, "Adjusting the parameters of metal oxide gapless surge arresters' equivalent circuits using the harmony search method," *Energies*, vol. 10, no. 12, 2168, 2017.

[22] C. R. Paul, *Analysis of Multiconductor Transmission Lines.* John Wiley and Sons, 2008.

[23] E. Stracqualursi, G. Pelliccione, S. Celozzi, and R. Araneo, "Tower models for power systems transients: a review," *Energies*, vol. 15, no. 13, 4893, Jul. 2022.

[24] F. Rachidi, W. Janischewskyj, A. M. Hussein, C. A. Nucci, S. Guerrieri, B. Kordi, and J.-S. Chang, "Current and electromagnetic field associated with lightning-return strokes to tall towers," *IEEE Trans. Electromagn. Compat.*, vol. 43, no. 3, pp. 356–367, 2001.

[25] P. Chowdhuri, A. Baker, G. Carrara, W. Chisholm, K. Feser, S. Grzybowski, A. Lux, and F. Newnam, "Review of research on nonstandard lightning voltage waves," *IEEE Trans. Power Del.*, vol. 9, no. 4, pp. 1972–1981, 1994.

[26] *CIGRE Technical Brochure 63: Guide to procedures for estimating the lightning performance of trasmission lines*, CIGRE Std., 1991.

[27] W. R. Gamerota, J. O. Elismé, M. A. Uman, and V. A. Rakov, "Current waveforms for lightning simulation," *IEEE Trans. Electromagn. Compat.*, vol. 54, no. 4, pp. 880–888, Aug. 2012.

Chapter 6

Frequency and transient response of actual grounding systems

Transient response of grounding systems to lightning or fault currents is fundamental for insulation coordination and safety purposes. This chapter concerns the computation of the harmonic impedance of grounding grids and systems in the FD by means of a hybrid code [1], which is based on EM field theory in layered media and a circuital approach (detailed in Appendix B).

The proper design of grounding grids is essential for operation of electrical systems and management of failures, which may threaten people safety and devices integrity. The grounding resistance should be designed to guarantee safety conditions through a limited GPR, admissible step and touch voltages, and coordination with the installed protection devices. Despite sizing the grounding system based on the prediction of the maximum ground fault current at industrial frequency, a noticeably larger impulse GPR may occur under fast transient surges due to the reactive behaviour of the grounding system, which is not taken into account in fault analysis. Hence, functioning and integrity of electrical equipment (even protection devices, e.g., surge arresters) may not be guaranteed.

In the literature, several different approaches have been proposed to model the frequency response of grounding systems. The most widespread approaches include modelling by lumped RLC circuits (computing the values of resistance, inductance, and capacitance from the geometrical features of the conductors and from the soil electrical properties [2], [3]), and TL equivalent circuits (assuming TEM propagation in the soil half-space [4]); codes implementing the finite element method [5], the Hybrid Electromagnetic Model (adopted here) [6]-[7], the Partial Element Equivalent Circuit [8], and alternative simplified pi-circuit approaches with parameters optimization [9] may be exploited as well to simulate the frequency behaviour of buried grounding systems.

The frequency behaviour and transient behaviour of grounding systems have

been addressed with reference to typical configurations of ground electrodes (i.e., vertical rod, horizontal electrode, ring) primarily by Grcev [10], [11], [12] who recently applied his electromagnetic model to large systems buried in a multilayered soil [13]. However, the constant resistance approach, modelling the grounding impedance as a frequency independent resistance computed at power frequency, is still frequently adopted in propagation studies along TLs as a conservative modelling approach [14]. Most results in the literature are related to grids, vertical and horizontal rods, often assuming an equivalent homogeneous soil model, accounting for its actual stratified structure [15].

Herein, results for a single grounding grid and for typical grounding systems installed at the base of the towers of the HV transmission lines are presented. The deviation of the grounding impedance from the low frequency resistive behaviour is investigated, and TD results with injected lightning currents (displaying a wide frequency range) are presented; the response of grounding structures buried in a homogeneous, double-layered or frequency-dispersive soil is computed. Ionization phenomena have not been considered, since the validity of the FD approach adopted here is limited to the study of linear phenomena and systems. Ionization and other aspects regarding grounding modelling in the time domain were covered in Chapters 4 and 5.

Definition of grounding impedance

Standards for safety of electrical networks give guidance on the design of grounding systems to regulate the value of the grounding impedance at power frequency [16–18]. References may be found to the transient response of grounding systems and to the available procedures for its measurement [17]. However, different definitions are adopted in the literature for the ground transient impedance; they relate the current injected at the ground node to its voltage with respect to a reference at remote distance:

- *harmonic input impedance*, ratio of frequency-dependent complex voltage and current [19]. It may be thought as a driving-point function, modelling the grounding system at the injection node:

$$Z_{\mathrm{g}}(f) = \frac{V(f)}{I(f)}; \tag{6.1}$$

- *transient grounding impedance*, ratio of time-dependent voltage and current [20]:

$$z_{\mathrm{g}}(t) = \frac{v(t)}{i(t)}; \tag{6.2}$$

  it should be noticed that the transient grounding impedance is not well-defined at $t = 0$.

- *impulse impedance*, ratio of the peak voltage over the peak current [10] (which may not occur simultaneously):

$$z_{\mathrm{g}} = \frac{v_{\mathrm{peak}}}{i_{\mathrm{peak}}}\,; \tag{6.3}$$

  the impulse impedance is of practical utility, allowing to estimate the maximum GPR from the known current peak value.

- *surge impedance*, ratio of voltage over current at the time instant t^* at which the current reaches its maximum value [17]:

$$z_{\mathrm{g}} = \frac{v\left(t^*\right)}{i\left(t^*\right)}\,, \tag{6.4}$$

  with t^* such that $\mathrm{d}i\left(t^*\right)/\mathrm{d}t = 0$.

The transient impedance $z_{\mathrm{g}}\left(t\right)$ should not be confused with the IFT of the harmonic impedance $Z_g\left(f\right)$ (i.e., the grounding system response to a unitary impulsive current). In fact, in this case, the voltage $v\left(t\right)$ would be equal to the time convolution of the TD impedance with the current, and would *not* be given by their dot product as in (6.2). Hence, while the harmonic impedance is an intrinsic feature of the grounding system, the impedance defined in (6.2) strongly depends on the injected current waveform and does not define the grounding electrical behaviour univocally.

Hence, the TD node voltage due to the injection of a known current source into a node of the analysed grounding systems will be computed as:

$$v\left(t\right) = \mathscr{F}^{-1}\left[Z_{\mathrm{g}}\left(f\right) I\left(f\right)\right] \tag{6.5}$$

where $\mathscr{F}^{-1}$ denotes the IFT, and $I\left(f\right)$ is the Fourier transform of the injected current $i\left(t\right) = \mathscr{F}^{-1}\left[I\left(f\right)\right]$.

As stated in the introduction of this chapter, results concerning the harmonic impedance will be discussed, the response of the grounding systems being computed in the FD. Nevertheless, the obtained results should not be intended to be solely exploited in studies conducted in the FD. Indeed, the inverse Fourier transform of $Z_{\mathrm{g}}\left(f\right)$ may be computed to get the unique impulsive response of the grounding system $z_{\delta\mathrm{g}}\left(t\right)$. The time convolution of $z_{\delta\mathrm{g}}\left(t\right)$ with the TD expression of the dispersed current $i\left(t\right)$ (which can display any amplitude, and excite any frequency range) will allow to compute the transient voltage at the injection node.

6.1 Modelling the soil electrical permittivity and resistivity

Physical properties of the soil influencing electromagnetic transients should be taken into account when dealing with transients studies. While the soil

Table 6.1. Values of a_k according to the Longmire and Smith model [27].

k	a_k	k	a_k	k	a_k
1	$3.40 \cdot 10^6$	6	$1.33 \cdot 10^2$	11	$9.80 \cdot 10^{-1}$
2	$2.74 \cdot 10^5$	7	$2.72 \cdot 10$	12	$3.92 \cdot 10^{-1}$
3	$2.58 \cdot 10^4$	8	$1.25 \cdot 10$	13	$1.73 \cdot 10^{-1}$
4	$3.38 \cdot 10^3$	9	4.80		
5	$5.26 \cdot 10^2$	10	2.17		

magnetic permeability μ_{g} may be considered approximately constant, and equal to the magnetic permeability of vacuum μ_0, experimental tests have shown that the ground electrical properties, i.e., conductivity σ_{g} and relative permittivity ϵ_{rg}, are frequency-dependent [7], [21], [22]. Several analytical expressions have been proposed in the literature to reproduce their frequency dependence, in order to enable modelling of a dispersive ground in TL or grounding design studies. In depth analysis of the available models was performed by Cavka *et al.* [23]. Here, three of these models are selected and briefly reviewed – i.e., the Longmire and Smith's model, the Messier's model, and the Portela's model – which have been successfully tested for the causality requirement in [23]: the real and the imaginary parts of the complex quantity $\epsilon_{\mathrm{g}} - j\sigma_{\mathrm{g}}/\omega$, computed by means of the frequency-dependent expressions of ϵ_{g} and σ_{g}, satisfy Kramers-Kronig relations [24].

The models require two additional parameters: the electrical permittivity at infinite frequency $\epsilon_{\mathrm{g}_\infty}$, and the low frequency conductivity $\sigma_{\mathrm{g_{DC}}}$ (or alternatively $\sigma_{\mathrm{g}_{100\,\mathrm{Hz}}}$, measured at 100 Hz).

Different polarization phenomena influence the trend of the soil electrical permittivity ϵ_{rg}: electronic, ionic, dipole, and interfacial polarization [25]. Each polarization type contributes at low frequency, and, depending on the corresponding physical mechanism involved, has reduced influence at the highest frequencies (resulting in the decreasing trend of ϵ_{rg}, e.g., in Fig. 6.2b). Furthermore, due to the non-homogeneous structure of the soil, the measured values of ϵ_{rg} and σ_{g} account simultaneously for relaxation phenomena in dielectrics and dispersion in conductive media [26].

6.1.1 Longmire and Smith model

A *universal soil* model was introduced by Longmire and Smith [27], based on measurements by Dr. Wilkelnfeld in the frequency range $10^6 - 10^8$ Hz, and by Scott in the frequency range $10^2 - 10^6$ Hz. The model is derived assuming a resistive-capacitive behaviour of the soil, and extrapolating values at low

and high frequency from measured data. The electrical permittivity $\epsilon_{\mathrm{g}}(f)$ and conductivity $\sigma_{\mathrm{g}}(f)$ are given by:

$$\epsilon_{\mathrm{g}}(f) = \epsilon_{\mathrm{g}_\infty} + \epsilon_0 \sum_{k=1}^{13} \frac{a_k}{1 + (f/F_k)^2} \tag{6.6a}$$

$$\sigma_{\mathrm{g}}(f) = \sigma_{\mathrm{g_{DC}}} + 2\pi\epsilon_0 \sum_{k=1}^{13} a_k F_k \frac{(f/F_k)^2}{1 + (f/F_k)^2} \tag{6.6b}$$

where

$$F_k = (125\sigma_{\mathrm{g_{DC}}})^{0.8312} \cdot 10^{k-1}\,. \tag{6.7}$$

Values for a_k for $k = 1 \ldots 13$ are in Table 6.1. As in [27], the value $\epsilon_{\mathrm{g}_\infty} = 5\epsilon_0$ has been assumed.

6.1.2 Messier model

Formulas for the soil permittivity and conductivity proposed by Messier are as follows:

$$\epsilon_{\mathrm{g}}(f) = \epsilon_{\mathrm{g}_\infty} \left(1 + \sqrt{\frac{\sigma_{\mathrm{g_{DC}}}}{\pi f \epsilon_{\mathrm{g}_\infty}}}\right) \tag{6.8a}$$

$$\sigma_{\mathrm{g}}(f) = \sigma_{\mathrm{g_{DC}}} \left(1 + \sqrt{\frac{4\pi f \epsilon_{\mathrm{g}_\infty}}{\sigma_{\mathrm{g_{DC}}}}}\right), \tag{6.8b}$$

where it is assumed that $\sigma_{\mathrm{g}}(f \to 0) \simeq \sigma_{\mathrm{g_{100Hz}}}$, and $\epsilon_{\mathrm{g}_\infty} = 8\epsilon_0$ [23].

6.1.3 Portela model

Expression 6.9 refers to the more recent formulation of Portela's soil model [28] (the interested reader is referred to [29] for the original formulation):

$$\sigma_{\mathrm{g}}(f) + j2\pi f \epsilon_{\mathrm{g}}(f) = \sigma_{\mathrm{g_{100Hz}}} + \Delta_P \left[\cot\left(\frac{\alpha\pi}{2}\right) \pm j\right] \left(\frac{f}{f_0}\right)^{\alpha}, \tag{6.9}$$

where $\sigma_{\mathrm{g}}(f \to 0) \simeq \sigma_{\mathrm{g_{100Hz}}}$. As for the values of Δ_P and α, the median values $\Delta_P = 11.71$ mS/m and $\alpha = 0.706$ [23] are assumed for the simulations, derived from cumulative distribution curves displayed by Portela in [29], and based on measurements performed on 68 soil samples up to 2 MHz.

6.2 Frequency response of grounding electrodes and grids

Results are computed by means of the hybrid code, originally developed by Araneo and Celozzi [30], and extended to include layered soil modelling. The theoretical basis underlaying the implementation of the hybrid code are assessed in detail in Appendix B.

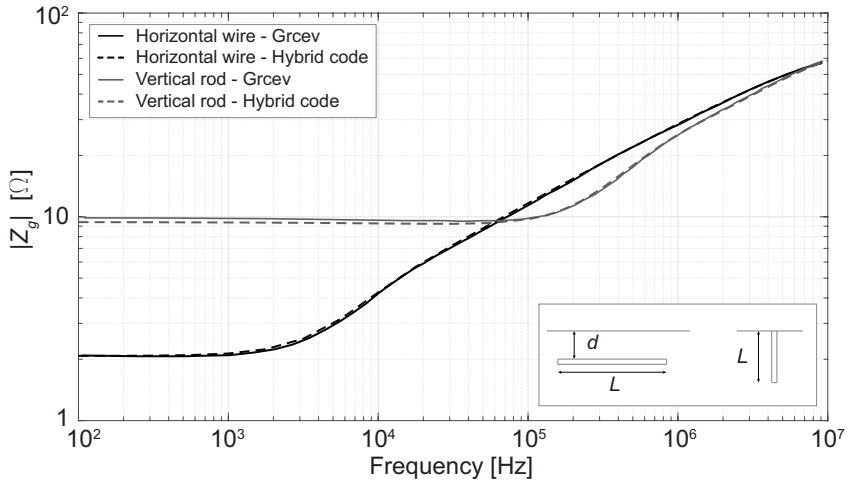

Figure 6.1. Magnitudes of grounding impedances of a vertical rod and a horizontal conductor, buried in soil with constant electrical properties ($\sigma_{\mathrm{g}} = 0.01$ S/m, $\epsilon_{rg} = 10$), computed by the hybrid code against results from Grcev ([31], [32]).

6.2.1 Validation

Results computed by the code, which were validated in [30] as to the value of the grounding impedance offered at power frequency by grounding systems with different geometries, are here validated in a wider frequency range (up to 10 MHz). Two reference cases were simulated, i.e., a single vertical rod with a=7 mm, L= 12 m, and a single horizontal wire with a=7 mm, L=100 m, d=0.8 m. L and a are the cylindrical conductor's length and radius, respectively; d is the depth of burial of the horizontal electrode. The soil is modelled with constant electrical properties $\sigma_{\mathrm{g}} = 0.01$ S/m, and $\epsilon_{rg} = 10$. The minimum wavelength $\lambda_{\min}$ (at f=10 MHz) in the ground half-space is $\lambda_{\min} \simeq 7.7$ m [2]. Hence, to fulfill the requirement of electrically short branches, the electrodes were discretized in branches with length equal to 0.7 m. In Fig. 6.1, results by the hybrid code are compared with those computed by Grcev for the same electrodes configurations and soil properties. The magnitude of the computed grounding impedances in Fig. 6.1 agrees well with results by Grcev in [31] and [32].

6.2.2 Grounding grid

The electrical conductivity and permittivity predicted by the three models are displayed in Fig. 6.2, with the input parameters in Table 6.2. The value of $\sigma_{\mathrm{g_{DC}}}$ required by (6.6), (6.7) is derived by numerically solving (6.6) to match the desired value of soil resistivity at 100 Hz.

The GPR of a simple square grounding grid is studied, referring to point A in Fig. 6.3 as the node of current injection. The electrical and geometrical characteristics of the simulated grid made of copper conductors are found in

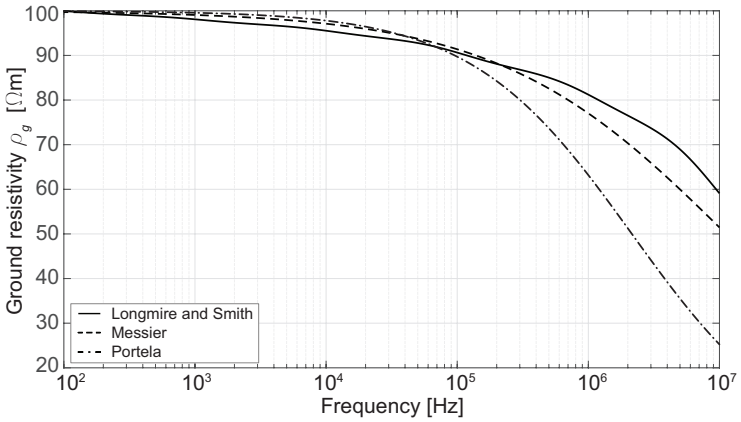

(a)

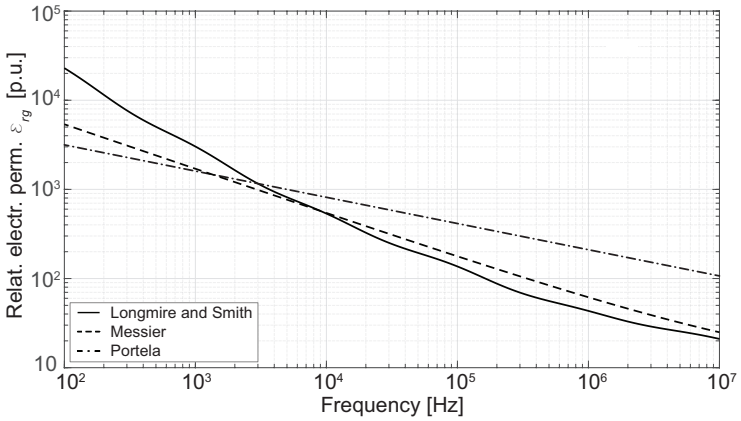

(b)

Figure 6.2. Electrical resistivity $\rho_{\mathrm{g}}(f)$ and relative permittivity $\epsilon_{r\mathrm{g}}(f)$ of the soil as functions of frequency, according to the dispersive ground models in Sec. 6.1.

Table 6.2. Values of the soil electrical properties used for simulation.

Layer 1				Layer 2
Constant parameters	Smith and Longmire	Messier	Portela	Constant parameters
σ_{g}=10 mS/m ϵ_{g}=20ϵ_0 F/m	$\sigma_{\mathrm{g_{DC}}}$=9.54 mS/m $\epsilon_{\mathrm{g}_\infty}$=5$\epsilon_0$ F/m	$\sigma_{\mathrm{g_{DC}}}$=10 mS/m $\epsilon_{\mathrm{g}_\infty}$=8$\epsilon_0$ F/m	Δ_P=11.71 mS/m α=0.706	σ_{g}=40 mS/m ϵ_{g}=20ϵ_0 F/m

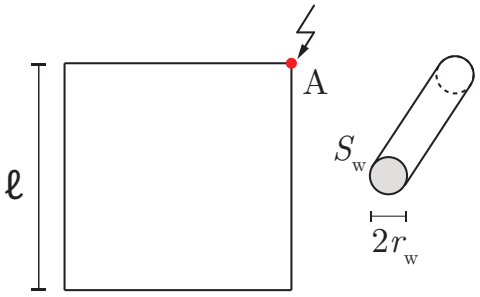

Figure 6.3. Square grounding grid, buried horizontally into the soil.

Table 6.3. Grid parameters.

ℓ	10 m
σ_w	$5.8 \cdot 10^7$ S/m
μ_w	μ_0
S_w	95 mm^2
r_w	5.5 mm

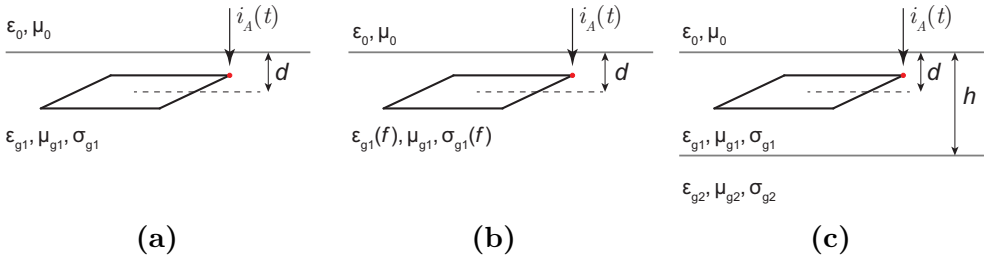

Figure 6.4. Analysed arrangements for the grounding grid in Fig. 6.3, with different soil models, $d = 0.8$ m. (a) Homogeneous soil with constant properties. (b) Homogeneous, frequency-dispersive soil. (c) Double-layered soil with constant properties.

Table 6.3. The three different scenarios depicted in Fig. 6.4 were simulated (i.e., soil with constant electric properties, frequency-dispersive soil, and double-layered soil with constant electrical properties). As to the implementation of the frequency-dispersive soil models, the input parameters required by the models by Messier and Longmire and Smith have been chosen to get a power frequency ground resistivity $\rho_{g100Hz} \simeq 100\ \Omega$m (under the assumption that $\sigma_{gDC} \simeq \sigma_{g100Hz}$ for the Messier model).

Table 6.4. Subsequent stroke parameters [33].

	$I_{peak,k}$ [kA]	τ_{1k} [μs]	τ_{2k} [μs]	n_k
k=1	10.7	0.25	2.5	2
k=2	6.5	2.1	230	2

The current $i_A(t)$, injected at node A to evaluate the GPR, is computed as the superposition of two Heidler's functions in order to reproduce a subsequent stroke current recorded at Mount San Salvatore [33]; this choice was made to highlight any deviation of the electrical behaviour of the grid from its low

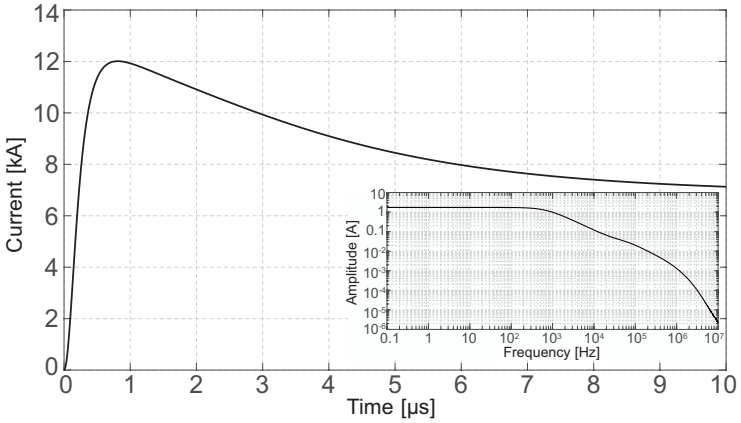

Figure 6.5. Subsequent stroke current from data measured at Monte San Salvatore [33]; the inset displays the current frequency spectrum (magnitude).

frequency resistance, by means of the higher frequency range typically covered by subsequent stroke currents. The lightning current waveform in the TD (given by expression (3.38) in Sec. 3.3.5, with parameters in Table 6.4 and $N_H = 2$) and its frequency spectrum are reported in Fig. 6.5.

FD results

In Fig. 6.6, the resistance and reactance of the computed $Z_{\mathrm{g}}(f)$ are displayed as functions of frequency for different soil models. Results for configurations (a) and (c) (in Fig. 6.4) are computed adopting the soil electrical properties in Table 6.2. As to configuration (c), different thicknesses for the upper soil layer h are simulated, namely, $h = 3, 5, 10$ m. In the following, R_{g} denotes the value of the resistive component of Z_{g} at low frequency (computed at 100 Hz).

As to the homogeneous soil model, the low frequency approximation $Z_{\mathrm{g}}(f) \simeq R_{\mathrm{g}} \simeq 5.2\ \Omega$ still holds up to 100 kHz. In the higher frequency range, the grid shows a resistive-inductive behaviour which affects its response under transient current excitation (the relevant TD results are presented in a next section). The low frequency approximation of Z_{g} to the corresponding power frequency resistance holds also for the case of double-layered soil. The deeper layer, due to the larger value of soil conductivity σ_{g_2}, contributes to reducing the power frequency harmonic impedance offered by the grounding grid. However, the computed Z_{g} with homogeneous and layered soil deviate more noticeably by their reactive components.

At growing frequencies, currents dispersed in the ground are progressively confined at smaller soil depths; hence, in this frequency range, the second ground layer holds minor influence as h increases. In Fig. 6.6 it can be observed that, in the analysed configuration, $h = 10$ m is sufficient to assume the soil to be an homogeneous half-space (with electrical properties equal to those of the upper layer); the influence of the deeper layer can be neglected at frequencies

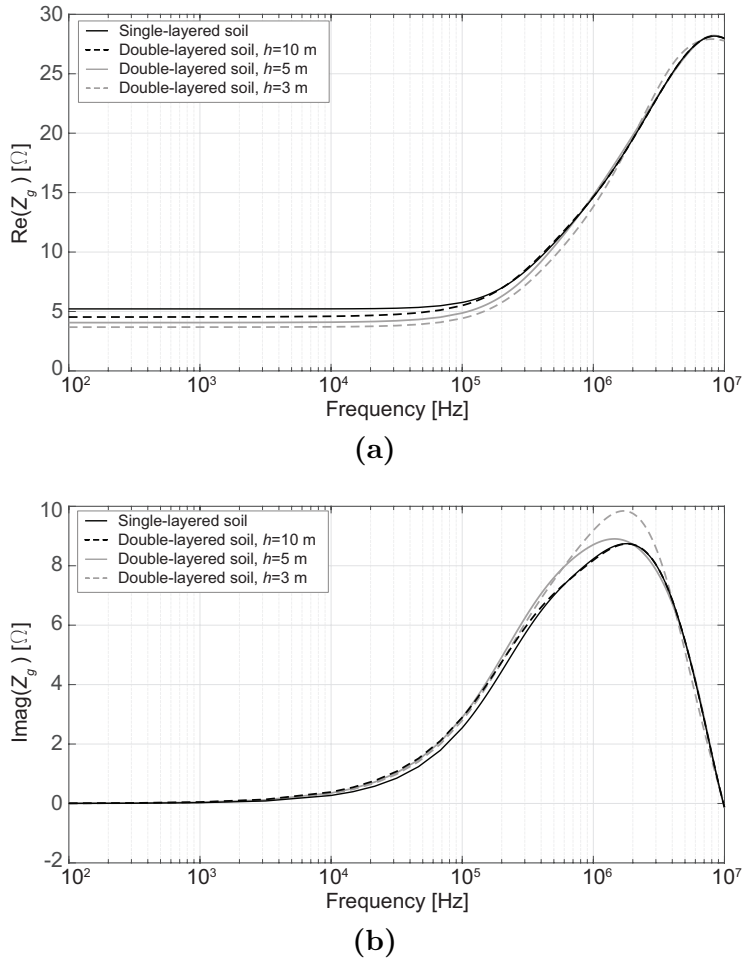

Figure 6.6. Resistive and reactive component of the grounding impedance of the grid in Fig. 6.4 in homogeneous and double-layered non-dispersive soil. (a) Resistive component of Z_{g}; (b) reactive component of Z_{g}.

above 5 MHz (hence, currents may be assumed to be confined in the upper soil layer).

Frequency-dispersive soil

The impedance offered by the grounding grid as a function of frequency is displayed in Fig. 6.7 when frequency-dispersive soil models by Longmire and Smith, Messier, and Portela are included in the simulations (the adopted electrical permittivity and conductivity are displayed in Fig. 6.2 as functions of frequency). Resistances and reactances computed by models by Longmire and Smith and Messier show a similar trend with frequency. On the other hand, the reactance computed by the Portela model presents a clear transition from inductive to capacitive in the MHz range. The capacitive behaviour is due to the enhanced contribution of displacement currents, as a result of

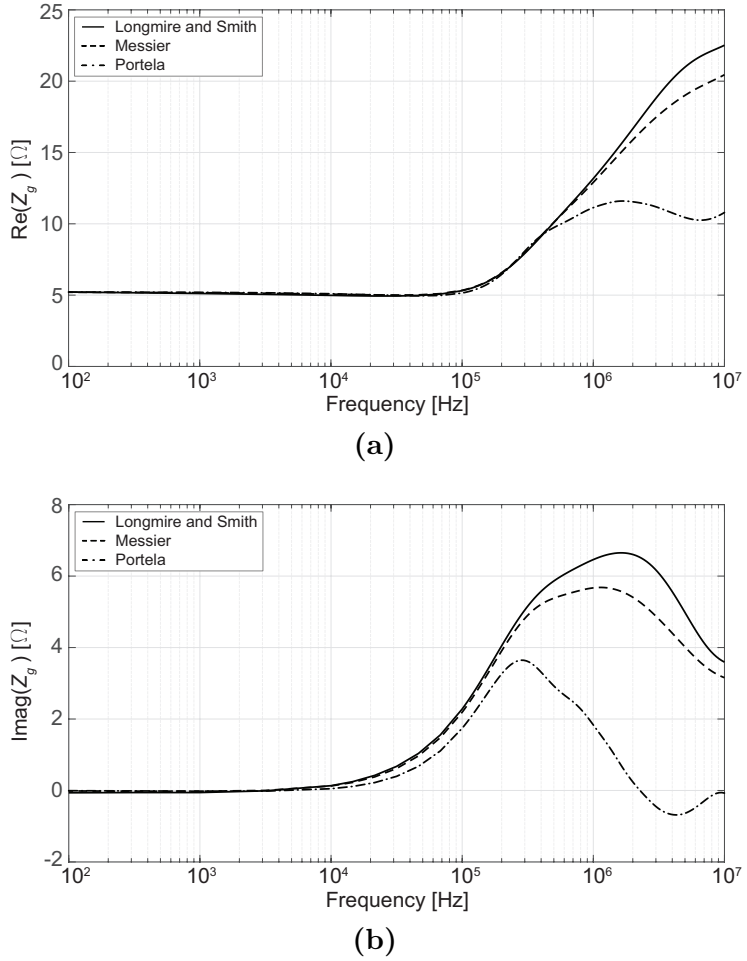

Figure 6.7. Resistive and reactive component of the grounding impedance associated with the grid buried in homogeneous and frequency-dispersive soil, according to models by Longmire and Smith, Messier, and Portela. (a) Resistive component of Z_{g}; (b) reactive component of Z_{g}.

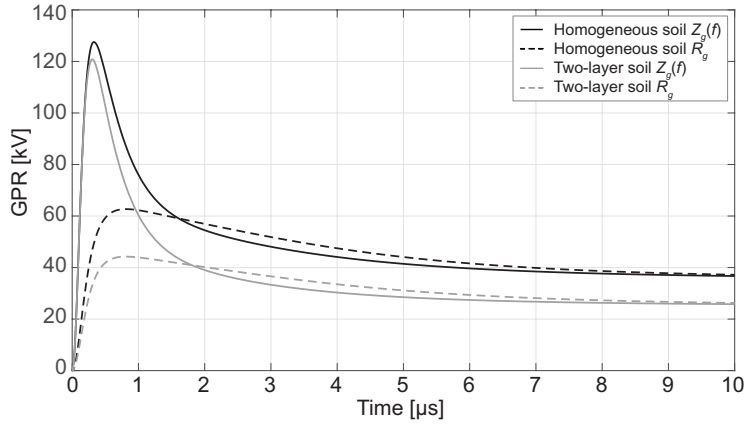

(a)

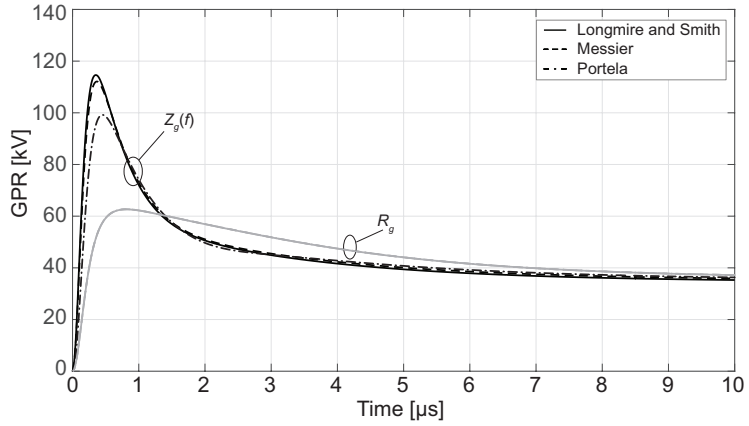

(b)

Figure 6.8. GPR at the injection node considering the frequency-dependent grounding impedance Z_{g} (the GPR corresponding to the power frequency grounding resistance R_{g} –computed at 100 Hz– is also displayed for reference). (a) Results for homogeneous and double-layered soil; (b) results with homogeneous, yet dispersive soil, according to the models presented in Sec. 6.1.

the larger $\epsilon_{rg}(f)$ computed at high frequency by the Portela model; in fact, compared to the value given by the other models, which is approximately 20, $\epsilon_{rg}(10\,\mathrm{MHz}) \simeq 107$ as computed by the Portela expression (6.9).

TD results

The GPR at node A is displayed in Figs. 6.8 for the three analysed configurations in Fig. 6.4, when the current $i_A(t)$ is injected at node A. All layers are non-magnetic with $\mu_{\mathrm{g}_1} = \mu_{\mathrm{g}_2} = \mu_0$. Figure 6.8a shows results obtained simulating the ground as a semi-infinite homogeneous layer or as double-layered (with $h = 3$ m). In the latter case, the voltage peak occurs slightly before compared to the case of homogeneous soil, due to the more pronounced inductive

behaviour of $Z_g(f)$ at higher frequencies. The introduction of the second layer with lower electrical resistivity, besides limiting the maximum voltage at node A, also reduces the late-time GPR, when the low frequency components of the lightning current hold a predominant contribution to the tail trend. The dashed line in Fig. 6.8a displays the GPR computed considering $Z_g(f) = R_g$ within the considered frequency range; as a result of the frequency dependence of Z_g, the voltage at node A differs noticeably both in the waveform and in the peak value, from results computed through the simplified approach with constant grounding resistance R_g. Predictions based on R_g would lead to a relative error on the estimation of the voltage peak at the injection node approximately equal to 50.9 % and the 63.4 % for homogeneous and double-layered soil, respectively.

As for the previous results, the GPR computed with frequency-dispersive soil models differs sensibly from the product of the corresponding R_g and the injected current (in Fig. 6.8b); the increment of the voltage peak value ranges approximately between the 65% of the expected peak value with power frequency resistance computed by the Portela model, to the 80% when the other models are considered.

The more pronounced inductive effect associated with models by Messier and Longmire-Smith with respect to the Portela model (in Fig. 6.7b) may be observed as well. The maximum values of the voltage by Longmire-Smith and Messier lead the peak of the dashed curves, as typically expected for devices showing a resistive-inductive behaviour; this effect is less pronounced for the curve computed by the Portela model, due to the phase obtained for $Z_g(f)$ in Fig. 6.7b (displaying the transition from an inductive to a capacitive reactance).

Considering the impulse impedance $v_{peak}/i_{peak} \neq R_g$, it is evident that with the chosen excitation source, the impedance offered by the grounding grid at frequencies larger than the characteristic value F_c (up to which $Z_g \simeq R_g$) influences the GPR. This may be observed also from the distortion of the waveform of $v(t)$ with respect to the waveform of the injected current $i_A(t)$.

6.2.3 Tower grounding systems

The grounding impedance of tower grounding systems commonly installed along Hellenic power lines with 150 kV rated voltage is considered here as a function of frequency. The geometry of the grounding systems is depicted (not in scale) in Fig. 6.9. Grounding system A consists in four rods with length $L_1 = 2$ m and radius $a_1 = 10$ mm; as to the grounding system denoted with B, installed in the real practice for highly resistive soils, it is provided with additional counterpoise horizontal wires with length $L_2 = 60$ m and radius $a_2 = 5$ mm. However, when the geological structure of the ground does not allow to install long counterpoise wires, or for limitations related to the right of way of the power line, case A grounding system may be installed as well for larger values of soil resistivity.

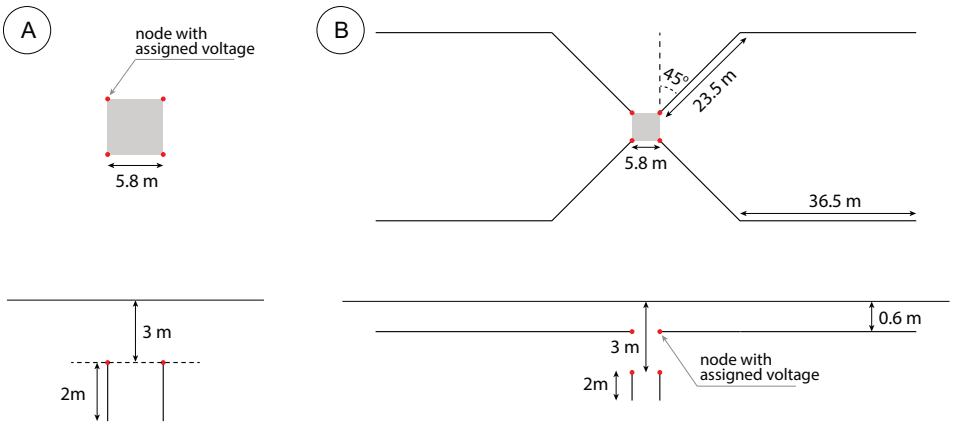

Figure 6.9. Typical grounding systems adopted for power lines at rated voltage 150 kV in Greece (courtesy of Z. G. Datsios).

Table 6.5. Soil electrical properties used for simulation - Case A.

		Case A - 4 rods						
R_{g}	$[\Omega]$	7	10	25	50	100	150	200
ρ_{g100Hz}	$[\Omega\mathrm{m}]$	59.9	85.5	213.9	427.7	855.4	1283.1	1710.8
ρ_{gDC}	$[\Omega\mathrm{m}]$	62.4	89.5	227.2	460.0	933.5	1416.0	1906.0
$\epsilon_{\mathrm{10MHz}}$	-	23.9	21.9	16.9	14.4	12.9	12.0	11.3
λ_{min}	[m]	4.9	5.4	6.6	7.4	8.0	8.4	8.7

Table 6.6. Soil electrical properties used for simulation - Case B.

		Case B - Counterpoise		
R_{g}	$[\Omega]$	7	10	25
ρ_{g100Hz}	$[\Omega\mathrm{m}]$	640.9	915.3	2288.8
ρ_{gDC}	$[\Omega\mathrm{m}]$	695.0	1001.0	2576.0
$\epsilon_{\mathrm{10MHz}}$	-	13.5	12.7	10.7
λ_{min}	[m]	7.8	8.1	9.0

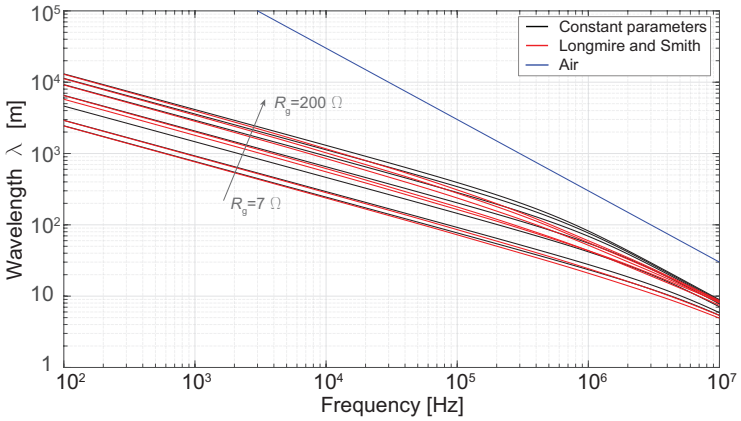

Figure 6.10. Wavelength in the ground half-space and reference wavelength in the air, for soil properties in Table 6.5, adopted to perform simulations for case A grounding system.

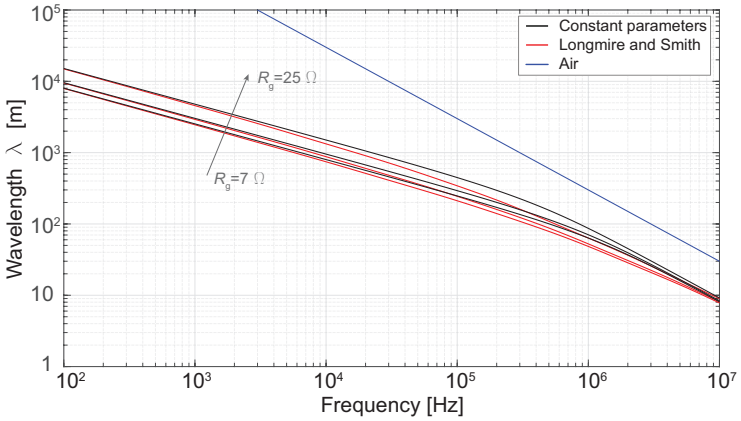

Figure 6.11. Wavelength in the ground half-space and reference wavelength in the air, for soil properties in Table 6.6, adopted to simulate case B grounding system.

In order to compute the grounding impedance Z_g, the same voltage value $V(f)$ is assigned to the nodes of the grounding systems where the current would be injected by the tower footing in the real operation conditions (dotted in red in Fig. 6.9). The total current $I(f)$, which is found to enter the aforementioned nodes, is plugged in the definition of harmonic impedance in (6.1). As a result, the solving system, associated with the application of the hybrid code, is modified according to the procedure illustrated in Sec. B.1.1. This procedure differs from the one adopted for the computation of Z_g for the grid in Sec. 6.2, consisting in injecting a current at the desired node and evaluating the resulting voltage. In fact, with reference to the counterpoise grounding system, due to the lack of rotational symmetry of the structure, it would be less accurate to assume that the total injected current is equally subdivided at

the four injection nodes. Indeed, the partitioning of the currents depends on the geometry of the structure (hence, on mutual effects between conductors) and on the dimensions of the buried wires. As for geometrical modelling of the grounding systems, the structure of the grounding system A (i.e., the four rods) was discretized through thin branches with length equal to 0.1 m; the structure of the grounding system B (i.e., the counterpoise) was discretized with branches with length 0.7 m. The length of the discretization branches was chosen to reach a compromise between the limitation of computational time and the requirement for electrically short branches. In the light of the latter consideration, wavelengths corresponding to the adopted values of the soil electrical properties for simulations of grounding systems A and B (in Tables 6.5 and 6.6) were computed as functions of frequency, and are displayed in Figs. 6.10 and 6.11.

The influence of constant and frequency-dependent soil electrical properties, according to the Longmire and Smith model [27], has been investigated. The model requires, as input parameters, the value of the electric permittivity at infinite frequency ($\epsilon_{g_\infty} = 5\epsilon_0$, [27]), and the DC value of soil resistivity $\rho_{g_{DC}} = 1/\sigma_{g_{DC}}$. Starting from the grounding resistance value R_g, corresponding to soil conductivity σ_{g100Hz}, the values of $\sigma_{g_{DC}}$ were chosen to get $\sigma_g(f^*) = \sigma_{g100Hz}$ at $f^* = 100$ Hz by application of the Longmire and Smith model. The computed values used for simulations are listed in Tables 6.5 and 6.6 for grounding system A and B, respectively. The soil relative permittivity ϵ_{10MHz} predicted at 10 MHz by the Longmire and Smith model is adopted as fixed value of ϵ_{rg} for simulations performed with constant electric properties of the soil. It should be noted that the independent variable of the problem when it comes to the design of grounding systems is the soil resistivity. However, preliminary simulations are often performed in order to identify the preferred value of R_g. This is the reason why results were produced selecting several values of R_g, and computing the soil conductivity accordingly.

From Figs. 6.12a-6.15a and 6.13a-6.16a, it can be observed that the shape of the frequency responses is different for the two cases (i.e., rods and counterpoise). This is due to the characteristic dimension of the systems. In fact, for the simulated soil properties, the length of each vertical rod ($L_1 = 2$ m) is shorter than λ_{min} within the considered frequency range (the minimum wavelength corresponds to the value computed at 10 MHz for all the considered soil properties, as shown in Fig. 6.10). Hence, propagation along the vertical rods holds a minor influence. On the contrary, it may be observed that the computed wavelength in the ground half-space (in Fig. 6.11) is approximately equal to 100 m (hence, within the same order of magnitude of the length of the counterpoise wires) already at 30-40 kHz depending on the values adopted for the soil electrical properties. Therefore, the higher frequencies oscillatory behaviour of the impedance magnitude should be associated with the periodic behaviour of the input impedance associated with any mode which may propagate along the structure, above a cutoff frequency.

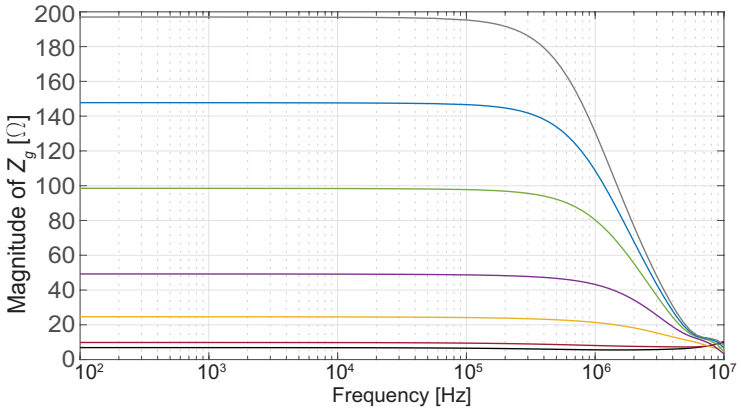

(a)

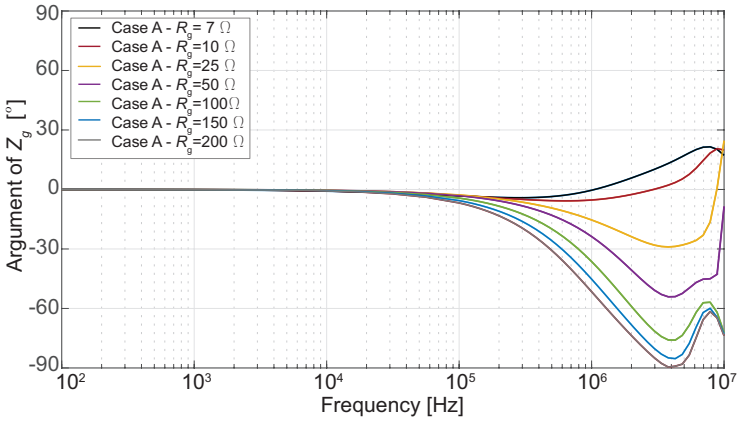

(b)

Figure 6.12. Frequency response of grounding system A in Fig. 6.9 with constant soil properties. (a) Magnitude of the grounding impedance; (b) argument of the grounding impedance.

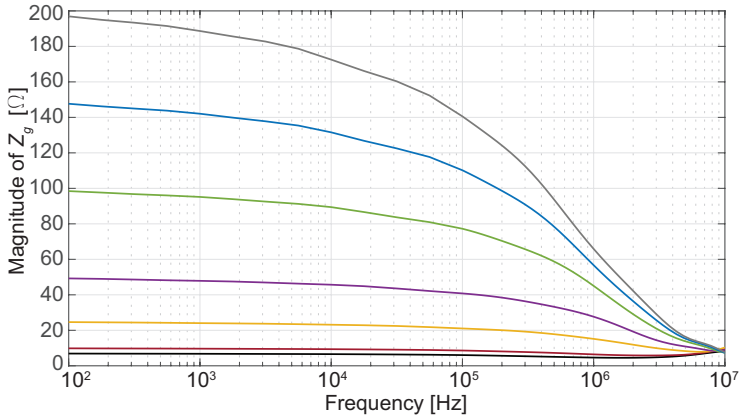

(a)

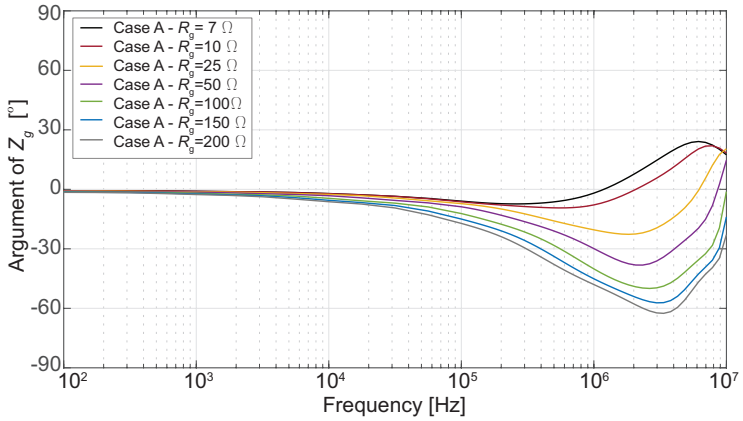

(b)

Figure 6.13. Frequency response of grounding system A in Fig. 6.9 with frequency-dependent soil properties. (a) Magnitude of the grounding impedance; (b) argument of the grounding impedance.

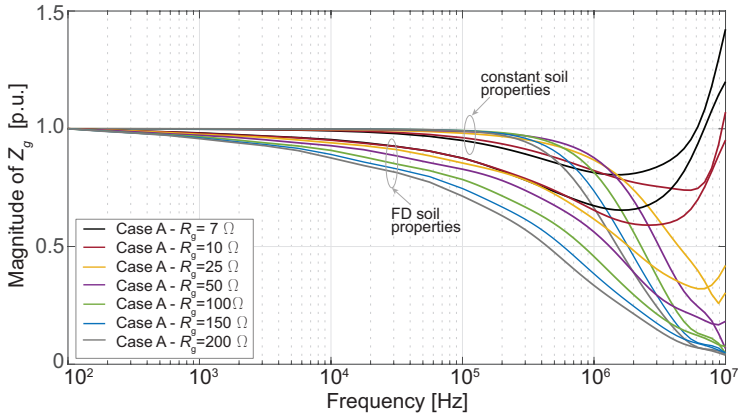

Figure 6.14. Magnitude of the grounding impedance computed for grounding system A in Fig. 6.9 with constant and frequency-dependent soil properties, normalised with respect to the corresponding R_g at low frequency (100 Hz).

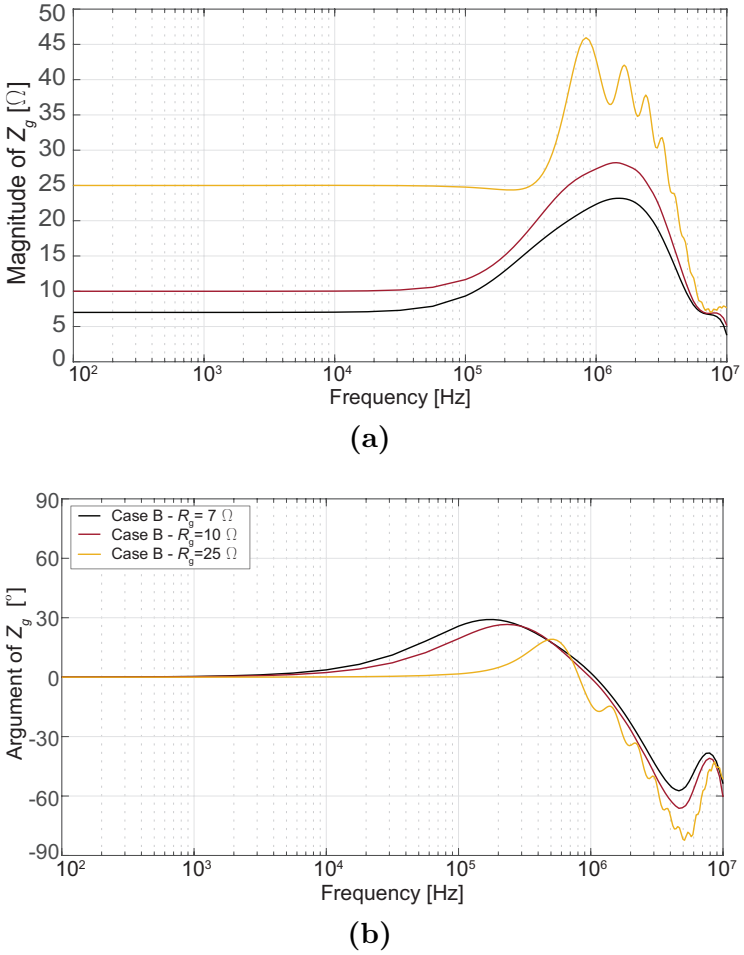

Figure 6.15. Frequency response of grounding system B in Fig. 6.9 with constant soil properties. (a) Magnitude of the grounding impedance; (b) argument of the grounding impedance.

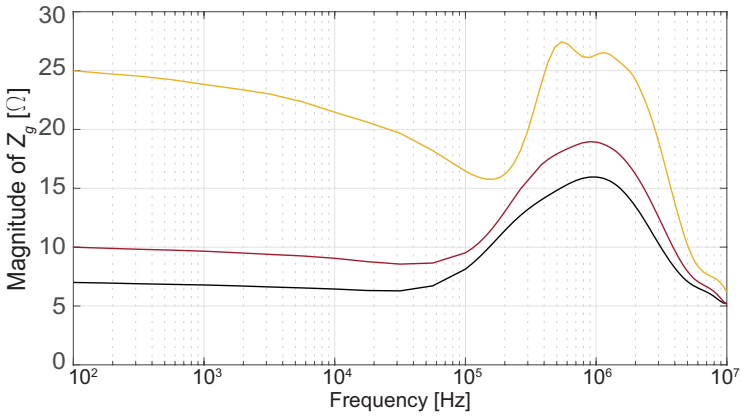

(a)

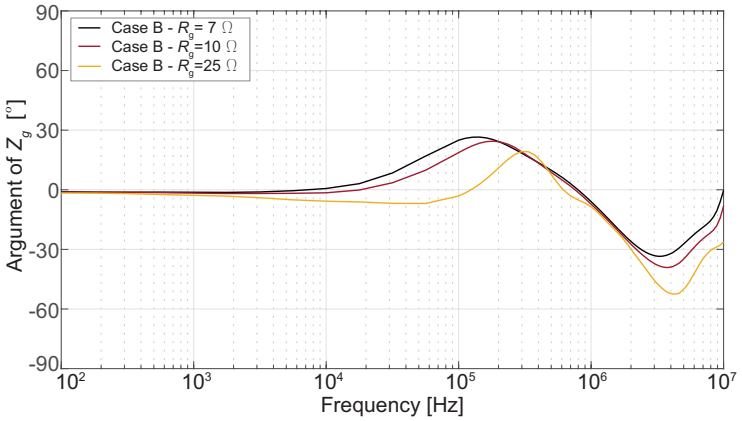

(b)

Figure 6.16. Frequency response of grounding system B in Fig. 6.9 with frequency-dependent soil properties. (a) Magnitude of the grounding impedance; (b) argument of the grounding impedance.

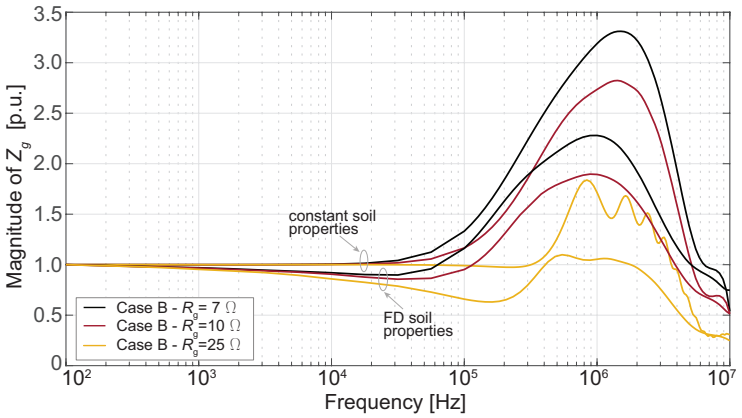

Figure 6.17. Magnitude of the grounding impedance computed for grounding system B in Fig. 6.9 with constant and frequency-dependent soil properties, normalised with respect to the corresponding R_g at low frequency (100 Hz).

As to case A (Fig. 6.12), the initial deviation of $Z_{\mathrm{g}}(f)$ from the power frequency value $Z_{\mathrm{g}}(100\mathrm{Hz}) \simeq R_{\mathrm{g}}$ is more evident for increasing values of R_{g}. This is due to the different contribution of conduction and displacement phenomena at different frequencies, and for the different sets of soil properties. With constant soil properties, short rods display a capacitive behaviour first, and lower values of the impedance magnitude $|Z_{\mathrm{g}}|$. On the contrary, extended structures show an inductive behaviour first (Fig. 6.15), and the grounding performance starts to be reduced ($|Z_{\mathrm{g}}|/R_{\mathrm{g}} > 1$) at lower frequencies with respect to the case of frequency-dependent soil properties.

With frequency-dependent soil properties, a non-negligible capacitive behaviour is observed at low frequency (Figs. 6.13b and 6.16b), regardless of the grounding configuration, i.e., of the length of the electrodes; this is due to the high values of ϵ_{rg} predicted by the Longmire and Smith model at low frequency. The values of ϵ_{rg}, along with the predicted decrease in $\rho_{\mathrm{g}}(f)$ at increasing frequency, result in maximum values of $|Z_{\mathrm{g}}|$ which are lower than in the case of frequency independent soil properties. This can be observed in Figs. 6.14 and 6.17, in which the grounding impedance magnitudes (computed for both constant and frequency-dependent soil properties), normalised with respect to their corresponding value at 100 Hz, are displayed for case A and B, respectively. Normalised curves corresponding to frequency-dependent soil properties converge at $f = 100$ Hz and start to decrease due to the capacitive component of the grounding impedance, lowering their magnitude.

Furthermore, from Figs. 6.14 and 6.17 it can be observed that a more pronounced capacitive behaviour is associated with larger values of R_{g}, even though larger values of the electric permittivity were used for simulations with lower R_{g}. This is due to the corresponding lower values of soil conductivity used for simulations, which enhance the prevailing role played by capacitive effects as to current dispersion. Exception is made for $R_{\mathrm{g}} = 7$ and 10 Ω with constant soil properties in Fig. 6.14, due to the particular choice of ϵ_{rg} and σ_{g}.

The frequency above which the validity of the approximation $Z_{\mathrm{g}} \simeq R_{\mathrm{g}}$ does not hold anymore is referred to characteristic frequency F_c [34]. An observation of general validity deduced from Figs. 6.14 and 6.17 is that lower values of F_c are observed for frequency-dependent soil properties. In the simulated configurations, for constant soil properties, the maximum error computed assuming $|Z_{\mathrm{g}}| = R_{\mathrm{g}}$ up to 100 kHz is 5.23% of the actual magnitude value for case A grounding system, and 24.92% for case B (for $R_{\mathrm{g}} = 7$ Ω and $f = 100$ kHz). A maximum relative error approximately equal to 5% for the counterpoise grounding system is computed at 40 kHz. Hence, due to the larger geometrical dimensions of the counterpoise horizontal wires, lower characteristic frequencies F_c are associated with this grounding configuration.

Four additional cases were simulated. The frequency response of grounding system A is computed considering the soil electrical properties used for simulations corresponding to $R_{\mathrm{g}} = 7$ Ω and $R_{\mathrm{g}} = 10$ Ω for grounding system B (Table 6.6). The aim is to compare the grounding impedances offered by the

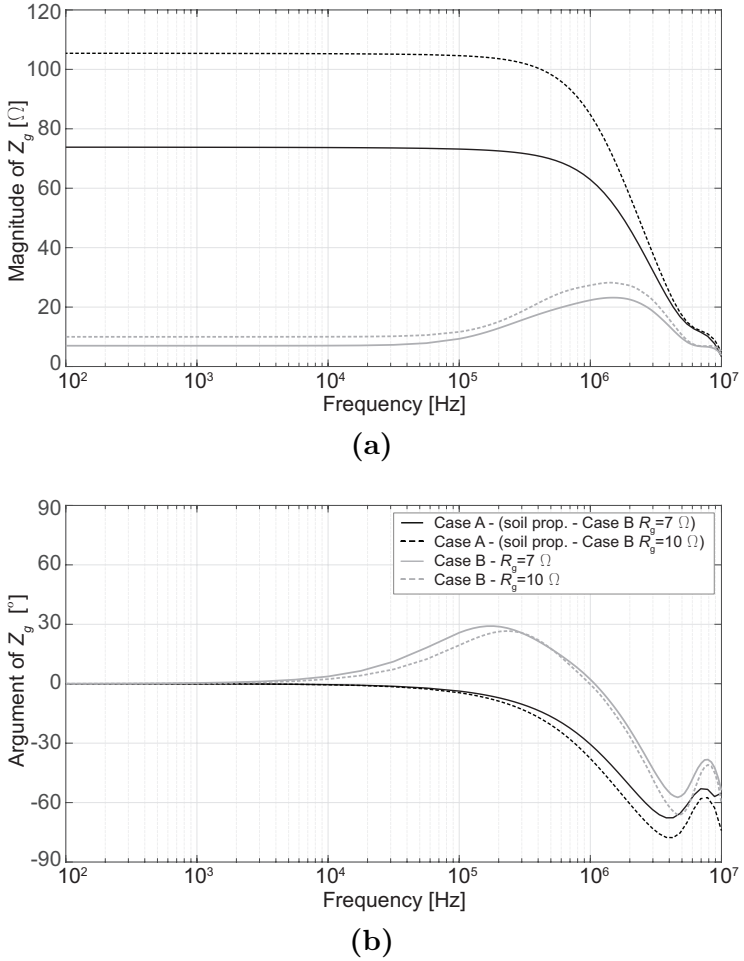

Figure 6.18. Frequency response of the two grounding systems in Fig. 6.9 with constant soil properties. (a) Magnitude of the grounding impedance; (b) argument of the grounding impedance.

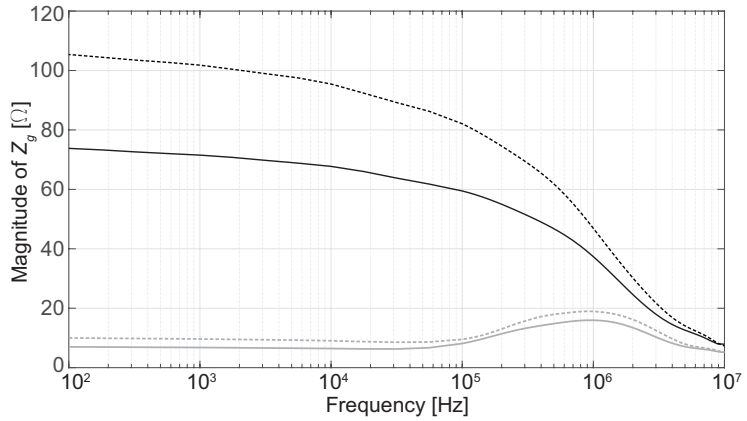

(a)

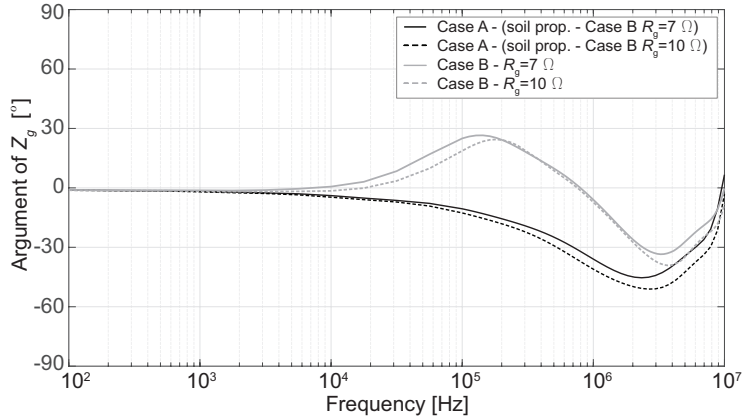

(b)

Figure 6.19. Frequency response of the two grounding systems in Fig. 6.9 with frequency-dependent soil properties. (a) Magnitude of the grounding impedance; (b) argument of the grounding impedance.

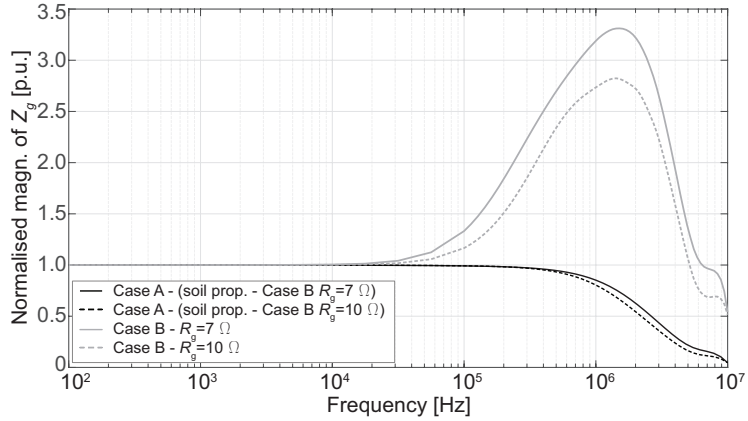

Figure 6.20. Magnitude of the grounding impedance computed for the grounding systems in Fig. 6.9 with constant soil properties, normalised with respect to the corresponding R_g at low frequency (100 Hz).

two systems when they are buried in the same soil. Figures 6.18 and 6.19 show magnitude and argument of Z_{g} computed for the two grounding systems with constant or frequency-dependent soil properties, respectively.

Some general observations may be drawn. In high resistivity soil, the extended grounding system is installed to reduce the grounding impedance at low frequency. In fact, with soil properties corresponding to $R_{\mathrm{g}} = 7\ \Omega$ and $10\ \Omega$ for the counterpoise case, the corresponding values of R_{g} computed for the four rods are $R_{\mathrm{g}} = 73.8\ \Omega$ and $R_{\mathrm{g}} = 105.4\ \Omega$. Additionally, the grounding systems show considerably different behaviours at frequencies above 10 kHz. While grounding system A, due to the limited dimension of the rods, results in a capacitive behaviour, the reactance associated with the counterpoise is inductive [34]. Figure 6.20 displays the magnitude of $Z_{\mathrm{g}}(f)$ (with constant soil properties) normalised with respect to the corresponding R_{g}. It may be observed that the performance of the four rods is improved at high frequency (compared to the low frequency grounding impedance), since the impedance magnitude decreases with increasing frequency. Opposite considerations can be made for the counterpoise grounding system. Furthermore, the characteristic frequencies F_c at which Z_{g} deviates from the corresponding value of R_{g} are lower for grounding system B. Therefore, for highly conductive soils, the 4 rods are installed; in fact, despite the smaller R_{g} associated with counterpoise-like grounding systems, the installation of the counterpoise wires would not be justified in terms of the larger cost and soil occupation, along with the impaired grounding performance at larger frequencies.

Frequency responses discussed in this chapter have been computed with a non-uniform frequency sampling, taking advantage of the smoothness of the curves up to approximately $10^4 - 10^5$ Hz (depending on the maximum geometrical dimension of the studied grounding system). The computational time required to compute the frequency response at a single frequency is approximately 3.5 minutes for the 4 rods configuration (case A), and 2.2 hours for the counterpoise grounding system (case B) on a desktop computer (AMD Ryzen 7 1800X, 64 GB RAM). However, the total time required by simulations may be sensibly reduced; indeed, the program is suitable for parallelization, since computations performed at each iteration of the loop spanning across the chosen vector of frequencies are fully independent. Furthermore, for short structures (with respect to the computed λ_{min} in the soil), as confirmed by Figs. 6.12-6.14, the frequency response is smooth and not oscillatory, and the number of sampling points in the FD may be reduced (hence, reducing the total computational time) without any loss in accuracy.

Further considerations on the influence of the grounding system modelling are included in [1].

Acknowledgement: I would like to thank Zacharias G. Datsios from the Aristotle University of Thessaloniki, Greece, for the fruitful collaboration, the helpful discussions, and for having shared his expertise on the topic of the present chapter.

References

[1] Z. G. Datsios, E. Stracqualursi, R. Araneo, P. N. Mikropoulos, and T. E. Tsovilis, "Estimation of the minimum backflashover current and backflashover rate of a 150 kV overhead transmission line: Frequency and current-dependent effects of grounding systems," in *2022 IEEE International Conference on Environment and Electrical Engineering and 2022 IEEE Industrial and Commercial Power Systems Europe (EEEIC/I&CPS Europe)*. IEEE, 2022, pp. 1–5.

[2] E. D. Sunde, *Earth conduction effects in transmission systems*. Dover Publications Inc., 1968.

[3] H. Dwight, "Calculation of resistances to ground," *Transactions of the American Institute of Electrical Engineers*, vol. 55, no. 12, pp. 1319–1328, 1936.

[4] A. R. J. de Araújo, W. L. M. de Azevedo, and J. Pissolato Filho, "Computing grounding impedance of rods buried in frequency-dependent stratified soils," in *2021 35th International Conference on Lightning Protection (ICLP) and XVI International Symposium on Lightning Protection (SIPDA)*, vol. 1. IEEE, 2021, pp. 01–08.

[5] B. Salarieh, H. J. De Silva, and B. Kordi, "Electromagnetic transient modeling of grounding electrodes buried in frequency dependent soil with variable water content," *Electric Power Systems Research*, vol. 189, p. 106595, 2020.

[6] S. Visacro and A. Soares, "HEM: A model for simulation of lightning-related engineering problems," *IEEE Trans. Power Del.*, vol. 20, no. 2, pp. 1206–1208, Apr. 2005.

[7] S. Visacro and R. Alipio, "Frequency dependence of soil parameters: Experimental results, predicting formula and influence on the lightning response of grounding electrodes," vol. 27, no. 2, pp. 927–935.

[8] P. Yutthagowith, A. Ametani, N. Nagaoka, and Y. Baba, "Application of the partial element equivalent circuit method to analysis of transient

potential rises in grounding systems," *IEEE Trans. Electromagn. Compat.*, vol. 53, no. 3, pp. 726–736, 2011.

[9] F. Gatta, A. Geri, S. Lauria, and M. Maccioni, "Generalized pi-circuit tower grounding model for direct lightning response simulation," *Electric Power Systems Research*, vol. 116, pp. 330–337, 2014.

[10] L. Grcev, "Time- and frequency-dependent lightning surge characteristics of grounding electrodes," *IEEE Trans. Power Del.*, vol. 24, no. 4, pp. 2186–2196, Oct. 2009.

[11] L. D. Grcev and M. Heimbach, "Frequency dependent and transient characteristics of substation grounding systems," *IEEE Trans. Power Del.*, vol. 12, no. 1, pp. 172–178, 1997.

[12] L. D. Grcev, A. Kuhar, V. Arnautovski-Toseva, and B. Markovski, "Evaluation of high-frequency circuit models for horizontal and vertical grounding electrodes," *IEEE Trans. Power Del.*, vol. 33, no. 6, pp. 3065–3074, 2018.

[13] B. Markovski, L. Grcev, and V. Arnautovski-Toseva, "Fast and accurate transient analysis of large grounding systems in multilayer soil," *IEEE Trans. Power Del.*, vol. 36, no. 2, pp. 598–606, 2021.

[14] Z. G. Datsios, P. N. Mikropoulos, T. E. Tsovilis, E. Thalassinakis, and G. Pagonis, "Application of non-gapped line surge arresters to the 150 kV overhead lines of Rhodes: An investigation through ATP-EMTP simulations," in *2021 35th International Conference on Lightning Protection (ICLP) and XVI International Symposium on Lightning Protection (SIPDA)*, vol. 1. IEEE, 2021, pp. 01–07.

[15] R. Alipio, D. Conceicao, A. De Conti, K. Yamamoto, R. N. Dias, and S. Visacro, "A comprehensive analysis of the effect of frequency-dependent soil electrical parameters on the lightning response of wind-turbine grounding systems," *Electric Power Systems Research*, vol. 175, p. 105927, 2019.

[16] "IEEE guide for safety in AC substation grounding," *IEEE Std 80-2013 (Revision of IEEE Std 80-2000/ Incorporates IEEE Std 80-2013/Cor 1-2015)*, pp. 1–226, 2015.

[17] "IEEE guide for measuring earth resistivity, ground impedance, and earth surface potentials of a grounding system," *IEEE Std 81-2012 (Revision of IEEE Std 81-1983)*, pp. 1–86, 2012.

[18] "IEEE Recommended Practice for Grounding of Industrial and Commercial Power Systems," *IEEE Std 142-2007 (Revision of IEEE Std 142-1991)*, pp. 1–225, 2007.

[19] D. Roubertou, J. Fontaine, J. Plumey, and A. Zeddam, "Harmonic input impedance of earth connections," in *1984 International Symposium on Electromagnetic Compatibility*. IEEE, 1984, pp. 1–4.

[20] R. Velazquez and D. Mukhedkar, "Analytical modelling of grounding electrodes transient behavior," *IEEE Trans. Power App. Syst.*, no. 6, pp. 1314–1322, 1984.

[21] M. Loewer, J. Igel, C. Minnich, and N. Wagner, "Electrical and dielectric properties of soils in the mHz to GHz frequency range," in *Proceedings of the 11th International Conference on Electromagnetic Wave Interaction with Water and Moist Substances (ISEMA)*. Florence, pp. 247–254.

[22] R. C. Bigelow and W. R. Eberle, "Empirical predictive curves for resistivity and dielectric constant of earth materials; 100 Hz to 100 MHz," US Geological Surveyt, Tech. Rep.

[23] D. Cavka, N. Mora, and F. Rachidi, "A comparison of frequency-dependent soil models: Application to the analysis of grounding systems," *IEEE Trans. Electromagn. Compat.*, vol. 56, no. 1, pp. 177–187, 2014.

[24] E. J. Rothwell and M. J. Cloud, *Electromagnetics*. CRC press, 2018.

[25] C. A. Balanis, *Advanced Engineering Electromagnetics*. New York: Wiley, 1989.

[26] B. D. Fuller and S. H. Ward, "Linear system description of the electrical parameters of rocks," vol. 8, no. 1, pp. 7–18.

[27] C. L. Longmire and K. S. Smith, "A universal impedance for soils," Mission Research Corp Santa Barbara CA, Tech. Rep., 1975.

[28] C. M. Portela, J. B. Gertrudes, M. Tavares, and J. Pissolato, "Earth conductivity and permittivity data measurements: Influence in transmission line transient performance," *Electric power systems research*, vol. 76, no. 11, pp. 907–915, 2006.

[29] C. Portela, "Measurement and modeling of soil electromagnetic behavior," in *1999 IEEE International Symposium on Electromagnetic Compatability*, vol. 2. IEEE, 1999, pp. 1004–1009.

[30] R. Araneo and S. Celozzi, "Transient behavior of wind towers grounding systems under lightning strikes," *Int. J. Energy Environ. Eng.*, vol. 7, no. 2, pp. 235–247, 2016.

[31] L. Grcev, "Impulse efficiency of ground electrodes," *IEEE Trans. Power Del.*, vol. 24, no. 1, pp. 441–451, 2008.

[32] L. Grcev and S. Grceva, "On HF circuit models of horizontal grounding electrodes," *IEEE Trans. Electromagn. Compat.*, vol. 51, no. 3, pp. 873–875, 2009.

[33] F. H. Silveira, A. De Conti, and S. Visacro, "Lightning overvoltage due to first strokes considering a realistic current representation," *IEEE Trans. Electromagn. Compat.*, vol. 52, no. 4, pp. 929–935, Nov. 2010.

[34] L. Grcev, "High-frequency grounding," in *Lightning Protection*. IET, 2010, pp. 503–529.

Chapter 7

Multiconductor transmission lines: Frequency Domain analysis

The chain matrix theory has been applied in order to assess the effect of SWs when dealing with a lightning striking the top of a TL tower [1–3]. In this chapter, the term *grounded wire* is alternatively employed to denote non-fed conductors (including SWs) placed near the phase conductors for the purposes of:

- reducing the incidence of direct lightning strokes to phase conductors;
- reducing induced voltages from external electromagnetic fields;
- raising the mutual surge impedance of a set of overhead ground wires to the protected phase conductors.

A grounded neutral, when installed beneath the phase conductors, mainly contributes according to the second and third points above.

Current practice in lightning protection of HV transmission lines favors the use of SWs [4]; for instance, IEEE Std. 1410 selects SWs as a preferable method to improve the lightning performance of distribution lines [5]. Appropriate selection of their number and placement usually reduces the risk of outages [6]. However, ground wires may be placed above and also below the phase conductors. The Underbuilt Ground Wire (UGW) was already introduced as a protective measure by Hileman [4], and more recently its role was discussed by Visacro *et al.* [7]. Even though the installation of UGWs in HV and distribution lines may represent an economical and technical challenge to Transmission and Distribution System Operators (due to difficulties in coordinating different conductor heights, especially under adverse climatic conditions), their role is still subject of ongoing research. In Japan, the use of UGWs in lines over mountainous terrain is receiving growing attention [8], with applications

extending from distribution to subtransmission voltage levels [9]. The topic has been recently reassessed to improve the lightning performance of lines displaying large grounding resistances at the towers [10].

In particular, the beneficial effects of UGWs (whether placed above or below the phase conductors) are being debated also in regard to distribution lines. Indeed, in the past, the use of SWs was not considered a valuable solution to improve the lightning performance of distribution lines under direct strokes, because of the GPR caused by lightning currents flowing through the grounding system at the poles and the limited clearence distances.

7.1 Chain matrix analysis of power lines with periodical grounding

Notation

- N_{c} Total number of conductors of the line;
- N_{pc} Number of phase conductors (power carrying conductors);
- N_{gw} Number of ground wires (including SWs);
- $\mathbf{v}_{\mathrm{pc}}$ vector of power carrying conductors voltages;
- $\mathbf{v}_{\mathrm{gw}}$ vector of ground wires voltages;
- $\boldsymbol{\gamma}$ vector of propagation constants;
- $\mathbf{Y}_{\mathrm{w}}$ matrix of characteristic admittances;
- $[\mathbf{1}]$ identity matrix;
- $[\mathbf{0}]$ null matrix;
- M Number of line sections (i.e., number of spans);
- M_L Number of line sections to the left of the struck pole;
- M_R Number of line sections to the right of the struck pole;
- $Pole\,0$ Pole struck by the lightning stroke;
- ℓ Span length.

The adopted methodology represents a further development of a previous approach by Araneo *et al.* [11] on the application of the transfer matrix theory in the FD. The approach consists in dividing the TL into arbitrary equal sections (cells) of the same length. The specific choice of the structure of the

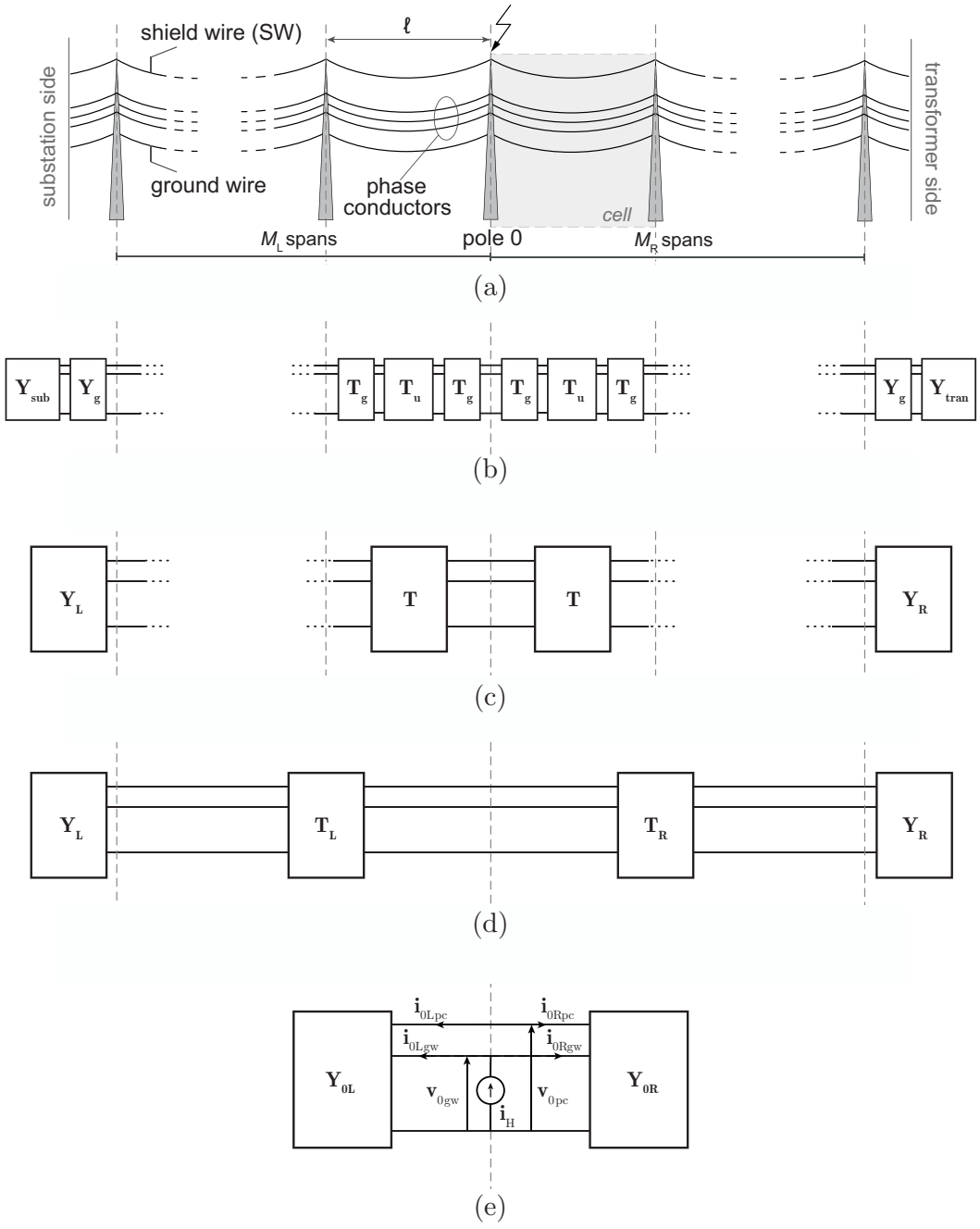

Figure 7.1. Periodic structure of the reference power line under study, and representation by means of the transfer matrix approach. (a) Line divided into cells; (b) transfer matrix representation of the cells components; (c) cascade of the transfer matrices within each cell; (d) chain matrix equivalent of the line sections at the left and right side of the impact point; (e) matrices of total equivalent admittances at the left and right side of the pole struck by the lightning, including the line terminations.

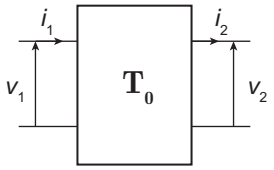

Figure 7.2. Voltages and currents at the terminations of a reference two-port network represented by the transfer matrix $\mathbf{T}_0$.

single cell represents the simplification introduced by the study presented in [1]: the line is modelled as a cascade of equal cells composed by a span, and two half poles at its right and left terminations. The structure of the cell, with length ℓ, is represented in Fig. 7.1a[1].

For the sake of clarity, the general relations for voltages and currents in the simple case of the two-port network in Fig. 7.2, represented by the 2×2 transfer matrix $\mathbf{T}_0$, are recalled:

$$\begin{bmatrix} v_1 \\ i_1 \end{bmatrix} = \underbrace{\begin{bmatrix} T_{11} & T_{12} \\ T_{21} & T_{22} \end{bmatrix}}_{\mathbf{T}_0} \begin{bmatrix} v_2 \\ i_2 \end{bmatrix} \tag{7.1}$$

where v_1, v_2 and i_1, i_2 are the voltages and currents at the two ports as displayed in Fig. 7.2, and T_{ij} (with $i, j \in \{1, 2\}$) is the generic element of $\mathbf{T}_0$.

As to the practical case of an MTL, from the basics of TL analysis in the FD [12], the transfer matrix (or chain matrix) $\mathbf{T}_\mathrm{u}$ linking conductors-to-ground voltages and line currents at the span terminations may be written as:

$$\mathbf{T}_\mathrm{u} = \begin{bmatrix} \mathbf{A}_\mathrm{u} & \mathbf{B}_\mathrm{u} \\ \mathbf{C}_\mathrm{u} & \mathbf{D}_\mathrm{u} \end{bmatrix}, \ \mathbf{B}_\mathrm{u} = \mathbf{B}_\mathrm{u}^T \tag{7.2}$$

where, due to the validity of the reciprocity theorem for electrical networks, $\mathbf{C}_\mathrm{u}$ and $\mathbf{D}_\mathrm{u}$ can be computed from $\mathbf{A}_\mathrm{u}$ and $\mathbf{B}_\mathrm{u}$ through

$$\mathbf{C}_\mathrm{u} = \mathbf{B}_\mathrm{u}^{-1} \left(\mathbf{A}_\mathrm{u}^2 - [\mathbf{1}] \right), \ \mathbf{D}_\mathrm{u} = \mathbf{A}_\mathrm{u}^T. \tag{7.3}$$

In (7.3), submatrices $\mathbf{A}_\mathrm{u}$, $\mathbf{B}_\mathrm{u}$, $\mathbf{C}_\mathrm{u}$, $\mathbf{D}_\mathrm{u}$ are square matrices of dimension N_c. The elements of the $2N_\mathrm{c} \times 2N_\mathrm{c}$ matrix $\mathbf{T}_\mathrm{u}$ are computed from the matrices of p.u.l. impedances $\mathbf{Z}'$ and admittances $\mathbf{Y}'$ of the MTL, assuming the N_c conductors to be at a constant height along the span. The matrix $\mathbf{Z}'$ accounts for the matrix of p.u.l. external inductances of the line, the p.u.l. internal

[1]To apply the proposed approach, the line should be modelled as a periodic structure; the conductors are at a constant height along consecutive spans, which are delimited by poles displaying the same electrical and geometric features, as well as the same grounding impedance.

impedance of the conductors, and the matrix of p.u.l. impedances associated with the ground return path.

The transfer matrix $\mathbf{T}_{\mathrm{g}}$ of the half pole is written as:

$$\mathbf{T}_{\mathrm{g}} = \begin{bmatrix} [\mathbf{1}] & [\mathbf{0}] \\ \mathbf{Y}_{\mathrm{g}} & [\mathbf{1}] \end{bmatrix} ; \tag{7.4}$$

each submatrix in (7.4) has dimension $N_{\mathrm{c}} \times N_{\mathrm{c}}$. Distinguishing between phase conductors and ground wires, the symmetric matrix of admittances $\mathbf{Y}_{\mathrm{g}}$ in (7.4) can be defined as

$$\mathbf{Y}_{\mathrm{g}} = \mathbf{Y}_{\mathrm{g}}^{T} = \frac{1}{2} \begin{bmatrix} [\mathbf{0}] & [\mathbf{0}] \\ [\mathbf{0}] & \mathbf{Y}_{\mathrm{gg}} \end{bmatrix} , \; \mathbf{i}_{\mathrm{pole}} = \mathbf{Y}_{\mathrm{gg}} \mathbf{v}_{\mathrm{gw}} \tag{7.5}$$

where $\mathbf{Y}_{\mathrm{gg}} = \mathbf{Z}_{\mathrm{gg}}^{-1}$ is a $N_{\mathrm{gw}} \times N_{\mathrm{gw}}$ complex symmetric matrix which relates the voltages $\mathbf{v}_{\mathrm{gw}}$ of the ground wires to the vertical currents $\mathbf{i}_{\mathrm{pole}}$ flowing through the pole, from the ground wires to ground. The entries of matrix $\mathbf{Y}_{\mathrm{gg}}$ are calculated based on the particular features of the poles and grounding impedance.

Details on the computation of the transfer matrix of the uniform span $\mathbf{T}_{\mathrm{u}}$, on the inclusion of the p.u.l. internal impedances of the conductors and of the impedance deriving from the ground return path are included in Sec. 7.1.1.

The transfer matrix $\mathbf{T}$, associated with the defined unit cell, is computed as the cascade of the transfer matrices associated with the half pole at the left termination, the uniform span, and the half pole at the right termination of the cell:

$$\mathbf{T} = \mathbf{T}_{\mathrm{g}} \mathbf{T}_{\mathrm{u}} \mathbf{T}_{\mathrm{g}} = \begin{bmatrix} \mathbf{A} & \mathbf{B} \\ \mathbf{C} & \mathbf{D} \end{bmatrix} . \tag{7.6}$$

From (7.2)-(7.4), due to the validity of the reciprocity theorem, and recalling the symmetry of the cell:

$$\mathbf{A} = \mathbf{A}_{\mathrm{u}} + \mathbf{B}_{\mathrm{u}} \mathbf{Y}_{\mathrm{g}} \tag{7.7a}$$

$$\mathbf{B} = \mathbf{B}_{\mathrm{u}} \tag{7.7b}$$

$$\mathbf{C} = \mathbf{B}^{-1} \left(\mathbf{A}^2 - [\mathbf{1}] \right) \tag{7.7c}$$

$$\mathbf{D} = \mathbf{A}^{T} . \tag{7.7d}$$

From the theory of modal analysis for MTLs, the vector of the N_{c} propagation constants $\boldsymbol{\gamma}$ and the $N_{\mathrm{c}} \times N_{\mathrm{c}}$ matrix of characteristic admittances $\mathbf{Y}_{\mathrm{w}}$, which are needed to describe the wave properties within the unit cell, satisfy the following relations:

$$\mathbf{M}^{-1} \mathbf{A} \mathbf{M} = [\cosh(\boldsymbol{\gamma} \ell)] \tag{7.8a}$$

$$\mathbf{Y}_{\mathrm{w}} = \mathbf{B}^{-1} \mathbf{M} [\sinh(\boldsymbol{\gamma} \ell)] \mathbf{M}^{-1} . \tag{7.8b}$$

In (7.8a) and (7.8b), $[\cosh(\boldsymbol{\gamma}\ell)]$ and $[\sinh(\boldsymbol{\gamma}\ell)]$ are diagonal matrices, whose diagonal element, placed at row i and column j with $i = j$, is given by $\cosh(\gamma_i\ell)$ and $\sinh(\gamma_i\ell)$, respectively. Matrix $\mathbf{M}$ is the modal transformation matrix. The computation of the N_c propagation constants can be easily performed observing that the RHS of (7.8a) is a diagonal matrix; hence, matrix $\mathbf{M}$ coincides with the diagonalizing matrix of $\mathbf{A}$, i.e., the matrix of eigenvectors of $\mathbf{A}$. The corresponding eigenvalues are represented by the non-zero elements of the diagonal matrix $[\cosh(\boldsymbol{\gamma}\ell)]$ in (7.8a). After having calculated the eigenvalues ν_i (with $i = 1 \ldots N_c$) and eigenvectors of $\mathbf{A}$, the generic propagation constant γ_i is computed as

$$\gamma_i = \cosh^{-1}(\nu_i) \ . \tag{7.9}$$

Figure 7.1a displays the MTL structure extending from $x = -M_L\ell$ (substation site) to $x = +M_R\ell$ (transformer site). The MTL is hit by a lightning stroke at the 0^{th} pole, placed at $x = 0$; the vectors of phase conductors and ground wires voltages at pole 0 are denoted by $\mathbf{v}_{0\text{pc}}$ and $\mathbf{v}_{0\text{gw}}$, respectively. $\mathbf{T}_\text{L}$ and $\mathbf{T}_\text{R}$ are the transfer matrices of the MTL sections towards the left and right direction with respect to the impact point (i.e., pole 0 in Fig. 7.1a).

In standard chain matrix analysis, $\mathbf{T}_\text{L}$ and $\mathbf{T}_\text{R}$ may be computed as:

$$\mathbf{T}_\text{L} = \prod_{L_k=1}^{M_L} (\mathbf{T})_{L_k} \tag{7.10a}$$

$$\mathbf{T}_\text{R} = \prod_{R_k=1}^{M_R} (\mathbf{T})_{R_k} \ , \tag{7.10b}$$

where matrices $(\mathbf{T})_{L_k}$ and $(\mathbf{T})_{R_k}$ denote the transfer matrices of the cells in which the line is divided, located at the left and at the right sides of pole 0. If, as it is assumed here, the MTL is modelled as a periodic structure, i.e., as a cascade of equal cells, the transfer matrices $\mathbf{T}_\text{L}$ and $\mathbf{T}_\text{R}$ can be computed as:

$$\mathbf{T}_\text{L} = \begin{bmatrix} \mathbf{A}_\text{L} & \mathbf{B}_\text{L} \\ \mathbf{C}_\text{L} & \mathbf{D}_\text{L} \end{bmatrix} = \begin{bmatrix} \mathbf{M}(\cosh(M_L\boldsymbol{\gamma}\ell))\mathbf{M}^{-1} & \mathbf{M}(\sinh(M_L\boldsymbol{\gamma}\ell))(\mathbf{Y}_\text{w}\mathbf{M})^{-1} \\ (\mathbf{Y}_\text{w}\mathbf{M})(\sinh(M_L\boldsymbol{\gamma}\ell))\mathbf{M}^{-1} & (\mathbf{M}(\cosh(M_L\boldsymbol{\gamma}\ell))\mathbf{M}^{-1})^T \end{bmatrix} \tag{7.11}$$

$$\mathbf{T}_\text{R} = \begin{bmatrix} \mathbf{A}_\text{R} & \mathbf{B}_\text{R} \\ \mathbf{C}_\text{R} & \mathbf{D}_\text{R} \end{bmatrix} = \begin{bmatrix} \mathbf{M}(\cosh(M_R\boldsymbol{\gamma}\ell))\mathbf{M}^{-1} & \mathbf{M}(\sinh(M_R\boldsymbol{\gamma}\ell))(\mathbf{Y}_\text{w}\mathbf{M})^{-1} \\ (\mathbf{Y}_\text{w}\mathbf{M})(\sinh(M_R\boldsymbol{\gamma}\ell))\mathbf{M}^{-1} & (\mathbf{M}(\cosh(M_R\boldsymbol{\gamma}\ell))\mathbf{M}^{-1})^T \end{bmatrix} . \tag{7.12}$$

Figure 7.1c displays the cascade of matrices modelling the portions of TL at the left and right sides of pole 0. These are connected, at the terminations, to matrices of admittances $\mathbf{Y}_{\text{subs}}$ and $\mathbf{Y}_{\text{tran}}$, representing the equivalent for the substation and the transformer, respectively.

However, since $\mathbf{T}_{\text{L}}$ and $\mathbf{T}_{\text{R}}$ are given by the cascade of the transfer matrices of some unit cells of the type (7.6), they only account for half a pole at each line termination; this is the reason why, the contributions of the other half of the very first and the very last pole of the line are to be included in the computation of the terminating matrices of admittances of the line $\mathbf{Y}_{\text{L}}$ and $\mathbf{Y}_{\text{R}}$:

$$\mathbf{Y}_{\text{L}} = \mathbf{Y}_{\text{subs}} + \mathbf{Y}_{\text{g}} \,. \tag{7.13}$$

$$\mathbf{Y}_{\text{R}} = \mathbf{Y}_{\text{tran}} + \mathbf{Y}_{\text{g}} \,. \tag{7.14}$$

Using the quantities above, the following expressions are derived

$$\mathbf{v}_0 = (\mathbf{A}_{\text{L}} + \mathbf{B}_{\text{L}}\mathbf{Y}_{\text{L}})\,\mathbf{v}_{\text{L}} \tag{7.15a}$$

$$\mathbf{i}_{0\text{L}} = (\mathbf{C}_{\text{L}} + \mathbf{D}_{\text{L}}\mathbf{Y}_{\text{L}})\,\mathbf{v}_{\text{L}} = \mathbf{Y}_{0\text{L}}\mathbf{v}_0 \tag{7.15b}$$

$$\mathbf{Y}_{0\text{L}} = (\mathbf{C}_{\text{L}} + \mathbf{D}_{\text{L}}\mathbf{Y}_{\text{L}})\,(\mathbf{A}_{\text{L}} + \mathbf{B}_{\text{L}}\mathbf{Y}_{\text{L}})^{-1} \tag{7.15c}$$

and

$$\mathbf{v}_0 = (\mathbf{A}_{\text{R}} + \mathbf{B}_{\text{R}}\mathbf{Y}_{\text{R}})\,\mathbf{v}_{\text{R}} \tag{7.16a}$$

$$\mathbf{i}_{0\text{R}} = (\mathbf{C}_{\text{R}} + \mathbf{D}_{\text{R}}\mathbf{Y}_{\text{R}})\,\mathbf{v}_{\text{R}} = \mathbf{Y}_{0\text{R}}\mathbf{v}_0 \tag{7.16b}$$

$$\mathbf{Y}_{0\text{R}} = (\mathbf{C}_{\text{R}} + \mathbf{D}_{\text{R}}\mathbf{Y}_{\text{R}})\,(\mathbf{A}_{\text{R}} + \mathbf{B}_{\text{R}}\mathbf{Y}_{\text{R}})^{-1} \;, \tag{7.16c}$$

where $\mathbf{Y}_{0\text{L}}$ and $\mathbf{Y}_{0\text{R}}$ are the matrices of input admittances seen at the left and right sides of pole 0; $\mathbf{v}_0$ is the vector of the conductors voltages at the struck pole; $\mathbf{i}_{0\text{L}}$ and $\mathbf{i}_{0\text{R}}$ are the vectors of currents flowing through the line conductors in the left and right direction with respect to pole 0. Hence, the whole system displayed in Fig. 7.1d is reduced to the one in Fig. 7.1e.

The vector $\mathbf{i}_{\text{H}}$, of dimension $N_{\text{gw}} \times 1$, is introduced to account for the lightning currents injected into the struck ground wires at pole 0. The element $I_{\text{H}_i}(\omega)$, with $i = 1 \ldots N_{\text{gw}}$, represents the lightning current injected in the i^{th} ground wire at pole 0 with angular frequency ω (performing the Fourier transform of the assumed TD lightning current):

$$\mathbf{i}_{\text{H}} = \left[I_{\text{H}_1}(\omega) \cdots I_{\text{H}_k}(\omega) \cdots I_{\text{H}_{N_{\text{gw}}}}(\omega) \right]^T \,, \tag{7.17}$$

with $I_{\text{H}_i}(\omega) = 0$ if the i^{th} ground wire is not struck by a lightning stroke.

The vector $\mathbf{i}_{\text{H}}$ allows for the analysis of different conditions, such as one or more ground wires struck at the same or different time instants by the same or different lightning currents.

With the purpose of expressing $\mathbf{v}_0$ (i.e. the conductor-to-ground voltages at pole 0) in terms of $\mathbf{i}_{\text{H}}$, $\mathbf{v}_0$ is decomposed into vectors of phase voltages $\mathbf{v}_{0\text{pc}}$ and ground wires voltages $\mathbf{v}_{0\text{gw}}$:

$$\mathbf{v}_0 = \begin{bmatrix} \mathbf{v}_{0\mathrm{pc}}\left(\mathbf{i}_{\mathrm{H}}\right) \\ \mathbf{v}_{0\mathrm{gw}}\left(\mathbf{i}_{\mathrm{H}}\right) \end{bmatrix} . \tag{7.18}$$

From (7.15) and (7.16), with reference to Fig. 7.1e, expressions (7.19) and (7.20) are computed:

$$\mathbf{i}_{0\mathrm{L}} = \begin{bmatrix} \left(\mathbf{i}_{0\mathrm{L}}\right)_{\mathrm{pc}} \\ \left(\mathbf{i}_{0\mathrm{L}}\right)_{\mathrm{gw}} \end{bmatrix} = \mathbf{Y}_{0\mathrm{L}} \begin{bmatrix} \mathbf{v}_{0\mathrm{pc}} \\ \mathbf{v}_{0\mathrm{gw}} \end{bmatrix} \tag{7.19a}$$

$$\mathbf{i}_{0\mathrm{R}} = \begin{bmatrix} \left(\mathbf{i}_{0\mathrm{R}}\right)_{\mathrm{pc}} \\ \left(\mathbf{i}_{0\mathrm{R}}\right)_{\mathrm{gw}} \end{bmatrix} = \mathbf{Y}_{0\mathrm{R}} \begin{bmatrix} \mathbf{v}_{0\mathrm{pc}} \\ \mathbf{v}_{0\mathrm{gw}} \end{bmatrix} \tag{7.19b}$$

$$\begin{bmatrix} [\mathbf{0}] \\ \mathbf{i}_{\mathrm{H}} \end{bmatrix} = \left(\mathbf{Y}_{0\mathrm{L}} + \mathbf{Y}_{0\mathrm{R}}\right) \begin{bmatrix} \mathbf{v}_{0\mathrm{pc}} \\ \mathbf{v}_{0\mathrm{gw}} \end{bmatrix} \tag{7.20}$$

where (7.20) was obtained by summing the two equations in (7.19), taking also into consideration the equivalencies $\left(\mathbf{i}_{0\mathrm{L}}\right)_{\mathrm{pc}} = -\left(\mathbf{i}_{0\mathrm{R}}\right)_{\mathrm{pc}}$ and $\left(\mathbf{i}_{0\mathrm{L}}\right)_{\mathrm{gw}} + \left(\mathbf{i}_{0\mathrm{R}}\right)_{\mathrm{gw}} = \mathbf{i}_{\mathrm{H}}$, which result from the direct application of KCL at pole 0, in Fig. 7.1e.

Furthermore, introducing for convenience the symmetric matrix of input impedances $\mathbf{Z}_0$,

$$\mathbf{Z}_0 = \begin{bmatrix} \mathbf{Z}_{\mathrm{pc,pc}} & \mathbf{Z}_{\mathrm{pc,gw}} \\ \mathbf{Z}_{\mathrm{gw,pc}} & \mathbf{Z}_{\mathrm{gw,gw}} \end{bmatrix} = \left(\mathbf{Y}_{0\mathrm{L}} + \mathbf{Y}_{0\mathrm{R}}\right)^{-1} , \tag{7.21}$$

$\mathbf{v}_0$ in (7.18) may be finally expressed as

$$\mathbf{v}_0 = \begin{bmatrix} \mathbf{v}_{0\mathrm{pc}} \\ \mathbf{v}_{0\mathrm{gw}} \end{bmatrix} = \begin{bmatrix} \mathbf{Z}_{\mathrm{pc,gw}}\mathbf{i}_{\mathrm{H}} \\ \mathbf{Z}_{\mathrm{gw,gw}}\mathbf{i}_{\mathrm{H}} \end{bmatrix} . \tag{7.22}$$

The computation of the insulator voltages at pole 0 is achieved by subtracting two voltage vectors:

$$\mathbf{v}_0^{\mathrm{ins}} = \mathbf{v}_0^{\mathrm{arm}} - \mathbf{v}_{0\mathrm{pc}} \, ; \tag{7.23}$$

the second term on the RHS of (7.23) gathers the already known phase voltages $\mathbf{v}_{0\mathrm{pc}}$; the first one gathers the yet unknown voltages $\mathbf{v}_0^{\mathrm{arm}}$ of the conductive pole arms, where insulators are hanging. Vector $\mathbf{v}_0^{\mathrm{arm}}$ can be determined using the information conveyed by the vector of the ground wires voltages $\mathbf{v}_{0\mathrm{gw}}$

$$\mathbf{v}_0^{\mathrm{arm}} = \mathbf{P}\mathbf{v}_{0\mathrm{gw}} \tag{7.24}$$

where the entries of the $N_{\mathrm{pc}} \times N_{\mathrm{gw}}$ matrix $\mathbf{P}$ depend on the type, geometry, and implemented circuit model of the pole.

Combining expressions (7.22)-(7.24), the following is obtained

$$\mathbf{v}_0^{\text{ins}} = \mathbf{P}\mathbf{v}_{0\text{gw}} - \mathbf{v}_{0\text{pc}} = \left(\mathbf{P}\mathbf{Z}_{\text{gw,gw}} - \mathbf{Z}_{\text{pc,gw}}\right)\mathbf{i}_{\text{H}}\,. \tag{7.25}$$

At any pole, located at $x = m_{\text{R}}\ell$ to the right of the lightning impact point, the vector of voltages across the insulators $\mathbf{v}_{m_{\text{R}}}^{\mathbf{ins}}$ is computed as

$$\mathbf{v}_{m_{\text{R}}}^{\mathbf{ins}} = \mathbf{P}\left(\mathbf{v}_{m_{\text{R}}}\right)_{\text{gw}} - \left(\mathbf{v}_{m_{\text{R}}}\right)_{\text{pc}} \tag{7.26}$$

where

$$\mathbf{v}_{m_{\text{R}}} = \begin{bmatrix} \left(\mathbf{v}_{m_{\text{R}}}\right)_{\text{pc}} \\ \left(\mathbf{v}_{m_{\text{R}}}\right)_{\text{gw}} \end{bmatrix} = \left(\mathbf{A}_{m_{\text{R}}} - \mathbf{B}_{m_{\text{R}}}\mathbf{Y}_{0\text{R}}\right)\mathbf{v}_0 \tag{7.27a}$$

$$\begin{cases} \mathbf{A}_{m_{\text{R}}} = \mathbf{M}\left(\cosh\left(m_{\text{R}}\boldsymbol{\gamma}\ell\right)\right)\mathbf{M}^{-1} \\ \mathbf{B}_{m_{\text{R}}} = \mathbf{M}\left(\sinh\left(m_{\text{R}}\boldsymbol{\gamma}\ell\right)\right)\left(\mathbf{Y}_{\text{w}}\mathbf{M}\right)^{-1}. \end{cases} \tag{7.27b}$$

Analogously, for any pole located to the left of the lightning impact point, at $x = -m_{\text{L}}\ell$, $\mathbf{v}_{m_{\text{L}}}^{\mathbf{ins}}$ is computed as

$$\mathbf{v}_{m_{\text{L}}}^{\mathbf{ins}} = \mathbf{P}\left(\mathbf{v}_{m_{\text{L}}}\right)_{\text{gw}} - \left(\mathbf{v}_{m_{\text{L}}}\right)_{\text{pc}} \tag{7.28}$$

where

$$\mathbf{v}_{m_{\text{L}}} = \begin{bmatrix} \left(\mathbf{v}_{m_{\text{L}}}\right)_{\text{pc}} \\ \left(\mathbf{v}_{m_{\text{L}}}\right)_{\text{gw}} \end{bmatrix} = \left(\mathbf{A}_{m_{\text{L}}} - \mathbf{B}_{m_{\text{L}}}\mathbf{Y}_{0\text{L}}\right)\mathbf{v}_0 \tag{7.29a}$$

$$\begin{cases} \mathbf{A}_{m_{\text{L}}} = \mathbf{M}\left(\cosh\left(m_{\text{L}}\boldsymbol{\gamma}\ell\right)\right)\mathbf{M}^{-1} \\ \mathbf{B}_{m_{\text{L}}} = \mathbf{M}\left(\sinh\left(m_{\text{L}}\boldsymbol{\gamma}\ell\right)\right)\left(\mathbf{Y}_{\text{w}}\mathbf{M}\right)^{-1}. \end{cases} \tag{7.29b}$$

When addressing the configuration of an MTL extending infinitely to the right and to the left of the 0^{th} pole, $\mathbf{Y}_{0\text{R}} = \mathbf{Y}_{0\text{L}} = \mathbf{Y}_{\text{w}}$ is to be considered; from (7.27) and (7.29), the insulator voltages at symmetric poles $m = m_{\text{R}} = m_{\text{L}}$ are indistinctly given by

$$\mathbf{v}_m^{\text{ins}} = \left(\mathbf{M}\,e^{-\gamma m\ell}\mathbf{M}^{-1}\right)\mathbf{v}_0^{\text{ins}}\,. \tag{7.30}$$

In this case, the insulator voltages at $x = 0$ and at $x = \pm m\ell$ would be simply related through an exponential propagation matrix.

The TD counterpart of the quantities estimated in the FD within a selected frequency range may be retrieved by performing an IFT. It should be noted that the proposed approach does not account for the coupling of the line with the EM field produced by the lightning current [13] (accounted for in Chapter 3 by means of distributed sources), which may be investigated by superposition of the effects.

7.1.1 Computation of fundamental matrices

In this section, the structure of some matrices relevant for the implementation of the method is analysed.

Matrix of the line p.u.l. impedances $\mathbf{Z}'$

The $N_\mathrm{c} \times N_\mathrm{c}$ matrix of longitudinal line p.u.l. impedances accounts for three contributions: the line external inductances, the internal impedance of each conductor, and the impedances associated with the ground return path.

The matrix of the p.u.l. external inductances $\mathbf{L}'_\mathrm{ext}$ is computed assuming that the propagation velocity of travelling waves along the MTL is equal to the speed of light in vacuum c_0. Hence, starting from the matrix of potential coefficients $\mathbf{P}'$ (which is computed by standard electrostatics relations in the transverse plane, under the assumption of TEM propagation of the electromagnetic field, and $\epsilon_\mathrm{g} \gg \epsilon_0$), $\mathbf{L}'_\mathrm{ext}$ is found as:

$$\mathbf{L}'_\mathrm{ext} = \frac{1}{c_0^2}\mathbf{P}' \,. \tag{7.31}$$

The matrix of the conductors p.u.l. internal impedances $\mathbf{Z}'_\mathrm{int}$ is a diagonal matrix of order N_c. The diagonal element $Z_{\mathrm{int},i}$, with $i = 1, \ldots, N_\mathrm{c}$, is computed by expression (1.12), based on Schelkunoff's theory [14], accounting for the conductors frequency-dependent p.u.l. losses and internal inductance.

As to the matrix of the impedances associated with the ground return path, the FD approach illustrated in Sec. 1.1.2 is applied. In particular, the expressions derived from Carson's theory and Semlyen's theory ([15], [16]) are implemented below and above the critical frequency f_L, respectively. The critical frequency (1.17) is used to approximate the ground to a good conductor at frequencies below f_L, or to an insulator in the higher frequency range, $f > f_L$. Hence, the generic element $Z'_{\mathrm{g},ij}$ of the matrix of p.u.l. ground impedances $\mathbf{Z}'_\mathrm{g}$ is computed as

$$Z'_{\mathrm{g},ij}(f) = \begin{cases} {Z^\mathrm{A}_{\mathrm{g},ij}}'(f) & f \le f_L \\ {Z^\mathrm{B}_{\mathrm{g},ij}}'(f) & f > f_L \,, \end{cases} \tag{7.32}$$

where ${Z^\mathrm{A}_{\mathrm{g},ij}}'$ and ${Z^\mathrm{A}_{\mathrm{g},ij}}'$ are computed by means of expressions (1.14) and (1.15) in Chapter 1, respectively.

Finally, the matrix of the longitudinal p.u.l. impedances of the MTL is computed as the sum of the three aforementioned contributions:

$$\mathbf{Z}' = \mathbf{Z}'_\mathrm{int} + \mathbf{Z}'_\mathrm{g} + j\omega\mathbf{L}'_\mathrm{ext} \,. \tag{7.33}$$

Tower admittance matrix $\mathbf{Y}_\mathrm{g}$ and auxiliary matrix $\mathbf{P}$

The structure of matrices $\mathbf{Y}_\mathrm{g}$ and $\mathbf{P}$, introduced in Sec. 7.1, is strongly dependent on the geometric features of the considered pole (i.e., height, equivalent radius, arms height) and on the arrangement of the ground wires.

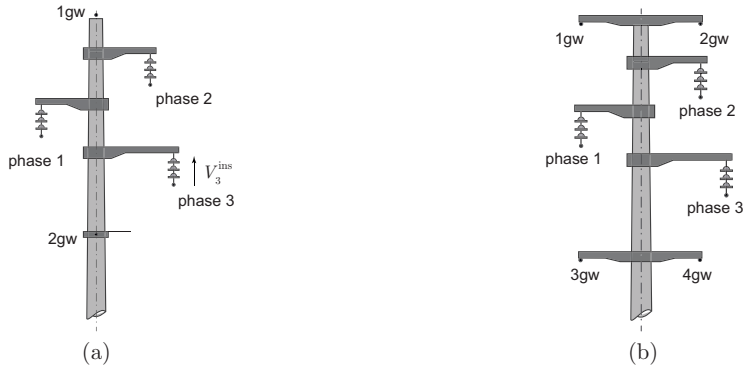

Figure 7.3. Reference configurations for the conductors arrangement at the poles, including SWs and UGWs. (a) *Example 1*, line with two ground wires; (b) *example 2*, line with four ground wires.

Two different pole geometries (which refer to the distribution line configurations considered for numerical results in Sec. 7.2) are described here, and are displayed in Fig. 7.3. In Fig. 7.3a (*example 1*), the pole consists in a hollow metallic cylinder with three arms for the three power carrying conductors; the line is equipped with two ground wires; in Fig. 7.3b (*example 2*), the pole supports, along with the three phase conductors, four additional ground wires. In both configurations, ground wires are installed both above and below the phase conductors.

Example 1

In Fig. 7.4, the geometrical features of the first analysed pole are included, and the equivalent circuit is depicted. The pole is divided into five sections, delimited by the points of connection of the arms to the pole body. The sections may be considered as electrically short, since the height of poles for distribution lines applications typically ranges between 10 and 15 m, and lightning currents may excite frequencies up to some MHz (with reference to subsequent stroke currents); hence, equivalent circuits of the pole with lumped parameters may be adopted.

For simulation purposes, the selected geometrical characteristics are those of a typical Italian MV distribution line (rated voltage 20 kV) with steel sheet welded poles. The top/bottom diameters and thickness of the hollow pole are, respectively, 280/661 mm and 6 mm.

In order to compute the impedances of the pole sections in Fig. 7.4b, an equivalent cylindrical structure has been considered for the pole, with average external radius $b = 0.235$ m, thickness 6 mm, and average internal radius $a = 0.229$ m.

The radii of the aluminum phase conductors and ground wires are 10 mm

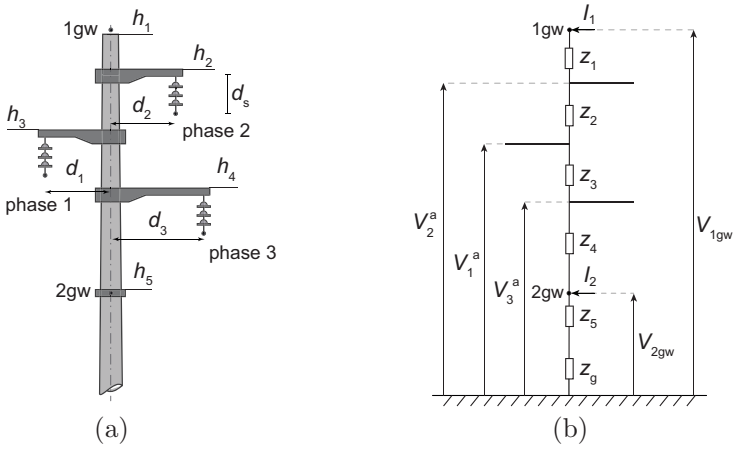

Figure 7.4. (a) Sketch of the pole (*example 1*); (b) equivalent circuit with lumped parameters.

and 19.6 mm, respectively. The pole has been modelled considering typical values of ANSI steel: $\sigma = 1.45$ MS/m and $\mu_r = 100$. It should be noted that the relative permeability μ_r of the steel depends on the current density and frequency. A nonlinear saturation model and a Debye form of the complex magnetic permeability could be required in lightning studies; this aspect is here neglected, adopting a linear model for the pole and a constant permeability value (valid at high frequencies for a large set of current densities [17]). Indeed, the external inductance is the one that contributes predominantly to the response of the pole.

In particular, the impedance of section i of length ℓ_i, with $i = 1 \dots 5$, is computed as the sum of two terms:

$$z_i\left(y_i, \ell_i, \omega\right) = z'_{\text{int}}\left(\omega\right) \ell_i + j\omega L_{\text{ext}i}\left(y_i, \ell_i\right) \ . \tag{7.34}$$

z'_{int} is the internal p.u.l. impedance of the hollow conductor, computed according to Schelkunoff's theory [14]

$$z'_{\text{int}}\left(\omega\right) = \frac{m}{2\pi\sigma b} \frac{K_1\left(x_1\right) I_0\left(x_2\right) + I_1\left(x_1\right) K_0\left(x_2\right)}{K_1\left(x_1\right) I_1\left(x_2\right) - I_1\left(x_1\right) K_1\left(x_2\right)} \ , \tag{7.35}$$

with $x_1 = ma$, $x_2 = mb$, and $m = \sqrt{j\omega\mu_0\mu_r\sigma}$ (valid when approximating the pole material to a good conductor).
$L_{\text{ext}i}$ is the external inductance associated with the i^{th} section, derived from the circulation of the magnetic vector potential $\overrightarrow{A}$

$$L_{\mathrm{ext}\,i}\,(y_i,\ell_i)=\frac{1}{I}\int_{y_i}^{y_i+\ell_i}A_y(b,y')\mathrm{d}y'=$$
$$=\frac{\mu_0}{4\pi}\left\{\sqrt{(h+y_i)^2+b^2}-\sqrt{(h-y_i)^2+b^2}\right.$$
$$+\sqrt{(\ell_i-h+y_i)^2+b^2}-\sqrt{(\ell_i+h+y_i)^2+b^2}$$
$$+(h-\ell_i-y_i)\ln\left[\sqrt{(-h+\ell_i+y_1)^2+b^2}-h+\ell_i+y_i\right]$$
$$+(h+\ell_i+y_i)\ln\left[\sqrt{(h+\ell_i+y_i)^2+b^2}+h+\ell_i+y_i\right]$$
$$+(y_i-h)\ln\left[\sqrt{(h-y_i)^2+b^2}-h+y_i\right]$$
$$\left.-(y_i+h)\ln\left[\sqrt{(h+y_i)^2+b^2}+h+y_i\right]\right\}\ . \quad (7.36)$$

The assumption $\overrightarrow{A}=A_y\hat{y}$ was made[2], neglecting the effect of the edges of the pole sections, and computing A_y in the surrounding medium as the superposition of the magnetic potential due to the y-invariant current I, flowing down the pole of external radius b, and its image:

$$A_y=\frac{\mu_0 I}{4\pi}\int_0^h\left[\underbrace{\frac{1}{\sqrt{(y-y')^2+b^2}}}_{\text{real structure}}+\underbrace{\frac{1}{\sqrt{(y+y')^2+b^2}}}_{\text{image structure}}\right]\mathrm{d}y'$$
$$=\frac{\eta_0 I}{4\pi c_0}\ln\left(\frac{y+h+\sqrt{(y+h)^2+b^2}}{y-h+\sqrt{(y-h)^2+b^2}}\right) \quad (7.37)$$

where η_0 is the free space impedance.

Matrices $\mathbf{Y}_{\mathrm{gg}}$ and $\mathbf{P}$ are derived using the pole equivalent circuit in Fig. 7.4b as a reference. I_1 and I_2 are the lightning currents injected by the ground wires into the pole, and dispersed into the ground through the pole grounding impedance z_{g}; $V_{1\mathrm{gw}}$ and $V_{2\mathrm{gw}}$ are the ground wires voltages. V_1^{a}, V_2^{a}, and V_3^{a} are the voltages of the pole arms. Using Kirchhoff's laws, and recalling the matrix $\mathbf{Z}_{\mathrm{gg}}=\mathbf{Y}_{\mathrm{gg}}^{-1}$ (introduced in (7.5)), the following are derived (Fig. 7.4b):

$$\mathbf{v}_{\mathrm{gw}}=\begin{bmatrix}V_{1\mathrm{gw}}\\V_{2\mathrm{gw}}\end{bmatrix}=\mathbf{Z}_{\mathrm{gg}}\underbrace{\begin{bmatrix}I_1\\I_2\end{bmatrix}}_{\mathbf{i}_{\mathrm{pole}}} \quad (7.38)$$

[2]Herein, $\hat{y}$ denotes the direction of the vertical axis, oriented upwards.

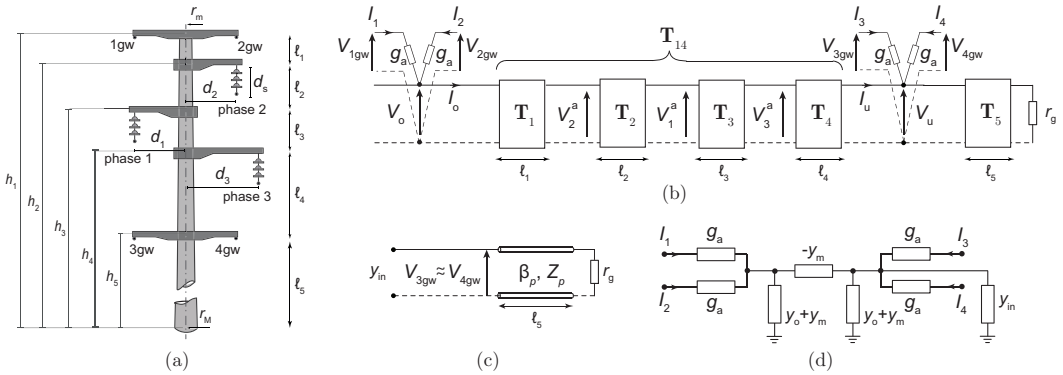

Figure 7.5. (a) Sketch of the pole (*example 2*); (b) equivalent circuit with distributed parameters by means of the transfer matrices associated with the pole sections; (c) lower section of the pole, closed on the grounding resistance r_{g}; (d) reduction to an equivalent circuit of admittances.

$$\mathbf{Z}_{\mathrm{gg}} = z_p \begin{bmatrix} 1 & 0 \\ 0 & 0 \end{bmatrix} + (z_5 + z_{\mathrm{g}}) \begin{bmatrix} 1 & 1 \\ 1 & 1 \end{bmatrix} \tag{7.39a}$$

$$\mathbf{Y}_{\mathrm{gg}} = z_p^{-1} \begin{bmatrix} 1 & -1 \\ -1 & 1 \end{bmatrix} + (z_5 + z_{\mathrm{g}})^{-1} \begin{bmatrix} 0 & 0 \\ 0 & 1 \end{bmatrix} \tag{7.39b}$$

with $z_p = z_1 + z_2 + z_3 + z_4$.

From the computed values of the ground wires voltages at the observed pole, the voltages of the pole arms are derived by applying voltage divider analysis to the circuit in Fig. 7.4b:

$$\begin{bmatrix} V_1^{\mathrm{a}} \\ V_2^{\mathrm{a}} \\ V_3^{\mathrm{a}} \end{bmatrix} = \mathbf{P} \begin{bmatrix} V_{1\mathrm{gw}} \\ V_{2\mathrm{gw}} \end{bmatrix}, \ \mathbf{P} = \begin{bmatrix} (1-\beta) & \beta \\ (1-\alpha) & \alpha \\ (1-\eta) & \eta \end{bmatrix} \tag{7.40}$$

where

$$\alpha = \frac{z_1}{z_p}, \ \beta = \frac{z_1 + z_2}{z_p}, \ \eta = \frac{z_1 + z_2 + z_3}{z_p} \, . \tag{7.41}$$

Example 2

In Fig. 7.5a, the geometrical features of the second pole are included, while Figs. 7.5b-7.5d display some relevant aspects of the adopted equivalent circuit with distributed parameters.

Following the same approach illustrated in *example 1*, the pole is divided into five sections, and reduced to an equivalent cylindrical structure with

diameter $2r_{\rm eq}$ (median value between the top/bottom diameters, equal to 304 mm and 661 mm, respectively). Each section is modelled as a lossless TL with characteristic impedance Z_i and propagation constant β_i ($i = 1 \dots 5$), given by

$$Z_i = Z_p = 60 \left[\ln \left(\frac{4h}{r_{\rm eq}} \right) - 1 \right] \tag{7.42a}$$

$$\beta_i = \beta_p = \frac{\omega}{c_0} \,, \tag{7.42b}$$

where $h = h_1$ (i.e., the pole height); expression (7.42a) corresponds to the revised formula by Jordan [18]. It should be noted that the same Z_p and β_p have been adopted for all the pole sections.

With reference to Fig. 7.5b, the $i^{\rm th}$ section is represented by the transfer matrix $\mathbf{T}_i$, linking voltages and currents at its input/output ends. Matrices $\mathbf{T}_i$ of dimension 2×2 can be written as:

$$\mathbf{T}_n \quad = \quad \left[\begin{array}{cc} A_n & B_n \\ C_n & D_n \end{array} \right] \quad = \quad \left[\begin{array}{cc} \cos\left(\beta_p \ell_n\right) & j Z_p \sin\left(\beta_p \ell_n\right) \\ j Z_p^{-1} \sin\left(\beta_p \ell_n\right) & \cos\left(\beta_p \ell_n\right) \end{array} \right] . \tag{7.43}$$

For convenience, the transfer matrix $\mathbf{T}_{m4}$ is introduced, accounting for the cascade connection of two-port networks located between network m and 4 in Fig. 7.5b:

$$\mathbf{T}_{m4} = \prod_{n=m}^{4} \mathbf{T}_n = \left[\begin{array}{cc} A_{m4} & B_{m4} \\ C_{m4} & D_{m4} \end{array} \right] = \\ = \left[\begin{array}{cc} \cos\left(\beta_p \ell_{m4}\right) & j Z_p \sin\left(\beta_p \ell_{m4}\right) \\ j Y_p \sin\left(\beta_p \ell_{m4}\right) & \cos\left(\beta_p \ell_{m4}\right) \end{array} \right] , \tag{7.44}$$

where $\ell_{m4} = \sum_{n=m}^{4} \ell_n$, $m = 1, 2, 3$.

The matrix $\mathbf{T}_{14}$, indicated in Fig. 7.5b and linking voltage $V_{\rm o}$ and $V_{\rm u}$, is first computed according to (7.44). Successively, it is converted into the admittance matrix $\mathbf{Y}_{14}$, in order to obtain the admittance matrix $\mathbf{Y}_{\rm gg}$:

$$\mathbf{Y}_{14} = \left[\begin{array}{cc} y_{\rm o} & y_{\rm m} \\ y_{\rm m} & y_{\rm o} \end{array} \right] = \left[\begin{array}{cc} D_{14} B_{14}^{-1} & -B_{14}^{-1} \\ -B_{14}^{-1} & A_{14} B_{14}^{-1} \end{array} \right] . \tag{7.45}$$

The section at the pole base, connected to the grounding resistance $r_{\rm g}$, is reduced to the corresponding input admittance $y_{\rm in}$, seen by the lower ground wires (denoted with 3gw and 4gw in Fig. 7.5c)

$$y_{\rm in} = Z_p^{-1} \frac{Z_p + j r_{\rm g} \tan\left(\beta_p \ell_5\right)}{r_{\rm g} + j Z_p \tan\left(\beta_p \ell_5\right)} \,. \tag{7.46}$$

The equivalent circuit of the pole, written in terms of admittances, is depicted in Fig. 7.5d, and can be solved by standard nodal analysis:

$$\underbrace{\begin{bmatrix} I_1 \\ \vdots \\ I_4 \end{bmatrix}}_{\mathbf{i}_{\text{pole}}} = \mathbf{Y}_{\text{gg}} \begin{bmatrix} V_{1\text{gw}} \\ \vdots \\ V_{4\text{gw}} \end{bmatrix}, \tag{7.47}$$

where $\mathbf{Y}_{\text{gg}}$ is

$$\mathbf{Y}_{\text{gg}} = \begin{bmatrix} g_{\text{a}} - \delta_2/\delta_4 & -\delta_2/\delta_4 & \delta_1/\delta_4 & \delta_1/\delta_4 \\ -\delta_2/\delta_4 & g_{\text{a}} - \delta_2/\delta_4 & \delta_1/\delta_4 & \delta_1/\delta_4 \\ \delta_1/\delta_4 & \delta_1/\delta_4 & g_{\text{a}} - \delta_3/\delta_4 & -\delta_3/\delta_4 \\ \delta_1/\delta_4 & \delta_1/\delta_4 & -\delta_3/\delta_4 & g_{\text{a}} - \delta_3/\delta_4 \end{bmatrix}, \tag{7.48}$$

with

$$\begin{aligned} \delta_1 &= y_{\text{m}} g_{\text{a}}^2 \\ \delta_2 &= g_{\text{a}}^2 \left(2g_{\text{a}} + y_{\text{o}} + y_{\text{in}}\right) \\ \delta_3 &= g_{\text{a}}^2 \left(2g_{\text{a}} + y_{\text{o}}\right) \\ \delta_4 &= \left(2g_{\text{a}} + y_{\text{o}}\right)\left(2g_{\text{a}} + y_{\text{o}} + y_{\text{in}}\right) - y_{\text{m}}^2 \,. \end{aligned} \tag{7.49}$$

In (7.47)-(7.49), g_{a} should be interpreted as the conductances of the pole arms. The voltages of the pole arms V^{a} can be obtained from the previously computed voltages of the ground wires (as from (7.47)). Indeed, assuming $1/g_{\text{a}} \simeq 0$ to be negligible, the approximated relations $V_{1\text{gw}} \simeq V_{2\text{gw}} \simeq V_{\text{o}}$ and $V_{3\text{gw}} \simeq V_{4\text{gw}} \simeq V_{\text{u}}$ hold. Consequently, considering the transfer matrix which relates voltages and currents along the pole, in correspondence with the upper and lower ground wires,

$$\begin{bmatrix} V_{\text{o}} \\ I_{\text{o}} \end{bmatrix} = \mathbf{T}_{14} \begin{bmatrix} V_{\text{u}} \\ I_{\text{u}} \end{bmatrix}, \; \mathbf{T}_{14} = \begin{bmatrix} A_{14} & B_{14} \\ C_{14} & D_{14} \end{bmatrix}, \tag{7.50}$$

the current I_{u} in Fig. 7.5d, flowing through the pole, is computed as

$$I_{\text{u}} = \frac{V_{\text{o}} - A_{14} V_{\text{u}}}{B_{14}} \,. \tag{7.51}$$

Using (7.44) and (7.51), the voltages of the pole arms V^{a} supporting the phase

Table 7.1. Lightning current parameters.

	Case I [20]				Case II [21]				Case III [22]			
k	$I_{peak,k}$ [kA]	n_k	τ_{1k} [μs]	τ_{2k} [μs]	$I_{peak,k}$ [kA]	n_k	τ_{1k} [μs]	τ_{2k} [μs]	$I_{peak,k}$ [kA]	n_k	τ_{1k} [μs]	τ_{2k} [μs]
1	28	2	1.8	95	3	2	4	20	3	2	3	76
2					3	3	4	20	4.5	3	3.5	25
3					3	9	4	20	3	5	5.2	20
4					3	11	4	20	3.8	7	6	60
5					20	85	4.5	23	13.6	44	6.6	60
6					15	2	20	240	11	2	100	600
7									5.7	15	11.7	48.5

conductors are given by

$$\begin{bmatrix} V_1^{\mathrm{a}} \\ V_2^{\mathrm{a}} \\ V_3^{\mathrm{a}} \end{bmatrix} = \mathbf{P} \begin{bmatrix} V_{\mathrm{o}} \\ V_{\mathrm{u}} \end{bmatrix}, \; \mathbf{P} = \begin{bmatrix} \chi_1 & \xi_1 \\ \chi_2 & \xi_2 \\ \chi_3 & \xi_3 \end{bmatrix} \tag{7.52}$$

where

$$\begin{aligned} \chi_1 &= \tfrac{B_{34}}{B_{14}} \quad \xi_1 = A_{34} - B_{34}\tfrac{A_{14}}{B_{14}} \\ \chi_2 &= \tfrac{B_{24}}{B_{14}} \quad \xi_2 = A_{24} - B_{24}\tfrac{A_{14}}{B_{14}} \\ \chi_3 &= \tfrac{B_{4}}{B_{14}} \quad \xi_3 = A_{4} - B_{4}\tfrac{A_{14}}{B_{14}} \; . \end{aligned} \tag{7.53}$$

It is interesting to note that if the pole is approximated as a short TL (i.e., $A_{m4} \cong 1$ and $B_{m4} \cong jZ_p\beta_p\ell_{m4}$), (7.52) and (7.53) reduce to the equations of a voltage divider, as in *example 1* (e.g., $V_1^{\mathrm{a}} = V_{\mathrm{u}} + (V_{\mathrm{o}} - V_{\mathrm{u}})\,\frac{\ell_{34}}{\ell_{14}}$).

From previous considerations, it can be deduced that, even though the final expressions for the elements of matrices $\mathbf{Y}_{\mathrm{g}}$ and $\mathbf{P}$ depend on the equivalent circuit adopted for the pole, the procedure to derive those expressions is versatile, and adaptable to different modelling approaches (e.g., lumped parameters circuits, equivalent TL circuits, etc.). Further considerations on pole modelling may be found in [19].

7.2 Numerical results

Lightning current used for numerical simulations

Numerical results discussed in this section refer to the case of a lightning current striking one of the upper SWs of the line under study. The analytical

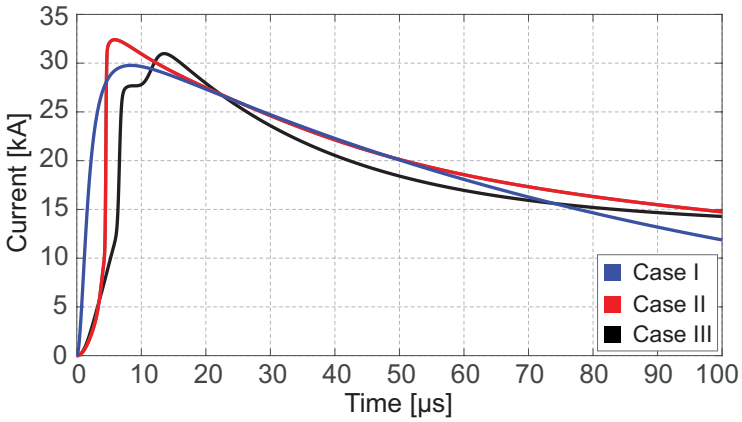

(a)

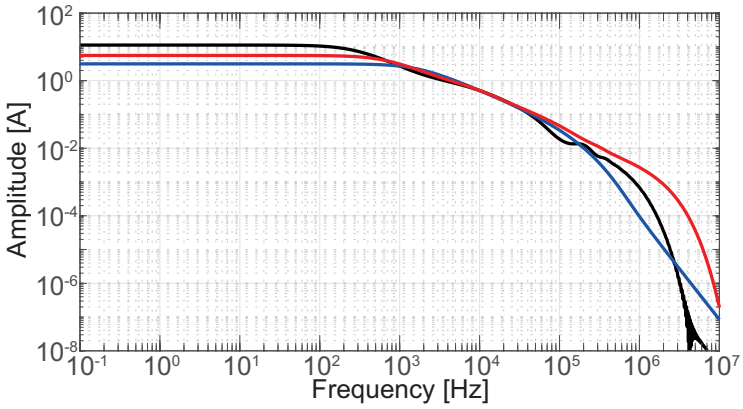

(b)

Figure 7.6. Return stroke currents used for simulations. (a) Time domain waveform. (b) Frequency spectrum of the currents (magnitude).

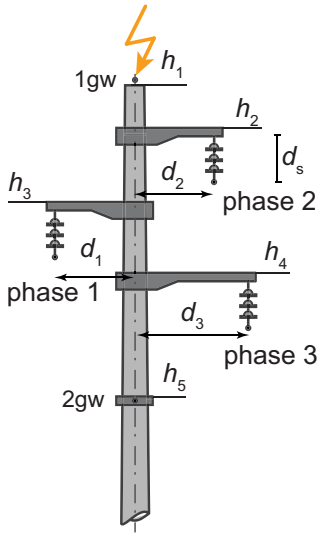

Figure 7.7. Investigated configuration (*example 1*).

Table 7.2. Line parameters (*example 1*).

h_1	13 m
h_2	12 m
h_3	11.3 m
h_4	10.6 m
h_5	9 m
d_1	0.9 m
d_2	1.1 m
d_3	1.2 m
d_s	0.5 m

expression used for the lightning current $i^{\mathrm{L}}(t)$ is given by the superposition of N_{H} Heidler's functions of the type described in Sec. 3.3.5.

In particular, results will refer to two return stroke currents proposed by Rachidi *et al.* [20], and Gamerota *et al.* [21], indicated as Case I and Case II and depicted in Fig. 7.6. The corresponding parameters are listed in Table 7.1.

Additional simulations will account for the double-peak current denoted as Case III in Fig. 7.6 (with parameters in Table 7.1), registered at Mount San Salvatore station by Silveira *et al.* [22].

Validation of the code results

Results obtained by the proposed method have been checked against voltages computed by the commercial software EMTP-RV in some reference configurations.

Simulations have been performed considering a typical Italian distribution line (rated voltage 20 kV). However, the studied line has been equipped with two additional ground wires for investigation purposes; the former (SW) is installed above the phase conductors, the latter below. The electrical and geometrical characteristics of the pole, along with the conductors' arrangement are included in Sec. 7.1.1 (*example 1*), and are depicted in Fig. 7.7. The line total length is equal to 3 km, and it consists of 30 spans, each with length $\ell = 100$ m. Each pole is grounded through a grounding system with grounding resistance $r_{\mathrm{g}} = 25\ \Omega$ (which is assumed not to vary along the line, in order to maintain the periodicity of the configuration). The ground wires are directly bonded to the poles. The soil is characterized by typical values of the electrical conductivity and relative permittivity (0.01 S/m and 10, respectively).

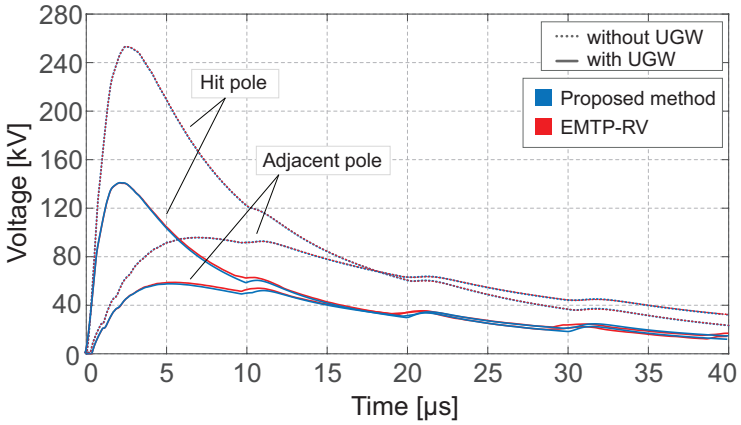

Figure 7.8. Comparison of results by the proposed method and EMTP-RV. Voltages across phase 3 insulators (open terminations, $r_g = 25\ \Omega$, $M_L = M_R = 15$) are given for the struck pole and the adjacent pole with and without the lower ground wire.

The investigated event consists in the upper SW being struck by the lightning current $i^{\mathrm{L}}(t)$ (with Case I parameters in Table 7.1) at the central pole of the line (i.e., $M_L = M_R = 15$).

In particular, simulations for the open circuit conditions, with and without the lower ground wire, have been performed. The voltages across the insulators of phase 3 at the struck and adjacent poles computed by the chain matrix approach are compared to results obtained by EMTP-RV in Fig. 7.8. Results show good agreement: minor differences can be observed only at the waveform tails, when the lower ground wire is in place. This is likely due to the different degree of accuracy reached over the excited frequency range by the proposed approach and EMTP-RV and to different modelling of the ground impedance terms.

7.2.1 Influence of the line terminations

The influence of line terminations has been investigated with reference to the same line analysed in the previous Sec. 7.2. The arrangement of the conductors at the pole (*example 1*) is displayed again for convenience in Fig. 7.7, while the corresponding geometrical details are included in Table 7.2. Case I current is considered to focus on the influence of the line terminations in the first place, being the most simple current expressed by a single Heidler function.

The first set of simulations concerns matched, open, and short circuit terminations, considering that the MTL is hit at the central pole by the lightning current. These terminations were simulated to get a conservative estimation of possible voltage bounds for the power line response.

Figure 7.9 shows voltages computed with and without the UGW. Voltages are computed at the struck pole and at the adjacent pole (no distinction is

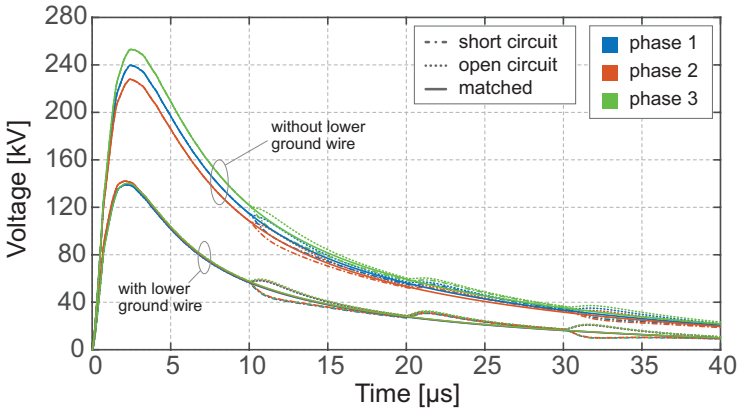

(a)

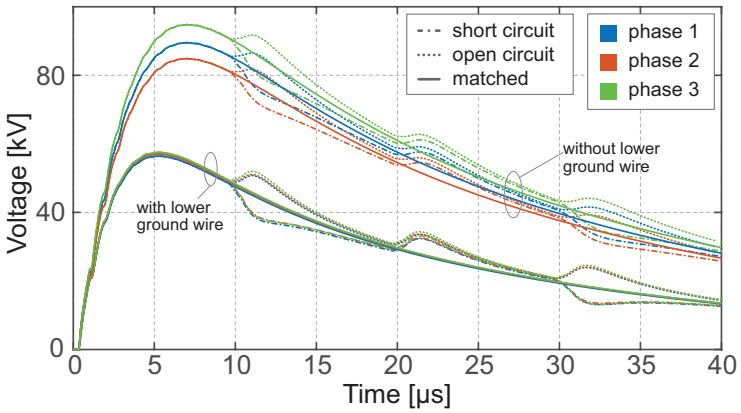

(b)

Figure 7.9. (a) Insulator voltages with different terminations (Case I current, $r_g = 25\ \Omega$, $M_L = M_R = 15$, with and without the UGW) computed at the struck pole; (b) insulator voltages at the adjacent pole.

made between the poles at the right and at the left side of pole 0, due to the symmetry of the analysed event). The constant grounding resistance r_g is equal to 25 Ω, which is an average value within the range of practical grounding resistances along MV feeders in Italy.

A rapid comparison of the results shows the beneficial role played by the additional lower ground wire in mitigating the expected overvoltages. Indeed, ground wires, regardless of their relative position with respect to the phase conductors, provide additional low impedance paths for the lightning current towards the ground. When the grounding resistance is sufficiently low, and the struck pole is far enough from the line terminations, these latter play no significant role, due to the additional grounding provided by the UGW along the MTL.

Two considerations should be made, based on the results in Fig. 7.9. The first observation is that the additional ground wire, placed below the phase conductors, contributes to lowering differences in the amplitude of the insulator overvoltages. Indeed, the range of variation of the voltages at the struck pole is below the 11% without the lower ground wire, reducing to less than the 2.5% when the ground wire is in place (with respect to the peak voltage across the least stressed insulator of the corresponding configuration).

Furthermore, the magnitude of the surges reflected at the line terminations (which appear in Fig. 7.9 with a period of approximately 10 μs) seems not to be affected by the presence of the UGW. In order to further investigate this aspect, Fig. 7.10c displays the actual conductor-to-ground voltages of ground wires and phase conductors at the pole adjacent to pole 0, with $r_g = 25$ Ω. It can be observed that the voltages of the ground wires are affected negligibly by reflection phenomena at the terminations in both cases (with and without the UGW); as a result, the insulator voltages in Fig. 7.10d are mainly affected by reflections of the voltage waves travelling along the phase conductors.

Figure 7.10 displays conductors-to-ground voltages and insulator voltages for different values of r_g, i.e., $r_g = 2500$ Ω, $r_g = 25$ Ω, and $r_g = 1$ Ω, computed at the pole adjacent to pole 0 with and without the UGW.

With $r_g = 2500$ Ω, ground wires voltages are affected by the line terminations mainly at $t \simeq 10$ μs, i.e., when the first reflections from the line endpoints can be observed at the pole; at the tail, the voltages of the ground wires display the same order of magnitude and similar waveform, regardless of the installation of the lower ground wire (Fig. 7.10a). Furthermore, it can be observed that ground wire voltages show a faster rate of decay with respect to the voltages of the phases, since the lightning current is progressively drained towards the ground through the poles grounding resistances. As a result, the subsequent reflections of the ground wires voltages at the terminations display smaller amplitudes and minor influence, also with respect to the insulator voltages in Fig. 7.10b. In fact, they are mainly affected by reflections of the voltage waves induced at the phase conductors; being attenuated only by the ground and wire internal impedances, as well as through coupling with the

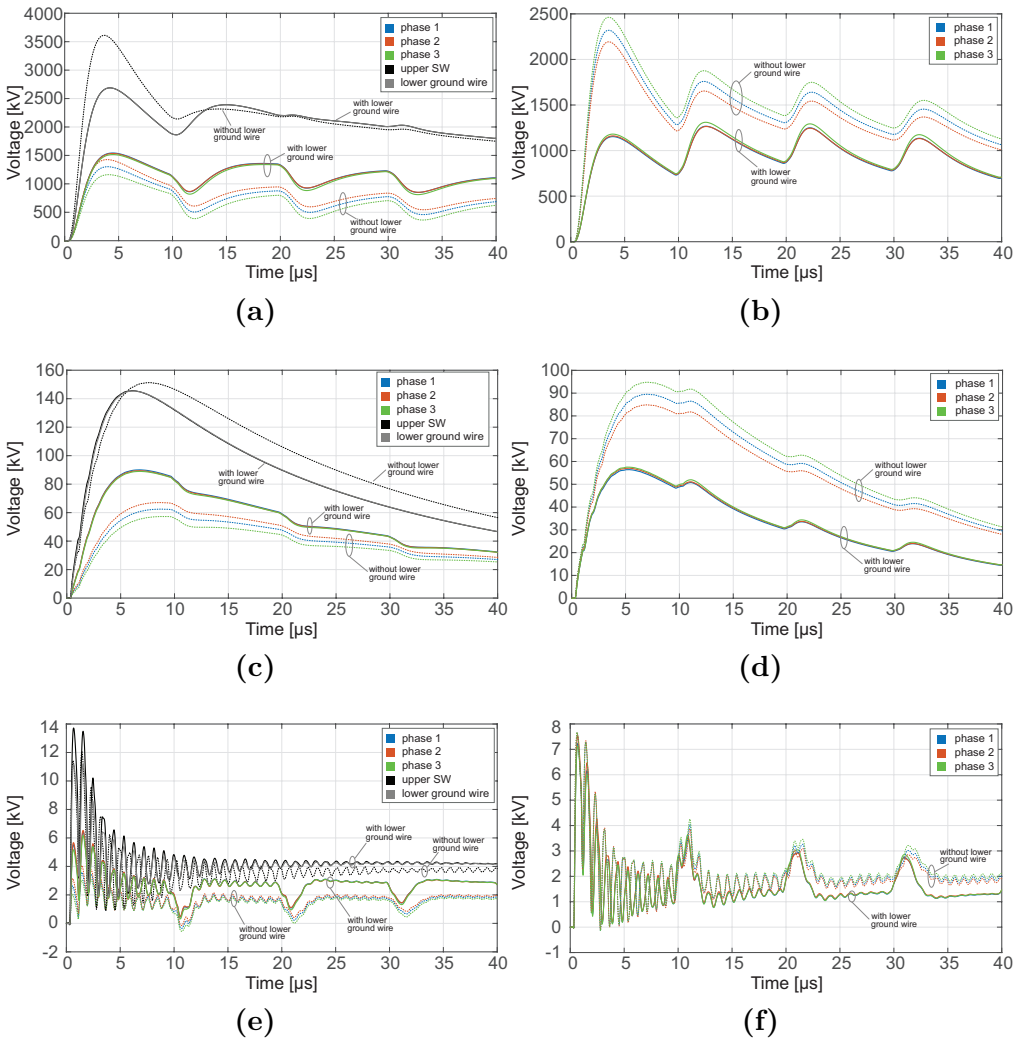

Figure 7.10. Voltages with open terminations (Case I current, $M_L = M_R = 15$, with and without UGW) computed at the pole adjacent to pole 0. (a) Conductors-to-ground voltages, $r_g = 2500\ \Omega$; (b) voltages across the insulators, $r_g = 2500\ \Omega$; (c) conductors-to-ground voltages, $r_g = 25\ \Omega$; (d) voltages across the insulators, $r_g = 25\ \Omega$; (e) conductors-to-ground voltages, $r_g = 1\ \Omega$; (f) voltages across the insulators, $r_g = 1\ \Omega$.

neutral wires and ground, the insulator voltages computed with $r_g = 2500\ \Omega$ would lead to insulation flashover for the line under study.

Similar considerations can be made for the cases $r_g = 25\ \Omega$ and $r_g = 1\ \Omega$, which are displayed in Figs. 7.10c-7.10d and 7.10e-7.10f, respectively. In particular, in Figs. 7.10e-7.10f, the enhanced mismatch between the grounding resistance value and the characteristic impedances of the ground wires causes additional reflections of lower amplitude (approximately every 0.66 μs), to be detected at the ground wires voltages; larger reflections are observed at the phase conductors due to the line terminations. The lower is the value of r_g, the lower is the influence of the line terminations on the voltages of the ground wires.

Figures 7.10a, 7.10c, 7.10e display the conductors-to-ground voltages when the UGW is or is not installed; it can be observed that the lower ground wire contributes to raising the average amplitude of the phase conductors voltages, compared to the configuration with the upper SW only. Indeed, when only the upper SW is in place, the voltage induced on phase 3 has smaller amplitude with respect to those ones at phases 2 and 1, due to its larger distance from the struck SW.

On the other hand, when the UGW is in place, a portion of the lightning current flows through it by means of the pole connection; the upper and the lower ground wires reach similar voltage levels. Hence, the UGW, placed sufficiently close to the phase conductors, induces voltages at the phases too; the stronger mutual coupling results in the similarity of the induced voltages at the phases, also displaying increased amplitude. The enhancement of the phase voltages in the configuration with the additional ground wire corresponds to a reduction of the voltages across the insulators.

It is evident that consecutive ground paths, provided by the periodic grounding, gradually drain the lightning currents to ground, reducing residual currents on the ground wires and induced effects on the phase conductors at the terminations. This observation is supported by voltages in Fig. 7.11, in which results for the impractical case of a grounding resistance equal to 1 kΩ illustrate the effects of a defective grounding; large differences in the response to the different terminations can be observed, since currents are not sufficiently drained to ground, and relevant induced effects may be still observed at close distance to the line endpoints.

The insulator voltages in Fig. 7.12 refer to simulations performed with $M_L = 3$ and $M_L = 9$, i.e., when the struck pole is the 3$^{\text{rd}}$ or the 9$^{\text{th}}$ from the line left termination ($r_g = 25\ \Omega$). Voltages across the insulator of phase 3 are shown with matched, open, and short circuit terminations (it should be noted that the most stressed insulator changes at different poles and for different values of r_g). The insulator voltages at the struck pole are shown in Fig. 7.12a; insulator voltages in Figs. 7.12b and 7.12c refer to the adjacent poles at the left and right sides of the struck pole, respectively. The inset in Fig. 7.12b is devoted to the comparison of the proposed model with EMTP-RV for $M_L = 3$.

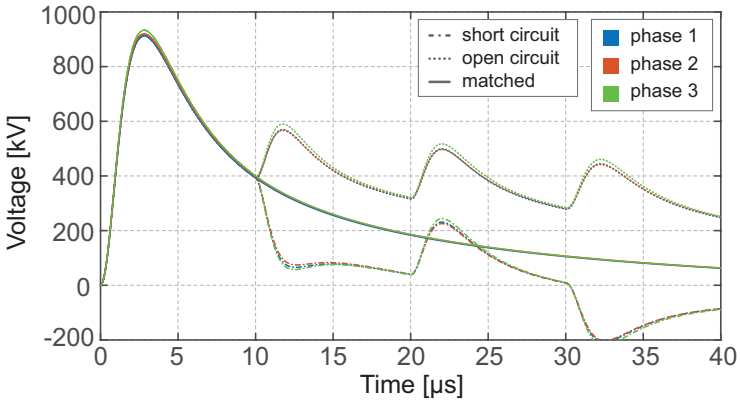

(a)

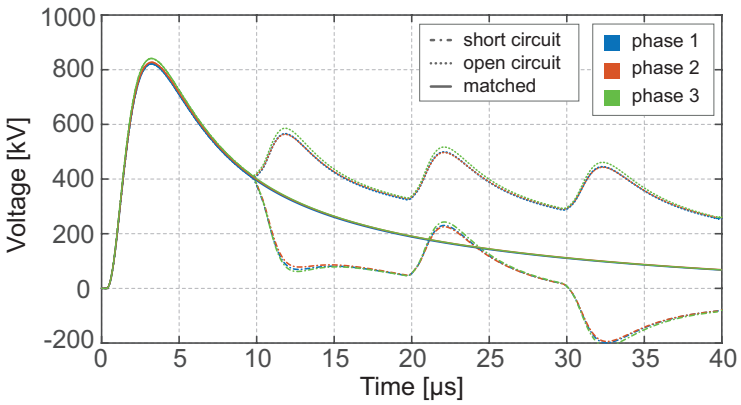

(b)

Figure 7.11. Voltages across the insulators of the phase conductors with different terminations (Case I current, $r_g = 1$ kΩ, $M_L = M_R = 15$). (a) Struck pole; (b) adjacent pole.

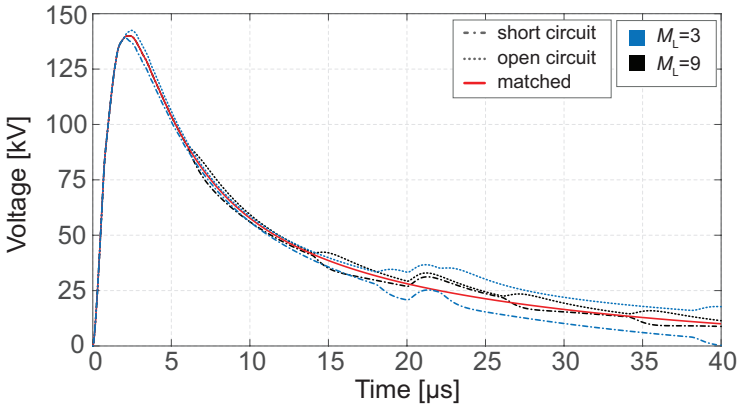

(a)

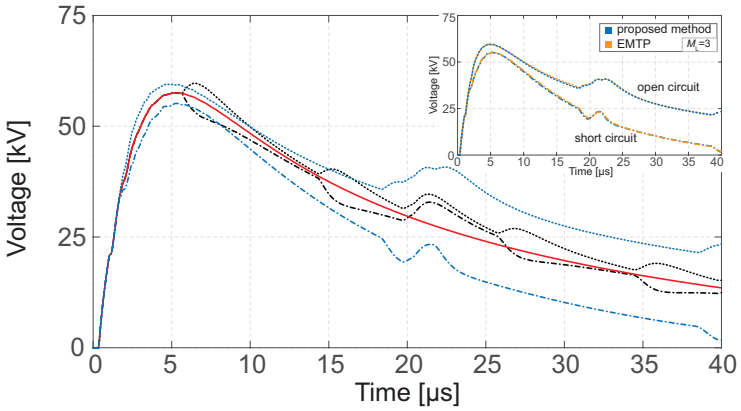

(b)

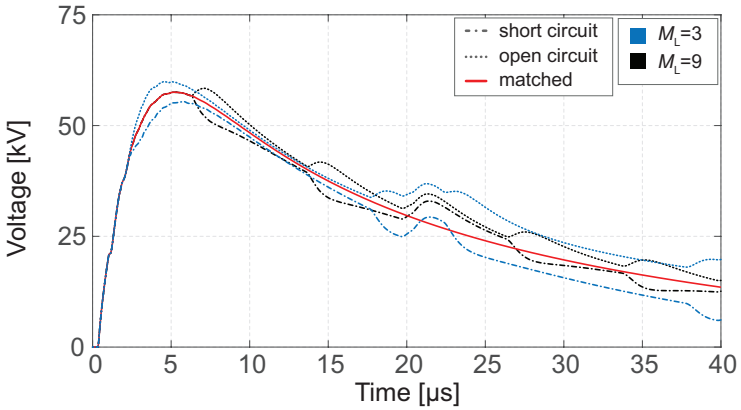

(c)

Figure 7.12. Voltages across the insulators of phase 3 with matched, open and short circuited terminations (Case I current, $r_g = 25\ \Omega$, $M_L = 3$ and $M_L = 9$). (a) Struck pole; (b) left adjacent pole (comparison with results from EMTP-RV for $M_L = 3$ in the inset); (c) right adjacent pole.

For open boundary conditions, results by the JMARTI line model were in good agreement with the ones computed by the chain matrix approach; the more accurate Wide-Band line model has turned necessary to get satisfactory results with short circuited terminations. In the analysed configuration and for the specific value of r_{g}, the terminations show negligible influence on the peak value of the insulator voltages at the struck pole, for $M_L, M_R \geq 3$; however, their effect cannot be neglected at adjacent poles, where the superimposed reflected waves may change the voltage amplitude and the time instant of occurrence of the voltage peak.

If the struck pole is sufficiently distant from the line endpoints, the waves reflected by the mismatched terminations will be back to the hit pole (and to the adjacent ones) when the voltages have already reached and overcome the first peak (as to the present example, after about 10 μs). As a consequence, even though reflected waves could be produced at the terminations resulting in constructive interferences, the interaction between incident and reflected waves will be at the tail of the voltages, i.e., at reduced voltage levels.

The effect of frequency-dependent mismatched terminations is also assessed simulating random couples of frequency-dependent loads. $\mathbf{Y}_{\mathrm{subs}}$ and $\mathbf{Y}_{\mathrm{tran}}$ in (7.13)-(7.14) have been computed through the following formulas:

$$\mathbf{Y}_{\mathrm{subs}}(\omega) = \frac{1}{2}\left[\mathbf{Y}_{\mathrm{w}}(\omega)\,\mathbf{D}_{\mathrm{s}} + \mathbf{D}_{\mathrm{s}}\mathbf{Y}_{\mathrm{w}}(\omega)\right] \tag{7.54a}$$

$$\mathbf{Y}_{\mathrm{tran}}(\omega) = \frac{1}{2}\left[\mathbf{Y}_{\mathrm{w}}(\omega)\,\mathbf{D}_{\mathrm{t}} + \mathbf{D}_{\mathrm{t}}\mathbf{Y}_{\mathrm{w}}(\omega)\right] \tag{7.54b}$$

where $\mathbf{D}_{\mathrm{s}}$ and $\mathbf{D}_{\mathrm{t}}$ are diagonal matrices of order N_{c}, whose entries are uniformly distributed random variables ranging from 0 to 10^2. The two extreme cases of open circuit and short circuit at both endpoints have been enforced to obtain a clear picture of the expected range of variation for the results. To emphasize the effect of the line terminations, the struck pole is assumed to be placed two spans away from the left termination ($M_L = 2$). Outputs for the struck pole, left and right adjacent poles are reported in Fig. 7.13. The blue curve corresponds to the open circuit case, while the black one to the short circuit case. In the middle, results are displayed for randomly selected terminations. As expected, terminations significantly affect the results only when the struck pole is close to the endpoints and the grounding resistance is high (in the analysed case, for $M_L < 3$ and $r_{\mathrm{g}} = 25\ \Omega$). Indeed, it can be observed that the computed peaks of the insulator voltages at the pole in the most critical position (i.e., between the line termination and the struck pole), show significant variations (approximately up to 20%) caused by severe reflection phenomena.

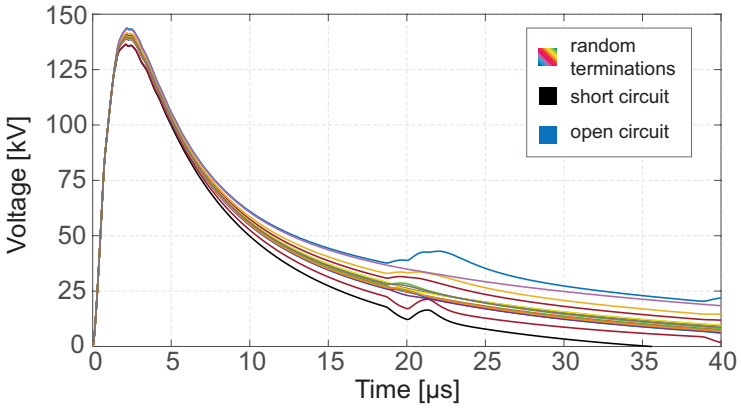

(a)

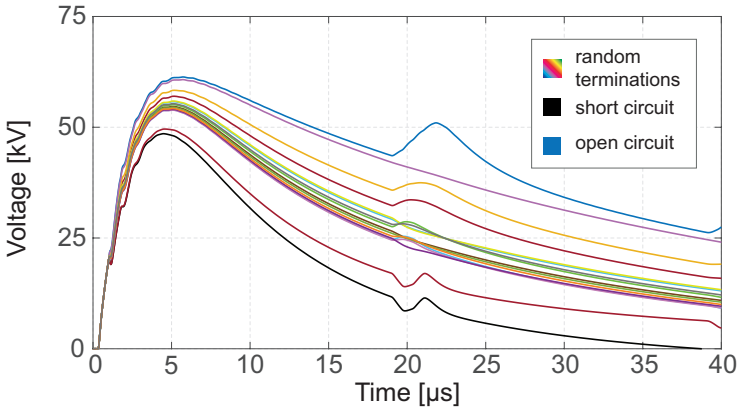

(b)

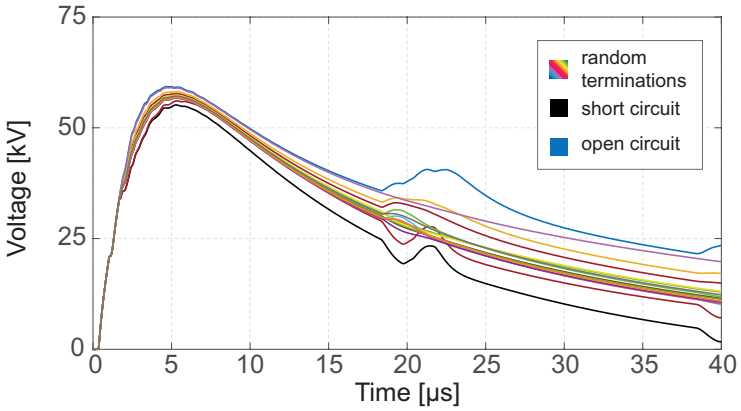

(c)

Figure 7.13. Voltages across the insulators of phase 3 with random terminations (Case I current, $r_g = 25\ \Omega$, $M_L = 2$). (a) Struck pole; (b) left adjacent pole; (c) right adjacent pole.

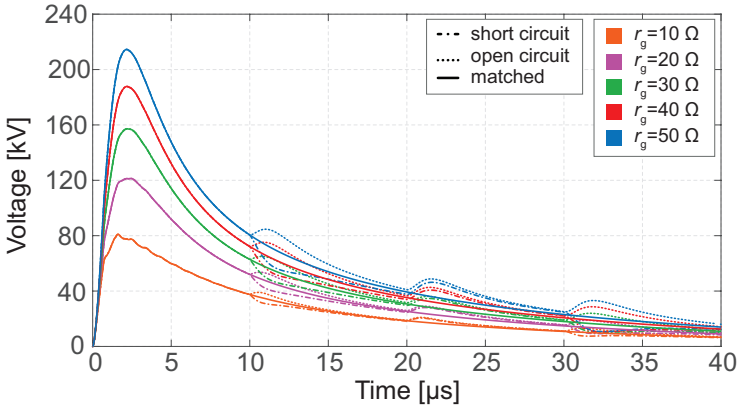

(a)

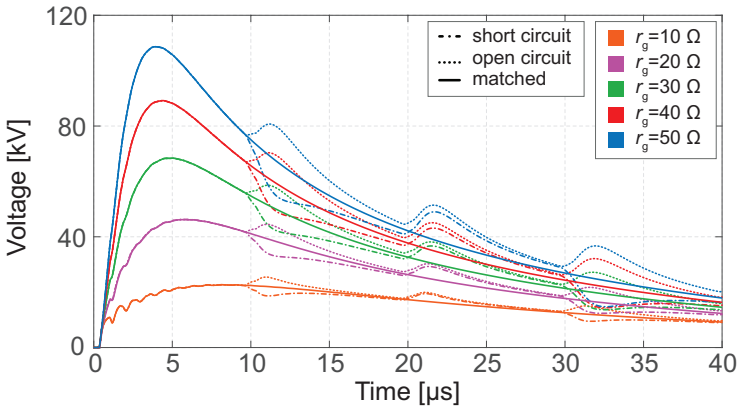

(b)

Figure 7.14. Largest voltages across the insulators with matched, open and short circuited terminations, and different r_g (Case I current, $M_L = M_R = 15$). (a) Struck pole; (b) adjacent pole.

7.2.2 Influence of the grounding impedance modelling

An electromagnetic approach was introduced in Chapter 6 to derive the frequency response of grounding electrodes in the FD, including their resistive and reactive behaviour. In this section, a common engineering approach has been adopted to account for the frequency dependence of the impedance z_{g} offered by the pole grounding system; a simplified expression for z_{g} is used, depending on the geometrical characteristic of the grounding system and on the soil electromagnetic properties.

The assumed grounding system consists in a grounding rod, with radius $a = 12.5$ mm and length $b = 3$ m, buried vertically in the soil with electrical conductivity and permittivity σ_{g} and ϵ_{g}, respectively.

As a second approach to simulate the frequency response of grounding rods, the grounding impedance z_{g} offered by a buried vertical electrode may be modelled through a lumped RLC circuit, as depicted in the inset of Fig. 7.15a:

$$z_{\mathrm{g}}(\omega) = j\omega l_{\mathrm{g}} + \frac{r_{\mathrm{g}}}{1 + j\omega r_{\mathrm{g}} c_{\mathrm{g}}} \ . \tag{7.55}$$

Several sets of formulas for the parameters of the RLC circuit are available from Sunde [23], Rudenberg [24], Tagg [25]. Here the following expressions are considered:

$$r_{\mathrm{g}} = \frac{\rho_{\mathrm{g}}}{2\pi b} w \ , \ l_{\mathrm{g}} = \frac{\mu_0 b}{2\pi} w \ , \ c_{\mathrm{g}} = \frac{2\pi\epsilon_{\mathrm{g}}\, b}{w} \tag{7.56}$$

where $w = \ln\left(\frac{4b}{a}\right) - 1$. Expressions (7.56) are based on the approximate method of the average potential [26], for $a \ll b$. In [27], [28], it was observed that the chosen model of the pole grounding system may affect the computed peak voltages.

First, the influence of the grounding system is assessed with different line terminations; different values of constant grounding resistance r_{g} are considered. Figure 7.14 shows the largest insulator voltages that occur at the central pole (Fig. 7.14a) and at the adjacent one (Fig. 7.14b) when r_{g} ranges between 10 Ω and 50 Ω ($M_L = M_R = 15$). Voltage increases for larger values of grounding resistance, since the periodic grounding progressively loses its capability to drain current towards the ground (confirming the beneficial impact of an effective grounding); however, while values of r_{g} below 50 Ω would be practical for many local utilities, due to the favorable geological conformation and limited electrical resistivity of the ground, in different areas these values may represent a technical challenge, to be faced with suitable design of the grounding electrodes.

Furthermore, in Fig. 7.14b, it can be observed that reflections from the line terminations actually contribute to increasing the peak voltages across the insulators for the lowest value of r_{g}; nevertheless, the lightning performance of the line would not be impaired by the increased voltages, still displaying low amplitudes due to the grounding effectiveness.

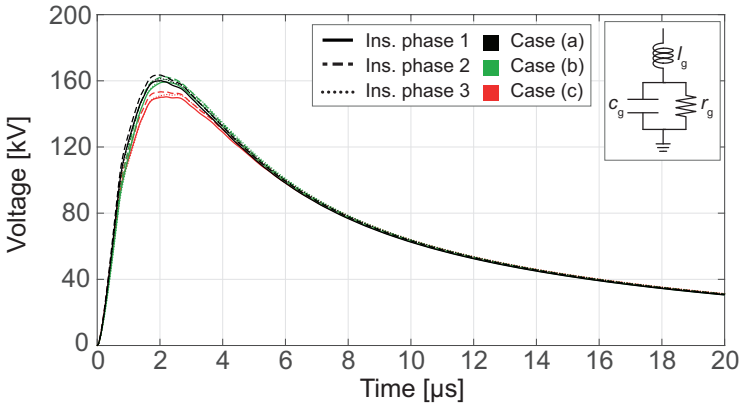

(a)

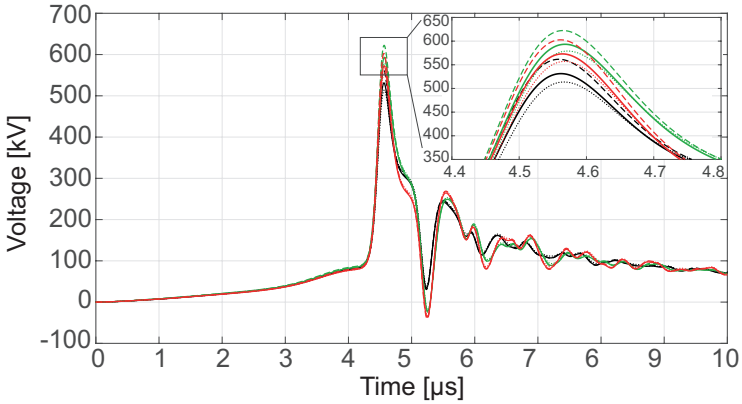

(b)

Figure 7.15. Voltages across the insulators at pole 0 (matched terminations, $M_L = M_R = 15$), with different grounding system models and soil properties. (a) Results for Case I lightning current in Fig. 7.6; (b) results for Case II lightning current in Fig. 7.6. The inset in (a) displays the adopted equivalent circuit for the grounding impedance associated with the grounding rod.

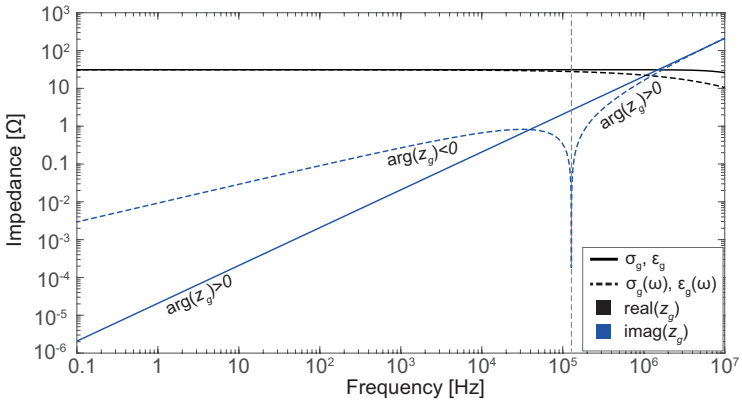

Figure 7.16. Resistive and reactive part of z_{g} associated with the buried vertical rod, computed according to (7.55), with constant or frequency-dependent soil properties according to the Messier's model.

Figure 7.15 shows voltages across the insulators at pole 0 for matched boundary conditions: results in Figs. 7.15a and 7.15b have been computed employing the lightning currents denoted as Case I and Case II in Fig. 7.6, respectively. Displayed curves refer to different grounding conditions and soil properties in the FD, listed below:

a. matrices of p.u.l. ground impedances account for the soil with constant electrical properties (i.e., $\sigma_{\mathrm{g_{DC}}}$, $\epsilon_{\mathrm{g}_\infty}$); the pole grounding system is modelled by r_{g}, computed with $\sigma_{\mathrm{g_{DC}}}$;

b. matrices of p.u.l. ground impedances account for the soil with constant electrical properties (i.e., $\sigma_{\mathrm{g_{DC}}}$, $\epsilon_{\mathrm{g}_\infty}$); the pole grounding system is modelled by z_{g}, computed with the same soil fixed properties;

c. matrices of p.u.l. ground impedances account for the soil with frequency-dependent electrical properties (i.e., $\sigma_{\mathrm{g}}(\omega)$, $\epsilon_{\mathrm{g}}(\omega)$); the pole grounding system is modelled by z_{g}, computed with the same soil properties.

The Messier's model (in Sec. 6.1.2) was implemented to account for the frequency-dependent behaviour of the soil, with $\epsilon_{\mathrm{g}_\infty} = 8\epsilon_0$, and $\sigma_{\mathrm{g_{DC}}} = 0.01$ S/m.

Figure 7.16 shows the frequency behaviour of the resistive and reactive part of z_{g} for constant ($\sigma_{\mathrm{g}}(\omega) = \sigma_{\mathrm{DC}}$, $\epsilon_{rg}(\omega) = 8$) or frequency-dependent soil properties. With constant soil properties, the higher the frequencies excited by the lightning current, the more pronounced is the inductive behaviour of the rod, compared to its impedance at low frequency (i.e., to the constant $r_{\mathrm{g}} \simeq 31.1\ \Omega$).

With frequency-dependent soil properties, the rod displays a capacitive reactance at lower frequencies, approximating only at higher frequencies the inductive reactance offered by z_{g} with constant soil properties.

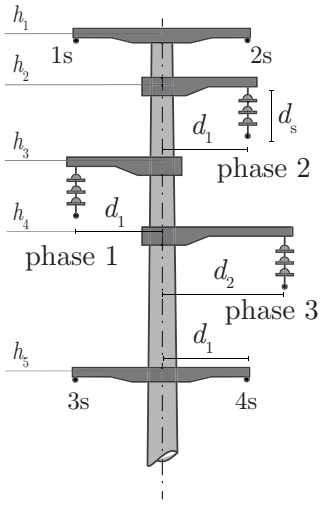

Figure 7.17. Investigated configuration (*example 2*).

Table 7.3. Line parameters (*example 2*).

h_1	12.2 m
h_2	12 m
h_3	11.3 m
h_4	10.6 m
h_5	9.4 m
d_1	0.9 m
d_2	1.0 m
d_s	0.5 m

As from Figs. 7.15a and 7.15b, the different simulated scenarios influence the computed peak values of the insulator voltages. With Case I current, voltages for scenarios (a) and (b) result in similar amplitudes; in scenario (c), voltages decrease due to the inclusion of frequency-dependent soil properties, and to the increasing conductivity of the soil with frequency according to the Messier's model.

When Case II current is considered, larger overvoltages are associated with scenario (b). Indeed, Case II current displays considerably larger frequency components in the range $10^5 - 10^7$ Hz with respect to Case I current; as a consequence, the inductive reactance of z_g at higher frequencies contributes non-negligibly to raising the peak values of the insulator voltages. In scenario (c), slightly lower amplitudes are observed due to the effect of the decreasing grounding resistivity with the frequency.

7.2.3 Influence of the number of ground wires

The influence of the number of ground wires has been investigated with reference to the 3 km line described in Sec. 7.1.1, with span length $\ell = 100$ m ($\sigma_g = 0.01$ S/m, $\epsilon_g = 10\epsilon_0$). The arrangement of the conductors at the pole (*example 2*) is displayed again for convenience in Fig. 7.17, while the corresponding geometrical details are included in Table 7.3. The lightning current used for simulation is that denoted as Case II in Table 7.1; the TD waveform and the corresponding frequency spectrum (magnitude) are displayed in Fig. 7.6. Pole 0 is located at the same distance from the line terminations ($M_L = M_R = 15$).

Results for three line configurations will be presented. These configurations, which are displayed in Fig. 7.18, consist in the same distribution line equipped

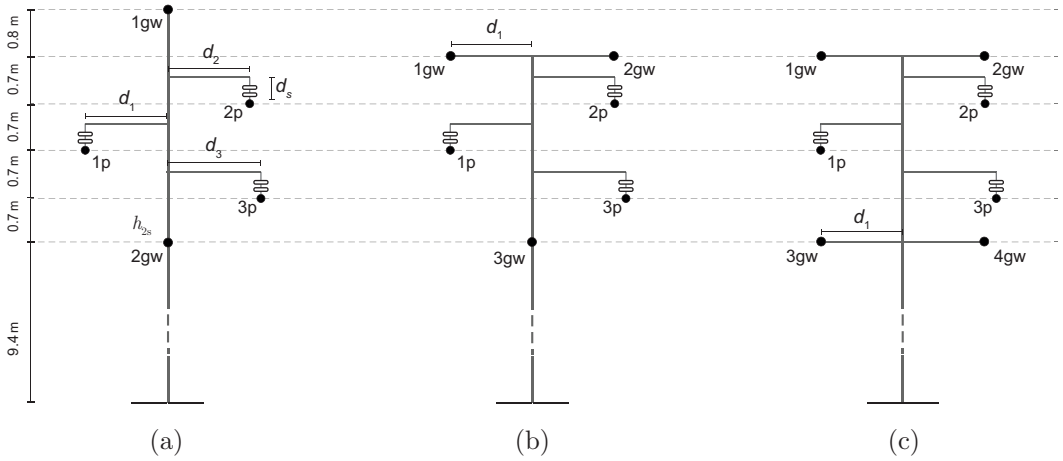

Figure 7.18. Conductors arrangements at the pole in the studied configurations, with two, three, or four ground wires. (a) One lower and one upper ground wire; (b) one lower and two upper ground wires; (c) two lower and two upper ground wires.

with an increasing number of ground wires. In particular, the line in Fig. 7.18a is equipped with two ground wires (one above and one below the phase conductors); the line in Fig. 7.18b is equipped with three ground wires (two above and one below the phase conductors); the line in Fig. 7.18c is equipped with four ground wires (two above and two below the phase conductors). With respect to the configuration dealt with in *example 1*, for conductors arrangement depicted in Figs. 7.18b and 7.18c, ground wires are located closer to the phase conductors to enhance mutual coupling and further reduce insulator voltages[3].

Voltages across the insulators at the struck pole and at the two consecutive poles (i.e., at distance ℓ and 2ℓ from pole 0) are computed.

Starting from the first line arrangement in Fig. 7.18a, the SW is placed at $h_1 = 13$ m above the ground. Figure 7.19 shows the computed voltages across the insulators of phase 2. The value $r_g = 25\ \Omega$ is assumed for the grounding resistance at the poles. Results are presented for matched, short circuited, and open circuited terminations. Indeed, as discussed in Sec. 7.2.1, the different terminations hold negligible influence on the observed peak voltages, due to the installation of the UGW and to an effective grounding system at the poles. Furthermore, it may be observed that significant electrical stress occurs within one or two spans, since at the second adjacent pole, the peak of the insulator voltage is reduced to approximately 20% of the corresponding value at the struck pole.

Finally, observing Fig. 7.19, different waveforms of the insulator voltages

[3]Geographical location, mechanical characteristics, and rated voltage of the line must be accounted when the analysed technical solution (namely, the installation of additional ground wires) is to be implemented in actual HV and MV lines, considering minimum clearance distances as from the relevant standards and guidelines.

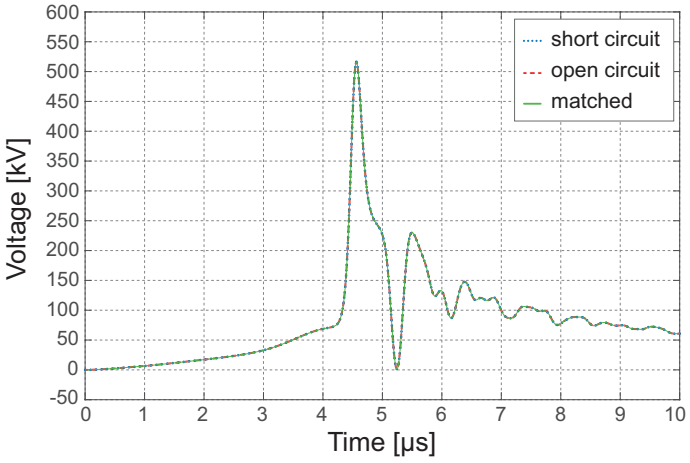

(a)

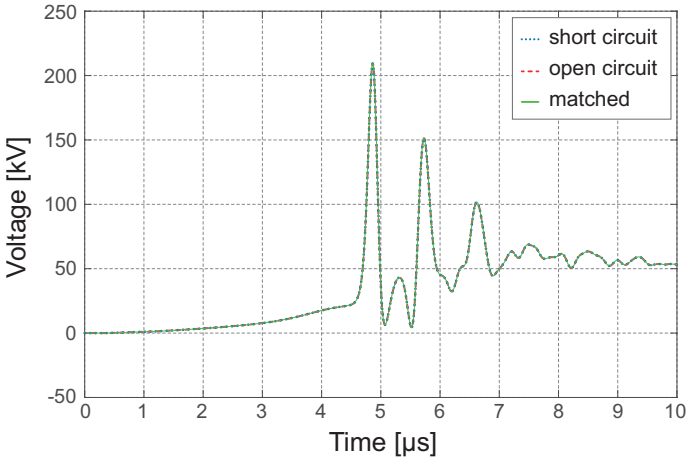

(b)

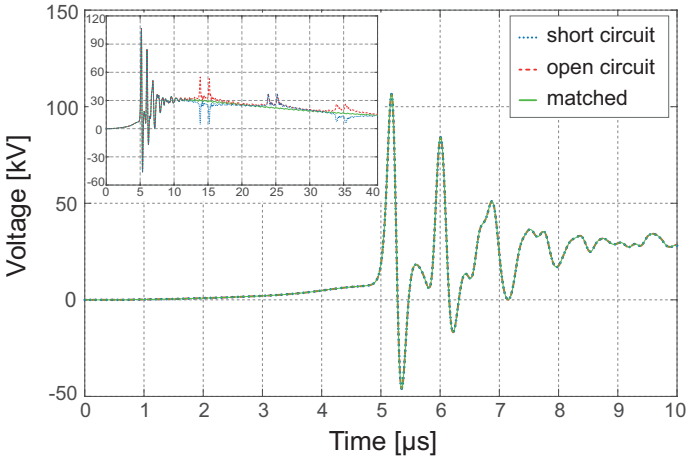

(c)

Figure 7.19. Voltages across the insulators of phase 2 for the line configuration in Fig. 7.18a, with different terminations (Case II lightning current, $r_g = 25\ \Omega$, $M_L = M_R = 15$). (a) Voltages at pole 0; (b) voltages at the adjacent poles at distance ℓ and (c) at distance 2ℓ.

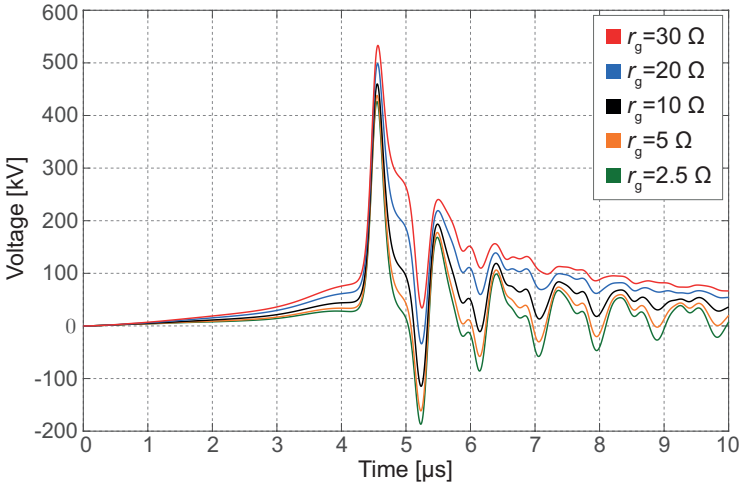

Figure 7.20. Voltages across the insulators of phase 2 at the struck pole, with matched terminations, and for different values of grounding resistance r_g (Case II lightning current, $M_L = M_R = 15$, reference configuration in Fig. 7.18a).

may be observed at the struck pole and adjacent ones, due to the superposition of waves reflected at the poles and at the line terminations. The single peak of the insulator voltage observed at the struck pole (Fig. 7.19a), and the double-peaked voltage at the two subsequent poles (Figs. 7.19b and 7.19c) result in different electrical stress at the insulators.

Following previous considerations on the impact of the line terminations, simulations were carried out for different values of the grounding resistance r_g (in the range $2.5 - 30\ \Omega$) and matched terminations. Although the overvoltage decreases with the value of r_g (Fig. 7.20), striving to further lower the grounding resistance below 10 Ω may result in minimal reduction of the insulator overvoltages. This is mainly due to the combination of two opposite effects. Indeed, by reducing r_g, the GPR is reduced, yet, the mismatch between the pole impedance and r_g is enhanced, resulting in reflected waves. In addition, the inductive behaviour of the pole (modelled, in this *example 2*, as a lossless TL) prevails for values of r_g below a certain threshold. Furthermore, values of grounding resistance of the order of 2.5 Ω, obtainable only in highly conductive soils, may result unpractical (especially when the line, extending for some kilometers, is supposed to be periodically grounded through the same r_g).

Figure 7.21 displays the voltages across the insulators computed for the three configurations in Fig. 7.18. It can be observed that, with $r_g = 10\ \Omega$, the peak voltage across phase 2 insulator computed with just two ground wires reduces to 60% and 52% of its value when one and two additional ground wires are installed. The computed insulator voltages in the studied case, with two or three ground wires, would cause an insulation breakdown. However, the probability of backflashover could be reduced if a fourth ground wire was installed. If measures to improve the line basic insulation level are taken, or any

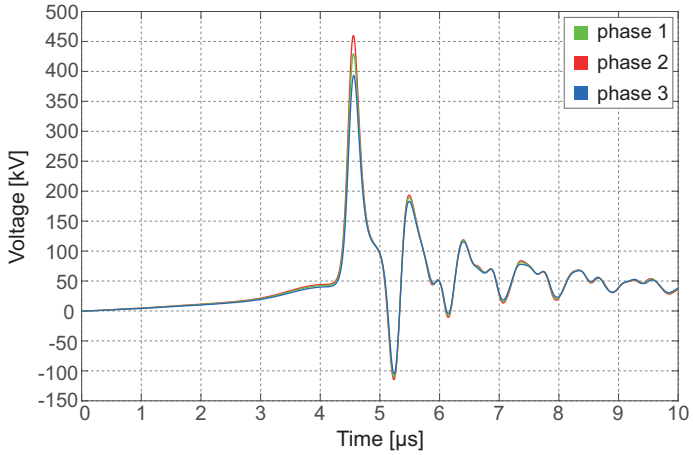

(a)

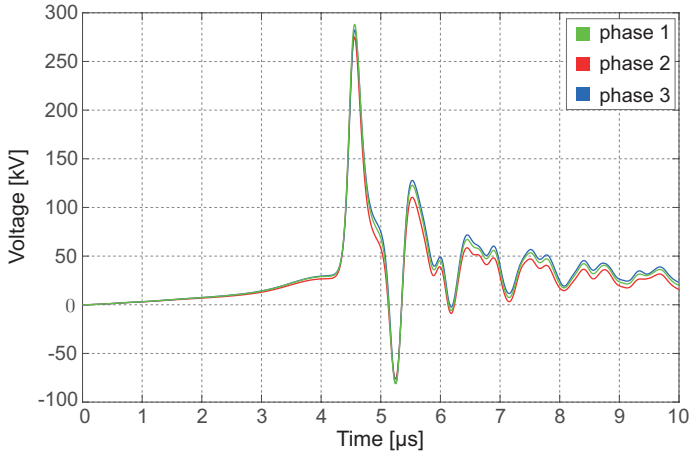

(b)

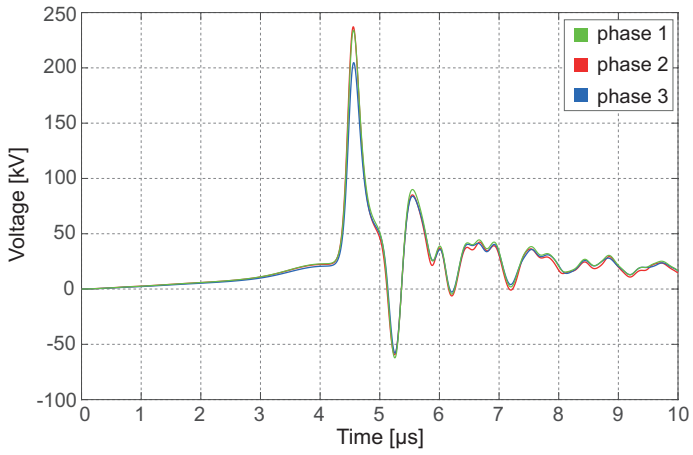

(c)

Figure 7.21. Voltages across the insulators of the phase conductors at the struck pole in the different configurations depicted in Fig. 7.18 ($r_g = 10\ \Omega$, matched terminations). (a) One upper and one lower ground wire; (b) two upper and one lower ground wires; (c) two upper and two lower ground wires.

effort is made to improve the effectiveness of the grounding impedance at the poles, the UGWs, placed at suitable distance from the phase conductors, could represent a valuable contribution to reduce the overall impedance towards the earth and protect the line against the effects of direct lightning. The effective positioning of the ground wires has been obtained through a large number of simulations, without applying any specific optimization algorithm. However, constrained optimization algorithms could be applied in order to optimize the position of the ground wires with respect to the phase conductors, considering geometrical constraint, right of ways, minimum clearances in air, etc.

The response of the line to a double-peaked negative first stroke current, namely, Case III lightning current in Fig. 7.6, has been evaluated as well. Parameters of the Heidler's functions necessary to reproduce the double-peaked current waveform are reported in Table 7.1; the current frequency spectrum (magnitude) is displayed in Fig. 7.6b. It should be noted that the peak value of the double-peak current is 31.0 kA (while the peak value of Case II lightning current in Fig. 7.6a is 32.4 kA). Voltages across insulators at the struck pole with $r_g = 10\ \Omega$ and $r_g = 30\ \Omega$, for the line arrangements in Fig. 7.18, are shown in Figs. 7.22a and 7.22b. With the double-peaked lightning current, the insulator voltages are reduced (Figs. 7.22a and 7.21 should be compared, both referring to $r_g = 10\ \Omega$). This is likely due to the lower amplitudes of frequency components of the double-peaked lightning current above 10 kHz compared to Case II current, not enhancing the contribution of the reactive behaviour of the pole.

Results presented in this section confirm that the installation of additional ground wires and, in particular, UGWs installed below the phase conductors, significantly contributes to reducing the electrical stress across the insulator of the analysed distribution lines (the effectiveness of this protective measure is being consolidated in the relevant literature [29]). A compact arrangement of the conductors at the pole will enhance mutual coupling effects; as a consequence, being increased the amplitude of the induced overvoltages on the phases, the voltage across the insulators will be reduced. However, further statistical studies should be conducted considering the following aspects in order to assess the effectiveness of the protection provided by additional UGWs: the probability density functions describing the probability of occurrence of lightning currents with given peak values and front duration; the actual critical flashover voltage associated with the line under study [30]; the time of occurrence of the lightning strike with respect to the steady-state voltages at power frequency feeding the phase conductors prior to the lightning event. The rigorous chain matrix approach for lines with periodical structure and grounding may be applied in the future to conduct further investigations on these specific aspects and assess practical case studies.

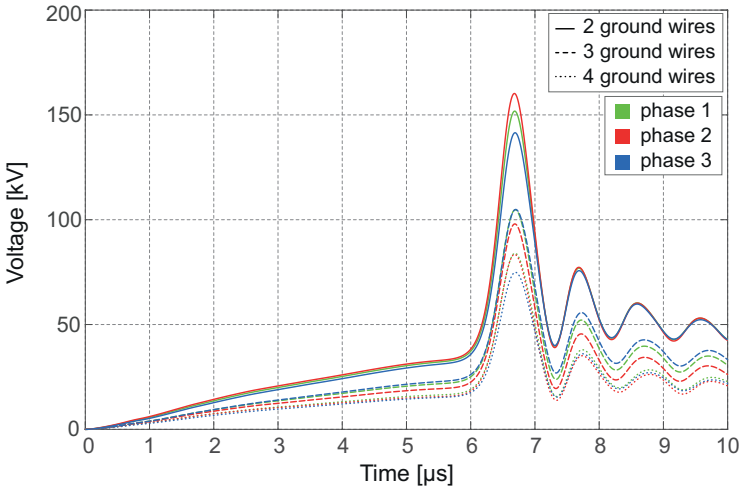

(a)

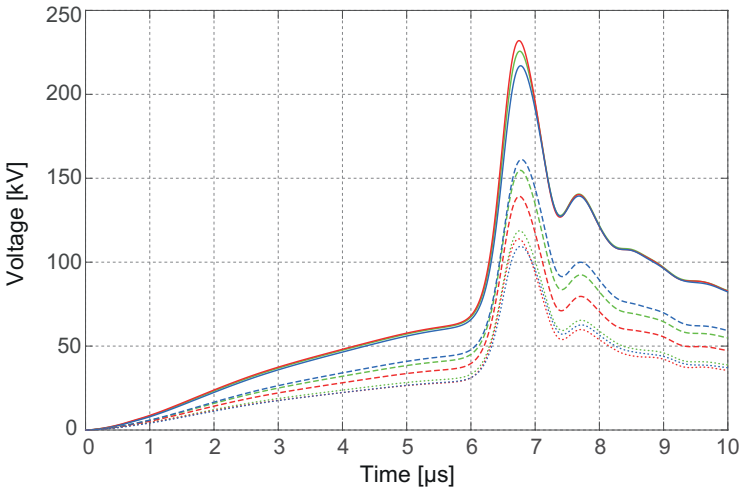

(b)

Figure 7.22. Voltages across the insulators of the struck pole for conductors arrangements in Fig. 7.18, with matched terminations (Case III lightning current). (a) $r_g = 10\ \Omega$; (b) $r_g = 30\ \Omega$.

References

[1] E. Stracqualursi, R. Araneo, J. A. Brandão Faria, and A. Andreotti, "Application of the transfer matrix approach to direct lightning studies of overhead power lines with underbuilt shield wires part I: Theory," *IEEE Trans. Power Del.*, vol. 37, no. 2, pp. 1226–1233, Apr. 2022.

[2] ——, "Application of the transfer matrix approach to direct lightning studies of overhead power lines with underbuilt shield wires part II: Simulation results," *IEEE Trans. Power Del.*, vol. 37, no. 2, pp. 1234–1241, Apr. 2022.

[3] ——, "Protection of distribution overhead power lines against direct lightning strokes by means of underbuilt ground wires," *Electric Power Systems Research*, vol. 202, 107571, Jan. 2022.

[4] A. R. Hileman, *Insulation Coordination for Power Systems*, C. Press, Ed., 1999.

[5] "IEEE guide for improving the lightning performance of electric power overhead distribution lines," *IEEE Std 1410-2004 (Revision of IEEE Std 1410-1997)*, pp. 1–50, 2004.

[6] J. He, Y. Tu, R. Zeng, J. B. Lee, S. H. Chang, and Z. Guan, "Numeral analysis model for shielding failure of transmission line under lightning stroke," *IEEE Trans. Power Del.*, vol. 20, pp. 815–822, Apr. 2005.

[7] S. Visacro, F. H. Silveira, and A. D. Conti, "The use of underbuilt wires to improve the lightning performance of transmission lines," *IEEE Trans. Power Del.*, vol. 27, no. 1, pp. 205–213, Jan. 2012.

[8] T. Thanasaksiri, "Improving the lightning performance of overhead lines applying additional underbuilt shield wire," in *2013 10th International Conference on Electrical Engineering/Electronics, Computer, Telecommunications and Information Technology*, May 2013, pp. 1–6.

[9] ——, "Improving the lightning performance of overhead distribution and subtransmission lines applying additional underbuilt shield wire," *ECTI Transactions on Electrical Engineering, Electronics, and Communications*, vol. 12, no. 8, pp. 1–8, 2014.

[10] N. V. Ninh, T. Pham, and T. V. Tran, "A method to improve lightning performance of transmission lines in high footing resistance areas," in *2017 International Symposium on Electrical Insulating Materials (ISEIM)*, vol. 2, pp. 761–764.

[11] R. Araneo, G. Lovat, S. Celozzi, J. A. Brandão Faria, A. Andreotti, and L. Verolino, "Improvement of lightning performance of overhead power lines by addition of underbuilt ground wires," in *2018 18th IEEE Int. Conf. Environ. and Electr. Eng.*, June 2018, pp. 1–5.

[12] C. R. Paul, *Analysis of Multiconductor Transmission Lines*. John Wiley and Sons, 2008.

[13] K. Ishimoto, F. Tossani, F. Napolitano, A. Borghetti, and C. A. Nucci, "Direct lightning performance of distribution lines with shield wire considering LEMP effect," *IEEE Transactions on Power Delivery*, vol. 37, no. 1, pp. 76–84, 2021.

[14] S. A. Schelkunoff, "The electromagnetic theory of coaxial transmission lines and cylindrical shields," *The Bell System Technical Journal*, vol. 13, no. 4, pp. 532–579, 1934.

[15] J. R. Carson, "Wave propagation in overhead lines with ground return," *Bell Sys. Tech. J.*, no. 5, pp. 539–554., 1926.

[16] A. Semlyen, "Ground return parameters of transmission lines an asymptotic analysis for very high frequencies," *IEEE Trans. Power App. Syst.*, no. 3, pp. 1031–1038, 1981.

[17] N. Bowler, "Frequency-dependence of relative permeability in steel," in *AIP Conference Proceedings*, vol. 820, no. 1. American Institute of Physics, 2006, pp. 1269–1276.

[18] A. De Conti, S. Visacro, A. Soares, and M. A. O. Schroeder, "Revision, extension, and validation of Jordan's formula to calculate the surge impedance of vertical conductors," *IEEE Trans. Electromagn. Compat.*, vol. 48, no. 3, pp. 530–536, Aug. 2006.

[19] E. Stracqualursi, G. Pelliccione, S. Celozzi, and R. Araneo, "Tower models for power systems transients: a review," *Energies*, vol. 15, no. 13, 4893, Jul. 2022.

[20] F. Rachidi, W. Janischewskyj, A. M. Hussein, C. A. Nucci, S. Guerrieri, B. Kordi, and J.-S. Chang, "Current and electromagnetic field associated with lightning-return strokes to tall towers," *IEEE Trans. Electromagn. Compat.*, vol. 43, no. 3, pp. 356–367, 2001.

[21] W. R. Gamerota, J. O. Elismé, M. A. Uman, and V. A. Rakov, "Current waveforms for lightning simulation," *IEEE Trans. Electromagn. Compat.*, vol. 54, no. 4, pp. 880–888, Aug. 2012.

[22] F. H. Silveira, A. De Conti, and S. Visacro, "Lightning overvoltage due to first strokes considering a realistic current representation," *IEEE Trans. Electromagn. Compat.*, vol. 52, no. 4, pp. 929–935, Nov. 2010.

[23] E. D. Sunde, *Earth conduction effects in transmission systems.* Dover Publications Inc., 1968.

[24] R. Rudenberg, *Electrical Shock Waves in Power Systems - Travelling Waves in lumped and distributed circuit element.* Harvard University Press, Cambridge, Massachusetts, 1968.

[25] G. Tagg, *Earth Resistance.* Gorge Newnes Limited, London, 1964.

[26] H. Dwight, "Calculation of resistances to ground," *Transactions of the American Institute of Electrical Engineers*, vol. 55, no. 12, pp. 1319–1328, 1936.

[27] M. R. Alemi and K. Sheshyekani, "Wide-band modeling of tower-footing grounding systems for the evaluation of lightning performance of transmission lines," *IEEE Trans. Electromagn. Compat.*, vol. 57, no. 6, pp. 1627–1636, Dec. 2015.

[28] R. Shariatinasab, J. Gholinezhad, K. Sheshyekani, and M. R. Alemi, "The effect of wide band modeling of tower-footing grounding system on the lightning performance of transmission lines: A probabilistic evaluation," *Electr. Power Syst. Res.*, vol. 141, pp. 1–10, 2016.

[29] S. Visacro and F. H. Silveira, "Review of measures to improve the lightning performance of transmission lines," *Electric Power Systems Research*, vol. 213, p. 108729, 2022.

[30] M. Paolone, F. Rachidi-Haeri, and C. A. Nucci, "IEEE guide for improving the lightning performance of electric power overhead distribution lines," IEEE, Tech. Rep., 2010.

Conclusions

The research activity presented in this thesis has focused on different aspects involving transmission line modelling and analysis, adopting approaches in the Time Domain and in the Frequency Domain.
In Chapter 1, the Finite-Difference Time-Domain (FDTD) implicit method implemented for the solution of the discretized telegrapher's equations in the Time Domain has been described. Aspects regarding its stability, accuracy, and numerical dispersion have been discussed in comparison with the main features of the commonly used Leap-Frog explicit method.

Chapter 2 has been devoted to the effect of the actual catenary profile of an overhead line conductor, as a distributed non-uniformity, on the static charge distribution along a single span; this has been achieved by introducing a 2D staircase-type approximation of the conductor's height above the ground. It has been confirmed, in a reference configuration with a single-conductor TL, that an average height h_{ave} value may be used to model the line with constant height; satisfactory agreement has been observed as to the amplitude and waveform of propagating voltage waves when the conductor is fed by a known voltage source at one line termination. However, new different results have been obtained in simulations of indirect lightning strikes. In fact, the variable conductor's height has been found to hold a non-negligible impact on the computed overvoltages, compared to simulations accounting only for the constant h_{ave}. This topic has been addressed in Chapter 3, regarding the implementation of the modified telegrapher's equations in the FDTD code, to account for the coupling of TLs with external electromagnetic fields, as from the formulation by Agrawal.

Chapters 4 and 5 have assessed the influence of distributed and lumped nonlinearities, respectively. As to distributed nonlinearities, a novel numerical technique has been adopted to simulate the inception and development of corona effect along overhead TLs, through distributed voltage-controlled current sources connected to the nodes of the discretized line. A synthesis of the relevant features of corona and a critical review of the most used corona models have been presented in Appendix A. Three models have been compared in terms of the attenuation and delay with respect to the propagation of fast- and

slow-front surges along an MTL, the outcome revealing the importance of a careful choice of the models' input parameters, since no agreement of the results computed by different models is to be expected in general. FDTD equations have been derived to perform simulations including surge arresters, which represent lumped nonlinearities installed at the towers. Their application has been discussed considering different installation scenarios and values of the grounding resistance at the towers.

In the final chapters, aspects involving grounding systems and propagation have been analysed adopting specific approaches in the Frequency Domain. In Chapter 6 an advanced hybrid method, merging circuit and field analyses in layered lossy media (introduced in Appendix B), has been exploited to compare the value of the low frequency grounding resistance offered by complex grounding structures, commonly installed along Hellenic HV transmission lines, with their response in the Frequency Domain, considering the resistive and reactive components of their actual grounding impedance. Different soil properties, both constant and frequency-dependent, have been taken into account; the behaviour of the grounding impedances observed at higher frequencies has been discussed in the light of the different shapes and leading dimensions of the considered grounding systems.

The chain matrix analysis has been applied to assess the effects of shield wires and additional ground wires, installed underneath the phase conductors, as a (protective) measure to mitigate overvoltages across the insulators caused by direct lightning of a tower/pole. In Chapter 7, an original solid formulation has been proposed to assess propagation by means of a single matrix of characteristic admittances, provided the periodicity of the line structure; matrix expressions have been derived to simulate towers/poles through circuits with lumped or distributed parameters, also accounting for a variable number of ground wires, in order to include their effect in the general chain matrix approach.

Perspectives

Time Domain

- Possible modification of the FDTD code to improve the non-centered, non-synchronised perturbation (currently computed at the previous time step) to the original telegrapher's equations, implemented to simulate nonlinear devices, grounding at the towers, corona effect, etc.;
- Further investigation on the effect of the catenary profile of the conductors in indirect lightning studies, with reference to MTLs configurations;
- Identification of a corona inception criterion, valid more rigourously for

applications involving corona developing along TLs;

- Analysis of the stress undertaken by installed surge arrester from an energetic point of view, considering their energy capabilities, with reference to different lightning currents and scenarios;
- Time domain modelling of line insulation flashover.

Frequency Domain

- Application of the proposed chain matrix approach and modelling of the pole in conjunction with a constrained-optimization method, to the aim of optimizing the number and position of the ground wires in an actual distribution line for protection against direct lightning.

Appendix A

Corona phenomenon

Corona is a nonlinear phenomenon, resulting in flow of energy (mainly electric and thermal energy) from a conductor to the external medium [1], when the electric field on the conductor surface reaches a threshold value. It consists in self-contained localised discharges in the proximity of electrode surfaces, characterised by local electric fields at high intensity, stressing the insulating strength of the surrounding dielectric medium [2].

Some of the very first references to this phenomenon date back to 1838, when Michael Faraday noticed a "*quiet phosphorescent continuous glow*", and stated that "*that form of disruptive discharge which appears as a glow [...] seems to depend on a quick and almost continuous charging of the air close to, and in contact with, the conductor*" [3].

Early relevant and extensive studies on corona were performed by Peek in the first decades of the 20^{th} century [4], [5]; when feeding a conductor with a voltage source (larger than a specific threshold value), a "*hissing noise*" and a pale luminosity were observed in the proximity of its surface [6]. Indeed, the high-frequency spectra typical of discharge processes result in emission of audible noise, and radio interference up to the MHz range, research being oriented towards prediction and mitigation of these side effects [7].

Interaction between charged particles under the accelerating effect of an external electric field, turning into an avalanche phenomenon and, finally, into a process of local discharge by breakdown of the insulating medium, raised the interest of industries. The recombination of ionized oxygen atoms, resulting from the discharge process, and oxygen molecules in the air is exploited for the production of ozone (O_3); on a utility-scale, ozone generators operated by corona technology need to trigger efficient discharges in a controlled environment in order to optimize the ozone production [8].

Therefore, since Peek's early works on this topic, a relevant contribution, supported by experimental data, was represented by the book of Gary and Moreau [9], addressing also the computation of the localized losses caused by the corona discharge. Researchers further investigated on the dependence of the value of the inception electric field on environmental and atmospheric

conditions [10], electric field distribution [11], polarity and steepness of the applied voltage waveform [12]. On the other side, some authors introduced techniques to account for the typical hysteretic relation between the voltage and the produced charge. The proposed models, which are reviewed in the following sections, are aimed at evaluating the effects of corona on surge propagation along TLs. Furthermore, the general validity of the reviewed models should be investigated, since they were frequently validated through comparison of simulated results with specific experimental data. Indeed, prior tuning of the parameters required by each model through available measured data turns fundamental when it comes to predict corona inception and development.

In the following sections, a brief reference to the phenomenology of corona and its related side effects is included, along with a description of the main physical mechanisms underlying corona inception and development [13]. In Sec. A.4, corona models available in the literature are reviewed in detail, and classified in physics-based models, empirical models, and models suitable to be included in any commercial transients program for network analyses.

A.1 Corona phenomenology

When dealing with power delivery by HV overhead TLs, corona discharge may be responsible for additional losses when the line design and specific operation conditions lead to corona inception. In fact, if the high voltages applied to the conductors — guaranteeing the efficiency of energy transmission at large distances — result in electric fields exceeding the insulating strength of the air in the proximity of the conductors, localised discharge processes may enhance p.u.l. losses [14]. This effect, undesired in normal operation conditions, may turn beneficial when unpredictable overvoltages (e.g., traveling lightning surges) propagate along the line, threatening electrical devices essential for the service continuity. However, enhanced induced voltages were obtained when the influence of corona was accounted for in indirect lightning simulations.

Along with the impact on the peak values of traveling waves and a reduction in the surges' propagation velocity [15], other peculiar phenomena associated with the corona discharge along power lines are briefly listed here, referring to the related bibliography for further investigation on these aspects (which are out of the aim of the work).

Luminosity
Laboratory measurements have shown characteristic patterns of the optical spectra in the proximity of test conductors under corona [16]; indeed, when the wavelength of corona emitted fields ranges between 380 nm and 780 nm, i.e., it is in the visible spectrum for the human eye, corona may be further detected by a violet luminosity [2].

Audible noise
An additional side effect of corona discharge is related to emissions in the audible spectrum (approximately in the range 20 Hz–20 kHz). The total emitted noise, similar to a buzzing sound, may be decomposed into broadband and single-tone components; the former are associated with discharges localised in the proximity of the conductor surface, causing rapid variations in air pressure, due to intense local heating [7]; single-tone components at power frequencies, observed in the case of intense corona along AC lines, are associated with space charge movement under the effect of the alternating electric field [17].

Radio interference
At higher frequencies, in the range between 0.01 MHz and 30 MHz, radio interference is a well-known disturbance phenomenon, which may be caused by corona development in proximity of high voltage DC and AC lines, affecting the quality of telecommunications [18]. The International Special Committee on Radio Interference (CISPR), involved in EMC issues and standardization, addresses this topic in detail in [19], with reference to radio interference due to overhead power lines. To assess the impact of corona on signal transmission at radio frequencies, three aspects are considered: frequency spectrum, lateral profile (i.e., attenuation of the field at ground level in the direction perpendicular to the source), and statistical distribution, to be evaluated following proper measurement procedures [18],[20]. Indeed, different weather conditions, features of the conductors surface (e.g., dirt, irregularities, etc.) strongly affect radio interference levels, and may be taken into account through long-term surveys and statistical analyses. Several empirical and analytical approaches have been proposed in the literature to predict the impact of corona audible noise and radio interference on the surrounding environment [21] under variable atmospheric conditions, in order to account for emissions limitation in the design of overhead HV lines and substations.

A.2 Corona inception and development

Corona is a self-sustained discharge process[1], developing in regions with high intensity electric fields, which includes ionization of the surrounding dielectric medium, drift and diffusion of charged species (electrons, or charged atoms or molecules). Microscopic or macroscopic approaches may be adopted to study and simulate this phenomenon.

[1]Self-sustained discharges do not necessitate of external sources, e.g., heating or ionizing radiations, for the ionization process to be sustained [22]. Indeed, localised discharges in the proximity of the electrodes develop through avalanche-type ions-electrons interactions favoured by the electric field distribution.

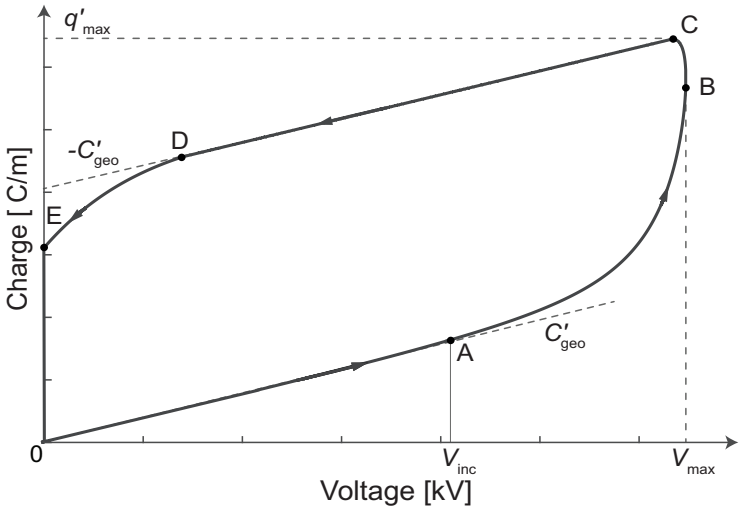

Figure A.1. Simplified representation of the main branches of the typical corona hysteretic relation between p.u.l. charge and applied voltage.

A.2.1 Microscopic level

In order for the inception to initiate, a ionization process needs to be started by production of ions and electrons at exponential rate, also denoted as avalanche mechanism, which was addressed by Townsend [23]. Referring to a cylindrical electrode in the air at atmospheric pressure, the main process involved in avalanches development is ionization of neutral molecules by collision with primary electrons; indeed, these electrons may be available in low concentration in the atmosphere and accelerated by the external electric field, or may be detached from existing negative ions and accelerated until collision. A statistical time lag τ_{st}, in the range of a few microseconds, is necessary for the formation of enough primary electrons to start the avalanche process. Experimental evidence showed that τ_{st} depends on the availability of free electrons, and on the rate of rise of the applied voltage; lower mean values of τ_{st} are associated with steeper voltage fronts [2]. Ionization by impact is generally modelled by Townsend's coefficient α, which accounts for the average number of ionizing collisions expected for a single electron along a 1 m path, and depends on the air pressure and electric field distribution [24].

When all the primary electrons have been involved in collisions, secondary electrons are necessary to act as "*seeds*" for the following avalanches. They may be produced by several mechanisms, e.g., photoionization for positive corona, which consists in the production of positive ions and electrons resulting from photon-molecule interactions [25], and secondary emission for negative corona, which corresponds to electrons emission by positive ions approaching the electrode surface and being successively neutralized [22].

Outside the ionization region, the only processes of interest are charge movement through drift (depending on the electric field and ion/electron

mobility), diffusion of charged species (linked to the gradient of the space charge density and ion/electron diffusivity), and subtraction of space charge through recombination and attachment.

DC, AC, impulse corona

Depending on the nature of the voltage source applied to the electrode under test, different corona modes develop. The work by Giao and Jordan [26] displays a detailed analysis on this topic; fundamental aspects are reported here:

- Negative DC corona: when a negative polarity voltage close to the inception value is applied, negative corona starts in the form of current pulses, known as "Trichel pulses"; the pulses frequency increases with increasing value of the applied voltage. The intermittent nature of these localised discharges is related to the space charge contribution to weaken the electric field in the electrode proximity (holding back the pulses), and to subsequent space charge removal. Further increase of the voltage leads to a pulseless glow, which may turn into negative streamers of growing length if the voltage reaches values close to the insulation breakdown [14].

- Positive DC corona: from experimental data [27], the inception voltage for positive DC corona is slightly lower compared to negative DC corona. According to [26], this is reasonably due to the electrons being accelerated in the direction of the increasing electric field, i.e., towards the anode, facilitating ionization processes. Mixed opinions may be found in the literature on this subject; for instance, in [14] corona discharge due to applied voltages with negative polarity is stated to occur at lower field values with respect to positive polarity (the difference being enhanced when sharp-shaped electrodes are considered). This is in accordance with experimental data in [28], and with values for the critical corona onset gradient in [29]. However, experimental activities aimed at assessing the corona onset field are strongly dependent on atmospherical conditions, humidity, configuration, and available free charges in the vicinity of the conductor under test. Fundamental steps in the study of positive DC corona are found in [30]. It first develops in the form of burst pulses; depending on the electrode radius, gap length, and magnitude of the applied voltage, some onset streamers may be produced as well, reaching larger radial distances from the electrode and being choked off by negative ions in the gap. Increasing voltage and higher densities of negative space charge suppress the onset streamers in favor of a diffused glow in the proximity of the anode (Hermstein's glow); streamers finally causing the insulation breakdown are observed at higher voltages, developing from the glow region [26].

- AC corona: when a sinusoidal voltage source triggers corona, combined modes typical of positive and negative DC corona are observed. In particular, a critical distance may be introduced, depending on the voltage peak value and frequency, accounting for the path covered by the charge particles during the quarters of periods from the voltage peaks to zero crossings; if the critical distance is such that no residual space charge is left by the end of the half period (i.e., suitable time has passed for the ions to migrate towards the electrode of opposite polarity and being neutralized), corona modes in the positive and negative half-cycles are expected to be equal to the DC modes with corresponding polarity. Otherwise, the residual space charge will influence the development of the corona modes during the subsequent half-cycle with opposite polarity [26].
- Impulse corona: with fast-front voltages, corona mainly develops in the streamer mode, being the role played by the space charge limited by its slower dynamics [31]. As to inception, for both positive and negative polarity, the inception voltage increases for decreasing durations of the applied voltage front time. A statistical threshold voltage V_{inc}, associated with a chosen minimum inception probability under the slowest voltage front time, may be derived experimentally for the studied configuration. The inception of corona may be detected in the proximity of the applied voltage peak V_{max}, during the voltage front, or at the voltage tail. Furthermore, values of V_{inc} under positive impulses are higher and suffer of higher dispersion with respect to those related to negative impulses [12]. Due to the stochastic nature of the phenomenon, the values of corona inception field should be described by probability distributions, accounting for the electric field distribution in the proximity of the conductor, rate of detachment of electrons, mean lifetime of ions, applied voltage, etc.; the probability of an electron to be located in a critical volume, and to be eligible to start an avalanche leading to corona inception is addressed by the critical volume theory [32].

A.2.2 Macroscopic level

Ionization and interactions among charges at microscopic level provoke a nonlinear and hysteretic relation between the total charge and the voltage at the electrode surface at macroscopic level, as sketched in Fig. A.1. When a monotonically increasing voltage is applied to a reference conductor, a proportionality factor, i.e., the conductor capacitance, governs the q-v relation until corona develops, in correspondence of the inception voltage V_{inc}; a further voltage increase results in the space charge to grow at a rate faster than linear, albeit delayed of a time τ_{sp} necessary for its formation[2] [25] (in the range

[2]Depending on the gap length, on the voltage rate of rise and peak value [2], [33].

between 25-100 μs in the hemisphere-plane gap configuration). Due to this delay time τ_{sp}, the peak value of the charge may be observed when the time derivative of the applied voltage has already reversed in sign; at later times, for decreasing values of voltage, the linearity of the q-v relation is restored. The last branch of the loop (D-E in Fig. A.1) shows a larger slope with respect to that of branch C-D. Along branch D-E, the higher rate of charge decrease ($\mathrm{d}q'/\mathrm{d}v < -C'_{geo}$ [34]) is caused predominantly by the mechanism of space charge subtraction under the effect of the electric field produced by the space charge itself; in fact, the charge reduction determined by the applied voltage source might be less relevant due to the dynamics and the magnitude of the applied source between points D and E.

As to the electric field inception value E_{inc}, different expressions have been proposed in the literature, accounting for different geometrical and electrical quantities relevant to the studied configuration. Various experimental activities [12], [35], supported by theoretical considerations [2], have put in evidence that the electric field inception value E_{inc} depends significantly on the steepness of the applied voltage.

A.2.3 Inception criterion

The approaches from Peek [5], Olsen and Yamazaki [11], and Mikropoulos and Zagkanas [36] are reviewed, their applicability is clarified, and the main ideas and considerations underlying each formulation are discussed. The majority of the inception criteria do not consider the influence of the steepness of the applied voltage on the value of the inception field, their validity being limited to DC or power frequency applications.

Criteria to be applied in TLs studies, which account for the voltage steepness influence and are rigorously valid in non-coaxial arrangements, are found to be lacking in the literature.

Furthermore, these criteria often refer to solid conductors; hence, an irregularity factor may be exploited to compute the inception voltage associated with stranded conductors and bundles.

A.3 Corona inception formulas

Inception field by Peek

Early experimental research activities by Peek [4–6] led to an expression for the inception field E_{inc} of the insulating air, i.e., the value of the electric field at which visual effects of corona, such as luminosity of the air surrounding the conductor, may be first observed:

$$E_{inc} = 30 \cdot m\delta f_p \left(1 + \frac{K_p}{\sqrt{\delta r_0}}\right) = E_0 \left(1 + \frac{K_p}{\sqrt{\delta r_0}}\right), \tag{A.1}$$

where $K_\mathrm{P} = 0.3$ in the original formulation by Peek. As expected, the inception field in (A.1), expressed in kV/cm, only depends on the conductor radius r_0 (to be expressed in centimeters when plugged into (A.1)); δ is the air density factor, and f_p is the polarity factor, related to the effect of voltage polarity on E_inc (with reference to the coaxial configuration, [37]); m is a parameter to take into account the irregularity of the conductor surface, distinguishing between perfectly smooth conductors and rough surfaces due to weather condition, debris, and aging under operation. From manipulation of (A.1), assuming $\delta = 1$ and axial-symmetric configuration, Peek's criterion may be alternatively interpreted as the value of the electric field at the conductor surface allowing to reach a field equal to E_0 at distance $\tilde{r} = r_0 + 0.3\sqrt{r_0}$ from the conductor axis (E_0 being independent from the configuration under analysis).

Indeed, according to (A.1), E_inc holds higher values for conductors presenting a smaller radius r_0, since the proposed formula, although expressed in terms of r_0, relies on a requirement for the electric field at $\tilde{r}$.

Many empirical formulas similar to (A.1) may be found in the literature, computing E_inc through the following general relation:

$$E_\mathrm{inc} = A\delta\left(1 + \frac{B}{(\delta r_0)^C}\right). \tag{A.2}$$

Coefficients A, B, and C in (A.2) (ranging between 23-35, 0.15-1, and 0.3-0.5, respectively) hold different values according to different expressions, which have been classified in [38] for DC corona.

Inception field by Olsen and Yamazaki

When dealing with the evaluation of corona inception field at power frequencies, the onset criterion by Olsen and Yamazaki [11] takes into account the predominant interactions among free charges in proximity of the conductor; in particular, the proposed corona onset criterion is associated not only with the maximum electric field at r_0, but also with the values of the electric field in the area surrounding the conductor, still not accounting for any steepness effect caused by the applied voltage. Two main phenomena are considered: charge formation through impact ionization, and space charge reduction through attachment. The former phenomenon is associated with Townsend's first ionization coefficient α, the latter with the attachment coefficient η. The inception criterion, derived from corona onset experimental data, is expressed by the following analytical condition:

$$\frac{K(r_0 + \delta_0)}{K(r_0)} = \exp\left(\int_{r_0}^{r_0+\delta_0} (\alpha - \eta)\, dr\right) \geq 3500\,. \tag{A.3}$$

In (A.3), $K(r)$ represents the number of free electrons at distance r from the conductor axis. Coefficients $\alpha = \alpha(p, E)$ and $\eta = \eta(p, E)$ have to be

intended as functions of the air pressure p and of the instantaneous electric field $E(r)$ (which is assumed to display just its radial component); δ_0 denotes the thickness of the corona layer, defined as the distance from the conductor surface at which free charges produced by impact ionization and those removed by attachment are equal, i.e., the distance where the following condition is verified:

$$\alpha\left(p, E\left(r_0+\delta_0\right)\right)=\eta\left(p, E\left(r_0+\delta_0\right)\right) . \tag{A.4}$$

Expressions for α and η can be found in [39], and read:

$$\alpha(p, E)=\begin{cases}4.7786\, p\, \mathrm{e}^{-0.221 \frac{p}{E}}, & \text{for } 0.025 \leq \frac{E}{p} \leq 0.060 \\ 9.682\, p\, \mathrm{e}^{-0.2642 \frac{p}{E}}, & \text{for } 0.060<\frac{E}{p} \leq 0.24\end{cases} \tag{A.5}$$

$$\eta(p, E)=0.01298\, p-0.541\, E+8.7 \frac{E^2}{p}, \tag{A.6}$$

where E is expressed in kV/cm, p in mmHg, α and η in cm^{-1}. Both the coefficients α and η are computed considering that the space charge influence on the electric field is negligible before inception occurs. The electric field $E(r)$, to be plugged into (A.5) and (A.6), may be found from the known applied voltage, considering the configuration under study (e.g., coaxial arrangement, conductor above a PEC surface) and the conductor's features (e.g., solid, stranded). Hence, relations (A.5), (A.6), along with the trend of the electric field surrounding the conductor, have to be taken into account simultaneously to compute E_{inc} from (A.3).

Inception field by Mikropoulos et Zagkanas

A modification to the general formula in (A.2) for the inception electric field (in kV/cm) has been proposed by Mikropoulos and Zagkanas in a coaxial arrangement [36]:

$$E_{\mathrm{inc}}=K_s \cdot 31.53\left(1+\frac{0.305}{\sqrt{r_0}}\right) \tag{A.7}$$

with

$$K_s=0.42 \cdot \operatorname{sign}\left(\left.\frac{\mathrm{d}v}{\mathrm{d}t}\right|_{10/90}\right)\left|\left.\frac{\mathrm{d}v}{\mathrm{d}t}\right|_{10/90}\right|^{0.345} \tag{A.8}$$

where the voltage time derivative on the RHS of (A.8) is the average steepness of the applied voltage in kV/μs, assuming a linear increase of the waveform between 10% and 90% of its peak value. In fact, experimental data from [36] are in good agreement with Peek's inception field only in the case of slow-front voltage sources (up to 10 kV/μs); when different impulse voltages are applied to a reference conductor, electric field onset values show a dependence on the impulse steepness, which is neglected by expressions based on Peek's formula. Hence, the steepness correction factor (A.8) has been introduced to take into

Table A.1. Main models for simulation of impulse corona.

	Model	Ref.	Model features
Physics-based models	Correia de Barros	[34], [40], [41], [42]	Multi-layer space discretization, solution of drift equations
	Malik *et al.*	[43]	One-layer model with time-dependent radius
	Cooray	[44]	Multi-layer model with time-dependent radii
Empirical models	Inoue	[45]	Expression of the corona capacitance
	Gary *et al.*	[46]	Expression of the total charge
	Podporkin and Sivaev	[47]	Expression of the total charge
	Suliciu *et al.*	[48]	Expression of the corona current
	CIGRÉ	[49]	Expression of the corona dynamic capacitance
Circuit models	Umoto and Hara	[50]	Voltage-dependent shunt capacitance and resistor
	Motoyama and Ametani	[51]	Shunt capacitor and resistor (piece-wise constant functions of the voltage)
	Maccioni, Araneo *et al.*	[52]	Voltage-dependent current generator and shunt resistor

account the increase of E_{inc} with the steeper fronts of the applied voltage. Although representing an improvement with respect to formulas not accounting for the steepness of the applied voltage, the applicability of the current approach for computation of corona inception voltages along TLs is limited; indeed, due to attenuation and distortion of propagating voltage waves, their steepness and peak value cannot be predicted *a priori* at different distances along the TL.

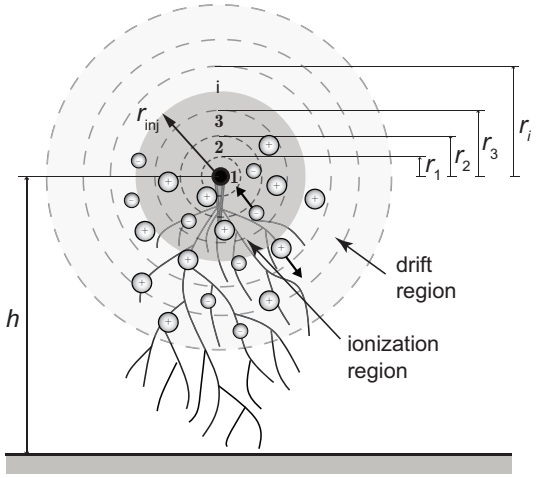

Figure A.2. Discretization of the space surrounding the conductor in coaxial cylindrical layers. The radius r_{inj} of the injection area is shown.

A.4 Models for impulse corona development

A.4.1 Physics-based models

Correia de Barros' model

An accurate analysis of the corona effect, originally referring to a single cylindrical conductor, has been proposed by Correia de Barros [53]; it was later extended to multiconductor systems [40]. Further details may be found in some earlier works as [42].

The model assumes that a time delay τ exists between the time t_{inc} at which the critical inception field E_{inc} is reached and the time at which the discharge is visibly triggered in the vicinity of the conductor surface. This time delay is composed of two different time lags, i.e., $\tau = \tau_{\mathrm{st}} + \tau_{\mathrm{sp}}$. The first term τ_{st} is the statistical time necessary for the formation of electrons by detachment (concentration of free electrons in standard atmospheric condition, associated with the electronegativity of oxygen in the air, would be too low to start an avalanche); the second term τ_{sp} is the critical time required for the formation of the space charge. τ_{st} depends on the gap size (i.e., on the conductor height), the pre-existing amount of available charged particles, and the magnitude of the overvoltage with respect to V_{inc} [25]; lower values of τ_{st} have been observed for larger applied voltages, tending towards a minimum value of 0.25 μs approximately [54].

The dynamics of formation and radial spread of the space charge around the conductor is modelled by considering a growing radius $r_{\mathrm{inj}}(t)$ of the injection layer, as well as an exponential growth of the generated space charge density. The key parameter $r_{\mathrm{inj}}(t)$ permits here, as in other models, to separate two distinct phenomenological regions: the injection/discharge region close to the

emitter conductor, where there is a source term for charge production; the drift region, at radial distance $r > r_{\text{inj}}$, where charge concentrations are low and charges are mainly electro-convected by the ruling electric field.

The space surrounding the conductor is subdivided into M cylindrical layers; the i^{th} layer (with $i = 1, 2 \dots M$) extends radially between r_{i-1} and r_i, with radial thickness $s_i = r_i - r_{i-1}$, as depicted in Fig. A.2. The configuration is studied through an equivalent coaxial one, in which the conductor holds the same geometric capacitance C'_{geo}; hence, the external radius r_M of the auxiliary coaxial arrangement is found as $r_M = r_0 \exp\left(2\pi\epsilon_0 / C'_{\text{geo}}\right) = 2h$ [34]. Assuming a average (constant) streamers velocity v_{st} [55], the instantaneous radius $r_{\text{inj}}(t)$ at time $t > t_{\text{inc}} + \tau$ is given by:

$$r_{\text{inj}}(t) = \min\left\{r_{\text{s}}, r_0 + v_{\text{st}} \cdot (t - t_{\text{inc}} - \tau)\right\} \ , \tag{A.9}$$

where r_{s} is the assumed maximum radial distance which might be covered by the injection area. The larger is r_{s}, the wider is the resulting $q - v$ loop, and the higher is the energy dissipated per cycle. From experimental evidences on transients events, the negative polarity corona is typically associated with less extended injection areas and narrower loops [46]; this may be taken into consideration by adopting a lower value of r_{s} under negative surges.

The algorithm consists in two main steps.

In the first step, the electric field $e_0(t)$ at r_0 is derived from the known applied voltage $v(t)$ and the space charge computed at the previous time step. Applying the electrostatics Green's reciprocity theorem [56] under the assumptions of linearity and soil electric permittivity much greater than ϵ_0, the following relations hold:

$$e_0(t) = \frac{1}{r_0 \ln\left(\frac{2h}{r_0}\right)} v(t) + \frac{1}{2\pi\epsilon_0 r_0} q'_{\text{ind}}(t) \tag{A.10}$$

with

$$q'_{\text{ind}}(t) = q_{\text{e}} \frac{C'_{\text{geo}}}{\epsilon_0} \sum_{i=1}^{M} k_i \left[p_i(t) - n_i(t)\right] - q'_{\text{sp}}(t) \tag{A.11}$$

and

$$k_i = \int_{r_{i-1}}^{r_i} r \ln\left(\frac{r}{r_0}\right) \mathrm{d}r \text{ with } i = 1, 2 \dots M \ , \tag{A.12}$$

where $q_{\text{e}} = 1,602 \cdot 10^{-19}$ C is the absolute value of the elementary electron charge and $q'_{\text{ind}}(t)$ is the p.u.l. charge induced on the conductor surface by the total space charge $q'_{\text{sp}}(t)$; k_i is a geometric coefficient with the dimensions of an area. In (A.11), p_i and n_i are the volumetric densities of positive and negative charged particles in the i^{th} layer (expressed in $1/\text{m}^3$). As discussed in detail in [57], the surface electric field $e_0(t)$ is found to remain almost constant during discharge and close to the onset field strength E_{inc}: this is known as Kaptzov's assumption [58], widely used in simulations to obtain quantitative

estimates of the glow corona with moderate computational effort; however, it should be applied to non-stationary corona studies only when the background electric field changes slowly [59].

When $|e_0(t)| > |E_{\text{inc}}|$, depending on the polarity of the electric field e_0, the ionization phenomenon is simulated through the injection of a new generated p.u.l. space charge of the same polarity, whose volumetric density $\mathrm{d}\rho(t)$ (charged particles injected per cubic meter) is assumed to be uniform in the injection area $r_0 < r < r_{\text{inj}}(t)$, and it is given by

$$\mathrm{d}\rho(t) = \frac{2\pi\epsilon_0 r_0 \left[E_{\text{inc}} - e_0(t)\right]}{q_{\text{e}} \left[\frac{C'_{\text{geo}}}{\epsilon_0} k_{\text{inj}}(t) - S_{\text{inj}}(t)\right]} \left(1 - \mathrm{e}^{-\frac{\Delta t}{\tau_0}}\right) , \tag{A.13}$$

where τ_0 accounts for the dynamics of space charge injection. In (A.13), $S_{\text{inj}}(t) = \pi \left[r_{\text{inj}}^2(t) - r_0^2\right]$ is the total injection area and $k_{\text{inj}}(t)$ corresponds to the integral in (A.12) performed between r_0 and $r_{\text{inj}}(t)$.

The electric field $e_i(t)$ at the separation surfaces between the M layers is found recursively from $e_{i-1}(t)$ as

$$r_i e_i(t) = r_{i-1} e_{i-1}(t) + s_i \overline{r}_i \left[p_i(t) - n_i(t)\right] \frac{q_{\text{e}}}{\epsilon_0} , \tag{A.14}$$

where s_i and $\overline{r}_i = \frac{r_i + r_{i-1}}{2}$ are the thickness and the average radius of the i^{th} layer, respectively.

In the second step of the algorithm, the positive and negative space charge densities $p_i(t)$ and $n_i(t)$ are computed from the electric fields of the previous step through the solution of the following system of $2M$ nonlinear differential drift equations (the time dependence of the quantities is omitted to ease the notation)

$$\begin{aligned} &\frac{\mathrm{d}p_i}{\mathrm{d}t} + \mu_{\text{p}} \frac{(r_i e_i p_\alpha - r_{i-1} e_{i-1} p_\beta)}{s_i \overline{r}_i} + R\, p_i n_i = 0 \\ &\frac{\mathrm{d}n_i}{\mathrm{d}t} + \mu_{\text{n}} \frac{(r_i e_i n_\alpha - r_{i-1} e_{i-1} n_\beta)}{s_i \overline{r}_i} + R\, p_i n_i = 0 , \end{aligned} \tag{A.15}$$

with $i = 1, 2, \ldots M$. These relations assume a constant mobility μ_{p} and μ_{n} of the positive and negative charges, respectively, as well as their recombination through a constant recombination coefficient R. Typical values for μ_{p}, μ_{n}, and R are reported in Table A.2. In (A.15), $\alpha = i$ and $\beta = i-1$ under positive electric field e_i, whereas $\alpha = i+1$ and $\beta = i$ under negative electric field e_i. Additionally, Dirichlet boundary conditions are assumed, i.e., $p_0 = p_{M+1} = n_0 = n_{M+1} = 0$. Once the space charge densities $p_i(t)$ and $n_i(t)$ are known, the total space charge $q'_{\text{sp}}(t)$ in (A.11) is computed as

$$q'_{\text{sp}}(t) = \pi q_{\text{e}} \sum_{i=1}^{M} \left[p_i(t) - n_i(t)\right] \left(r_i^2 - r_{i-1}^2\right) . \tag{A.16}$$

Table A.2. Values of the input parameters required by Correia de Barros' model.

Parameter	Value
r_s	$(10 \div 30) \cdot r_0$
v_{st}	$(0.3 \div 1.1) \cdot 10^6$ m s^{-1}
τ_{st}	$0.25 \div 0.7$ μs
τ_0	~ 0.5 μs
μ_p	$1.5 \cdot 10^{-4}$ m^{2}V^{-1}s^{-1}
μ_n	$1.8 \cdot 10^{-4}$ m^{2}V^{-1}s^{-1}
R	$1.5 \cdot 10^{-12}$ m^{3}s^{-1}

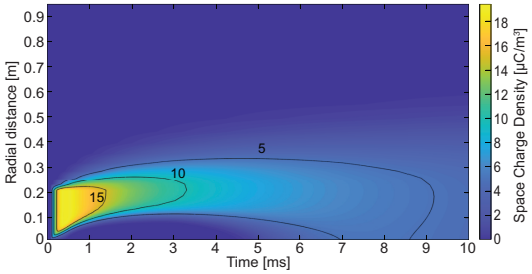

Figure A.3. Correia de Barros' model: distribution of the space charge density ρ_{sp} at increasing distance from the conductor axis, as a function of time t and radial distance r.

Finally, the total p.u.l. charge $q'(t)$ needed to obtain the $q - v$ hysteretic loop is computed as $q'(t) = C'_{geo} v(t) + q'_{ind}(t) + q'_{sp}(t)$. From the numerical derivative dq'/dv, the dynamic capacitance C'_{dyn} may be computed.

The main parameters required for the implementation of the model are synthesised in Table A.2; the range of variability given for τ_{st}, v_{st}, and r_s allows to select these parameters to fit experimental data. In Fig. A.3, the trend of the space charge density ρ_{sp} is shown, when a voltage source is applied to a conductor of radius $r_0 = 1.32$ cm at height $h = 7.5$ m over a PEC surface; the electric field at the conductor surface and the total p.u.l. charge are displayed in Fig. A.4. The waveform of the voltage source is given by the following expression:

$$v(t) = \frac{V_{max}}{\eta} \left(e^{-t/T_2} - e^{-t/T_1} \right) , \tag{A.17}$$

where $V_{max} = 2V_{inc}$, $V_{inc} = 263.25$ kV, $\eta \approx 0.78$, $T_1 = 167$ μs and $T_2 = 2648$ μs, time to peak $T_p = 493$ μs, rise time (between 10% and 90% of the voltage peak value) $T_r = 250$ μs, and time to half-value $T_h = 2500$ μs.

Malik's model

In this model [43], as long as the voltage $v(t)$ is greater than V_{inc}, the corona phenomenon is simulated through an apparent increase of the conductor radius

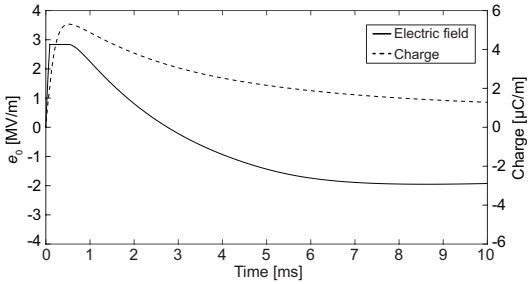

Figure A.4. Correia de Barros' model: trend of the electric field on the conductor surface $e_0(t)$ (solid line) and of the total p.u.l. charge $q'(t)$ (dashed line) as functions of time, under the same simulation conditions of Fig. A.3.

Table A.3. Typical values of the input parameters required by Malik's model.

Parameter	Positive Corona	Negative Corona
α	$0.5 \div 0.9$	
τ	$0.1 \div 0.5$ μs	

r_0 which is replaced by the radius $r_c(t) \geq r_0$. The latter quantity corresponds to the external boundary of the whole space charge area around the conductor, and it should not be confused with r_{inj} of the previous model, defining only the injection area.

The model is developed for a single conductor at height h above a PEC plane and assumes a time delay τ (ranging between 0.1 μs and 0.5 μs) in the formation of corona charge with respect to the instantaneous value of the voltage feeding the conductor. The time-dependent p.u.l. charge $q'(t)$ is given by

$$q'(t+\tau) = 2\pi\epsilon_0\alpha E_{inc} r_c(t) \frac{2h - r_c(t)}{2h} + C'_{geo}\left[v(t+\tau) - v(t)\right] , \qquad (A.18)$$

where the radius $r_c(t)$ in the presence of corona can be determined by solving the following nonlinear equation at each time instant t:

$$r_c(t)\left\{1 + \frac{2h - r_c(t)}{2h} \ln\left[\frac{2h - r_c(t)}{r_c(t)}\right]\right\} = r_0 + \frac{v(t)}{\alpha E_{inc}} . \qquad (A.19)$$

In (A.18) and (A.19), $\alpha < 1$ is a multiplicative factor taking into account the reduction of the electric field in the corona area after the inception. The main assumption of the model is to consider a constant electric field inside the corona sheath ($r_0 \leq r \leq r_c$), equal to αE_{inc}; consequently, the surface electric field $e_0(t)$ (contrary to the Kaptzov's assumption) undergoes an abrupt discontinuity when the corona discharge starts, which may result in a discontinuity in the q-v relation. Expression (A.19) shows that the parameter α introduces a step

discontinuity between r_0 and $r_c(t)$ at t_{inc}; the lower is α, the larger is the step discontinuity and the wider is the resulting corona hysteretic loop. Along with τ, α is the main parameter to be tuned for optimal fitting of measured results (in Table A.3).

From (A.18), the dynamic capacitance C'_{dyn} is computed as dq/dv; after reaching the maximum p.u.l. charge, the dynamic capacitance is considered constant and equal to the geometric capacitance C'_{geo} for decreasing values of the applied voltage $v(t)$.

Cooray's model

Herein, the approach by Cooray [44], originally formulated for arrangements displaying radially symmetric electric field, is extended to the practical configuration of a cylindrical conductor over a PEC plane; expressions suitable for comparison with other models are obtained, yet still adopting the approximation of a radially symmetric electric field.

Cooray describes the physics of the corona phenomenon identifying four different stages. In the first stage, an increasing voltage $v(t)$ is applied to the conductor; hence, a proportional relation is assumed between $q'(t)$ and $v(t)$, being C'_{geo} the proportionality factor. As the voltage reaches the inception threshold V_{inc}, the discharge starts (second stage). For a positive (negative) voltage surge, positive (negative) space charge progressively settles around the conductor; this phenomenon is taken into account through a time-dependent increasing radius $r_c(t)$. The model is based on some relevant assumptions on the physical development of the discharge phenomenon. Denoting with $r_c(t)$ the external radius of the corona charge distribution, the corresponding electric field $e_c(t) = e(t, r_c)$ is forced to the value E_c which depends on atmospheric conditions, conductor characteristics, and applied voltage polarity. A time-dependent expression is adopted for the electric field at the conductor surface $e_0(t) = e(t, r_0)$: it decays exponentially from its inception value E_{inc} to E_c, which is assumed to be the minimum field value necessary to guarantee streamers propagation. The expression reads:

$$e_0(t) = E_c + (E_{inc} - E_c)\, e^{-\frac{t - t_{inc}}{\tau_d}} \ . \tag{A.20}$$

In (A.20) τ_d is the time constant defining the electric field decay, t_{inc} denotes the corona inception time. The distribution of the corona space charge q'_{sp_+} (without loss of generality, the analysis will be hereafter limited to positive corona) is assumed to be dependent on the inverse of the radial distance r from the conductor axis (i.e., of the type $\rho_{sp_+} r^{-1}$).

It is worthy noting that, unlike previous models, any time delay in the formation of space charges is neglected. Based on these assumptions, relation (A.21) may be derived from trivial electrostatics considerations, given $h \gg r_0$ and radial symmetry:

$$q'(t) = q'_0(t) + q'_{sp_+}(t) \ . \tag{A.21}$$

Table A.4. Values of the input parameters required by Cooray's model.

Parameter	Value
E_{c}	$< E_{\mathrm{inc}}$
τ_{d}	0.5 μs
E_{ib}	–

In (A.21), the total charge $q'(t)$ is the sum of the charge on the conductor surface $q'_0(t)$ and the corona space charge $q'_{\mathrm{sp}_+}(t)$, related to the electric field through the following:

$$e_{\mathrm{c}}(t) = E_{\mathrm{c}} = \frac{q'_0(t) + q'_{\mathrm{sp}_+}(t)}{2\pi\epsilon_0 r_{\mathrm{c}}(t)} \tag{A.22a}$$

$$e_0(t) = \frac{q'_0(t)}{2\pi\epsilon_0 r_0}\,, \tag{A.22b}$$

with

$$q'_{\mathrm{sp}_+}(t) = \int_{r_0}^{r_{\mathrm{c}}} \frac{\rho_{\mathrm{sp}_+}(t)}{r} 2\pi r\, dr = 2\pi\rho_{\mathrm{sp}_+}(t)\left[r_{\mathrm{c}}(t) - r_0\right] \tag{A.23}$$

where $2h \gg r_0, r_c(t)$ (as in the case of TLs conductors), and $\rho_{\mathrm{sp}_+}(t)\, r^{-1}$ represents the radial distribution assumed for the p.u.l. space charge density in $\mathrm{C/m^3}$.

From (A.22) and (A.23), the expression below is obtained

$$\rho_{\mathrm{sp}_+}(t) = \frac{\epsilon_0\left[r_{\mathrm{c}}(t)\, e_{\mathrm{c}}(t) - r_0 e_0(t)\right]}{r_{\mathrm{c}}(t) - r_0}\,. \tag{A.24}$$

Considering both the conductor and its perfect image located at depth h below the ground surface, the instantaneous voltage is given by

$$v(t) = \frac{q'_0}{2\pi\epsilon_0}\ln\left(\frac{2h}{r_0}\right) + \frac{\rho_{\mathrm{sp}_+}}{\epsilon_0}\left(r_{\mathrm{c}} - r_0\right)\ln\left(\frac{2h}{r_{\mathrm{c}}}\right) + \\ + \frac{\rho_{\mathrm{sp}_+}}{\epsilon_0}\left(r_{\mathrm{c}} - r_0\right) - \frac{\rho_{\mathrm{sp}_+}}{\epsilon_0} r_0 \ln\left(\frac{r_{\mathrm{c}}}{r_0}\right)\,, \tag{A.25}$$

where the time dependence of $r_{\mathrm{c}}(t)$ has been omitted for conciseness. Inserting (A.24) into (A.25) leads to a nonlinear equation, which can be solved by an iterative method in the unknown $r_{\mathrm{c}}(t)$; then, the total charge $q'(t)$ is obtained by (A.21) and (A.22).

After the inception, the ionised area is supposed to expand as long as the sign of the voltage derivative is positive. The third stage of the model starts when the voltage attains its maximum value and its derivative changes sign. The model assumes that the corona sheath radius and the charge density are fixed to their maximum values r_{c}^M and $\rho_{\mathrm{sp}_+}^M$, respectively, due to the slow

mobility of the space charges. The voltage decrease is associated with an initial progressive reduction and a subsequent change in the sign of $q'_0(t)$, until $e_0(t) = E_{\mathrm{ib}}$, i.e., the electric field at the conductor surface is equal to the value causing the inception of back-corona and the development of negative space charges.

The back-corona phenomenon is the fourth stage of the model. A second ionising process starts from r_0 in the radial direction, neutralizing progressively the previously settled positive charge, and setting new negative space charge $q'_{\mathrm{sp}_-}(t)$. This new negative charge is assumed distributed (with the same distribution as in (A.23)) in the area between r_0 and an increasing radius $r_{\mathrm{cb}}(t)$. The electric field is assumed constant and equal to E_{ib} in the back-corona region, i.e., $r_0 \leq r \leq r_{\mathrm{cb}}(t)$. Hence, the negative charge density is readily obtained as $\rho_{\mathrm{sp}_-} = \epsilon_0 E_{\mathrm{ib}}$. Finally, the voltage of the conductor may be expressed as follows:

$$\begin{aligned} v(t) =& \frac{q'_0}{2\pi\epsilon_0}\ln\left(\frac{2h}{r_0}\right) + \frac{\rho_{\mathrm{sp}_-}}{\epsilon_0}(r_{\mathrm{cb}} - r_0)\ln\left(\frac{2h}{r_{\mathrm{cb}}}\right) + \\ &+ \frac{\rho_{\mathrm{sp}_-}}{\epsilon_0}\left[(r_{\mathrm{cb}} - r_0) - r_0\ln\left(\frac{r_{\mathrm{cb}}}{r_0}\right)\right] + \\ &+ \frac{\rho^M_{\mathrm{sp}_+}}{\epsilon_0}(r_{\mathrm{c}_M} - r_{\mathrm{cb}})\ln\left(\frac{2h}{r_{\mathrm{c}_M}}\right) + \\ &+ \frac{\rho^M_{\mathrm{sp}_+}}{\epsilon_0}\left[(r_{\mathrm{c}_M} - r_{\mathrm{cb}}) - r_{\mathrm{cb}}\ln\left(\frac{r_{\mathrm{c}_M}}{r_{\mathrm{cb}}}\right)\right] . \end{aligned} \tag{A.26}$$

Equation (A.26) can be solved to find $r_{\mathrm{cb}}(t)$; once the radius is known, the total charge is computed as $q'(t) = q'_0(t) + q'_{\mathrm{sp}_+}(t) + q'_{\mathrm{sp}_-}(t)$.

A last remark concerns the transition between the first and the second stage. Focusing on the instant of corona inception, if $r_c(t)$ was assumed to be a continuous function of time, then $r_c(t) \to r_0$ for $t \to t_{\mathrm{inc}}$; the application of (A.22) would lead to

$$q'_{\mathrm{sp}_+} = 2\pi\epsilon_0(E_{\mathrm{c}} r_{\mathrm{c}} - E_{\mathrm{inc}} r_0) \to 2\pi\epsilon_0 r_0(E_{\mathrm{c}} - E_{\mathrm{inc}}) \neq 0 . \tag{A.27}$$

According to (A.27), a negative space charge should exist in a ionised corona of infinitesimal thickness close to the conductor surface at t_{inc}. This physically unfeasible outcome proves in an intuitive manner the importance of predicting an initial step discontinuity for $r_{\mathrm{c}}(t)$, as for Malik's model.

A.4.2 Empirical models

Inoue's model

The expression proposed for the p.u.l. dynamic capacitance [45] is

$$C'_{\mathrm{dyn}}(v) = C'_{\mathrm{geo}} + \alpha\,\kappa\frac{[v(t) - V_{\mathrm{inc}}]^{\alpha-1}}{v(t)} , \tag{A.28}$$

with the ratio $[v(t) - V_{\text{inc}}]^{\alpha_1 - 1}/v(t)$ considered as dimensionless, and

$$\kappa = \sigma_\kappa \sqrt{\frac{r_0}{2h}} \,. \tag{A.29}$$

In (A.28) α ranges in the interval $2 \div 2.1$, and in (A.29) the value of σ_κ is in the interval $100 \div 450$ pF/m. Both the values have to be optimized to fit experimental data; to this aim, the branch of the measured q-v loop ranging between V_{inc} and the maximum voltage value $V_{\max}$ may be fitted through two connected curves with different values of κ and α in the voltage intervals $[V_{\text{inc}}, v_x]$ and $[v_x, V_{\max}]$, respectively [45].

The model does not make any distinction between positive and negative corona discharge. The capacitance $C'_{\text{dyn}}(t)$ is continuous with C'_{geo} at the inception instant, when $v(t) = V_{\text{inc}}$; no discontinuity due to the formation of the space charge is predicted.

Gary's model

According to the model presented by Gary [46], the p.u.l. charge after corona inception and for $\mathrm{d}v/\mathrm{d}t > 0$ is given by

$$q'(t) = C'_{\text{geo}} V_{\text{inc}} \left[\frac{v(t)}{V_{\text{inc}}}\right]^B \,, \tag{A.30}$$

and the dynamic capacitance of a single conductor under corona can be computed as

$$C'_{\text{dyn}}(v) = C'_{\text{geo}} B \left[\frac{v(t)}{V_{\text{inc}}}\right]^{B-1} \,, \tag{A.31}$$

where the coefficient B is given by the following experimental formula, which distinguishes the cases of impulses with different polarity:

$$B = \begin{cases} 2.924 r_0^{0.153} & \text{positive polarity} \\ 1.121 + 6.8 r_0 & \text{negative polarity.} \end{cases} \tag{A.32}$$

The model predicts a step discontinuity between $C'_{\text{dyn}}(t)$ and C'_{geo} at the inception of corona discharge ($C'_{\text{dyn}}(t) \to BC'_{\text{geo}}$ for $v(t) \to V_{\text{inc}}$), which depends on the parameter B in (A.32), i.e., on the surge polarity and the conductor radius r_0.

Podporkin and Sivaev's model

Podporkin and Sivaev originally proposed in [47] an expression for the p.u.l. charge $q'(t)$ under corona:

$$q'(t) = C'_{\text{geo}} V_{\text{inc}} \left[\frac{v(t)}{V_{\text{inc}}}\right]^{\left(\kappa_1 + \frac{v(t)}{V_{\text{inc}}} a h^{-\kappa_2}\right)} \,. \tag{A.33}$$

From the definition given in (4.2) for the dynamic capacitance, C'_{dyn} is computed as:

$$C'_{\mathrm{dyn}}(v) = h^{-\kappa_2}\frac{C'_{\mathrm{geo}}}{V_{\mathrm{inc}}}\left[\frac{v(t)}{V_{\mathrm{inc}}}\right]^{\left[\kappa_1-1+\frac{ah^{-\kappa_2}v(t)}{V_{\mathrm{inc}}}\right]} \cdot\left\{\kappa_1 h^{\kappa_2}V_{\mathrm{inc}} + av(t)\left\{1+\ln\left[\frac{v(t)}{V_{\mathrm{inc}}}\right]\right\}\right\}, \quad \text{(A.34)}$$

where $\kappa_1 = 1.17$, $\kappa_2 = 0.87$, and a is equal to 0.08 and 0.036 for positive and negative impulses, respectively.

Expression (A.34) is valid for a single conductor, while a modified expression suitable for bundles may be found in [47]. At inception, the method predicts a discontinuity in the transition from geometric to dynamic capacitance: in fact, $C'_{\mathrm{dyn}}(t) \to \kappa_1 C'_{\mathrm{geo}} + aC'_{\mathrm{geo}}h^{-\kappa_2}$ as $v(t) \to V_{\mathrm{inc}}$.

Suliciu's model

The corona phenomenon is simulated assuming that the current i'_{c} (expressed in A/m) drained to ground by any elemental section of the line can be calculated as the sum of two contributions [48]:

$$i'_{\mathrm{c}}(t) = i'_{\mathrm{sp}}(t) + C'_{\mathrm{geo}}\frac{\mathrm{d}v(t)}{\mathrm{d}t}. \quad \text{(A.35)}$$

The p.u.l. current i'_{sp}, which corresponds to the time derivative of the space charge only, can be computed as follows:

$$i'_{\mathrm{sp}}(t) = \frac{\mathrm{d}q'_{\mathrm{sp}}}{\mathrm{d}t} = \begin{cases} 0, & g_2(t) < 0 \\ g_2(t), & g_1(t) \le 0 \le g_2(t) \\ g_1(t) + g_2(t), & g_1(t) > 0 \end{cases} \quad \text{(A.36)}$$

where

$$g_j(t) = K_j\left[\left(C'_j - C'_{\mathrm{geo}}\right)[v(t) - \tilde{v}_j] - q'_{\mathrm{sp}}(t)\right] \text{ with } j = 1, 2, \quad \text{(A.37)}$$

and $C'_2 > C'_1 > C'_{\mathrm{geo}}$, $K_1 > 0$ and $K_2 > 0$; a common choice for $\tilde{v}_1 > 0$ and $\tilde{v}_2 > 0$ is $\tilde{v}_1 = \tilde{v}_2 = V_{\mathrm{inc}}$. Parameters C'_2, C'_1 are on the order of C'_{geo} in pF/m, while K_1 and K_2 range between less than 1 kHz and 5 MHz; however, the values of these parameters should be adapted in order to fit measured data.

Integrating (A.36) over time to get $q'_{\mathrm{sp}}(t)$, the total charge may be computed through the following relation:

$$q'(t) = q'_{\mathrm{sp}}(t) + C'_{\mathrm{geo}}v(t). \quad \text{(A.38)}$$

Finally, the dynamic capacitance C'_{dyn} may be found by performing the numeric derivative of the p.u.l. charge in (A.38) with respect to the applied voltage $v(t)$. Huang *et al.* extended the original model to simulate corona under applied oscillating voltages [60].

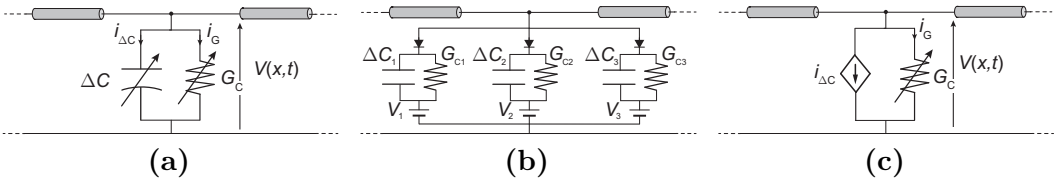

Figure A.5. Corona circuit models. (a) Model by Umoto and Hara; (b) model by Motoyama and Ametani; (c) model by Maccioni-Araneo *et al.*

CIGRÉ model

An alternative approach for corona modelling may be found in [49], in which a linear charge-voltage relation is assumed at voltages lower than V_{inc}, and for the descending branch of the q-v loop (i.e., for $\mathrm{d}v/\mathrm{d}t < 0$); instead, the following expression is considered for the total charge during corona development:

$$q'(t) = \left[C'_{\text{geo}} + C'_{\text{I}} + K\left(v(t) - V_{\text{inc}}\right)\right] v(t) \ . \tag{A.39}$$

In (A.39) K is a constant to be determined from fitting of experimental data, or approximated by values derived from tables in [49] (depending on the conductor diameter).

Recalling that (A.39) is to be applied only after the corona inception, and comparing the limit values of the p.u.l. capacitance for $v(t) \to V_{\text{inc}}^{+}$ and $v(t) \to V_{\text{inc}}^{-}$, a step discontinuity equal to C'_{I} is obtained. From the definition given for the dynamic capacitance, C'_{dyn} can be computed as

$$C'_{\text{dyn}}(t) = C'_{\text{geo}} + C'_{\text{I}} - K_{\text{I}} + 2Kv(t) \ , \tag{A.40}$$

with $K_{\text{I}} = K\,V_{\text{inc}}$. The quantity C'_{I} should be adjusted to fit measured data, while not exceeding 1 pF/m [49].

A.4.3 Circuit-based models

Umoto and Hara's model

Several models are based on the assumption that the p.u.l. corona losses p' can be computed through the following quadratic frequency-dependent relation originally proposed by Peek, and expressed in W/m [4]:

$$p'(t) = \frac{\kappa}{\delta}\sqrt{\frac{r_0}{2h}}\, f\left[v(t) - V_{\text{inc}}\right]^2 \ , \tag{A.41}$$

where f is the frequency in Hz, $v(t)$ and V_{inc} are in V, δ is the air relative density, and κ is a corona loss constant, expressed in s/(Ωm), found from analysis of experimental data.

Starting from (A.41), Umoto and Hara proposed to include the effect of corona in a FDTD updating scheme by connecting to the line nodes the parallel

of two lumped nonlinear voltage-dependent components, as the electric field $e_0(t)$ reaches the inception value E_{inc}. The equivalent circuit is represented in Fig. A.5a; additional lumped shunt branches include the capacitance ΔC, modelling the effect of the corona space charge, and a conductance G_{C}, accounting for additional corona losses. The expressions for the currents drained by the branches, $i_{\Delta C}$ and i_{G} respectively, were originally proposed in [50], and then recalled by Lee [61]:

$$i_{\Delta C} = \Delta C \frac{\mathrm{d}v(t)}{\mathrm{d}t} = 2\kappa_{\text{C}} \left[1 - \frac{V_{\text{inc}}}{v(t)}\right] \frac{\mathrm{d}v(t)}{\mathrm{d}t} \Delta x \tag{A.42a}$$

$$i_{\text{G}} = G_{\text{C}}\, v(t) = \kappa_{\text{G}} \left[1 - \frac{V_{\text{inc}}}{v(t)}\right]^2 v(t)\ \Delta x\,, \tag{A.42b}$$

with

$$\Delta C = 2\kappa_{\text{C}} \left[1 - \frac{V_{\text{inc}}}{v(t)}\right] \Delta x \tag{A.43a}$$

$$G_{\text{C}} = \kappa_{\text{G}} \left[1 - \frac{V_{\text{inc}}}{v(t)}\right]^2 \Delta x\,. \tag{A.43b}$$

Factors κ_{C} and κ_{G} may be expressed as

$$\kappa_{\text{C,G}} = \sigma_{\text{C,G}} \sqrt{\frac{r}{2h}} \cdot 10^{-11} \tag{A.44}$$

where σ_{C} is approximately in the range $15 \div 35$ F/m, and σ_{G} (corona loss constant) is in the interval $5 \cdot 10^6 \div 20 \cdot 10^6$ S/m, depending on the configuration under study.

For sufficient accuracy, the distance between voltage nodes equipped with additional lumped corona branches should be less than $\Delta x = 70$ m; indeed, a further increment in Δx would result in noticeable deviation from benchmark experimental data [61].

Motoyama and Ametani's model

In order to avoid nonlinear components in Umoto and Hara's model, Motoyama and Ametani proposed a further development [51]. Expressions (A.43) for the lumped equivalent capacitance and conductance are replaced by three piece-wise constant functions of the voltage $v(t)$, which are valid for $\mathrm{d}v/\mathrm{d}t > 0$:

$$\Delta C(v) = \begin{cases} \Delta C_1, & V_{\text{inc}} \le v(t) < 2V_{\text{inc}} \\ \Delta C_1 + \Delta C_2, & 2V_{\text{inc}} \le v(t) < 3V_{\text{inc}} \\ \Delta C_1 + \Delta C_2 + \Delta C_3, & v(t) \ge 3V_{\text{inc}}\,, \end{cases} \tag{A.45}$$

and

$$G_{\mathrm{C}}(v) = \begin{cases} G_{\mathrm{C1}}, & V_{\mathrm{inc}} \le v(t) < 2V_{\mathrm{inc}} \\ G_{\mathrm{C1}} + G_{\mathrm{C2}}, & 2V_{\mathrm{inc}} \le v(t) < 3V_{\mathrm{inc}} \\ G_{\mathrm{C1}} + G_{\mathrm{C2}} + G_{\mathrm{C3}}, & v(t) \ge 3V_{\mathrm{inc}}\,, \end{cases} \tag{A.46}$$

where

$$\Delta C_k = 2\kappa_{\mathrm{C}} \left(1 - \frac{V_{\mathrm{inc}}}{V_{\mathrm{inc}} + V_k}\right) \Delta x \tag{A.47a}$$

$$G_{\mathrm{C}k} = \kappa_{\mathrm{G}} \left(1 - \frac{V_{\mathrm{inc}}}{V_{\mathrm{inc}} + V_k}\right)^2 \Delta x \tag{A.47b}$$

with $V_k = k\,V_{\mathrm{inc}}$, k =1,2,3.

Parameters κ_{C} and κ_{G} are given by expressions (A.44), in which σ_{C} ranges approximately between 2 and 33 F/m, and σ_{G} is in the interval $0.5 \cdot 10^6 \div 13 \cdot 10^6$ S/m. The proposed model may be easily embedded in any transients program, plugging the equivalent circuit in Fig. A.5b to selected voltage nodes; the model is claimed to be more practical with respect to Lee's model: it should allow to plug lumped circuits for corona at larger intervals still holding accuracy, even just at the line towers for $\Delta x \simeq \ell$ in the range $350 \div 450$ m [51].

Maccioni-Araneo *et al.* model

The model refers to a single conductor, and introduces two lumped shunt branches [52] as shown in Fig. A.5c: the first branch consists in the voltage-controlled current generator $i_{\Delta \mathrm{C}}(t)$, simulating the increment in the capacitive current; the second branch is represented by a nonlinear conductance $G_{\Delta \mathrm{C}}(t)$, accounting for corona losses. As the voltage $v(t)$ reaches V_{inc}, the voltage-controlled current generator is turned on, fictitiously reproducing the increase of the conductor capacitance $\Delta C(t)$ due to corona. As the voltage starts to decrease, the generator is turned off; hence, the charge associated with the line section displays a linear dependence on the voltage throughout the descending branch of the q-v curve ($C'_{\mathrm{geo}} \Delta x$ being the proportionality factor).

Following the theory of the physics-based models, when $\mathrm{d}v/\mathrm{d}t > 0$, $\Delta C(t)$ is computed as

$$\Delta C(t) = 2\pi\varepsilon_0 \left[\frac{1}{\ln \frac{2h}{r_{\mathrm{c}}(t)}} - \frac{1}{\ln \frac{2h}{r_0}}\right] \Delta x\,, \tag{A.48}$$

where the time-dependent radius $r_{\mathrm{c}}(t)$ is computed as the solution of the following nonlinear equation:

$$v(t) = r_{\mathrm{c}}(t)\, E_{\mathrm{inc}} \ln\left[\frac{2h}{r_{\mathrm{c}}(t)}\right]\,. \tag{A.49}$$

The current generator $i_{\Delta \mathrm{C}}(t) = \mathrm{d}\left[\Delta C(t)\, v(t)\right]/\mathrm{d}t$ is given by

$$i_{\Delta \mathrm{C}}(t) = \begin{cases} 0, & v(t) < V_{\mathrm{inc}} \text{ or } \mathrm{d}v/\mathrm{d}t < 0 \\ v(t)\, \frac{\mathrm{d}(\Delta C(t))}{\mathrm{d}t} + \Delta C(t)\, \frac{\mathrm{d}v(t)}{\mathrm{d}t}, & v(t) \ge V_{\mathrm{inc}} \text{ and } \mathrm{d}v/\mathrm{d}t > 0. \end{cases} \tag{A.50}$$

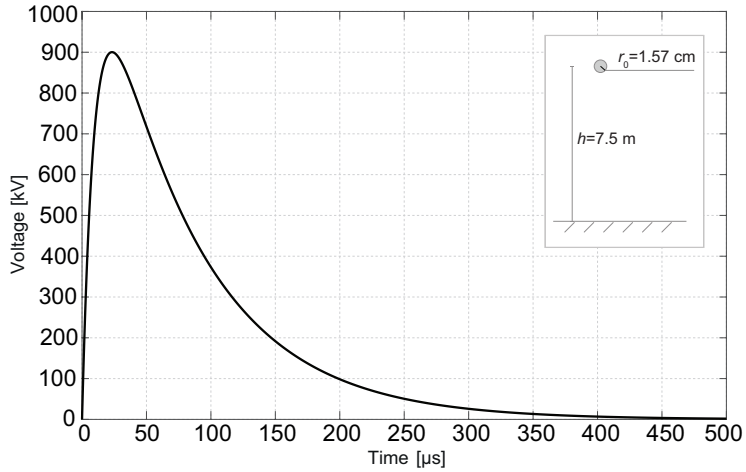

Figure A.6. Reference voltage applied to the conductor in the configuration displayed in the inset.

Equations (A.48) to (A.50) may be easily inserted into any FDTD code.

The value of the lumped equivalent conductance $G_{\mathrm{C}}(v)$ is computed according to (A.43b) [61] for $v(t) \geq V\mathrm{inc}$ and $\mathrm{d}v/\mathrm{d}t > 0$. Once the voltage applied to the conductor has reached its maximum value $V_{\max}$ and begins to decrease, the conductance G_{C} is kept connected to the line, according to [62]; however, G_{C} is no longer considered a voltage-dependent quantity, but it is assumed constant and equal to the value attained by (A.43b) when the corona radius has reached its maximum value $r = r_{\max}$.

With reference to (A.49), the main simplifying hypothesis adopted by this model consists in assuming the corona sheath to be conductive enough so that the voltage drop across the ionised area may be disregarded; hence, the potential $v(t)$ is intended to be measured at the outer surface of the space charge region, *not* on the conductor surface.

A.5 Comparison of the models sensitivity to the input parameters

Table A.5 is provided to compare the reviewed models in terms of the number of required input parameters. As to their applicability with respect to the type of voltage source, all the models should be exploited when a unipolar waveform is applied to the conductor, except for the model by Correia de Barros, which is suitable for studies involving any voltage waveform, both impulsive and AC steady-state (due to the modelling of the drift of negative and positive charges). In this section, curves will be provided to address the influence of the parameters required by each model on the shape of the final q-v curves. The voltage impulse displayed in Fig. A.6 is applied to a reference conductor

Table A.5. Input parameters required by the corona models.

	Number of input parameters	Input parameters
Correia de Barros	7	r_s, v_st, τ_st, τ_0 μ_p, μ_n, R
Malik *et al.*	2	α, τ
Cooray *et al.*	3	E_c, E_ib, τ_d
Inoue	2	α, σ_κ
Gary *et al.*	1	B
Podporkin and Sivaev	3	κ_1, κ_2, a
Suliciu *et al.*	4	C_1', C_2', K_1, K_2
CIGRÉ	2	K, C_I'
Umoto and Hara	2	σ_C, σ_G
Motoyama and Ametani	2	σ_C, σ_G
Maccioni, Araneo *et al.*	1	σ_G

(the geometrical configuration is shown in the inset of Fig. A.6):

$$v\left(t\right) = \frac{V_\mathrm{max}}{\eta}\left[\exp\left(\frac{-t}{\tau_2}\right) - \exp\left(\frac{-t}{\tau_1}\right)\right], \tag{A.51}$$

where $\tau_1 = 10$ μs, $\tau_2 = 75$ μs, and $\eta = 0.636$. The voltage peak value has been chosen equal to $V_\mathrm{max} = 3V_\mathrm{inc}$; $V_\mathrm{inc} = 300$ kV is computed according to the commonly used Peek's formula (A.1), since the validity of the formula proposed by Mikropoulos and Zagkanas is limited to coaxial configurations [63], and the criterion proposed by Olsen and Yamazaki applies to power frequencies [11].

The following sections investigate the variability of the hysteretic q-v loops computed by the different approaches, with respect to the input parameters required by the models. In particular, for a model depending on n_p input parameters, an n_p-dimensional finite region of space is defined, where the n_p parameters may vary in well-defined ranges of admissible values; q-v curves are computed for one hundred points of this space, i.e., for one hundred different combinations of the input parameters (which are randomly extracted from a

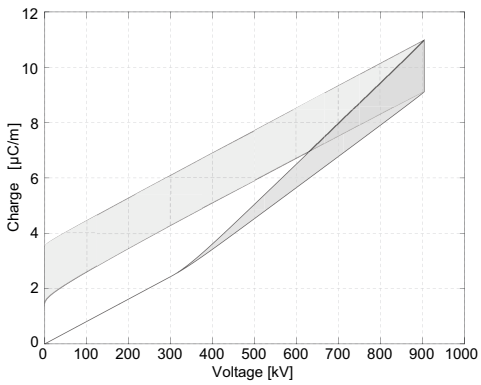

(a) Correia de Barros' model.

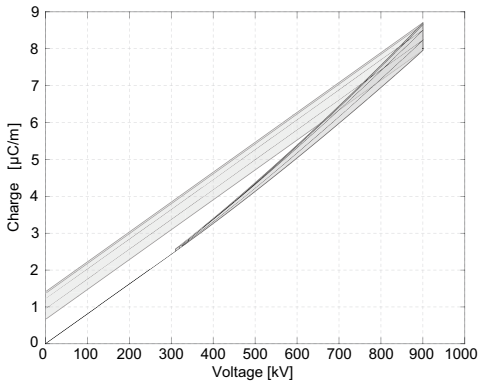

(b) Malik's model.

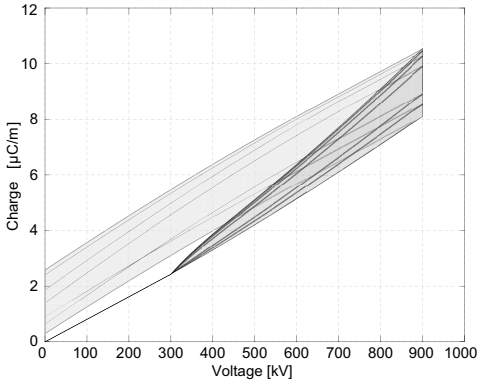

(c) Cooray's model.

Figure A.7. Charge-voltage loops displaying the sensitivity of physics-based models to the variation of the input parameters.

uniform distribution in their variability range). The overall areas swiped by the curves corresponding to the different corona models will be displayed.

A.5.1 Sensitivity curves for physics-based models

Results related to the implementation of physics-based models (in Sec. A.4.1) are displayed in Figs. A.7.

Figure A.7a shows the area swiped by q-v loops by Correia de Barros' model. The input parameters range in the following intervals (derived from data found in the relevant literature): $r_s \in [10 \cdot r_0, 30 \cdot r_0]$, $v_{st} \in [0.3 \cdot 10^6, 1.1 \cdot 10^6]$, $\tau_{st} \in [0.5, 0.7]$ μs, $\tau_0 = 0.5$ μs.

Results by Malik's model are in Fig. A.7b. The input parameters required by the model, i.e., τ and α, range between $0.1 \div 0.5$ μs and $0.5 \div 0.9$, respectively. The model does not show significant dependence on the input parameters; their impact may be noticed mainly at the inception. The different time delays τ result in slight variations in the location of the discontinuity in the q-v loops at

corona inception. Indeed, some additional curves are displayed for the reader's convenience to highlight this observation. Lower values of α result in a faster growth of the equivalent external radius, hence the slope of the rising branch in Fig. A.7b is more pronounced, enlarging the total loop area.

Charge-voltage curves computed by Cooray's model are shown in Fig. A.7c. The variability ranges assumed for the input parameters are: $\tau_{\mathrm{d}} = 0.5$ μs, $E_{\mathrm{c}} \in [0.2 \cdot E_{\mathrm{inc}}, 0.8 \cdot E_{\mathrm{inc}}]$, $E_{\mathrm{ib}} \in [-0.8 \cdot E_{\mathrm{inc}}, -0.2 \cdot E_{\mathrm{inc}}]$. The slope of the ascending branch of the loops, after the inception, is influenced by E_{c}: values of E_{c} closer to (much smaller than) E_{inc} result in a slow (fast) growth of the charge with respect to the voltage. If the electric field on the conductor surface reaches the value E_{ib} at the tail of the applied voltage, the charge decay will be faster, with lower values of residual p.u.l. charge. Indeed, the descending branch will deviate from the expected linear trend (with slope equal to C'_{geo}).

As to the shape of the hysteretic curves, the models result in different shapes. With reference to Malik's model, the loops are tight and with definite shape, predicting maximum values of the p.u.l. charge which are lower with respect to results obtained by Cooray's and Correia de Barros' models.

Comparison of the descending branches of the curves reveals some differences. The constant value of the p.u.l. capacitance assumed by Malik, equal to C'_{geo}, results in the constant slope of the corresponding branch. Instead, Cooray's curves show more pronounced slopes for $\mathrm{d}v/\mathrm{d}t < 0$, due to the progressive accumulation of negative p.u.l. charge on the conductor surface, and to the subsequent inception of back-corona (depending on the value of E_{ib}).

Results relative to Correia de Barros' model have been computed for a larger time window, up to 1 ms, in order to properly show the curvature of the descending branches for $v(t) \to 0$. If the other models present a residual p.u.l. charge caused by the applied voltage amplitude and time derivative, $q'(t)$ vanishes in Fig. A.7a for $v(t) \to 0$ and $t \to \infty$, due to the gradual drift of residual charged particles in the medium surrounding the conductor.

A.5.2 Sensitivity curves for empirical models

Figure A.8 collects corona q-v loops computed by means of the empirical models in Sec. A.4.2. Sensitivity studies have been conducted by considering some variability ranges for the input parameters (which should be set by fitting experimental data), starting from values previously adopted in the literature (if available), or choosing arbitrarily.

Inoue's model is associated with the widest range of variability of the output curves; hence, its predictive capability is questionable, and comparison with measured data is essential to tune the input parameters and get reliable results. The curves in Fig. A.8a were obtained for $\alpha \in [2, 2.1]$ and $\sigma_\kappa \in [100, 450]$ pF/m (similar values are adopted in [45] for the first branch of the q-v loop after the inception). The product $\sigma_\kappa \cdot \alpha$ determines the slope of the nonlinear sections.

Gary's model should be tuned on experimental data by means of the

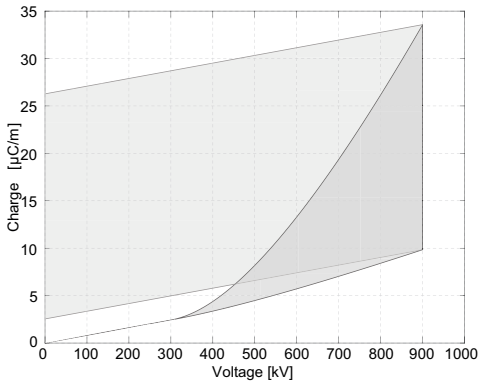

(a) Inoue's model.

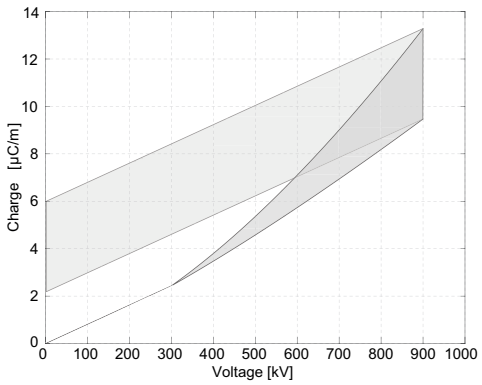

(b) Gary's model.

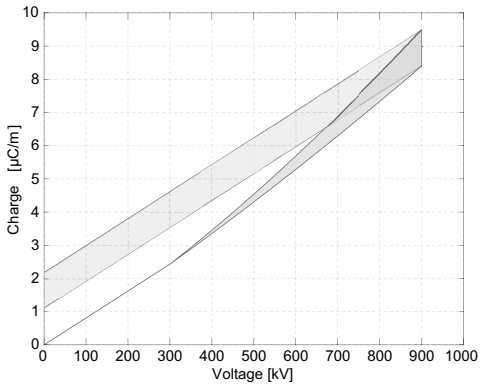

(c) Podporkin and Sivaev's model.

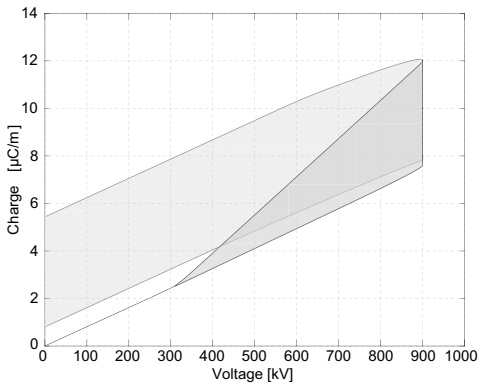

(d) Suliciu's model.

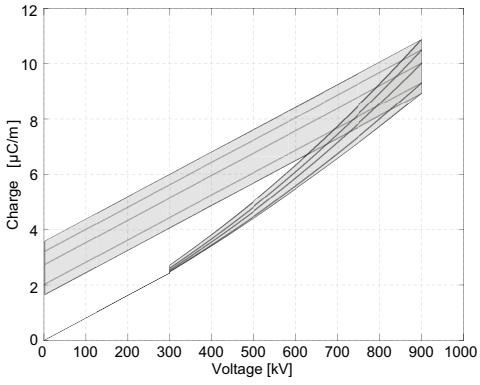

(e) Cigré model.

Figure A.8. Charge-voltage loops displaying the sensitivity of empirical models to the variation of the input parameters.

parameter B (the original values by Gary are found in (A.32)). In order to address the model dependence on B, curves in Fig. A.8b were computed with $B \in 1.23 \div 1.55$, i.e., in the range defined by values in (A.32). Wider loops correspond to larger values of B.

Figure A.8c presents the area covered by Podporkin and Sivaev's curves. Since $\kappa_1 = 1.17$ and $\kappa_2 = 0.87$ should be values of practical use for $0.5 < r_0 < 3$ cm and $10 < h < 30$ m [47], here, arbitrary and heuristical ranges of variability are selected to account for the different height of the conductor $h = 7.5\text{m} < 10$ m): $\kappa_1 \in [1.1, 1.2]$, $\kappa_2 \in [0.8, 0.9]$, while a is in the interval $0.036 \div 0.08$.

As to Suliciu's model, the following set of input parameters was chosen: $C_1' \in \left[C'_{\text{geo}}, 2C'_{\text{geo}}\right]$, $C_2' \in \left[C'_{\text{geo}}, 4C'_{\text{geo}}\right]$ ensuring $C_2' > C_1'$, $K_1 \in [0.5, 5]$ MHz, and $K_2 \in [0.5, 5]$ kHz. The output curves show a characteristic shape; in particular, the maximum p.u.l. charge value may not correspond to the maximum applied voltage. This is due to the fact that the capacitive current flowing towards the ground depends not only on the voltage time derivative, but also on the voltage instantaneous value (in (A.35)-(A.37)).

Sensitivity curves computed by Cigré model with respect to C_{I}' and K are shown in Fig. A.8e. Considering values of K in [49] corresponding to the diameter of the reference conductor, q-v loops are computed for $K \in [2.5 \cdot 10^{-6}, 5 \cdot 10^{-6}]$ pF/(V·m); the value of $C_{\text{I}}' \leq 1$ pF/m was chosen between $0.1 \div 1$ pF/m. Growing values of C_{I}' introduce harsher step-like discontinuities at the inception voltage, i.e., at $v \simeq 300$ kV; instead, larger values of K enhance the rate of rise of the nonlinear branch of the curves.

A.5.3 Sensitivity curves for circuit-based models

In Sec. A.4.3, the parameter σ_{C} is responsible for the variation of the total capacitance. In Figs. A.9a and A.9b, curves computed by the models of Umoto-Hara and Motoyama-Ametani are presented, respectively, with σ_{C} ranging in the interval $15 \div 35$ F/m (from values adopted in [61], in good agreement with [51]). Both models are strongly dependent on the input parameters, as may be deduced by the range covered by the displayed curves. Larger values of σ_{C} correspond to wider q-v loops.

The hysteretic curves in Fig. A.9b are wider than the curves in Fig. A.9a. This is due to the simplified approach proposed by Motoyama and Ametani (Sec. A.4.3). In fact, for the voltage intervals $V_{\text{inc}} \leq v(t) < 2V_{\text{inc}}$ and $2V_{\text{inc}} \leq v(t) < 3V_{\text{inc}}$, the piece-wise constant capacitance defined by Motoyama and Ametani exceeds the values computed by means of Umoto and Hara's approach.

The single parameter required by the model of Maccioni-Araneo *et al.* is σ_{G}, i.e., the conductance accounting for the corona losses in its equivalent circuit representation. Instead, the capacitive current, denoted with $i_{\Delta\text{C}}$ in (A.50), only depends on the geometrical features of the configuration under study and on the conductor-to-ground voltage. Hence, the total charge corresponding to the applied voltage (which is derived as the sum of the instantaneous electrostatic charge and the time integral of the additional corona capacitive

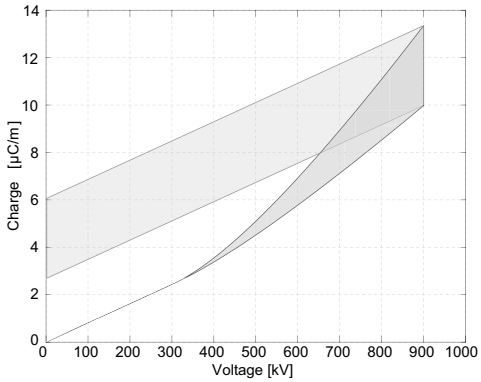

(a) Umoto and Hara's model.

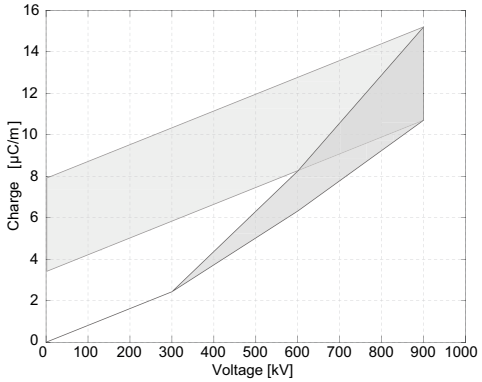

(b) Motoyama and Ametani's model.

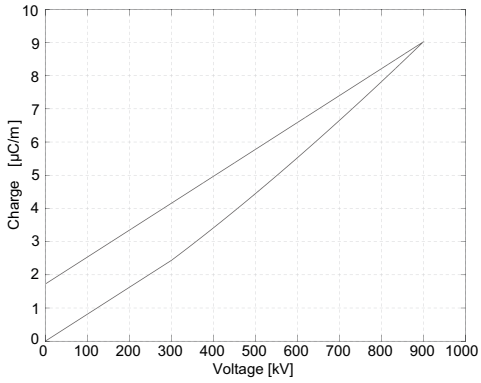

(c) Maccioni-Araneo *et al.* model.

Figure A.9. Charge-voltage loops displaying the sensitivity of circuit-based models to the variation of the input parameters.

current $i_{\Delta C}$) is displayed in Fig. A.9c (the independence of any input parameter results in a single q-v loop).

A.6 Discussion

Inception voltages computed using Peek's equation agree well with measured data, provided that an appropriate value of the irregularity factor m is adopted [64]. Despite its simplicity, Peek's equation, which is largely used for engineering purpose, strongly depends on the correct choice of m, and this choice is not trivial, since m varies significantly [37] with conductors geometry, surface state, and weather conditions. Hence, a suitable value should be derived from available measurements.

As to stranded conductors, the electrical field at the tip of each strand is about 14% higher than the field on the surface of a smooth cylindrical conductor showing the same outer diameter [65]. Engineers usually refer to an equivalent (smooth) conductor when it comes to bundles too. However, since

the surface maximum electric field of the equivalent conductor is less intense than that of the bundle, further corrections are needed when calculating the onset voltage.

As to the different reviewed models, a practical overview on the considerations to be made when choosing a specific model for implementation is presented in Table A.6. Only Correia de Barros' approach accounts for the drift of the charged particles. Hence, it allows to consider the dynamics of the p.u.l. charge, approaching zero for large simulation times and for decaying values of the applied voltage; the drawback is the heavier computational burden. On the contrary, Malik's and Cooray's models, being based on a macroscopic approximation of the physical phenomenon, are easier to implement. In particular, since the shape of the q-v loops computed through Malik's model is narrower and hardly dependent on the input parameters (Fig. A.7b), the model may turn not suitable to fit measured q-v curves with different shapes.

Only Inoue's model does not predict discontinuities in the p.u.l. capacitance value at corona inception; with reference to Suliciu's approach, a discontinuity may be introduced depending on the values attributed to $\tilde{v}_j$ $(j = 1, 2)$. Harsh discontinuities of the p.u.l. dynamic capacitance (i.e., abrupt changes in the propagation velocity of travelling waves) should be carefully handled in FDTD approaches, to avoid numerical instability [66].

Finally, the implementation of circuit-based models requires a compromise to be made between the simplicity of plugging a limited number of shunt branches to the equivalent circuit of the TL under study, and the accuracy in modelling the corona effect as a distributed phenomenon.

Table A.6. Features of the reviewed models.

	Advantages	Disadvantages
Correia de Barros	· Accurate physical model; · Drift of the charges is simulated.	· Structured coding is necessary; · Longer computation times; · Multiple parameters required.
Malik	· Simple implementation.	· Narrow q-v curves; · Limited versatility when fitting experimental data.
Cooray	· Simple implementation; · Implementation of back-corona.	· Instantaneous q-v relation (unlike other physics-based models).
Inoue	· Simple implementation; · Versatility when fitting experimental data.	· Strong dependence on the input parameters: questionable predicting capability; · No distinction between positive and negative corona.
Gary *et al.*	· Simple implementation; · Distinction between positive and negative corona.	· Discontinuity of dynamic capacitance at inception.
Podporkin, Sivaev	· Simple implementation.	· Discontinuity of dynamic capacitance at inception.
Suliciu	· Maximum values of q and v are not simultaneous.	· Multiple parameters required.
CIGRÉ	· Simple implementation.	· Discontinuity of dynamic capacitance at inception.
Umoto, Hara	· Trivial implementation in EMTPs.	· Less accurate representation of corona as a distributed phenomenon.
Motoyama, Ametani	· Trivial implementation in EMTPs; · Limited computational burden.	· Excessive simplification of the nonlinear phenomenon (constant-valued ΔC); · Less accurate representation of corona as a distributed phenomenon.
Maccioni, Araneo *et al.*	· Simple implementation.	· q-v curves have fixed shape; · Less accurate representation of corona as a distributed phenomenon.

References

[1] P. A. Laplante, *Electrical engineering dictionary.* CRC Press LLC, 2000.

[2] I. Gallimberti, "The mechanism of the long spark formation," *Le Journal de Physique Colloques*, vol. 40, no. C7, pp. C7–193, 1979.

[3] M. Faraday, "VIII. experimental researches in electricity.—thirteenth series," *Philosophical Transactions of the Royal Society of London*, no. 128, pp. 125–168, 1838.

[4] F. W. Peek, "The law of corona and the dielectric strength of air," *Proceedings of the American Institute of Electrical Engineers*, vol. 30, no. 7, pp. 1485–1561, Jul. 1911.

[5] ——, "The law of corona and dielectric strength of air - II," *Proceedings of the American Institute of Electrical Engineers*, vol. 31, no. 6, pp. 1085–1126, 1912.

[6] ——, *Dielectric phenomena in high voltage engineering.* McGraw-Hill Book Company, Incorporated, 1920.

[7] F. A. M. Rizk and G. N. Trinh, *High voltage engineering.* CRC Press, 2018.

[8] M. Goldman, A. Goldman, and R. Sigmond, "The corona discharge, its properties and specific uses," *Pure and Applied Chemistry*, vol. 57, no. 9, pp. 1353–1362, 1985.

[9] C. Gary and M. Moreau, "L'effet de couronne en tension alternative," *Collection de la Direction des Etudes et Recherches d'Electricité de France Paris*, 1976.

[10] J.-R. Riba, W. Larzelere, and J. Rickmann, "Voltage correction factors for air-insulated transmission lines operating in high-altitude regions to limit corona activity: a review," *Energies*, vol. 11, no. 7, 1908, 2018.

[11] K. Yamazaki and R. G. Olsen, "Application of a corona onset criterion to calculation of corona onset voltage of stranded conductors," *IEEE Trans. Dielectr. Electr. Insul.*, vol. 11, no. 4, pp. 674–680, 2004.

[12] E. I. Bousiou, P. N. Mikropoulos, and V. N. Zagkanas, "Experimental investigation of the overvoltage steepness effects on corona inception characteristics," in *The International Symposium on High Voltage Engineering*. Springer, 2019, pp. 1413–1422.

[13] E. Stracqualursi, R. Araneo, and S. Celozzi, "The corona phenomenon in overhead lines: Critical overview of most common and reliable available models," *Energies*, vol. 14, no. 20, 6612, Oct. 2021.

[14] R. Lings, *EPRI AC Transmission Line Reference Book: 200 kV and Above, Third Edition*. Palo Alto: Electric Power Research Institute, 2005.

[15] C. F. Wagner and B. L. Lloyd, "Effects of corona on traveling waves," *Electrical Engineering*, vol. 74, no. 12, pp. 1071–1071, Dec. 1955.

[16] S. Krzewiński, P. Frącz, I. Urbaniec, and T. Turba, "Comparative analysis of optical signals emitted by corona on a laboratory model of transmission lines made of various materials," *Journal of Spectroscopy*, vol. 2017, 2017.

[17] Z. Engel and T. Wszołek, "Audible noise of transmission lines caused by the corona effect: analysis, modelling, prediction," *Applied Acoustics*, vol. 47, no. 2, pp. 149–163, 1996.

[18] "IEEE standard procedures for the measurement of radio noise from overhead power lines and substations," *IEEE Std 430-2017 (Revision of IEEE Std 430-1986)*, pp. 1–34, 2017.

[19] IEC, *CISPR TR 18-1 Radio interference characteristics of overhead power lines and high-voltage equipment - Part 1: Description of phenomena*, 2017.

[20] W. G. C4.202, "Guide for measurement of radio frequency interference from HV and MV substations," *Brochure*, vol. 391, 2009.

[21] A. Donini, R. Spezie, R. Cortina, E. A. Piana, and R. Turri, "Accurate prediction of the corona noise produced by overhead transmission lines," in *AEIT International Annual Conference*, 2016, pp. 1–6.

[22] Y. P. Raizer and J. E. Allen, *Gas discharge physics*. Springer Berlin, 1997, vol. 2.

[23] J. S. Townsend, *Electricity in gases*. New York: Clarendon Press, 1915.

[24] G. E. Georghiou, A. Papadakis, R. Morrow, and A. Metaxas, "Numerical modelling of atmospheric pressure gas discharges leading to plasma production," *Journal of Physics D: Applied Physics*, vol. 38, no. 20, p. R303, 2005.

[25] C. Wadhwa, *High voltage engineering*. New Age International, 2006.

[26] T. N. Giao and J. B. Jordan, "Modes of corona discharges in air," *IEEE Trans. Antennas Propag.*, no. 5, pp. 1207–1215, 1968.

[27] E. Bousiou, P. Mikropoulos, and V. Zagkanas, "Experimental investigation of negative DC corona on conductor bundles: A comparison with positive corona," in *2017 52nd International Universities Power Engineering Conference (UPEC)*. IEEE, 2017, pp. 1–5.

[28] P. Mikropoulos, V. Zagkanas, and T. Koustoulidis, "Experimental investigation of DC corona on stranded conductors under variable air density," in *2012 47th International Universities Power Engineering Conference (UPEC)*. IEEE, 2012, pp. 1–6.

[29] W. CIGRE, "Addendum to doc.20 : Interferences produced by corona effect of electric systems." *CIGRE*, 1966.

[30] L. B. Loeb, "Electrical coronas: their basic physical mechanisms," 1965.

[31] M. Abdel-Salam, *High-voltage engineering: theory and practice, revised and expanded*. CRC Press, 2018.

[32] E. Bousiou, P. Mikropoulos, and V. Zagkanas, "Application of the critical volume theory to estimating impulse corona characteristics in the coaxial cylindrical electrode arrangement," in *2017 52nd International Universities Power Engineering Conference (UPEC)*. IEEE, 2017, pp. 1–5.

[33] G. Baldo, I. Gallimberti, H. Garcia, B. Hutzler, J. Jouaire, and M. Simon, "Breakdown phenomena of long gaps under switching impulse conditions influence of distance and voltage level," *IEEE Trans. Power App. Syst.*, vol. 94, no. 4, pp. 1131–1140, 1975.

[34] M. T. Correia de Barros, "Efeito coroa em linhas de transporte de energia," Ph.D. dissertation, Doctor's Degree Thesis, IST-Tecnical University of Lisbon, 1985.

[35] P. S. Maruvada, H. Menemenlis, and R. Malewski, "Corona characteristics of conductor bundles under impulse voltages," *IEEE Trans. Power App. Syst.*, vol. 96, no. 1, pp. 102–115, 1977.

[36] P. Mikropoulos and V. Zagkanas, "Impulse corona inception in the coaxial cylindrical electrode arrangement in air: effects of the steepness of the applied voltage," in *Proc. 18th International Symposium on High Voltage Engineering*, 2013.

[37] E. I. Bousiou, P. N. Mikropoulos, and V. N. Zagkanas, "Corona inception field of typical overhead line conductors under variable atmospheric conditions," *Electric Power Systems Research*, vol. 178, p. 106032, 2020.

[38] P. Mikropoulos and V. Zagkanas, "Threshold inception conditions for positive dc corona in the coaxial cylindrical electrode arrangement under variable atmospheric conditions," *IEEE Trans. Dielectr. Electr. Insul.*, vol. 22, no. 1, pp. 278–286, 2015.

[39] P. S. Maruvada and W. Janischewskyj, "DC corona on smooth conductors in air. Steady-state analysis of the ionisation layer," in *Proc. of the Institution of Electrical Engineers*, vol. 116, no. 1. IET, 1969, pp. 161–166.

[40] M. T. Correia De Barros, "Identification of the capacitance coefficients of multiphase transmission lines exhibiting corona under transient conditions," *IEEE Trans. Power Del.*, vol. 10, no. 3, pp. 1642–1648, Jul. 1995.

[41] C. De Jesus and M. T. Correia De Barros, "Modelling of corona dynamics for surge propagation studies," *IEEE Trans. Power Del.*, vol. 9, no. 3, pp. 1564–1569, 1994.

[42] M. T. Correia de Barros and C. De Jesus, "Wide bandwidth modeling of corona on high voltage transmission lines," *Annual Report Conference on Electrical Insulation and Dielectric Phenomena*, vol. 1, no. 1, p. 846, 1993.

[43] X.-R. Li, O. P. Malik, and Z.-D. Zhao, "A practical mathematical model of corona for calculation of transients on transmission lines," *IEEE Power Eng. Rev.*, vol. 9, no. 4, pp. 75–75, Apr. 1989.

[44] V. Cooray, "Charge and voltage characteristics of corona discharges in a coaxial geometry," *IEEE Trans. Dielectr. Electr. Insul.*, vol. 7, no. 6, pp. 734–743, 2000.

[45] A. Inoue, "Propagation analysis of overvoltage surges with corona based upon charge versus voltage curve," *IEEE Trans. Power App. Syst.*, no. 3, pp. 655–662, 1985.

[46] C. Gary, G. Dragan, and I. Langu, "Impulse corona discharge energy around the conductors," in *IEEE Industry Applications Society Annual Meeting*, Oct.Oct 1990, pp. 922–924.

[47] G. V. Podporkin and A. D. Sivaev, "Lightning impulse corona characteristics of conductors and bundles," *IEEE Trans. Power Del.*, vol. 12, no. 4, pp. 1842–1847, Oct. 1997.

[48] M. Mihailescu-Suliciu and I. Suliciu, "A rate type constitutive equation for the description of the corona effect," *IEEE Trans. on Power Apparatus and Systems*, vol. PAS-100, no. 8, pp. 3681–3685, Aug. 1981.

[49] *CIGRE Technical Brochure 63: Guide to procedures for estimating the lightning performance of trasmission lines*, CIGRE Std., 1991.

[50] J. Umoto and T. Hara, "Numerical analysis of surge propagation on single-conductor systems considering corona losses," *Electr. Eng. Japan, Vol*, vol. 89, no. 5, pp. 21–728, 1969.

[51] H. Motoyama and A. Ametani, "Development of a linear model for corona wave deformation and its effects on lightning surges," *Electr. Eng. Japan, Vol*, vol. 107, no. 2, pp. 98–106, 1987.

[52] R. Araneo, M. Maccioni, S. Lauria, A. Geri, F. M. Gatta, and S. Celozzi, "Comparison of corona models for computing the surge propagation in multiconductor power lines," in *2016 16th IEEE Int. Conf. Environ. and Electr. Eng.*, June 2016, pp. 1–6.

[53] C. De Jesus and M. T. Correia de Barros, "Modelling of corona dynamics for surge propagation studies," *IEEE Trans. Power Del.*, vol. 9, no. 3, pp. 1564–1569, 1994.

[54] R. Waters and R. Jones, "The impulse breakdown voltage and time-lag characteristics of long gaps in air I. the positive discharge," *Philosophical Transactions of the Royal Society of London. Series A, Mathematical and Physical Sciences*, vol. 256, no. 1069, pp. 185–212, 1964.

[55] S. Nijdam, J. Teunissen, and U. Ebert, "The physics of streamer discharge phenomena," *Plasma Sources Science and Technology*, vol. 29, no. 10, p. 103001, Nov. 2020.

[56] W. R. Smythe, *Static and dynamic electricity*. McGraw-Hill, 1950.

[57] R. Morrow, "The theory of positive glow corona," *Journal of Physics D: Applied Physics*, vol. 30, no. 22, pp. 3099–3114, Nov. 1997.

[58] N. A. Kapzow, *Elektrische Vorgänge in Gasen und im Vakuum; 2nd ed.*, ser. Hochschulb ucher für Physik. Berlin: Deutscher Verl. der Wissenschaften, 1955.

[59] X. Guo and Q. Zhang, "Effects of geometrical parameters of two height-unequal adjacent objects on corona discharges from their tips during a thunderstorm," *Atmospheric Research*, vol. 190, pp. 113 – 120, 2017.

[60] K. Huang, X. Zhang, and S. Tao, "Electromagnetic transient analysis of overhead lines including corona and frequency-dependence effects under damped oscillation surges," *IEEE Trans. Power Del.*, vol. 33, no. 5, pp. 2198–2206, 2018.

[61] K. C. Lee, "Non-linear corona models in an electromagnetic transients program (EMTP)," *IEEE Trans. Power App. Syst.*, vol. PAS-102, no. 9, pp. 2936–2942, Sep. 1983.

[62] T. J. Gallagher and I. M. Dudurych, "Model of corona for an EMTP study of surge propagation along HV transmission lines," *IEE Proc. C*, vol. 151, no. 1, pp. 61–66, Jan. 2004.

[63] P. N. Mikropoulos and V. N. Zagkanas, "Impulse corona inception in the coaxial cylindrical electrode arrangement in air: effects of the steepness of the applied voltage," in *Proc. 18th International Symposium on High Voltage Engineering*, 2013.

[64] M. Xu, Z. Tan, and K. Li, "Modified Peek formula for calculating positive dc corona inception electric field under variable humidity," *IEEE Trans. Dielectr. Electr. Insul.*, vol. 19, no. 4, pp. 1377–1382, 2012.

[65] A. Carsimamovic, A. Mujezinovic, S. Carsimamovic, Z. Bajramovic, M. Kosarac, and K. Stankovic, "Analyzing of AC corona discharge parameters of atmospheric air," *Procedia Computer Science*, vol. 83, pp. 766–773, 2016.

[66] E. Stracqualursi, R. Araneo, and A. Andreotti, "The impact of different corona models on FD algorithms for the solution of multiconductor transmission lines equations," *High Voltage*, vol. 6, no. 5, pp. 822–835, Sep. 2021.

Appendix B

Hybrid method for grounding systems

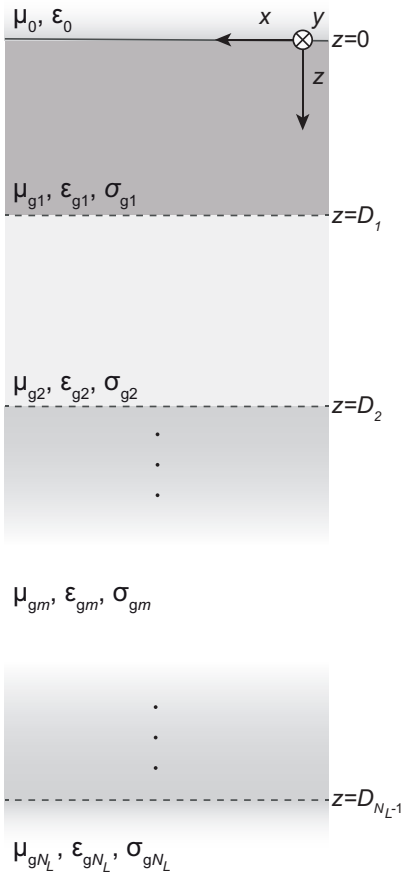

Figure B.1. Horizontally layered medium, with N_L layers.

A hybrid method has been implemented to evaluate the frequency response of metallic structures buried in the ground, i.e., to evaluate the resistive and reactive components of the grounding impedance offered by grounding devices in a wide frequency range. The structure may be buried in a homogeneous ground, modelled as a semi-infinite layer, or in a horizontally stratified ground consisting of N_L layers; in the latter case, each layer $m \in \{1, \ldots, N_L\}$ is modelled as a homogeneous medium, characterised by electrical permittivity ϵ_{g_m}, electrical conductivity σ_{g_m}, and magnetic permeability μ_{g_m} (Fig. B.1).

Denoting with $f_{\max}$ the upper limit of the investigated frequency range, a fundamental parameter is the minimum wavelength $\lambda_{\min}$ associated with the electrical and magnetic properties of the medium. The quantity $\lambda_{\min_m}$ may be evaluated as the minimum value assumed by the wavelength λ_m in the m^{th} layer (referring to the propagation of uniform plane waves) [1]:

$$\lambda_m(\omega) = \frac{2\pi}{\beta_m} = \frac{2\pi}{\omega\sqrt{\mu_{\mathrm{g}_m}\epsilon_{\mathrm{g}_m}}\left\{\frac{1}{2}\left[\sqrt{1+\left(\frac{\sigma_{\mathrm{g}_m}}{\omega\epsilon_{\mathrm{g}_m}}\right)^2}+1\right]\right\}^{1/2}}, \tag{B.1}$$

where $\omega = 2\pi f$ is the angular frequency; β_m and α_m are the phase and attenuation constants in the m^{th} ground layer, respectively, $k_m = \beta_m - i\alpha_m$ [2]. The value

$$\lambda_{\min} = \min\left\{\lambda_{\min_1}, \ldots, \lambda_{\min_{N_L}}\right\} \tag{B.2}$$

should be considered when assessing the preliminary step of the method; it consists in discretizing the structure into N_{B} elements (as sketched in Fig. B.2), referred to as "branches", which are connected by N_{N} nodes, so that the length of the j^{th} branch, L_j, is sensibly shorter than the minimum wavelength, i.e., $L_j \ll \lambda_{\min}/(2\pi)$. Therefore, the following quantities may be defined:

- N_{B} - Number of branches;
- N_{N} - Number of nodes;
- V_k - Node voltage;
- J_j^{co} - Longitudinal conduction current flowing along the j^{th} branch;
- J_j^{le} - Leakage current drained from the lateral surface of the j^{th} branch;
- U_j - Branch voltage. If the reference branch j is delimited by node k and node $k+1$ (without loss of generality, the limiting nodes may be not denoted by subsequent indices), the branch voltage is defined as $U_j = (V_k + V_{k+1})/2$, by virtue of the approximation of "electrically short" branch;
- $\mathbf{K}$ - Voltage transformation matrix of dimension $N_{\mathrm{B}} \times N_{\mathrm{N}}$;

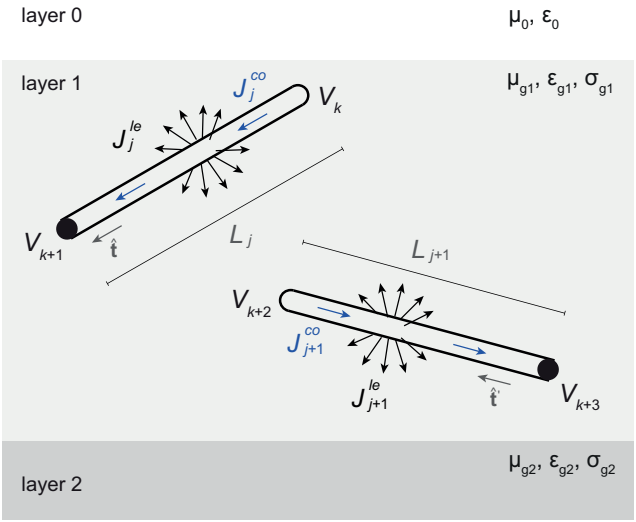

Figure B.2. Branch j and $j+1$ of the discretized structure under study; main electrical and geometrical quantities related to each branch.

- $\mathbf{A}$ - Branch-to-node incidence matrix of dimension $N_{\mathrm{N}} \times N_{\mathrm{B}}$;
- $\mathbf{V}$ - Vector of node voltages of dimension $N_{\mathrm{N}} \times 1$;
- $\mathbf{J}^{co}$ - Vector of longitudinal conduction currents of dimension $N_{\mathrm{B}} \times 1$;
- $\mathbf{J}^{le}$ - Vector of leakage currents of dimension $N_{\mathrm{B}} \times 1$;
- $\mathbf{I}^{\mathrm{ext}}$ - Vector of currents externally injected at the nodes of dimension $N_{\mathrm{N}} \times 1$;
- $\mathbf{Z}^{\mathrm{RL}}$ - Matrix of resistive-inductive impedances of dimension $N_{\mathrm{B}} \times N_{\mathrm{B}}$;
- $\mathbf{Y}^{\mathrm{RL}} = \left(\mathbf{Z}^{\mathrm{RL}}\right)^{-1}$ - Matrix of resistive-inductive admittances of dimension $N_{\mathrm{B}} \times N_{\mathrm{B}}$;
- $\mathbf{Z}^{\mathrm{GC}}$ - Matrix of resistive-capacitive impedances of dimension $N_{\mathrm{B}} \times N_{\mathrm{B}}$;
- $\mathbf{Y}^{\mathrm{GC}} = \left(\mathbf{Z}^{\mathrm{GC}}\right)^{-1}$ - Matrix of resistive-capacitive admittances of dimension $N_{\mathrm{B}} \times N_{\mathrm{B}}$.

The scalar electric potential at each node V_k is computed considering the reference potential to be at remote distance. Furthermore, $j \in [1, N_{\mathrm{B}}]$, $k \in [1, N_{\mathrm{N}}]$. The generic element κ_{jk} and α_{kj} belonging to matrix $\mathbf{K}$ and $\mathbf{A}$, respectively, is

written as [3]:

$$\kappa_{jk} = \begin{cases} 1/2 & \text{if node } k \text{ is an endpoint of branch } j \\ 0 & \text{otherwise} \end{cases} \tag{B.3a}$$

$$\alpha_{kj} = \begin{cases} 0 & \text{if node } k \text{ is not an endpoint of branch } k \\ 1 & \text{if branch } j \text{ is oriented towards node } k \\ -1 & \text{otherwise} \end{cases} \tag{B.3b}$$

where an arbitrarily oriented unit vector should be chosen to set the orientation of branch j in (B.3b).

Since the method is based on a FD approach, nonlinear phenomena (e.g., corona effect and soil ionization) are neglected.

The adopted approach, namely, the implemented hybrid method, consists in decoupling the problem into two subproblems: computation of the electromagnetic field distribution, and description of the configuration under investigation through an auxiliary matrix of impedances.

In order to convey the theory underlying the method, the two aforementioned subproblems are illustrated; the circuit approach is described in Sec. B.1, while Sec. B.2 is devoted to the associated electromagnetic problem.

B.1 Circuit problem

In order to model mutual coupling between branches by means of circuit theory, the electromagnetic field distribution in layered media is to be computed first (Sec. B.2).

The generic element z_{ij}^{GC} of the matrix of resistive-capacitive impedances $\mathbf{Z}^{\mathrm{GC}}$ is obtained by integrating the Green function for the electric scalar potential G_ϕ, accounting for the mutual coupling between branches i and j:

$$z_{ij}^{\mathrm{GC}} = \frac{1}{j\omega\epsilon_0} \int_{L_i} \frac{dl}{L_i} \int_{L_j} G_\phi\left(\mathbf{r}, \mathbf{r}'\right) \frac{dl'}{L_j} \,. \tag{B.4}$$

In (B.4), $\mathbf{r}$ and $\mathbf{r}'$ denote the position vector of the observation point $\mathbf{r} = x\hat{\mathbf{x}} + y\hat{\mathbf{y}} + z\hat{\mathbf{z}}$, and of the source point $\mathbf{r}' = x'\hat{\mathbf{x}} + y'\hat{\mathbf{y}} + z'\hat{\mathbf{z}}$. The configuration under analysis is sketched in Figs. B.1 and B.2.

The generic element z_{ij}^{RL} of the matrix of impedances $\mathbf{Z}^{\mathrm{RL}}$ is computed as follows:

$$z_{ij}^{\mathrm{RL}} = \delta_{ij} z_{ii} + j\omega\mu_0 \int_{L_i} dl \int_{L_j} \hat{\mathbf{t}} \cdot \mathbf{G}_{\mathrm{A}}\left(\mathbf{r}, \mathbf{r}'\right) \cdot \hat{\mathbf{t}}' dl' \tag{B.5}$$

where δ_{ij} is the Kronecker delta.

As to (B.5), z_{ii} denotes the self-impedance of the i^{th} branch, which may be modelled as a thin solid cylindrical conductor with external radius r_{i0}, or a hollow conductor with external radius r_{i0} and internal radius r'_{i0}. Furthermore,

different radii may be associated with different branches. In the aforementioned cases, $z_{ii} = z'_{ii} L_i$ is computed as the product of the branch length L_i and the p.u.l. self-impedance z'_{ii} given by the Schelkunoff's theory at $\omega \neq 0$ [4]:

$$z'_{ii} = \begin{cases} \frac{\eta_c}{2\pi r_0} \frac{I_0(\beta_c r_0)}{I_1(\beta_c r_0)} & \text{solid conductors} \\ \frac{\eta_c}{2\pi r_0} \frac{\left[I_0(\beta_c r_0) K_1\left(\beta_c r'_0\right) + K_0(\beta_c r_0) I_1\left(\beta_c r'_0\right)\right]}{I_1(\beta_c r_0) K_1\left(\beta_c r'_0\right) - I_1\left(\beta_c r'_0\right) K_1(\beta_c r_0)} & \text{hollow conductors} \end{cases} \tag{B.6}$$

and, for $\omega = 0$

$$z'_{ii} = \begin{cases} \frac{1}{\pi r_0^2 \sigma_w} & \text{solid conductors} \\ \frac{1}{\pi\left(r_0^2 - r_0'^2\right)\sigma_w} & \text{hollow conductors}\,. \end{cases} \tag{B.7}$$

In (B.6) and (B.7), subscript i, denoting the radius of the i^{th} conductor, was omitted to ease the notation; σ_w and μ_w are the branch electric conductivity and magnetic permeability, respectively; $\eta_c = \sqrt{(j\omega\mu_w/\sigma_w)}$ denotes the characteristic impedance of the conductor, and $\beta_c = \sigma_w \eta$. As to hollow branches, z'_{ii} corresponds to the impedance offered by the conductor when the current flows in the proximity of its outermost surface with an external return path (i.e., at $r > r_0$).

The computation of z'_{ii} through standard routines made available by commercial codes and softwares (e.g., Fortran, Matlab) may lead to divergence in the evaluation of the Bessel functions for large values of their arguments. For these reasons, the following large-argument asymptotic expressions have been adopted whenever the capabilities of the available routines were leading to undesired divergence:

Solid conductor

$$z'_{ii} \to \frac{1}{2r_0} \sqrt{\frac{\mu_w}{2\pi^2 \sigma_w}} \sqrt{\omega} \tag{B.8}$$

Hollow conductor

$$\begin{aligned} z'_{ii} \to \\ \to \frac{\eta}{2\pi r_0} \frac{e^{\beta_c\left(r_0 - r'_0\right)}\left(1 + \frac{1}{8\beta_c r_0}\right)\left(1 + \frac{3}{8\beta_c r'_0}\right) + e^{\beta_c\left(r'_0 - r_0\right)}\left(1 - \frac{1}{8\beta_c r_0}\right)\left(1 - \frac{3}{8\beta_c r'_0}\right)}{e^{\beta_c\left(r_0 - r'_0\right)}\left(1 - \frac{3}{8\beta_c r_0}\right)\left(1 + \frac{3}{8\beta_c r'_0}\right) - e^{\beta_c\left(r'_0 - r_0\right)}\left(1 - \frac{3}{8\beta_c r'_0}\right)\left(1 + \frac{3}{8\beta_c r_0}\right)} \to \\ \frac{\eta}{2\pi r_0} \frac{\left(1 + \frac{1}{8\beta_c r_0}\right)\left(1 + \frac{3}{8r'_0}\right)}{\left(1 - \frac{3}{8\beta_c r_0}\right)\left(1 + \frac{3}{8\beta_c r'_0}\right)}\,. \end{aligned} \tag{B.9}$$

Having computed the elements of the matrices of admittances and impedances, the following matrix relation is derived:

$$\mathbf{I}^{\text{ext}} - \mathbf{I}^{le} = \mathbf{I}^{co} \tag{B.10}$$

with

$$\mathbf{I}^{le}\left(\mathbf{J}^{le}\right) = \left(\mathbf{K}^{\mathrm{T}}\mathbf{Y}^{\mathrm{GC}}\mathbf{K}\right)\mathbf{V} \tag{B.11a}$$

$$\mathbf{I}^{co}\left(\mathbf{J}^{co}\right) = \left(\mathbf{A}\mathbf{Y}^{\mathrm{RL}}\mathbf{A}^{\mathrm{T}}\right)\mathbf{V}\,. \tag{B.11b}$$

In (B.10), $\mathbf{I}^{\mathrm{ext}}$, $\mathbf{I}^{le}$, and $\mathbf{I}^{co}$ are current vectors of dimension $N_{\mathrm{N}} \times 1$. The equation expressed by the k^{th} row of (B.10) corresponds to the application of the KCL at node k, i.e., to the algebraic summation of the currents entering the k^{th} node. $\mathbf{I}^{\mathrm{ext}}$ is the vector of external currents injected at selected nodes (as if they were ideal, single-tone current sources at the investigated frequency); hence, the element I_k^{ext} is non-zero only if a current source is connected to node k. $\mathbf{I}^{le}$, computed as in (B.11a), is the vector of lumped leakage currents, which is derived assuming that the total leakage current drained by the lateral surface of the j^{th} branch is split into equal lumped contributions at the branch limiting nodes; therefore, I_k^{le} is computed as the sum of the contributions related to all the branches terminating at node k. Likewise, the generic element I_k^{co} of $\mathbf{I}^{co}$ corresponds to the algebraic sum of conduction currents drained by branches limited by node k. The transformation of branch current vectors $\mathbf{J}^{co}$ and $\mathbf{J}^{le}$ to node current vectors $\mathbf{I}^{co}$ and $\mathbf{I}^{le}$, respectively, is achieved by means of $\mathbf{A}$ and $\mathbf{K}$; the values of the elements of these matrices, given in(B.3), are based on the topology of the discretization mesh (nodes and branches) employed to model the structure under investigation.

From (B.10) and (B.11), a system of linear equations in the vector of the unknown node voltages $\mathbf{V}$ may be written, identifying with $\mathbf{Y}^{\mathrm{N}}$ its matrix of coefficients:

$$\mathbf{I}^{\mathrm{ext}} = \left(\mathbf{K}^{\mathrm{T}}\mathbf{Y}^{\mathrm{GC}}\mathbf{K} + \mathbf{A}\mathbf{Y}^{\mathrm{RL}}\mathbf{A}^{\mathrm{T}}\right)\mathbf{V} = \mathbf{Y}^{\mathrm{N}}\mathbf{V}\,. \tag{B.12}$$

The system's solution is computed by means of the IMSL Fortran routine LSACG [5], solving linear systems with complex valued matrices of coefficients through LU factorization and iterative refinement.

B.1.1 Voltages enforcement

The final formulation of the problem in (B.12) may be modified in order to account also for voltage enforcement at selected nodes; accordingly, an equal number of unknown current sources is to be plugged at the corresponding nodes of voltage enforcement (e.g., if the voltage value $\hat{V}_k$ is enforced at node k, the unknown current I_k^{ext} should be injected at the same node). Expanding

the matrix relation (B.12)

$$\begin{bmatrix} 0 \\ \vdots \\ I_k^{\text{ext}} \\ 0 \\ \vdots \\ 0 \end{bmatrix} = \begin{bmatrix} y_{1,1} & \cdots & \cdots & y_{1,N_\text{N}} \\ \vdots & \ddots & & \\ y_{1,k} & & \ddots & \\ & & & \ddots \\ \vdots & & & \\ y_{N_\text{N},1} & \cdots & & y_{N_\text{N},N_\text{N}} \end{bmatrix} \begin{bmatrix} V_1 \\ \vdots \\ V_k \\ \\ \vdots \\ V_{N_\text{N}} \end{bmatrix}, \tag{B.13}$$

and enforcing $V_k = \hat{V}_k$, the system (B.13) may be modified as follows:

$$\begin{bmatrix} -\hat{V}_k y_{1,k} \\ \vdots \\ -\hat{V}_k y_{k,k} \\ -\hat{V}_k y_{k+1,k} \\ \vdots \\ -\hat{V}_k y_{N_\text{N},k} \end{bmatrix} = \begin{bmatrix} y_{1,1} & 0 & \cdots & y_{1,N_\text{N}} \\ \vdots & \vdots & & \\ y_{1,k} & -1 & \ddots & \\ & 0 & \ddots & \\ \vdots & \vdots & & \\ y_{N_\text{N},1} & \cdots\ 0 & & y_{N_\text{N},N_\text{N}} \end{bmatrix} \begin{bmatrix} V_1 \\ \vdots \\ I_k^{\text{ext}} \\ \\ \vdots \\ V_{N_\text{N}} \end{bmatrix} \tag{B.14}$$

in which the vector of unknown terms is a *mixed* vector, since it is now expressed in terms of unknown voltages and currents. A suitable modification of (B.13) into (B.14) may be exploited to enforce equipotentiality of selected nodes of the structure.

B.2 Electromagnetic problem

In (B.4) and (B.5), the scalar Green function for the electric scalar potential G_ϕ, and the dyadic Green function for the magnetic vector potential $\mathbf{G}_\text{A}$ have been introduced.

In homogeneous media or in the case of an air-PEC interface, a unique solution may be found for the Hertzian potential associated with an horizontal electric dipole, only consisting in a vector component in the horizontal direction [6]. However, in layered media, the uniqueness of the solution is not guaranteed, and different formulations have been proposed in the literature (e.g., [7]). In particular, the vector Hertzian potential associated with an horizontal electric dipole cannot be expressed by a single vector component parallel to the dipole source if the continuity of the tangential electric and magnetic field needs to be fulfilled at the interfaces between different media.

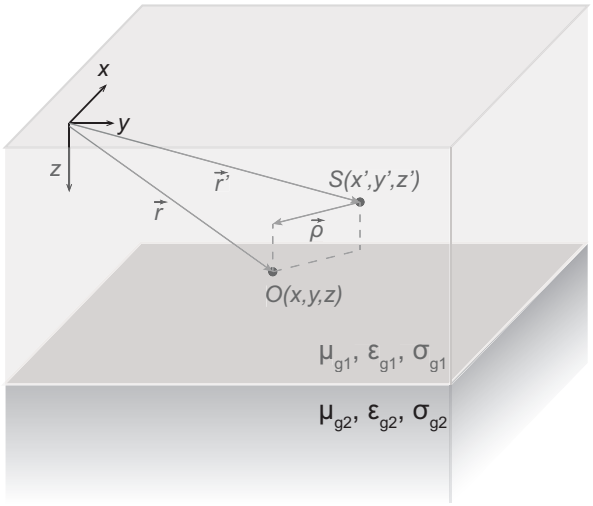

Figure B.3. Source point $S\left(x', y', z'\right)$, observation point $O\left(x, y, z\right)$, and coordinate reference systems adopted to assess propagation in the layered medium.

Introducing the system of cylindrical coordinates (ρ, z) in Fig. B.3, the definition proposed by Kourkoulos and Cangellaris will be adopted here for $\mathbf{G}_{\mathrm{A}}$ (assuming $\mu_{g_m} = \mu_0$ for the m^{th} layer) [8]:

$$\mathbf{G}_{\mathrm{A}}\left(\rho; z, z'\right) = \begin{bmatrix} G_{\mathrm{A}}^{xx}\left(\rho; z, z'\right) & 0 & -G_{\mathrm{A}}^{zx}\left(\rho; z, z'\right) \\ 0 & G_{\mathrm{A}}^{yy}\left(\rho; z, z'\right) & -G_{\mathrm{A}}^{zy}\left(\rho; z, z'\right) \\ G_{\mathrm{A}}^{zx}\left(\rho; z, z'\right) & G_{\mathrm{A}}^{zy}\left(\rho; z, z'\right) & G_{\mathrm{A}}^{zz}\left(\rho; z, z'\right) \end{bmatrix}. \tag{B.15}$$

In order to compute the terms G_{A}^{ij}, with $i, j \in \{x, y, z\}$, the problem is first transferred in the spectral domain (k_ρ, z), by means of the following Sommerfeld integral transform:

$$\tilde{f}\left(k_\rho, z\right) = \tilde{S}_n\left\{f\left(\rho, z\right)\right\} = \frac{1}{2\pi}\int_0^\infty f\left(\rho, z\right) J_n\left(k_\rho \rho\right) \rho \mathrm{d}\rho\,, \tag{B.16}$$

in which $\tilde{f}\left(k_\rho, z\right)$ is the spectral counterpart of $f\left(\rho, z\right)$, originally defined in the spatial domain; J_n is the Bessel function of first kind and order $n = 0$ or $n = 1$.

Introducing (B.17)

$$f\left(\rho, z\right) = S_n\left\{\tilde{f}\left(k_\rho, z\right)\right\} = \frac{1}{2\pi}\int_0^\infty \tilde{f}\left(k_\rho, z\right) J_n\left(k_\rho \rho\right) k_\rho \mathrm{d}k_\rho\,, \tag{B.17}$$

the terms G_{A}^{ij} in (B.15) are computed by the following transformations [8],[9]:

$$G_{\mathrm{A}}^{xx}(\rho;z,z') = G_{\mathrm{A}}^{yy}(\rho;z,z') = S_0\left\{\tilde{G}^{vv}(k_\rho;z,z')\right\} \tag{B.18a}$$

$$G_{\mathrm{A}}^{zz}(\rho;z,z') = S_0\left\{\tilde{G}^{zz}(k_\rho;z,z')\right\} \tag{B.18b}$$

$$G_{\mathrm{A}}^{zx}(\rho;z,z') = -j\cos\varphi S_1\left\{\tilde{G}^{zu}(k_\rho;z,z')\right\} \tag{B.18c}$$

$$G_{\mathrm{A}}^{zy}(\rho;z,z') = -j\sin\varphi S_1\left\{\tilde{G}^{zu}(k_\rho;z,z')\right\} \tag{B.18d}$$

$$G_{\phi}(\rho;z,z') = S_0\left\{\tilde{G}_{\phi}(k_\rho;z,z')\right\} \tag{B.18e}$$

where, given the source point $S(x',y,',z')$ and the observation point $O(x,y,z)$

$$\varphi = \arctan\left(\frac{y-y'}{x-x'}\right). \tag{B.19}$$

The computation of the spectral transforms of the Green functions in (B.18) will be addressed in Sec. B.2.2.

Noticeably, integrals in (B.18), involving Bessel functions J_0 and J_1, are oscillating integrals referred to as *Sommerfeld integrals*. The numerical technique employed to compute Sommerfeld integrals is addressed in Sec. B.2.1.

B.2.1 Numerical computation of Sommerfeld integrals

In order to inverse-transform quantities from the spectral to the spatial domain, integrals of the type (B.17) need to be computed. Equation (B.17) is here particularized:

$$G(\rho;z,z') = \frac{1}{2\pi}\int_0^{\infty}\tilde{G}(k_\rho;z,z')\,J_n(k_\rho\rho)\,k_\rho \mathrm{d}k_\rho\,. \tag{B.20}$$

In (B.20), the generic Green function defined in the spatial domain $G(\rho;z,z')$ is computed as the transform of its spectral domain counterpart $\tilde{G}(k_\rho;z,z')$.

However, the integrand in (B.20) may present singularities and branch points along the first part of the integration path; therefore, a common integration technique consists in splitting the integration interval into two sub-intervals, namely, $[0,\xi_0]$ and $[\xi_0,\infty)$:

$$\begin{aligned} G(\rho;z,z') = {} & \frac{1}{2\pi}\int_0^{\xi_0}\tilde{G}(k_\rho;z,z')\,J_n(k_\rho\rho)\,k_\rho \mathrm{d}k_\rho + \\ & + \frac{1}{2\pi}\int_{\xi_0}^{\infty}\tilde{G}(k_\rho;z,z')\,J_n(k_\rho\rho)\,k_\rho \mathrm{d}k_\rho = \frac{1}{2\pi}\left(H_n^I + T_n^I\right). \end{aligned} \tag{B.21}$$

In (B.21), ξ_0 denotes the upper and lower limit of integration of the two integral contributions, respectively.

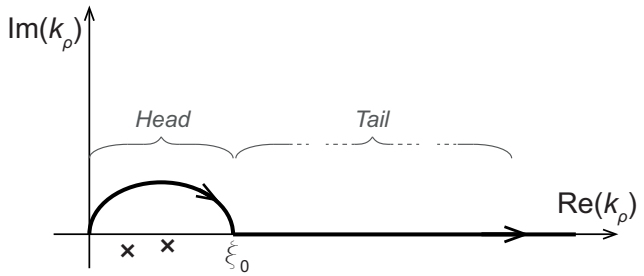

Figure B.4. Deformation of the integration path of the Sommerfeld integral (B.20) in the first quadrant of the complex plane.

To avoid singularities, the integration path of the former integral H_n^I, referred to as *head*, is deformed into the first quadrant of the complex plane (as from Fig. B.4). Hence, it is computed through standard quadrature formulas. The latter integral T_n^I, with no singularities, is known as *Sommerfeld tail*, and holds the greatest computational burden. In fact, since the Bessel functions at the integrand are oscillatory functions, the convergence of semi-infinite integrals of the type of T_n^I is slow; in order to speed up the computation of the second integral term, several numerical acceleration techniques are available [10], e.g., the integration then summation algorithms [11] (consisting in evaluating the integral as the sum of the contributions given by definite integrals computed over suitable intervals, with carefully chosen break points), the weighted averages algorithm [12] (which, in its basic formulation, consists in an iterative procedure starting from partial sums and computing their mean values), and double exponential formulas [13].

Due to the reduced computational burden associated with double exponential formulas [14], this approach was implemented for numerical integration of the Sommerfeld tail; the main rationale underlying this acceleration technique is recalled in what follows.

As to the tail of the integral, the change of variables (B.22) is adopted, and the integral T_n^I is reduced to (B.23):

$$k_\rho \rho = \Phi(t)\,,\ \Phi(t) = \frac{\pi}{h} t \tanh\left(\frac{\pi}{2}\sinh(t)\right) + \xi_0 \rho \cosh^{-1}\left(\frac{\pi}{2}\sinh(t)\right) \quad \text{(B.22)}$$

$$T_n^I = \int_0^\infty \mathscr{F}_n(\Phi(t)) \left(\frac{\mathrm{d}\Phi}{\mathrm{d}t}\right) \mathrm{d}t \quad \text{(B.23)}$$

with

$$\mathscr{F}_n(t) = \frac{1}{\rho^2} t \tilde{G}\left(\frac{t}{\rho}; z, z'\right) J_n(t)\ . \quad \text{(B.24)}$$

Sommerfeld tails T_0^I and T_1^I involving Bessel functions J_0 and J_1, respectively, are computed as [14]:

$$T_0^I \approx h \sum_{k=1}^{N} w_{0k} \mathscr{F}_0\left(\Phi\left(h\frac{\xi_{0k}}{\pi}\right)\right) \Phi'\left(h\frac{\xi_{0k}}{\pi}\right) \quad \text{(B.25)}$$

$$T_1^I \approx h \sum_{k=1}^{N} w_{1k} \mathcal{F}_1 \left(\Phi \left(h \frac{\xi_{1k}}{\pi} \right) \right) \Phi' \left(h \frac{\xi_{1k}}{\pi} \right) + \left(2h - \frac{\xi_0 \rho h^2}{2} \right) \mathcal{F}_1 \left(\xi_0 \rho \right) \quad \text{(B.26)}$$

where $h = 1/32$ [14], $\Phi' = \mathrm{d}\Phi/\mathrm{d}t$, and the weights w_{nk} (for $n = 0, 1$) are computed as:

$$w_{nk} = \frac{2}{\pi \xi_{nk} J_{n+1}^2 \left(\xi_{nk} \right)} \,. \quad \text{(B.27)}$$

In (B.25)-(B.27), quantities ξ_{nk} denote the zeros of the Bessel function of first kind and order $n = 0, 1$.

The name *double exponential* has to do with the asymptotic behaviour obtained for the integrand in (B.23). In fact, the application of a transformation of the type (B.22) is performed in order to make the integrand in (B.23) decay with a double exponential trend for $|t| \to \infty$ [15]:

$$\left| \mathcal{F} \left(\Phi \left(t \right) \right) \left(\frac{\mathrm{d}\Phi}{\mathrm{d}t} \right) \right| \xrightarrow{|t| \to \infty} \exp \left(-c \exp |t| \right) \,, \quad \text{(B.28)}$$

where c is a constant.

The function $\Phi(t)$ in (B.22) is specifically chosen since it tends to $\Phi(t) \to \pi t/h$ for $t \to \infty$. Hence, when evaluating the terms of the summations in (B.25) and (B.26) for large values of ξ_{nk}, the actual argument of $\Phi(\cdot)$ is large as well, allowing for the points in which the Bessel functions are to be evaluated in (B.24) to asymptotically approach their zeros:

$$J_n \left(\Phi \left(h \frac{\xi_{nk}}{\pi} \right) \right) \to J_n \left(\xi_{nk} \right) = 0 \,. \quad \text{(B.29)}$$

As a result, (B.25) and (B.26) can be evaluated satisfactorily by means of a limited number of terms.

The double exponential asymptotic behaviour allows to truncate the summation after a reasonable number N of terms, reaching rapidly the desired asymptotic behaviour. Furthermore, depending on the different type of slowly converging integral that is to be evaluated, other transform functions $\Phi(t)$ may be employed [13].

B.2.2 Spectral domain: TL equivalent problem

As introduced previously in this section, the evaluation of the sought Green function, given a source and an observation point, may be simplified by transferring the problem to the spectral domain, namely, from (x, y, z) to (k_ρ, z).

In the spectral domain, following the procedure presented in [6], the propagation of the electric and magnetic field may be studied by means of the transmission line formalism: two auxiliary transmission lines are introduced, accounting for the TE and TM components of the electromagnetic field with

respect to the z direction. Auxiliary voltages and currents propagating along these TLs are denoted as (V^e, I^e) and $\left(V^h, I^h\right)$ for the TM and the TE case, respectively.

The following TLs equations may be written in a generic medium with relative electric permittivity ϵ_r and relative magnetic permeability μ_r [9]:

$$\frac{\mathrm{d}V_i^P}{\mathrm{d}z} = -jk_z^P Z^P I_i^P \tag{B.30a}$$

$$\frac{\mathrm{d}I_i^P}{\mathrm{d}z} = -jk_z^P Y^P V_i^P + \delta\left(z - z'\right) \tag{B.30b}$$

$$\frac{\mathrm{d}V_v^P}{\mathrm{d}z} = -jk_z^P Z^P I_v^P + \delta\left(z - z'\right) \tag{B.30c}$$

$$\frac{\mathrm{d}I_v^P}{\mathrm{d}z} = -jk_z^P Y^P V_v^P \tag{B.30d}$$

where

$$k_z^P = \sqrt{k^2 - \nu^P k_\rho^2} \tag{B.31a}$$

$$Z^e = \left(Y^e\right)^{-1} = \frac{k_z^e}{\omega\epsilon_0\epsilon_r} \tag{B.31b}$$

$$Z^h = \left(Y^h\right)^{-1} = \frac{\omega\mu_0\mu_r}{k_z^h} \tag{B.31c}$$

with $k^2 = k_0^2\epsilon_r\mu_r$, $k_0^2 = \omega^2\epsilon_0\mu_0$, and $P = e, h$. The quantity ν^P is the anisotropy factor, corresponding to $\nu^e = \epsilon_t/\epsilon_z$ and $\nu^h = \mu_t/\mu_z$. In fact, the method allows to account for dyadic electric permittivity and magnetic permeability, displaying different values in the z direction or in the $t$ransverse direction. Herein, $\nu^e = \nu^h = 1$, assuming the layers to be isotropic.

Four different TLs should be studied: (V_i^e, I_i^e) and (V_v^e, I_v^e) are to be found as to the TM mode, and $\left(V_i^h, I_i^h\right)$ and $\left(V_v^h, I_v^h\right)$ are to be found as to the TE mode. Subscripts i and v are adopted to distinguish auxiliary voltages and currents propagating when a shunt current source or a series voltage source is plugged at $z = z'$ along the TL, respectively.

The spectral quantities introduced in (B.18) may be derived as linear functions of V^P, I^P as follows [8] (the derivation is omitted for conciseness, the interested reader is referred to [6]):

$$\tilde{G}^{vv} = \frac{1}{j\omega\mu_0} V_i^h \tag{B.32a}$$

$$\tilde{G}^{zz} = \frac{\eta_0^2}{j\omega\mu_0}\left[\left(\frac{\mu_r}{\epsilon_r'} + \frac{\mu_r'}{\epsilon_r}\right) I_v^e + \frac{k_0^2\mu_r'\mu_r}{k_\rho^2}\left(I_v^h - I_v^e\right)\right] \tag{B.32b}$$

$$\tilde{G}^{zu} = \frac{\mu_r}{jk_\rho}\left(I_i^h - I_i^e\right) \tag{B.32c}$$

$$\tilde{G}_\phi = -\frac{j\omega\epsilon_0}{k_\rho^2}\left(V_i^h - V_i^e\right) \tag{B.32d}$$

where properties of the source layer are μ_r' and ϵ_r', while the observation point is located in the layer with properties μ_r and ϵ_r[1].

TL solving methodology

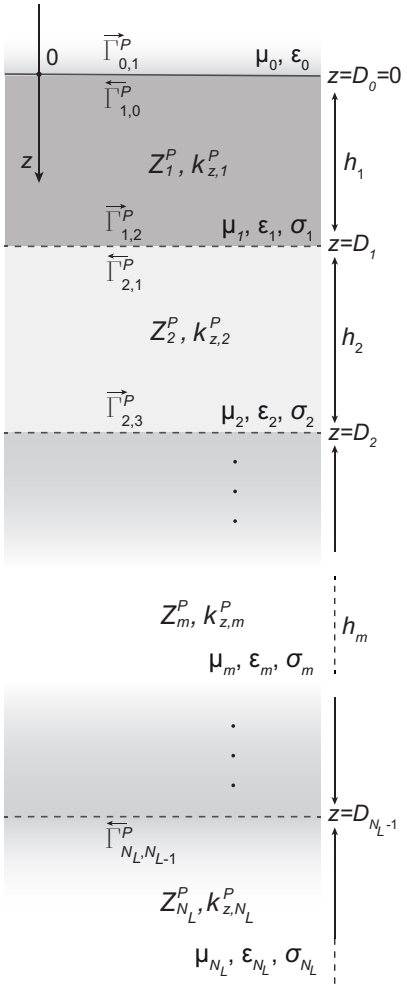

Figure B.5. Sketch of the layered configuration under analysis.

Herein, an efficient solving methodology for the auxiliary TL problems introduced in (B.30) is recalled. Without loss of generality, the layered medium shown in Fig. B.5 is considered. Referring to the origin of the z-axis, which

[1]Expressions in (B.32) may appear not coherent if a dimensional analysis of the terms is performed. The incongruence is only apparent, and it is due to the choice of impulsive sources as given by (B.30), in which $\delta(z - z')$ denotes both current and voltage sources located at depth z' along the equivalent TLs. As a result, voltages and currents along the auxiliary lines are given in per unit of the corresponding source amplitude (e.g., V_i^P and V_v^P are to be considered in [V/A] and [V/V], respectively).

is orthogonal to the horizontal interfaces between adjacent layers, h_m is the depth of the m^{th} layer (extending in the range $D_{m-1} \leq z \leq D_m$), the semi-infinite layer 0 being the air at negative z. Propagation is studied by means of the cascade of TLs accounting for the electrical and magnetic properties of each layer. In particular, the secondary line constants of the equivalent TL associated with the m^{th} (isotropic) layer are:

$$k_{z,m}^P = \sqrt{k_m^2 - k_\rho^2} \tag{B.33a}$$

$$Z_m^e = \frac{k_{z,m}^e}{\omega\epsilon_0\bar{\epsilon}_{r,m}} \tag{B.33b}$$

$$Z_m^h = \frac{\omega\mu_0\mu_{r,m}}{k_{z,m}^h} \tag{B.33c}$$

where $k_m^2 = k_0^2\bar{\epsilon}_{r,m}\mu_{r,m}$; $\bar{\epsilon}_{r,m} = \epsilon_{r,m} + \frac{\sigma_m}{j\omega\epsilon_0}$ in (B.33b) denotes the complex relative electrical permittivity of layer m, accounting for the layer electrical conductivity σ_m.[2]

The observation point is assumed to be at depth z and the source point to be located at $z' < z$. Solution for the opposite case, in which the source point is at greater depth with respect to the observation point may be derived by applying the reciprocity theorem [16].

Two reflections coefficient may be associated with each layer m: $\overrightarrow{\Gamma}_{m,m+1}^P$ and $\overleftarrow{\Gamma}_{m,m-1}^P$, i.e., the reflection coefficient for waves propagating from layer m towards $m+1$, and from m to $m-1$, respectively. They are computed as follows:

$$\overrightarrow{\Gamma}_{m,m+1}^P = \frac{Z_{m+1}^P - Z_m^P}{Z_{m+1}^P + Z_m^P} \tag{B.34a}$$

$$\overleftarrow{\Gamma}_{m,m-1}^P = \frac{Z_{m-1}^P - Z_m^P}{Z_{m-1}^P + Z_m^P}\,. \tag{B.34b}$$

When referring to the semi-infinite layer 0 (i.e., the air layer at negative values of z), only $\overrightarrow{\Gamma}_{0,1}^P$ is defined, since the reflection coefficient in the opposite direction is null. Likewise, only $\overleftarrow{\Gamma}_{N_L,N_L-1}^P$ is defined for the deepest layer N_L.

Furthermore, the total reflection coefficients $\overrightarrow{\Gamma}_m^P$, $\overleftarrow{\Gamma}_m^P$ associated with layer m are computed recursively as:

$$\overrightarrow{\Gamma}_m^P = \frac{\overrightarrow{\Gamma}_{m,m+1}^P + \overrightarrow{\Gamma}_{m+1}^P e^{-j2k_{z,m+1}^P h_{m+1}}}{1 + \overrightarrow{\Gamma}_{m,m+1}^P \overrightarrow{\Gamma}_{m+1}^P e^{-j2k_{z,m+1}^P h_{m+1}}} \tag{B.35a}$$

$$\overleftarrow{\Gamma}_m^P = \frac{\overleftarrow{\Gamma}_{m,m-1}^P + \overleftarrow{\Gamma}_{m-1}^P e^{-j2k_{z,m-1}^P h_{m-1}}}{1 + \overleftarrow{\Gamma}_{m,m-1}^P \overleftarrow{\Gamma}_{m-1}^P e^{-j2k_{z,m-1}^P h_{m-1}}}\,. \tag{B.35b}$$

[2]It should be noted that, when applying this methodology to the study of the grounding impedance of grounding systems in layered media, $\epsilon_{r,m} = \epsilon_{\text{g}_m}/\epsilon_0$, $\mu_{r,m} = \mu_{\text{g}_m}/\mu_0$ and $\sigma_m = \sigma_{\text{g}_m}$ for the m^{th} layer of the soil.

Likewise, a generalized transmission coefficient, $\overrightarrow{\tau}^P_n$, may be associated with each layer n; when restricting the investigation to the aforementioned case $z > z'$:

$$\overrightarrow{\tau}^P_n = \frac{1 - \overrightarrow{\Gamma}^P_{n-1,n}\overrightarrow{\Gamma}^P_{n-1}}{1 - \overrightarrow{\Gamma}^P_{n-1,n}} \,. \tag{B.36}$$

Hence, the total transmission coefficient between layer m (source layer) and layer n (observation layer) is:

$$\overrightarrow{T}^P_{m,n} = \overrightarrow{\tau}^P_n \prod_{i=m+1}^{n-1} \overrightarrow{\tau}^P_i e^{-jk^P_{z,i}h_i} \tag{B.37}$$

with $m < n$.

In order to compute the required Green functions in (B.32) in the spectral domain, the auxiliary TLs problems should be solved, determining voltages and currents at the observation point z, when voltage and current sources are located at z'. The two possible cases will be addressed: z and z' are located in the same m^{th} ground layer (i.e., in the same m^{th} section of the equivalent configuration B.5); z and z' are located in different ground layers. To ease the notation, superscript $P = e, h$ are henceforth omitted, and the following quantities are introduced ($z > z'$):

$$\sigma = \begin{cases} +1 & T = V \\ -1 & T = I \end{cases}, \quad \sigma' = \begin{cases} +1 & T' = v \\ -1 & T' = i \end{cases} \tag{B.38}$$

$$s = \begin{cases} +1 & T = V \\ +\frac{1}{Z_m} & T = I \end{cases}, \quad s' = \frac{1}{2}\begin{cases} U & T' = v \\ Z_n J & T' = i \end{cases} \tag{B.39}$$

where $T = \{V, I\}$ denotes the electrical quantity of interest at the observation point, and $T' = \{v, i\}$ denotes the source type; U and J are to be considered as unitary amplitude of the lumped voltage and current sources; Z_m and Z_n are the characteristic impedances of the m^{th} and n^{th} TLs sections (defined in (B.33)).

Source and observation point laying in the same layer

Firstly, the source and the observation points are assumed to lay in the same layer m, with $z > z'$. The configuration may be investigated through the equivalent TL corresponding to layer m, loaded at both terminations. The loads are to be identified with the TLs corresponding to layers denoted with $n \neq m$. By manipulating the expression given in [17], the following is derived for the case $z > z'$:

$$T_{T'}(z, z') = ss' \left[e^{-jk_{z,m}|z-z'|} + \frac{1}{D_\Gamma} \sum_{i=1}^{4} a_i e^{-jk_{z,m}\delta_i} \right] \tag{B.40}$$

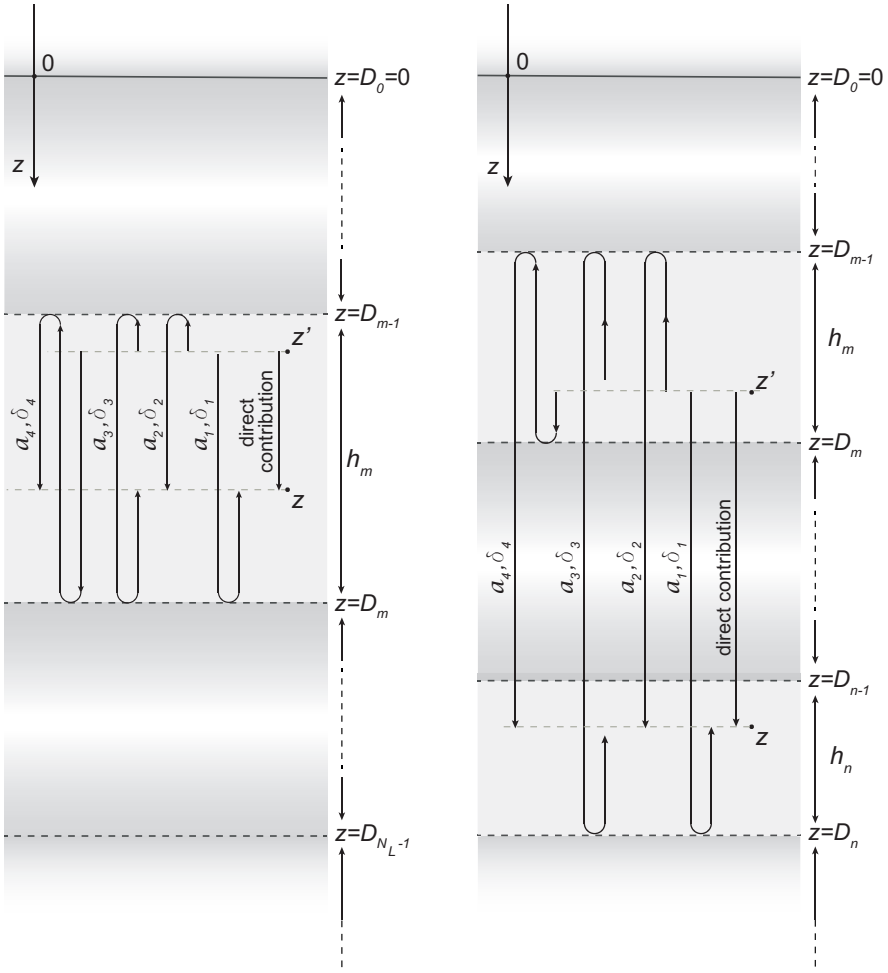

Figure B.6. Layered structure under investigation in the spectral domain, and intuitive representation of the contributions in (B.40) and (B.42) to the determination of voltages and currents at z when the source is located at $z' < z$. (a) Source and observation points are located in the same layer m; (b) source in layer m and observation point in layer n, with $n \neq m$.

with

$$\begin{aligned} a_1 &= \sigma\overrightarrow{\Gamma}_m & \delta_1 &= 2D_m - |z+z'| \\ a_2 &= -\sigma'\overleftarrow{\Gamma}_m & \delta_2 &= |z+z'| - 2D_{m-1} \\ a_3 &= -\sigma\sigma'\overrightarrow{\Gamma}_m\overleftarrow{\Gamma}_m & \delta_3 &= 2\left(D_m - D_{m-1}\right) - |z-z'| \\ a_4 &= \overrightarrow{\Gamma}_m\overleftarrow{\Gamma}_m & \delta_4 &= 2\left(D_m - D_{m-1}\right) + |z-z'| \end{aligned} \tag{B.41}$$

where the complex constant D_Γ, linked to the characteristics of the layer where the source is located, is derived from the relation $\overleftarrow{\Gamma}_m\overrightarrow{\Gamma}_m e^{-j2k_{z,m}h_m} = 1 - D_\Gamma$. An intuitive explanation of (B.41) is sketched in Fig. B.6a.

Source and observation point laying in different layers

Leaving the position of the source point unchanged, the observation point is supposed to be located in a different layer n, assuming $n > m$, with reference to Fig. B.6b. Following again the approach presented in [17], and manipulating the final expression of the sought electrical quantity to get an intuitive insight of its physical meaning, the following are obtained:

$$T_{T'}(z,z') = s\acute{s}\left[e^{-jk_{z,m}(D_m - z')}\overrightarrow{T}_{m,n}e^{-jk_{z,n}(z-D_{n-1})} + \frac{\overrightarrow{T}_{m,n}}{D_\Gamma}\sum_{i=1}^{4} a_i e^{-j\delta_i}\right] \tag{B.42}$$

with

$$\begin{aligned} a_1 &= \sigma\overrightarrow{\Gamma}_n & \delta_1 &= k_{z,m}\left(D_m - z'\right) + k_{z,n}\left[2\left(D_n - z\right) + \left(z - D_{n-1}\right)\right] \\ a_2 &= -\sigma'\overleftarrow{\Gamma}_m & \delta_2 &= k_{z,m}\left[2\left(z' - D_{m-1}\right) + \left(D_m - z'\right)\right] + k_{z,n}\left(z - D_{n-1}\right) \\ a_3 &= -\sigma\sigma'\overleftarrow{\Gamma}_m\overrightarrow{\Gamma}_n & \delta_3 &= k_{z,m}\left[2\left(z' - D_{m-1}\right) + \left(D_m - z'\right)\right] + k_{z,n}\left[\left(z - D_{n-1}\right) + \right. \\ & & & \left. + 2\left(D_n - z\right)\right] \\ a_4 &= \overrightarrow{\Gamma}_m\overleftarrow{\Gamma}_m & \delta_4 &= k_{z,m}\left[2\left(D_m - D_{m-1}\right) + \left(D_m - z'\right)\right] + k_{z,n}\left(z - D_{n-1}\right). \end{aligned} \tag{B.43}$$

The distinct contributions in (B.42) are identified in Fig. B.6b.

Method limitations

The method shows a limitation which is linked to an implicitly adopted low frequency approximation. In fact, conduction currents are accounted for by means of the scalar Green function G_ϕ, accepting for the voltage at any observation point to be approximated by the scalar electric potential ϕ. This is a good approximation of the real physics of the problem up to frequencies at which the electric field dependence on the magnetic vector potential may be neglected.

However, when it comes to any approach aiming at deriving equivalent circuits of devices under study, the validity of the definition of node voltage itself should be questioned when the tool is exploited to carry investigations at very high frequencies.

References

[1] L. Grcev, "High-frequency grounding," in *Lightning Protection*. IET, 2010, pp. 503–529.

[2] E. J. Rothwell and M. J. Cloud, *Electromagnetics*. CRC press, 2018.

[3] R. Araneo and S. Celozzi, "Transient behavior of wind towers grounding systems under lightning strikes," *Int. J. Energy Environ. Eng.*, vol. 7, no. 2, pp. 235–247, 2016.

[4] S. A. Schelkunoff, "The electromagnetic theory of coaxial transmission lines and cylindrical shields," *The Bell System Technical Journal*, vol. 13, no. 4, pp. 532–579, 1934.

[5] Visual Numerics, "IMSL Fortran numerical library user's guide, version 7.0," 2010.

[6] A. Sommerfeld, *Partial differential equations in physics*. Academic press, 1949.

[7] A. Erteza and B. Park, "Nonuniqueness of resolution of Hertz vector in presence of a boundary, and the horizontal dipole problem," vol. 17, no. 3, pp. 376–378, 1969.

[8] V. N. Kourkoulos and A. C. Cangellaris, "Accurate approximation of Green's functions in planar stratified media in terms of a finite sum of spherical and cylindrical waves," *IEEE Trans. Antennas Propag.*, vol. 54, no. 5, pp. 1568–1576, May 2006.

[9] K. A. Michalski and J. R. Mosig, "Multilayered media Green's functions in integral equation formulations," *IEEE Trans. Antennas Propag.*, vol. 45, no. 3, pp. 508–519, Mar. 1997.

[10] K. A. Michalski, "Extrapolation methods for Sommerfeld integral tails," *IEEE Trans. Antennas Propag.*, vol. 46, no. 10, pp. 1405–1418, Oct. 1998.

[11] I. Longman, "Note on a method for computing infinite integrals of oscillatory functions," in *Mathematical Proceedings of the Cambridge Philosophical Society*, vol. 52, no. 4. Cambridge University Press, 1956, pp. 764–768.

[12] J. R. Mosig, "Weighted averages and double exponential algorithms," *IEICE transactions on communications*, vol. 96, no. 10, pp. 2355–2363, 2013.

[13] H. Takahasi and M. Mori, "Double exponential formulas for numerical integration," *Publications of the Research Institute for Mathematical Sciences*, vol. 9, no. 3, pp. 721–741, 1974.

[14] A. G. Polimeridis and J. R. Mosig, "Fast computation of Sommerfeld integral tails via direct integration based on double exponential-type quadrature formulas," *IEEE Trans. Antennas Propag.*, vol. 59, no. 2, pp. 694–699, Feb. 2011.

[15] M. Mori and M. Sugihara, "The double-exponential transformation in numerical analysis," *J. Comput. Appl. Math.*, vol. 127, no. 1-2, pp. 287–296, Jan. 2001.

[16] L. B. Felsen and N. Marcuvitz, *Radiation and Scattering of Waves.* Piscataway, NJ: IEEE Press, 1994.

[17] P. Crespo Valero, "Electromagnetic modelling of planar circuits in bounded layered media," Ph.D. dissertation, EPFL, 2007.

Appendix C

Soil ionization

Soil ionization is a nonlinear phenomenon which, similarly to corona effect, occurs in the form of localised or distributed discharges in the proximity of the surfaces of grounding electrodes for large values of local electric fields. Similarly to corona, an hysteretic behaviour of the phenomenon was observed [1]; the current polarity was shown to affect the impulse resistance of the electrodes negligibly [2]. Models with different degree of complexity are available (e.g., the simple model by Cigré [3], and the model based on energy considerations by Sekioka *et al.* [4]) to simulate the development of soil ionization when high-peaked impulse currents are injected into the ground through suitable grounding electrodes.

Despite the majority of engineering approaches consider the soil ionization to develop with a rotational symmetry around the electrode, the high degree of nonlinearity of the phenomenon results in the formation of branched discharges which are affected by the electrode geometry, soil electrical properties and water content, and soil uniformity (size of the soil particles, pattern and dimension of air vacua, etc.) [5]. The influence of the commonly adopted approximations was investigated by Mousa in [6].

When dealing with intense currents flowing through grounding systems, e.g., when lightning strokes hit shield wires or towers of on overhead TL, soil ionization determines the favourable drop of the grounding impedance, limiting the ground potential rise; indeed, the discharge process may be equivalently studied in terms of a decrease in the resistivity ρ_g of the portion of soil subjected to ionization.

A three-zones model was introduced by Liew and Darveniza to account for the ionization development [1]. As in common studies on electric discharges, the critical field E_g is defined as the threshold field (orthogonal to the grounding electrode surface, modelled as a perfect conductor) causing the start of soil ionization.

The determination of the average critical electric field is complex, being dependent on the specific properties of the soil. Hence, common values in the range between 400 kV/m [3] and 1000 kV/m [7] are assumed, or derived by

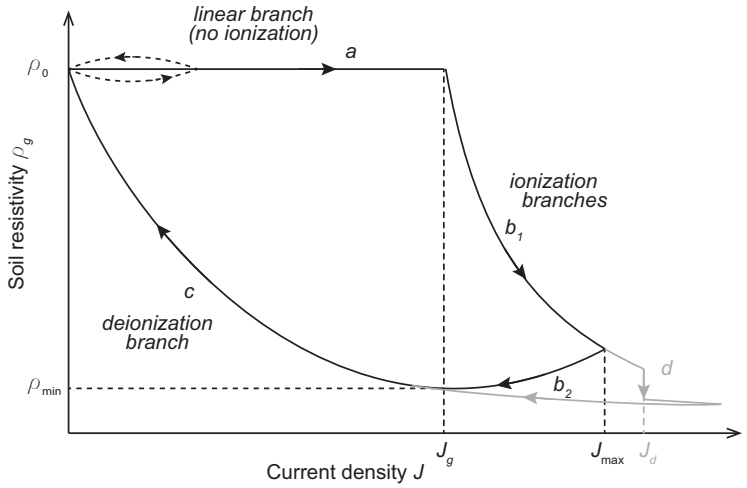

Figure C.1. Sketch of the soil resistivity dependence on the current density as from Liew *et al.* model (figure adapted from [1], [5]).

fitting simulation results to experimental data.

The critical current density J_g and critical electric field E_g are linked by means of the local Ohm's law $E_g = \rho_g J_g$. Branch a of the $\rho_g - J$ hysteresis curve in Fig. C.1 corresponds to low current densities, resulting in a constant-valued soil resistivity ρ_0 and no soil ionization. Branches b_1, b_2, and c display a nonlinear relation between the electric soil resistivity and the current density. In the first zone, the actual ionization zone (represented by branches b_1 and b_2 in Fig. C.1), the soil resistivity $\rho_g(t, J)$ decreases; after the maximum current density, $J_{\max}$, is reached, the soil resistivity decreases continuously as the current density is reduced again to the value $J(t) = J_g$ (branch b_2). In the third zone, or deionization zone (i.e., branch c), the soil resistivity increases again, until its original low-current value is restored. It should be noted that a dynamic change with time is assumed for ρ_g, even though Fig. C.1 represents just its dependence on the current density:

$$\rho_g(t, J) = \begin{cases} \rho_0 & J < J_g \\ \rho_0 \exp\left[\frac{-(t-t_1)}{\tau_1}\right] & J \geq J_g, t \geq t_1 \\ \rho_{\min} + (\rho_0 - \rho_{\min})\left(1 - \exp\left[\frac{-(t-t_2)}{\tau_2}\right]\right)\left(1 - \frac{J}{J_g}\right)^2 & J \leq J_g, t \geq t_2. \end{cases} \tag{C.1}$$

In (C.1), t_1 and t_2 (derived empirically) are the time constants associated with the ionization and deionization of the soil, respectively; t_1 denotes the time instant at which the critical current density is injected in the soil (causing the start of the ionization process), and t_2 is the time instant at which the soil deionization is considered to occur (namely, after the current density reaches again the critical value J_g, in correspondence with the minimum soil resistivity $\rho_{\min}$). Some simplified approaches assume that the largely decreased soil resistivity in the conductor's surroundings ($\rho_{\min} < 0.1\rho_0$, as from [5]) may

be represented by a fictitious increase in the grounding electrode dimensions [8], [9].

An extended phenomenological interpretation of the soil ionization phenomenon was proposed by He and Zang [5], who introduced an additional branch (i.e., the grey trace in Fig. C.1): if the current density exceeds a limit value J_d (associated with a different – empirically derived [7] – critical electric field) a sharp decrease in the soil resistivity may be observed (branch d) due to the development of relevant arc discharges in the soil.

References

[1] A. Liew and M. Darveniza, "Dynamic model of impulse characteristics of concentrated earths," in *Proceedings of the Institution of electrical Engineers*, vol. 121, no. 2. IET, 1974, pp. 123–135.

[2] P. Bellaschi, R. Armington, and A. Snowden, "Impulse and 60-cycle characteristics of driven grounds—II," *Electrical Engineering*, vol. 61, no. 6, pp. 349–363, 1942.

[3] *CIGRE Technical Brochure 63: Guide to procedures for estimating the lightning performance of trasmission lines*, CIGRE Std., 1991.

[4] S. Sekioka, M. I. Lorentzou, M. P. Philippakou, and J. M. Prousalidis, "Current-dependent grounding resistance model based on energy balance of soil ionization," *IEEE Trans. Power Del.*, vol. 21, no. 1, pp. 194–201, 2005.

[5] J. He and B. Zhang, "Progress in lightning impulse characteristics of grounding electrodes with soil ionization," *IEEE Trans. Ind. Appl.*, vol. 51, no. 6, pp. 4924–4933, 2015.

[6] A. M. Mousa, "The soil ionization gradient associated with discharge of high currents into concentrated electrodes," *IEEE Trans. Power Del.*, vol. 9, no. 3, pp. 1669–1677, 1994.

[7] E. Oettle, "A new general estimation curve for predicting the impulse impedance of concentrated earth electrodes," *IEEE Trans. Power Del.*, vol. 3, no. 4, pp. 2020–2029, 1988.

[8] R. Velazquez and D. Mukhedkar, "Analytical modelling of grounding electrodes transient behavior," *IEEE Trans. Power App. Syst.*, no. 6, pp. 1314–1322, 1984.

[9] Z. G. Datsios, P. N. Mikropoulos, E. T. Staikos, T. E. Tsovilis, D. Vlachopoulos, and S. Ganatsios, "Laboratory measurement of the impulse characteristics of wet sand," in *2020 IEEE International Conference on Environment and Electrical Engineering and 2020 IEEE Industrial and Commercial Power Systems Europe (EEEIC/I&CPS Europe)*. IEEE, 2020, pp. 1–6.

List of acronyms

AC Alternating Current.

ADI Alternating Direction Implicit.

BIL Basic Insulation Level.

CFL Courant–Friedrichs–Lewy.

CN Crank-Nicolson.

DC Direct Current.

EM Electromagnetic.

EMI Electromagnetic Interference.

EMTP Elecgromagnetic Transients Program.

FD Frequency Domain.

FDTD Finite-Difference Time-Domain.

GPR Ground Potential Rise.

HV High Voltage.

HVDC High Voltage Direct Current.

IEMI Intentional Electromagnetic Interference.

IFT Inverse Fourier Transform.

IVP Initial Value Problem.

KCL Kirchhoff Current Law.

KVL Kirchhoff Voltage Law.

LF Leap-Frog.

LHS Left Hand Side.

MOV Metal Oxide Varistor.

MTL Multiconductor Transmission Line.

MTLD Modified Transmission Line model with Derived attenuation function.

MTLE Modified Transmission Line model with Exponential attenuation.

MTLL Modified Transmission Line model with Linear attenuation.

MV Medium Voltage.

p.u. per unit.

p.u.l. per unit length.

PEC Perfect Electric Conductor.

RHS Right Hand Side.

SW Shield Wire.

TD Time Domain.

TE Transverse Electric.

TEM Transverse Electromagnetic.

TL Transmission Line.

TM Transverse Magnetic.

UGW Underbuilt Ground Wire.